ISSN 1573-160X

Vol. 32, Iss. 1 January – February 2025

Physical Oceanography

http://physical-oceanography.ru/

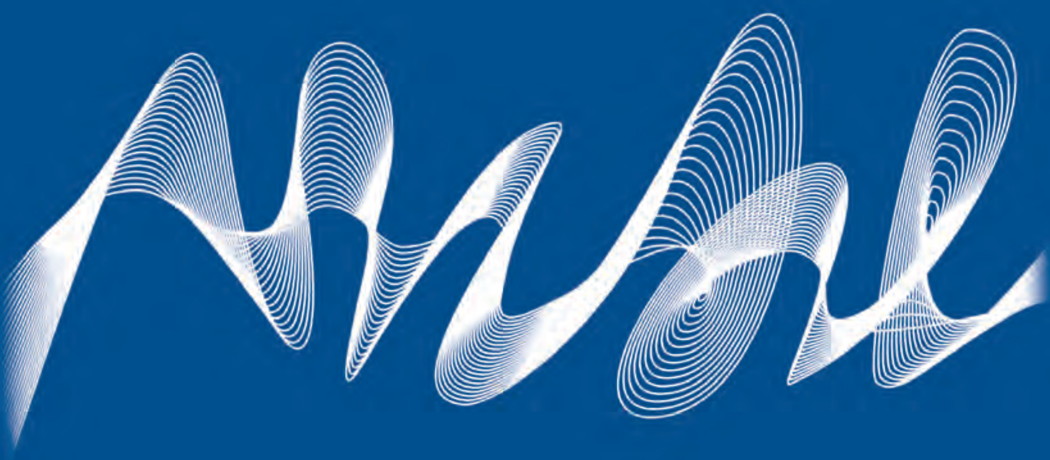

CONTENTS

Vol. 32, no. 1. 2025 **January – February, 2025**

THERMOHYDRODYNAMICS OF THE OCEAN AND THE ATMOSPHERE

ANALYSIS OF OBSERVATIONS AND METHODS OF CALCULATING HYDROPHYSICAL FIELDS IN THE OCEAN

EXPERIMENTAL AND FIELD RESEARCH

MATHEMATICAL MODELING OF MARINE SYSTEMS

SATELLITE HYDROPHYSICS

ISSN 1573-160X, *PHYSICAL OCEANOGRAPHY*, VOL. 32, Iss. 1, pp. 3-16 (2025)
Original Russian Text © D. A. Iarovaia, V. V. Efimov, 2025,
published in *Morskoy Gidrofizicheskiy Zhurnal*, 2025, Vol. 41, Iss. 1, p. 5–19

Original article

Numerical Modeling of Winter Cooling in the Black Sea

D. A. Iarovaia ✉, V. V. Efimov

Marine Hydrophysical Institute of RAS, Sevastopol, Russian Federation
✉ *darik777mhi-ras@mail.ru*

Abstract
Purpose. The work is aimed at studying the changes in the thermal structure of the Black Sea upper layer during seasonal winter cooling in 2009−2010.
Methods and Results. The NEMO-OASIS-WRF (NOW) coupled sea-atmosphere mesoscale model with the 2 km horizontal resolution is used. The changes in the sea upper layer during the 01.12.2009–28.02.2010 period are reproduced, and the temporal variability of water temperature at different depths is considered. For a characteristic point in the deep-sea part, it has been shown that the upper mixed layer thickness increased with time, whereas the cold intermediate layer upper boundary lowered as a result of the entrainment of colder water from below to the warmer upper mixed layer. It is also indicated that lowering of the cold intermediate layer upper boundary is accompanied by an increase of its temperature. In order to describe the cold intermediate layer evolution during winter cooling, two criteria are proposed: minimum water temperature in the 0−120 m layer, and difference between this value and the sea surface temperature. Vertical temperature profiles at different stages of winter cooling are obtained, and the main changes in thermal structure of the sea upper layer are considered. It is particularly shown that in course of winter cooling, the cold but less salty water at the northwestern shelf does not mix with the open sea waters due to a large horizontal density gradient.
Conclusions. When describing the seasonal winter changes in the upper mixed layer, it is necessary to take into account not only heat transfer to the atmosphere through its upper boundary, but also the vertical turbulent exchange through its lower boundary. Heat accumulated over summer in the upper mixed layer is transferred not only to the atmosphere; its small part also goes to the lower levels, which leads to an increase of the cold intermediate layer temperature. The influence of boundary conditions, namely the inflow of waters with different features from the Marmara Sea, can lead to the formation of areas where the cold intermediate layer, though formally absent as a layer between two 8 °C isotherms, exists as an intermediate layer of colder (by 3−4 °C) water as compared to the upper mixed layer. During the 2009−2010 winter, vertical mixing including the transfer of warmer and less salty waters from the upper mixed layer to the lower ones was most intensive in the western part of the sea. This fact is assumed to be a result of the inhomogeneous sea cooling: heat flux directed from the sea surface to the atmosphere decreases from 200 W/m^2 in the northwestern part of the sea up to 50 W/m^2 in its southeastern part.

Keywords: mesoscale coupled modeling, NOW sea-atmosphere model, cold intermediate layer, winter cooling, Black Sea

Acknowledgements: The study was carried out within the framework of state assignment on theme FNNN-2024-0014 "Fundamental studies of interaction processes in the ocean-atmosphere system determining variability of physical state of marine environment at various spatiotemporal scales".

For citation: Iarovaia, D.A. and Efimov, V.V., 2025. Numerical Modeling of Winter Cooling in the Black Sea. *Physical Oceanography*, 32(1), pp. 3-16.

Introduction

A notable characteristic of the vertical structure of the upper layer of the northern seas is the presence of a low-temperature layer, which is the result of seasonal winter cooling from the sea surface. This layer is limited from below by a stable layer of increased salinity, known as the halocline, and is overlaid in summer by a warm upper mixed layer (UML) and a seasonal thermocline. The cold intermediate layer (CIL) is a distinctive feature of the northern seas, particularly in regions with relatively low winter temperatures. These include the North Atlantic, specifically the Baltic Sea, and the Black Sea.

The CIL development is based on the thermal structure of the upper sea layer, which is formed during the final stage of seasonal autumn-winter cooling. Following the termination of seasonal cooling, the cold layer can occupy the entire upper section of the sea up to the surface, thereby no longer serving as an intermediate layer. The subsequent development of this cold region, together with the onset of seasonal heating, and its subsequent formation as an intermediate layer located under the summer thermocline is influenced by various factors, including dissipation rates and advective processes within the layer itself. According to the processing data of buoy measurement results in the sea, the isolated CIL lifetime can reach two to three years [1].

The primary reason for the CIL renewal is linked to the uneven seasonal cooling of the upper Black Sea layer during the autumn-winter period. As is known, the most pronounced UMC cooling occurs in the central regions of the western and eastern cyclonic gyres within the deep-water part of the sea, while in the shallow areas, it is evident on the northwestern shelf (NWS) [1] [2, 3]. These colder waters subsequently spread to the rest of the sea, descending along the main pycnocline to the periphery of the gyres and being transported by the alongshore Rim Current and the coastal mesoscale eddies associated with it [4–6]. In addition to long-term and gradual seasonal cooling, the Black Sea also experiences short periods of intense UML cooling during cold air intrusions (in the western part of the sea) [7, 8] and the Novorossiysk bora (in the eastern part) [9].

The cold intermediate layer in the Black Sea has exhibited considerable variation over time, manifesting interannual fluctuations. Studies of its interannual variability have been conducted repeatedly, using both observational data [10, 11] and numerical models [12]. These studies have revealed that in some years the CIL also experiences periods of absence. In the last decade, this tendency of significant weakening and even disappearance of the CIL has been discussed in the literature and is sometimes associated with global warming [13–15].

A typical example of the temporal variability of CIL is the period of 2009–2010. Below, the process of CIL destruction during the winter cooling of late 2009 – early 2010 will be examined. This process was reproduced in a coupled atmosphere-sea model with high spatial resolution. In our previous work [7], numerical experiments were carried out on a shorter time interval of 5 days to determine the sensitivity to individual physical mechanisms of deep penetrating cooling.

---

[1] Filippov, D.M., 1968. *Circulation and Structure of the Black Sea Waters*. Moscow: Nauka, 136 p. (in Russian).

Numerical modeling in brief

The parameters selected for the NEMO-OASIS-WRF (NOW) coupled mesoscale model [16], consisting of the WRF atmospheric model and the NEMO marine model, are described in more detail in our previous works [7]. The spatial resolution of the coupled model was 2 km. The atmospheric model incorporated 37 vertical levels, while the marine model used 75 levels, with 38 of these levels located within the upper 100-meter layer. The Yonsei University scheme was employed to parameterize the planetary boundary layer in WRF and the Generic Length Scale scheme was used to parameterize vertical turbulent mixing in NEMO. Output interval of the modeling results was 1 hour. The initial conditions for the marine model, as well as the bottom topography, were taken from the Copernicus global reanalysis with a resolution of 1/12°, and the initial and boundary conditions for the atmospheric model were taken from the ERA5 reanalysis. The calculation was performed from December 1, 2009 to February 28, 2010. The atmospheric model employed a technique known as spectral "nudging", which involves correction of atmospheric fields every 6 hours during the course of the modeling process, thereby aligning them with large-scale reanalysis fields.

Vertical structure of the upper sea layer

Figure 1 shows the time course of the sea surface temperature (SST) and the temperature at 60 and 80 m depths, along with the surface wind speed and the total (sensible + latent + shortwave + longwave) heat flux from the surface. It is evident (Fig. 1, *c*) that during the first two months of the seasonal winter cooling, the surface temperature demonstrated a consistent decline from 14 °C to a minimum of ~ 8 °C. The temperature graphs also show inertial oscillations with a period of ~ 17 h.

A notable feature that deviates from the prevailing trend of upper layer cooling is evident in two episodes of a sharp increase in the rate of decrease in SST: December 12–16, 2009, and particularly January 22–27, 2010 (highlighted in Fig. 1 with black circles). These episodes are accompanied by a sharp increase in surface wind speed and an increase in the heat flux from the sea surface to the atmosphere (Fig. 1, *a*, *b*). The latter episode, characterized as a case of cold air intrusion into the atmosphere of the Black Sea region, has been previously studied [7].

Figure 1, *c* also shows that in December and January the SST variations (*sst* graph) do not affect the CIL temperature (t_{60} and t_{80} graphs). However, beginning in February, the SST has dropped below 8 °C, and the temperature fluctuations at the three levels have occurred in approximately the same phase. This indicates that the vertical mixing in February covers the entire upper layer, extending down to the 80 m depth.

Figure 2 illustrates the changes in the vertical structure of the temperature field throughout the considered period of winter cooling. The upper mixed layer is clearly visible, exhibiting a decline in temperature to 8 °C with the depth increase from the initial value of 35 m to > 50 m. A notable characteristic of the CIL transformation is its reduction in thickness, leading to its dissolution as an intermediate cold layer. The observed decrease in CIL thickness is due to the lowering of the upper boundary of this layer.

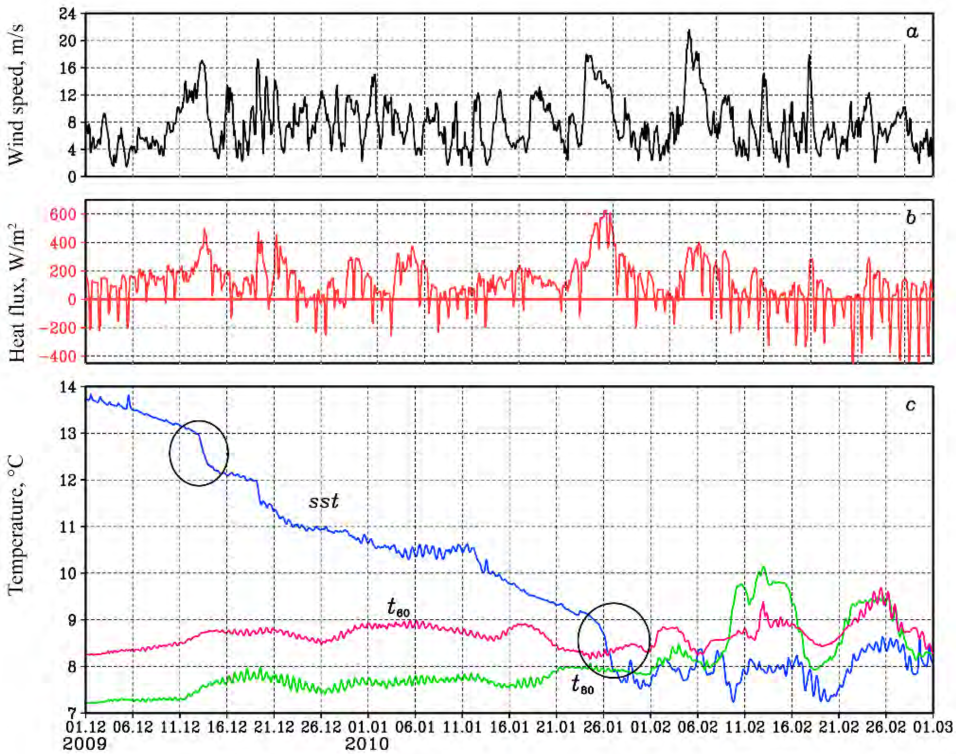

F i g. 1. Temporal changes of wind speed at the 10 m height (*a*), total heat flux (*b*) and water temperature at the surface and at depths 60 and 80 m (*c*) at point 32°E, 43.5°N for the period 01.12.2009–28.02.2010 (two cases of sharp drops in sea surface temperature are highlighted by black circles)

The nature of the change in the upper layer parameters during seasonal cooling is demonstrated more clearly by the vertical profiles of temperature, salinity gradient dS/dz and buoyancy frequency N, as shown in Fig. 3 for the same point as in Fig. 2. The profiles are shown for three successive moments of time: December 3, 2009 (the beginning of the calculation period), January 20, 2010 (the middle of the period, immediately before the beginning of the last episode of cold invasion) and February 28, 2010 (the end of the calculation period). The aforementioned feature of CIL transformation at the final stage of its disappearance is clearly visible. The physical mechanism of this phenomenon, i.e., the lowering of its upper boundary, is the entrainment of colder water into the warmer UML. It should be noted that the mechanism of entrainment at the lower UML boundary at the initial stage of autumn deepening is well-known and has been the subject of many studies [17].

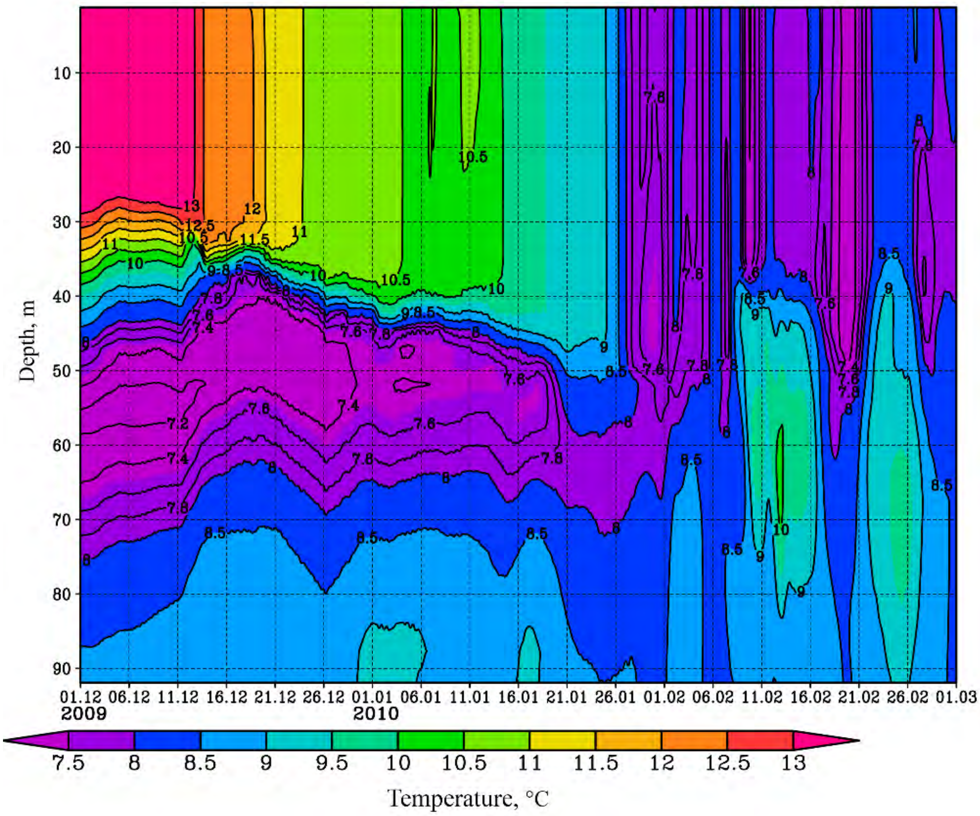

F i g. 2. Change in vertical temperature profiles at point 32°E, 43.5°N for the period 01.12.2009–28.02.2010. The temperature field is smoothed over time using a sliding average of 17 points

Lowering of the upper CIL boundary in December and January is accompanied by strengthening of the halocline (Fig. 3, *b*). In contrast to temperature, salinity is predominantly influenced by advection and vertical mixing, with the effect of evaporation from the sea surface being negligible. Over the duration of three months, the total change in salinity at the sea surface in the specified area was < 2% (for comparison, the SST change was ≈ 40%). It is evident that, even after the first month of calculation, the water temperature at the point of interest changes slightly with depth (Fig. 3, *a*), and stable stratification in the 40–60 m layer is ensured exclusively by the vertical salinity gradient. According to Fig. 3, *b*, *c*, the *dS/dz* and *N* graphs for January and February are very similar.

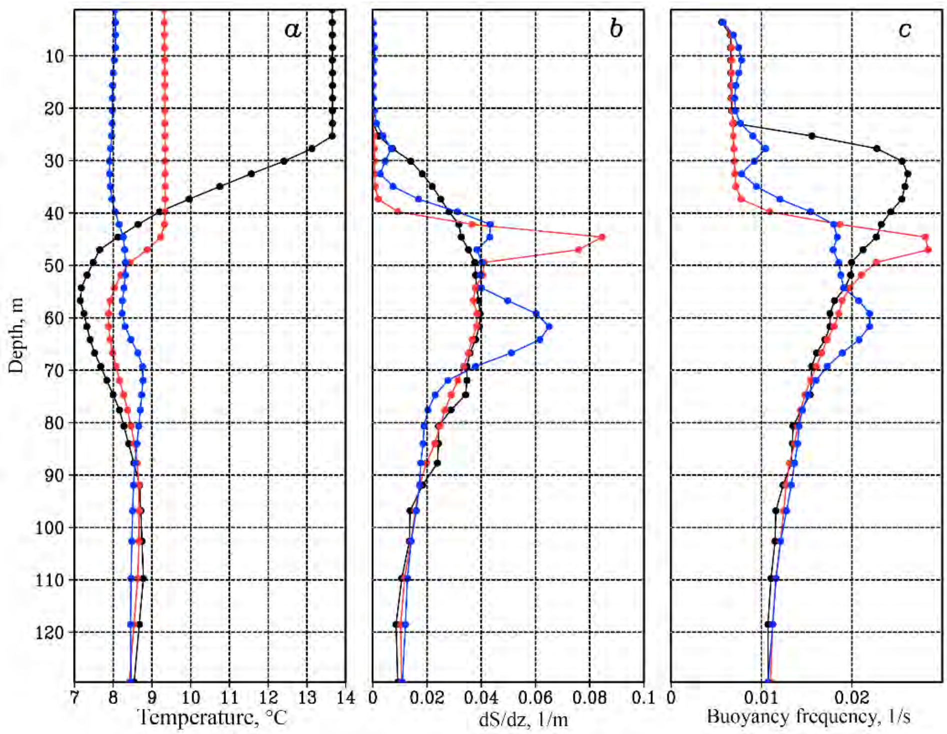

F i g. 3. Profiles of temperature (*a*), vertical salinity gradient (*b*) and buoyancy frequency (*c*) at point 32°E, 43.5°N in December (black curve) 2009, January (red curve) and February (blue curve) 2010

The buoyancy frequency graphs describe the CIL disappearance well. As the temperature equalizes with depth, it is evident that the buoyancy frequency decreases (Fig. 3, *c*). The *N* maximum falls on the lower boundary of the UML, and as this layer deepens, it also shifts downwards.

Figures 2, 3 show that the lowering of the upper CIL boundary is accompanied by an increase in its temperature. Over the course of two months, the minimum temperature in the CIL at the point under consideration increased from 7 to 8 °C. Consequently, during the seasonal UML cooling phase, a portion of the heat accumulated during summer does not fully escape into the atmosphere. Instead, some of this heat is transferred to the underlying levels, resulting in a reduction in the cold reserve of the CIL and its subsequent disappearance as an intermediate layer in depth.

Spatial structure of CIL

The spatial distribution of the CIL in the Black Sea is not as easily delineated as the individual parameters of the marine environment, such as temperature or salinity. This is due to the uncertainty and variability of the determining parameters. Traditionally, CIL in the Black Sea has been defined as a layer within the boundaries of the 8 °C isotherms. However, recently the criteria of 8.35 and 8.7 °C have also been used [18]. The average depth of the CIL in the Black Sea is 60 m, but in coastal regions it can reach depths of 100–120 m. To illustrate the changes in the spatial distribution of the CIL in the Black Sea, the water temperature fields at different depths are examined directly, rather than relying on formal criteria.

Figure 4, *a*, *c*, *e*, shows the spatial distribution of the minimum water temperature (t_{min}) in the upper 120 m layer, which is essentially the CIL core temperature, on 1 December 2009, 10 January and 26 February 2010. The arrows indicate the currents at the 20 m depth. Figure 4, *b*, *d*, *f*, shows the difference (Δt) between t_{min} and sea surface temperature for the aforementioned time moments. The Δt can be considered as the temperature difference between the UML and the CIL core. This value may be crucial when contemplating the role of the CIL in regulating heat and mass exchange between the UML and the halocline.

Figure 4, *a*, *b*, shows that at the beginning of intense winter cooling in the shallow part of the sea north of 44.5°N, as well as along the western and southwestern coast, the water temperature in the entire layer down to the bottom was above 11−12 °C. In the areas where depth < 30 m, the water is well mixed vertically, and the temperature difference $|\Delta t| < 0.1$ °C. In the deep-water part, the CIL is well expressed: the temperature of its core is 7−8 °C, and the Δt varies from −8 to −4 °C. An exception to this phenomenon is observed in the southwestern part of the sea, where t_{min} values are relatively large: temperature from the surface to a depth of 120 m is above 9−10 °C, i.e., formally, the CIL is absent. The underlying cause of this anomaly is attributed to the inflow of warmer and saltier waters from the Sea of Marmara, resulting in the presence of deep positive anomalies in the temperature and salinity fields. It is noteworthy that these anomalies are present in the initial conditions of the NEMO marine model, as represented by the Copernicus data. Based on Fig. 4, *a*, *b*, the absence of a formal CIL as a layer between the 8 °C isotherms does not necessarily imply the absence of a temperature drop with depth. In the regions of increased t_{min} values, the temperature difference between the intermediate layer core and the UML can reach 4 °C.

The modeled field of near-surface currents contains known features of the Black Sea circulation. In particular, in Fig. 4, *a*, coastal anticyclonic eddies in the Rim Current area, such as the Sevastopol, Kaliakra and Bosphorus gyres with centers at (32.5°E, 44.5°N), (29.2°E, 43.7°N) and (28.5°E, 42.5°N), as well as a cyclonic gyre specific for winter in the southeastern corner of the sea (41°E, 42°N), are distinguished.

Figure 4, *c*, *d* shows the same fields as Fig. 4, *a*, *b*, but one and a half months after the calculation period began. As can be seen, in the northern part of the sea, there is still a clear boundary between the warmer and less salty waters of the NWS and the coastal area and the denser waters of the open sea. The water temperature in the shallow part is still relatively high, > 9 °C, and only north of 44.5° N, where depth < 30 m, cold waters with a temperature of 6−7 °C are observed. In the deep part of the sea, the $|\Delta t|$ value is found to be less than at the beginning of the calculation, with a range of 2 to 4 °C.

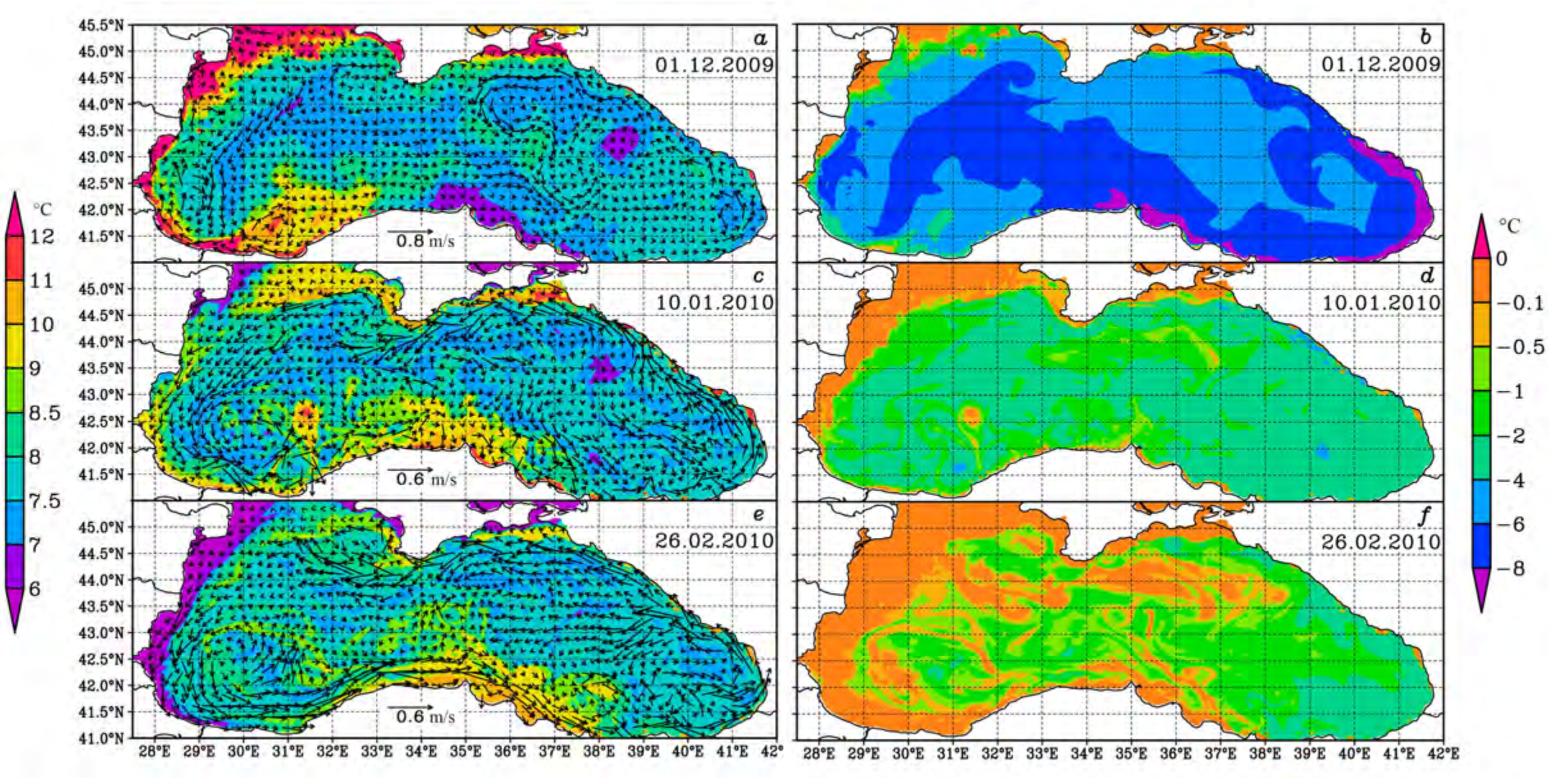

F i g. 4. Minimum water temperature, $t_{\min}$, in the 0–120 m layer (*left*) and difference $t_{\min} - \mathrm{SST}$ (*right*). Vectors show current velocity at the 20 m depth

Figure 4, *c*, *e* shows the impact of the currents on the spatial distribution of the water temperature. The influence of the Black Sea Rim Current caused an anomaly of warm salt water from the southwestern part to shift along the coast to the central and southeastern parts of the sea. This anomaly was slightly captured by the western cyclonic gyre (WCG), which led to the emergence of small positive anomalies of $t_{\min}$ in the southwestern part of the sea, even after the main anomaly shifted to the east.

Figure 4, *b*, *d*, *f* illustrates the dissipation of the CIL in the deep-water part of the sea, attributable to winter cooling and vertical mixing. According to Fig. 4, *f*, two months after the start of the calculations along the northern branch of the Rim Current, in the Kerch cyclonic gyre (36°E, 44.5°N), as well as on the WCG periphery, $|\Delta t|$ did not exceed 0.1 °C. In this region, the temperature was equalized in depth within the upper 120-meter layer, leading to the dissipation of the CIL. Following two months of winter cooling, the CIL was best preserved in the southeastern part of the sea, where the temperature difference ranged from −4 to −2 °C. In contrast, in the western part, the absolute value of Δt did not exceed 2 °C.

The subsequent analysis will address the changes in the vertical structure of the temperature field throughout the sea during seasonal cooling. Figures 5 and 6 show the temperature fields for three distinct time moments on vertical sections drawn along 43.5°N and 31.5°E. As illustrated in Fig. 5, in the eastern part of the sea, with the exception of the area near the Caucasian coast, the upper boundary of the CIL is located at a slightly higher level than in the western part. The difference in occurrence depth reaches 10 m. Figure 5, *a*, *b* demonstrates the lowering of the upper boundary of the CIL during seasonal cooling, attributable to the increase in UML thickness. In the region west of 31°E, the UML thickness increased by 10 m over the span of nearly a month and a half (Fig. 5, *b*). In contrast, in the eastern part, the lowering of the upper boundary of the CIL is negligible due to the rise of 8–9 m in the layer core, caused by the intensification of the eastern cyclonic circulation during winter. In the western part, the rise in the cold-sea layer core was less pronounced, with an increase of 3–4 m.

Two months after the calculation start, the CIL remained predominantly in the eastern part of the sea, with a depth of 40–50 m within the 35–38°E region and 80–90 m near the Caucasian coast (Fig. 5, *c*). It is noteworthy that by the end of the calculation, a warm intermediate layer had already formed in certain areas at depths of 60 m. This layer consists of water with a higher (> 0.5–1 °C) temperature compared to the SST, explained by the strengthening of the main halocline during seasonal cooling and the subsequent vertical mixing.

As illustrated in Figs. 4, 5, the mixing of warmer and fresher waters from the UML to the underlying levels appears to have been most intense in the western part of the sea. This may be due to the uneven cooling of the sea during the period under consideration. It is indicated that the heat flux directed from the sea surface to the atmosphere decreases from 200 W/m^2 in the northwestern part of the sea to

50 W/m^2 in the southeastern one (not shown). This, in turn, is due to the non-uniform distribution of surface wind speed and air temperature. In the northwestern part, the mean values of wind speed and air temperature, averaged over a period of time, were ~ 10 m/s and 0 °C, in the southeastern part these values were ~ 5 m/s and 10 °C.

The heat flux from the surface (Q) is one of the two primary factors changing the SST in combination with vertical mixing [7]. The change in the UML temperature can be calculated by adding up the quantities $\frac{3600}{C_p \rho} \frac{Q_i}{h_i}$, where C_p and ρ represent the heat capacity and seawater density, respectively; h_i is the thickness of the mixed layer at the i-moment in time (defined in the model as the level depth below which the turbulent exchange coefficients are negligible); Q_i denotes the heat flux at the i-moment in time; 3600 s is the time step with which the modeling results were output. For the section in Fig. 5, *c*, the decline in temperature over a period of two months is ~ 4.5−5 °C in the western and 3.5−4 °C in the eastern deep-water part of the sea.

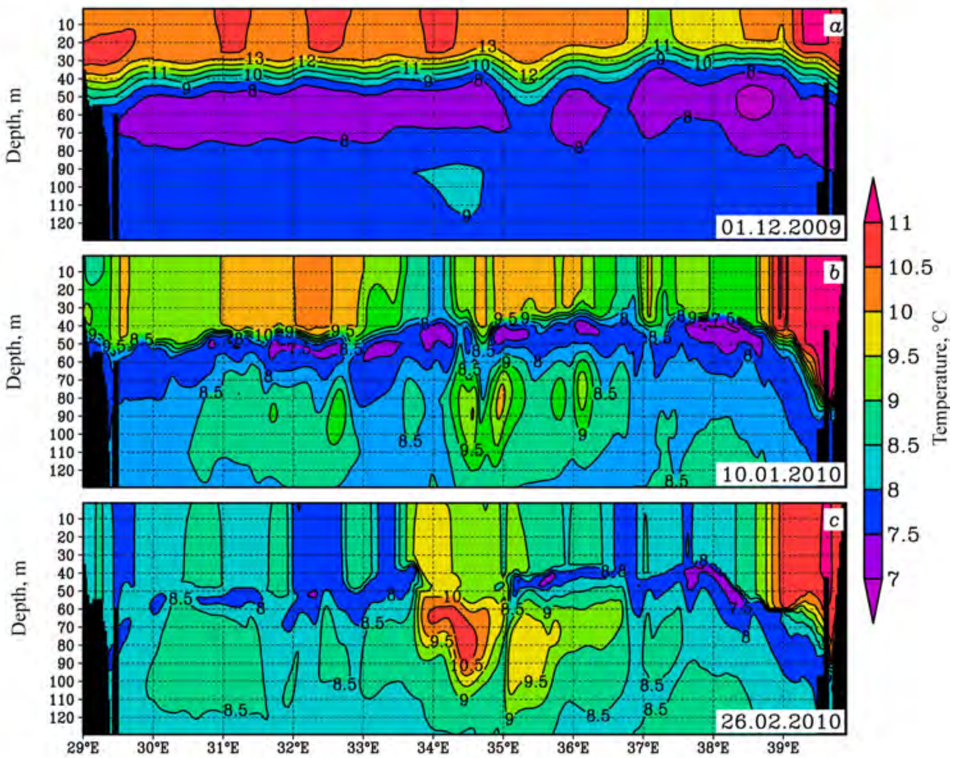

F i g. 5. Water temperature on a vertical section along 43.5°N for the same periods as in Fig. 4. Land is shaded in black

The vertical structure of the temperature and density fields in the NWS region was analyzed over time on a meridional section drawn along 31.5°E (Fig. 6). At the beginning of the calculation, to the south of 42.5°N, the area of waters with relatively high temperatures, as shown in Fig. 4, *a*, was clearly delineated. The average depth of the CIL on the section is 60 m, and its core temperature varies from 7–7.5 °C in the northern part of the section to 9–10 °C in the southern. The temperature difference between the CIL and the UML is significant even in the southern part, reaching 3–4 °C (Fig. 6, *a*).

As the seasonal cooling develops in the coastal region, a deflection of the primary pycnocline emerges and intensifies within the area of the continental slope (Fig. 6, *c*). Subsequently, following the winter cooling, the coastal region experiences an accumulation of relatively warm water, with the temperature 1°C higher than the surrounding environment (44.5–44.7°N). The eastern current velocity in this area also reaches high values, up to 0.6 m/s (not shown). Apparently, the elevated temperature values in the area of the continental slope are maintained by the Rim Current, which transports warm water (Fig. 4, *e*). At the same time, the cold water of the NWS does not mix with the waters of the open sea due to the presence of a large horizontal density gradient (Fig. 6, *c*).

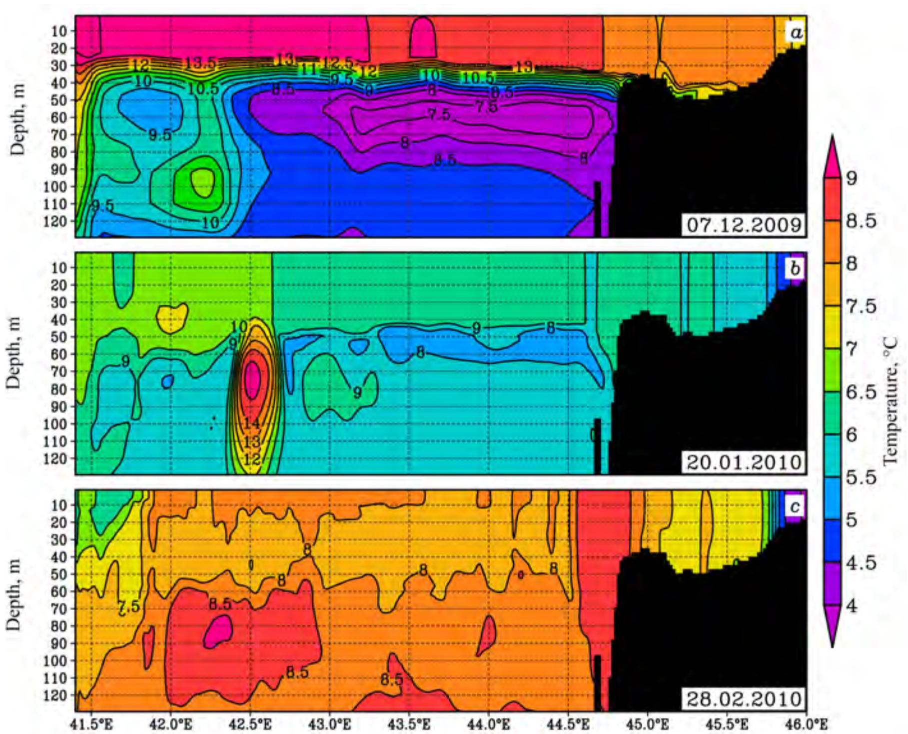

F i g. 6. Water temperature on a vertical section along 31.5°E. Land is shaded in black

It should be noted that the considered example and the CIL development features refer to a period in which the winter cooling was sufficiently intense to allow deep penetrating cooling to occur within the CIL area. In the case of a warmer winter season, the subsequent CIL development in the following year occurs in the context of a cold layer preserved underneath it.

Conclusion

The present paper explores the evolution of the CIL during seasonal cooling, using the winter of 2009–2010 as a case study. It has been demonstrated that when describing the seasonal winter changes in the UML, it is necessary to take into account not only the heat transfer to the atmosphere through the upper boundary, but also the vertical turbulent exchange through the lower boundary. This process leads to a gradual increase in the CIL temperature and a decrease in thickness due to the upper boundary lowering.

During the winter cooling season, the penetration of colder and saltier waters into the UML results in the strengthening of the halocline at depths of 40–60 m. This phenomenon ensures the preservation of high values of buoyancy frequency in the upper layer, despite the almost complete disappearance of the vertical temperature gradient.

It has been demonstrated that the influence of boundary conditions, manifesting as an inflow of waters with distinct properties from the Sea of Marmara, can significantly change the spatial distribution of the CIL. In the regions characterized by elevated temperatures, the CIL, despite its formal absence as a layer between two 8 °C isotherms, manifests as an intermediate layer of colder water (> 3−4 °C) in comparison to the UML. During this period, with minor exceptions, the cold intermediate layer occupies the greater portion of the sea.

A comparison of the western and eastern parts of the sea reveals a difference in the intensity of mixing. Following a two-month period of winter cooling, the CIL remained predominantly in the southeastern part. This can be due to the uneven cooling of the sea during the specified period. The heat flux directed from the sea surface to the atmosphere was ~ 200 W/m^2 in the northwestern part of the sea and ~ 50 W/m^2 in the southeastern part.

The modeled zonal temperature sections demonstrate that, in the western part of the sea, seasonal cooling resulted in an increase in the UML thickness. In the eastern part, the UML thickness increase was accompanied by an intensive rise in the main core of the CIL due to the activation of the winter circulation in the Black Sea.

The meridional sections of temperature, density, and current velocity demonstrate that, in the case under consideration, the vertical distribution of temperature in the northwestern part of the sea, in the area of the continental slope, was determined mainly by the warm Black Sea Rim Current.

REFERENCES

1. Akpinar, A., Fach, B.A. and Oguz, T., 2017. Observing the Subsurface Thermal Signature of the Black Sea Cold Intermediate Layer with Argo Profiling Floats. *Deep Sea Research Part I: Oceanographic Research Papers*, 124, pp. 140-152. https://doi.org/ 10.1016/j.dsr.2017.04.002

2. Ivanov, L.I., Beşiktepe, Ṣ. and Özsoy, E., 1997. The Black Sea Cold Intermediate Layer. In: E. Özsoy and A. Mikaelyan, eds., 1997. *Sensitivity to Change: Black Sea, Baltic Sea and North Sea*. Dordrecht: Springer, pp. 253-264. https://doi.org/10.1007/978-94-011-5758-2_20

3. Ovchinnikov, I.M. and Popov, Yu.I., 1987. Evolution of the Cold Intermediate Layer in the Black Sea. *Oceanology*, 27(5), pp. 739-746.

4. Stanev, E.V., Bownam, M.J., Peneva, E. and Staneva, J.V., 2003. Control of Black Sea Intermediate Water Mass Formation by Dynamics and Topography: Comparison of Numerical Simulations, Surveys and Satellite Data. *Journal of Marine Research*, 61(1), pp. 59-99. https://doi.org/10.1357/002224003321586417

5. Staneva, J.V. and Stanev, E.V., 1997. Cold Intermediate Water Formation in the Black Sea. Analysis on Numerical Model Simulations. In: E. Özsoy and A. Mikaelyan, eds., 1997. *Sensitivity to Change: Black Sea, Baltic Sea and North Sea*. Dordrecht: Springer, pp. 375-393. https://doi.org/10.1007/978-94-011-5758-2_29

6. Korotayev, G.K., Knysh, V.V. and Kubryakov, A.I., 2014. Study of Formation Process of Cold Intermediate Layer Based on Reanalysis of Black Sea Hydrophysical Fields for 1971–1993. *Izvestia, Atmospheric and Oceanic Physics*, 50(1), pp. 35-48. https://doi.org/10.1134/S0001433813060108

7. Efimov, V.V. and Yarovaya, D.A., 2024. Numerical Modeling of the Black Sea Response to the Intrusion of Abnormally Cold Air in January 23–25, 2010. *Physical Oceanography,* 31(1), pp. 120-134.

8. Efimov, V.V. and Yarovaya, D.A., 2014. Numerical Simulation of Air Convection in the Atmosphere during the Invasion of Cold Air over the Black Sea. *Izvestia, Atmospheric and Oceanic Physics*, 50(6), pp. 610-620. https://doi.org/10.1134/S0001433814060073

9. Efimov, V.V., Komarovskaya, O.I. and Bayankina, T.M., 2019. Temporal Characteristics and Synoptic Conditions of Extreme Bora Formation in Novorossiysk. *Physical Oceanography*, 26(5), pp. 361-373. https://doi.org/10.22449/1573-160X-2019-5-361-373

10. Belokopytov, V.N., 2011. Interannual Variations of the Renewal of Waters of the Cold Intermediate Layer in the Black Sea for the Last Decades. *Physical Oceanography*, 20(5), pp. 347-355. https://doi.org/10.1007/s11110-011-9090-x

11. Dorofeev, V.L. and Sukhikh, L.I., 2017. Study of Long-Term Variability of Black Sea Dynamics on the Basis of Circulation Model Assimilation of Remote Measurements. *Izvestia, Atmospheric and Oceanic Physics*, 53(2), pp. 224-232. https://doi.org/10.1134/S0001433817020025

12. Miladinova, S., Stips, A., Garcia-Gorriz, E. and Macias Moy, D., 2017. Black Sea Thermohaline Properties: Long-Term Trends and Variations. *Journal of Geophysical Research: Oceans*, 122(7), pp. 5624-5644. https://doi.org/10.1002/2016JC012644

13. Demyshev, S.G., Korotaev, G.K. and Knysh, V.V., 2002. Evolution of the Cold Intermediate Layer in the Black Sea According to the Results of Assimilation of Climatic Data in the Model. *Physical Oceanography*, 12(4), pp. 173-190. https://doi.org/10.1023/A:1020156026089

14. Miladinova, S., Stips, A., Garcia-Gorriz, E. and Macias Moy, D., 2018. Formation and Changes of the Black Sea Cold Intermediate Layer. *Progress in Oceanography*, 167, pp. 11-23. https://doi.org/10.1016/j.pocean.2018.07.002

15. Stanev, E.V., Peneva, E. and Chtirkova, B., 2019. Climate Change and Regional Ocean Water Mass Disappearance: Case of the Black Sea. *Journal of Geophysical Research: Oceans*, 124(7), pp. 4803-4819. https://doi.org/10.1029/2019JC015076

16. Samson, G., Masson, S., Lengaigne, M., Keerthi, M. G., Vialard, J., Pous, S., Madec, G., Jourdain, N. C., Jullien, S., Menkes, C. and Marchesiello, P., 2014. The NOW Regional Coupled Model: Application to the Tropical Indian Ocean Climate and Tropical Cyclone Activity. *Journal of Advances in Modeling Earth Systems,* 6(3), pp. 700-722. https://doi.org/10.1002/2014MS000324

17. Kraus, E.B. and Turner, J.S., 1967. A One-Dimensional Model of the Seasonal Thermocline II. The General Theory and Its Consequences. *Tellus*, 19(1), pp. 98-106. https://doi.org/10.1111/j.2153-3490.1967.tb01462.x

18. Morozov, A.N. and Mankovskaya, E.V., 2020. Cold Intermediate Layer of the Black Sea according to the Data of the Expedition Field Research in 2016–2019. *Ecological Safety of Coastal and Shelf Zones of Sea*, (2), pp. 5-16. https://doi.org/10.22449/2413-5577-2020-2-5-16 (in Russian).

Submitted 29.05.2024; approved after review 01.11.2024;
accepted for publication 20.11.2024.

About the authors:

Darya A. Iarovaia, Senior Research Associate, Marine Hydrophysical Institute of RAS (2 Kapitanskaya Str., Sevastopol, 299011, Russian Federation), CSc (Phys.-Math), **ResearcherID: Q-4144-2016, ORCID ID: 0000-0003-0949-2040, Scopus Author ID: 57205741734**, darik777mhi-ras@mail.ru

Submitted 29.05.2024; approved after review 01.11.2024;
accepted for publication 20.11.2024.

Vladimir V. Efimov, Head of Atmosphere-Ocean Interaction Department, Marine Hydrophysical Institute of RAS (2 Kapitanskaya Str., Sevastopol, 299011, Russian Federation), DSc (Phys.-Math), Professor, **ResearcherID: P-2063-2017, Scopus Author ID: 6602381894**, vefim38@mail.ru

Contribution of the co-authors:

Darya A. Iarovaia – performance of calculations, interpretation of modeling results, formulation of conclusions

Vladimir V. Efimov – problem statement, discussion of modeling results and formulation of conclusions

The authors have read and approved the final manuscript.
The authors declare that they have no conflict of interest.

ISSN 1573-160X, *PHYSICAL OCEANOGRAPHY*, Vol. 32, Iss. 1, pp. 17-31 (2025)
Original Russian Text © D. V. Korzinin, 2025,
published in *Morskoy Gidrofizicheskiy Zhurnal*, 2025, Vol. 41, Iss. 1, pp. 20–35

Original article

A Storm in the Attenuation Stage as a Factor in Seasonal Deformations of a Sandy Coastal Profile

D. V. Korzinin

Shirshov Institute of Oceanology, Russian Academy of Sciences , Moscow, Russian Federation
✉ *korzinin@ocean.ru*

Abstract
Purpose. The purpose of the study is to consider both the features of storms in the attenuation stage as a factor in the coastal profile restoration after storm erosion, and a potential cause of seasonal deformations.
Methods and Results. Seasonal morphodynamics of accumulative coastal areas was studied in the regions both of the Vistula Spit (South-Eastern Baltic) based on the monitoring measurements of coastal profile performed by the employees of the Shirshov Institute of Oceanology, RAS, from May 2019 to March 2022 and the Oktyabrskaya Spit (western Kamchatka) using the measurement data taken in 2010–2011. Two indices describing the storm structure are used: the ratio of the attenuation stage duration to the total storm duration R_t, and the ratio of the median value of storm wave height during the attenuation stage to the peak wave height of the storm event R_{Hs}. The variations in R_t and R_{Hs} during a year are statistically analyzed based on the *ERA*5 long-term wave reanalysis data. It is found that the R_t index does not tend to change on a seasonal scale. When the R_{Hs} index is close to one and changes slightly during a year, the coastal profile does not experience seasonal changes. If R_{Hs} changes in course of a year decreasing significantly during the period of more intense waves, the coast experiences seasonal changes.
Conclusions. The variations in wave intensity during a year do not always result in the change of average position of the coastal profile. The key factor may consist in the seasonal trends in wave parameter changes within a storm cycle. The proposed index R_{Hs} can be regarded as a criterion for the behavior type of sandy coasts on a seasonal scale.

Keywords: sandy coast, coastal profile, wave regime, underwater bar, morphodynamics, seasonal deformations, stages of storm

Acknowledgements: The research was supported by the Russian Science Foundation (RSF, grant 24-27-00238). The author is grateful to M. N. Shtremel, P. M. Belova and A. Kazakov who participated in the field work on the Vistula Spit, and to S. L. Gorin, $\boxed{\text{E. A. Kravchunovskaya}}$ and I. I. Tembrel who took part in the field work in the settlement Oktyabrsky in the Western Kamchatka and thanks to whom the valuable data on the coastal profile morphodynamics were obtained.

For citation: Korzinin, D.V., 2025. A Storm in the Attenuation Stage as a Factor in Seasonal Deformations of a Sandy Coastal Profile. *Physical Oceanography*, 32(1), pp. 17-31.

Introduction and theoretical background of the study

According to existing concepts, seasonal deformations of the coastal accumulative profile are characterized by the removal of sand sediments to depth with the isolation of the underwater bar during the storm season and the accumulative terrace adjoining to the coast during the season of moderate waves (Fig. 1). It is believed that the observed sandy coast morphodynamics are indicative of a change in wave intensity between seasons or are associated with a series of storm events (see, for example, [1–4]). At the same time, there are coasts that exhibit resistance to wave energy fluctuations on a seasonal scale, yet are sensitive to individual storm events or undergo unidirectional changes over several years [5, 6]. The study of such properties of individual storms or their series that can determine the nature of coastal profile deformations on a seasonal scale is of undoubted interest to coastal science. The identification of these properties will allow for the forecasting of one or another character of morphodynamics of accumulative sandy coasts.

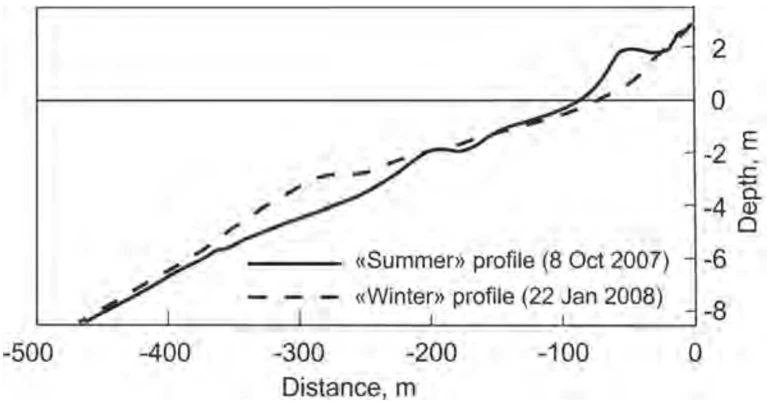

F i g. 1. Seasonal differences in the sand profile (San Diego, California, USA) (adapted from [1, p. 41])

The initial documentation of seasonal deformation of the coastal sand profile was conducted by F. Shepard, who used the California coast [1] as a case study. Subsequent studies along this coastline contributed to the formulation of the main theoretical principles related to deformations of this nature [1, 7]. The main principle asserts that the fluctuation in wave energy throughout the year causes a change in the accumulation and erosion modes of the coastal profile. The so-called "winter" profile (Fig. 1) is essentially an erosion profile, and the "summer" profile is an accumulation profile or a profile restored after erosion.

It should be noted that the wave conditions of the California coast, where the study of seasonal deformations of the sandy coast was conducted for the first time, are characterized by intense waves during the storm season and a relatively long period of influence by gentle Pacific swell waves during the moderate season. This phenomenon determines the corresponding differences in the coastal profile (see Fig. 1). In fetch-limited conditions, where short and steep wind waves predominate during the storm period and the swell effect is expressed

[1] Shepard, F.P., 1950. *Beach Cycles in Southern California*. Technical Memorandum; no. 20. Beach Erosion Board, 26 p.

insignificantly, the limiting states of the profile characteristic of different seasons may be less contrasting [8, 9].

As previously mentioned, seasonal deformations are associated with fluctuations in the intensity and steepness of waves throughout the year. The author of this study proposes a hypothesis that the possible cause of seasonal rhythms in the accumulative coast morphodynamics is the variable nature of storm events throughout the year.

A separate storm can be described by the maximum wave parameters and by the dynamics of changes in these parameters during the full storm cycle – from an intensive increase in wave heights at the initial stage to complete attenuation at the end stage. To describe these changes during the full storm cycle, the concept of "storm structure" [2] was proposed. Storm structure is characterized by the duration and energy of the waves of the three main stages (phases) of the storm: development, stabilization, and attenuation. In the event of coastal erosion during the development and stabilization stage of a storm (the erosive phase), a partial or complete recovery of the affected area may occur during the attenuation stage (the recovery period).

Sediments removed to a certain depth during the process of wave erosion of the coastal profile at the storm development and stabilization stage can be displaced toward the coast at the attenuation stage due to wave transport. This phenomenon occurs as a consequence of wave velocity asymmetry during nonlinear transformation of waves [10, 11]. The greater the intensity of the storm maximum phase, the deeper the sediments are transported during erosion. In the event of significantly reduced heights of storm waves at the attenuation stage relative to previous maximums, the wave transport toward the coast also weakens, owing to the decreased depth of the wave effect on the bottom. Accordingly, if the energy of storm waves at the attenuation stage approaches the magnitude of storm waves in the peak phase, the wave transport intensifies contributing to an increased return of sediments toward the coast.

This pattern can also be explained by the erosion profile property, which states that a profile of this nature is formed due to the removal of sediment to depth during the intensification and stabilization of storms. The erosion profile and the accumulation profile, two limiting states of a sand profile, can be correlated with the dissipative and reflective states of the coastal profile. This correlation is possible within the framework of the concept of an accumulative coast evolution, which was proposed by Australian researchers L. Wright and A. Schott [12]. According to this concept, dissipative profiles are relatively resistant to erosion. However, in cases of higher wave energy exposure, the dissipative profile becomes susceptible to erosion, leading to a restoration phase characterized by the accumulation of sediments (see the area outlined by a rectangular contour in Fig. 2). In cases of lower wave energy, the accumulation intensity decreases. The intensity of waves in this approach is estimated using the Dean's parameter [13]:

[2] Dolotov, Yu.S., 1989. *Dynamic Settings of Coastal-Marine Relief Formation and Sedimentation*. Moscow: Nauka, 269 p. (in Russian).

$$\Omega = \frac{H_b}{w_s T_p}, \tag{1}$$

where H_b is the wave height at breaking; w_s is the sediment fall velocity; T_p is the peak period of waves.

In other words, if wave regime at the stabilization stage can be characterized by a certain value Ω_{eq} (Fig. 2), and the wave regime during attenuation – by the value Ω, then the intensity of accumulation at this stage will be determined by the value $\Delta\,\Omega$ [14]:

$$\Delta\,\Omega = \Omega - \Omega_{eq}$$

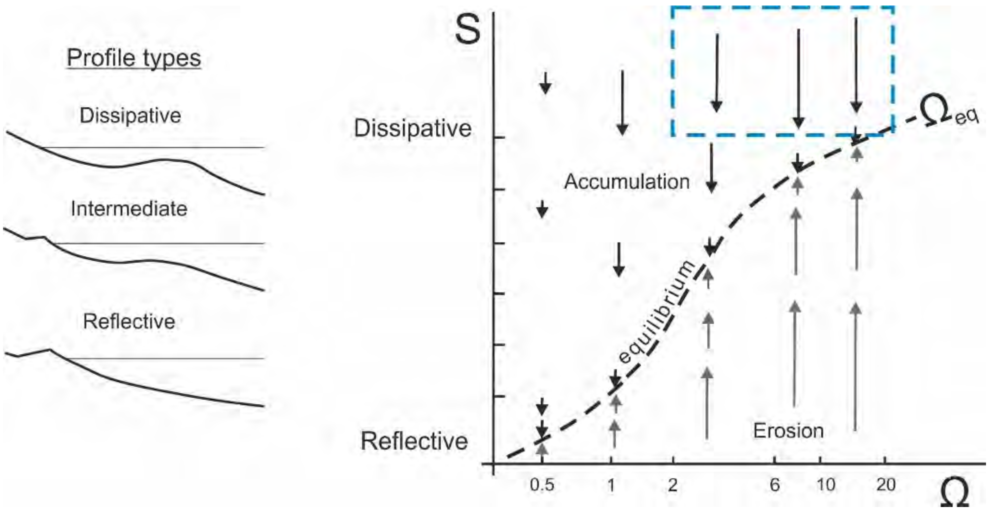

F i g. 2. Conceptual diagram illustrating the relationship between the type of coastal accumulative profile (indicative parameter *S*), the amount of wave energy (the Dean parameter Ω) and the relative intensity of accumulation and erosion (proportional to the arrow lengths). Blue dashed contour highlights the conditions of intense accumulation at higher wave energy on the dissipative profile (adapted from [12, p. 114])

When the intensity of the waves at the attenuation stage decreases, $\Delta\,\Omega < 0$, and, according to [14], the greater the difference between the Ω and Ω_{eq} values, the lower the intensity of the accumulative process.

Thus, the aforementioned arguments show that if the waves at the attenuation stage are closer in intensity to the storm waves in the peak phase, then this contributes to the restoration of the coastal profile after erosion.

The existing coastal science indicators that describe the storm event structure are based on characteristics such as wave energy and the duration of certain stages. Based on the results of long-term observations conducted at six locations along the Baltic and Black Sea coasts, a storm structure coefficient has been proposed: [3]

[3] Yurkevich, M.G., 1976. Short-Term Deformations of the Submarine Slope Relief of the Upper Shelf Zone. In: *Lithodynamics, Lithology and Geomorphology of the Shelf.* Moscow: Nauka, pp. 257-266 (in Russian).

$$r = \frac{E_A + E_S}{E_R}, \quad (2)$$

where E_A, E_S, E_R are the total wave energy at the development, stabilization, and attenuation stages, respectively, expressed as a percentage of the total storm energy. It is shown that positive deformations are observed at $r < 0.7$, while negative deformations are observed at $r > 1.2$.

The ratio of the duration of the maximum storm phase to the attenuation stage determines the so-called storm coefficient [15]:

$$R_S = \frac{T_a}{T_w}, \quad (3)$$

where T_a is the duration of the storm stabilization phase; T_w is the duration of the storm attenuation stage. As the coefficient approaches zero, the role of the wave attenuation stage becomes more pronounced, thereby reducing the final erosion of the profile. This pattern is based on observations of the coastal profile dynamics in experimental wave setups and in natural conditions.

The ratio of the duration of the storm attenuation stage to the total storm event duration forms the basis of the concept of effective wave height H_e [16]. Based on this concept, an analytical model describing the deformations of the coastal profile over a full storm cycle is proposed:

$$H_e = H_{\max} - (H_{\max} - H_{\min})(T_w/T_{\Sigma}), \quad (4)$$

where $H_{\max}$ is the maximum height of storm wave, $H_{\min}$ is its minimum height at the end of the storm (conventionally designated as 1 m), and T_w and T_{Σ} are duration of the attenuation stage and the total storm duration, respectively.

Thus, the theoretical justifications and examples from published sources demonstrate that the key parameters of storm structure are the duration of specific stages and the amount of wave energy associated with these stages. In the case of a prolonged or more “energetic” storm in the attenuation stage, a greater quantity of sediment will be transported towards the coast by the end of the storm event.

This paper aims to investigate the impact of these variations in storm behavior during the attenuation stage on the behavior of the sandy coast.

Initial data and methods

In order to achieve the set goal, two specific coastal regions were selected for study: the Vistula Spit area (South-Eastern Baltic) and the Oktyabrskaya Spit area (Oktyabrsky settlement, western Kamchatka, eastern part of the Sea of Okhotsk). These regions are associated with extended barrier forms of the coastal sand bar type.The differences between the selected regions are that the Western Kamchatka coast in the Oktyabrskaya Spit area is characterized by tides, with a maximum amplitude of 3 m [17]. A distinctive feature of this coast is the presence of ice on the beach from December to May, inclusive. In this regard, changes in relief, typical for a sandy coast and caused by waves, can only be observed from June to November. In contrast, the coasts of the South-Eastern Baltic are non-tidal, with ice in the coastal zone being extremely rare and limited to a period of no more than a few days.

The average slope of the coastal profile at the Vistula Spit, extending from the water's edge to a depth of 7.5 m, is 0.014, and at the Oktyabrskaya Spit – 0.008 (Fig. 3). The coastal profile at the Vistula Spit is complicated by the presence of a well-defined underwater bar. The classification of coastal accumulative profiles by the type of prevailing dynamic environment based on the Dean parameter (Ω), as outlined in [12], indicates that both banks are classified as dissipative: $\overline{\Omega}$ = 5.13 for the Vistula Spit and $\overline{\Omega}$ = 6.41 for the Oktyabrskaya Spit. To calculate the values of Ω, expression (1) and *ERA*5 wave reanalysis data for a long-term period were used, as discussed below.

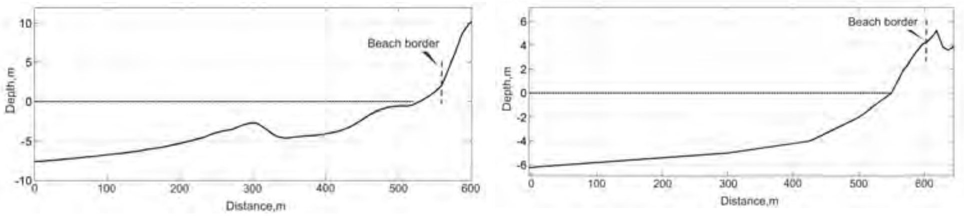

a *b*

F i g. 3. Coastal profiles typical for the regions of the Vistula (*a*) and Oktyabrskaya (*b*) spits

For the selected regions, data concerning the dynamics of the coastal profile in various seasons were obtained. The coastal profile was measured along the Baltic Sea coast from May 2019 to March 2022 as a part of the monitoring work conducted by the Shirshov Institute of Oceanology of RAS on the Vistula Spit. On the Sea of Okhotsk coast, measurements were carried out in 2010–2011 as part of the work performed to develop recommendations for the Oktyabrskaya Spit protection from storm erosion [18]. On the coast of Oktyabrskaya Spit, repeated measurements were carried out only for the above-water part of the coastal profile.

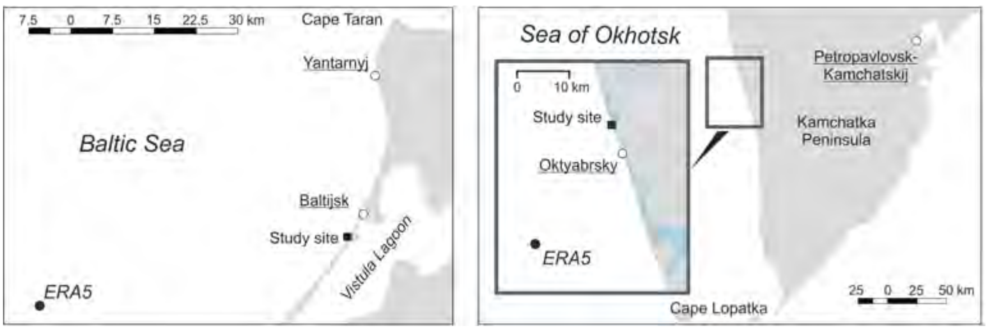

F i g. 4. Sites of coastal profile measurements: *on the left* – in the Baltic Sea; *on the right* – in the Sea of Okhotsk (coastline site marked with black rectangle is shown enlarged in the inset). Points of wave reanalysis data unloading are marked with the circles labeled "*ERA*5"

The wave conditions were calculated using the $ERA5$ wave reanalysis data [19] from the European Centre for Medium-Range Weather Forecasts (ECMWF) for the calculation points closest to the field observation areas: 54.5°N, 19°E for the South-Eastern Baltic and 52.5°N, 156°E for the Sea of Okhotsk (Fig. 4). The $ERA5$ point for the South-Eastern Baltic is located 10 km off the coast (the point depth applied in the calculations of the $ERA5$ reanalysis wave model is 54 m), and the point near the Western Kamchatka coast is 21 km off the shore (the corresponding depth is 209 m). The wave data studied were collected at 3-hour intervals. For the Baltic Sea, the $ERA5$ wave reanalysis data were verified based on measurements of wave parameters in the coastal zone using the Spoondrift Spotter buoy [20]. It was revealed that the reanalysis data have quite satisfactory convergence with the measured wave parameters.

The $ERA5$ reanalysis datasets contain significant wave heights H_S (m) that are characterized by extreme values. H_S values for individual storm events were extracted from the wave data time series in the Matlab software environment. The selection of storm events was based on the criterion of wave height exceeding 1 m and a storm duration of at least 12 h. Storm events for which the development or attenuation stage is not determined, i.e., the maximum wave height is confined to the initial or final time point of the storm, were not taken into account. As a result, 1,355 storm events (1979–2020, 42 years) were considered for the South-Eastern Baltic, and 1,459 storm events (1992–2021, 30 years) for the Western Kamchatka.

To calculate the Dean's parameter ($\Omega = H_b / w_s T_p$), the wave height at breaking H_b was calculated using the expression [21]:

$$\frac{H_b}{H_\infty} = 0.53 \left(\frac{H_\infty}{L_\infty}\right)^{-0.24},$$

where H_∞ is the wave height in deep water (here and below, we use significant wave height H_S as the H value according to the $ERA5$ reanalysis data); L_∞ is the wavelength in deep water, determined by the ratio $L = gT^2/2\pi$ (in this case, the average wave period T_m is used as T according to the $ERA5$ reanalysis data). The sediment fall velocity (w_s) was calculated using the expression [22]:

$$w_s = 0.155 d_s - 0.0075,$$

where d_s is the diameter of sand deposits. For both coastal areas, an approximate value of the median diameter of sand deposits on the underwater coastal slope was determined to be 0.25 mm, according to the works [4] [23, 24]. The peak period of waves (T_p) was calculated using the expression [25]

$$T_p = 1.25 T_m.$$

According to the aforementioned theoretical background of the study, the key parameters of a storm in the attenuation stage are relative characteristics of its

[4] Vtyurin, B.I. and Svitoch, A.A., eds., 1978. *Recent Deposits and Pleistocene Paleography in Western Kamchatka*. Moscow: Nauka, 122 p. (in Russian).

duration and wave intensity. For the quantitative assessment of each storm event in this stage, the following characteristics were determined:

- storm event duration (T_{St}, h);
- duration of the storm attenuation stage (T_{At}, h);
- maximum wave height of storm ($H_{St\_\max}$, m);
- median value of storm wave height in the attenuation stage (H_{At_med}, m).

The median value of the storm wave height in the attenuation stage (H_{At_med}) is applied to estimate the wave energy due to the fact that the average value is highly sensitive to outliers. In this case, outliers are short-term peaks or minimums of the wave height, which will have little effect on the morphodynamics. This is due to the fact that the coastal profile reshaping is associated with a relatively long-term wave effect, as demonstrated during experimental studies [21, 26].

The author proposes two special indices of storm structure. The index R_t characterizes relative duration of storm attenuation stage:

$$R_t = \frac{T_{At}}{T_{St}}.$$

The R_H index characterizes the relative value of storm wave energy in the attenuation stage:

$$R_H = \frac{H_{At\_\text{med}}}{H_{St\_\max}}.$$

The closer the values of R_t and R_H indices are to one, pointed that storm in the attenuation phase has a higher potential for recovering the coastal profile. Previously developed approaches to assessing storm structure (expressions (2)–(4)) [15, 16] were applied for developing these indices. Statistical analysis of these indices is possible due to the use of wave reanalysis data for a long-term period. In turn, field data on the seasonal morphodynamics of accumulative coastal areas allow us to verify the results.

Study results

At the outset of the study, an analysis of the seasonality in the storm activity distribution was performed. The following indices were determined for each month (Fig. 5, 6):

- $H_{\max}$ is maximum wave height (m);
- $H_{\max(avg)}$ is average wave height from the maximum ones for each storm event (m);
- t_m is mean duration of storm events (h);
- N_m is mean number of storm events;
- $t_{mon(\text{avg})}$ is monthly average number of hours with storms ($t_m \cdot N_m$).

A study of two specific water areas revealed common features in the annual dynamics of storm activity. It was shown that maximum wave heights and their average values ($H_{\max}$, $H_{\max(\text{avg})}$) exhibit well-defined seasonal variability, with a minimum in May – July, followed by an increase in wave intensity until November (Fig. 5).

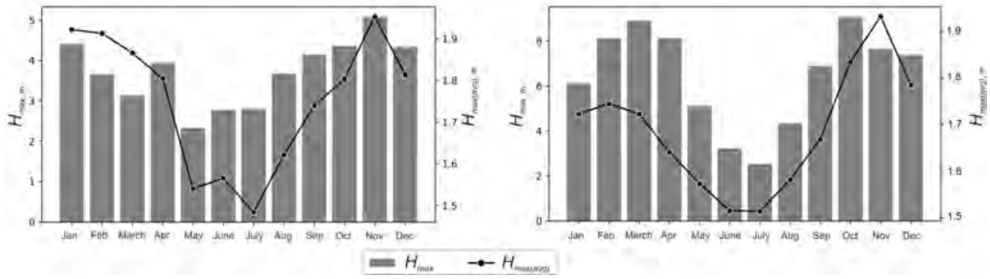

a *b*

F i g. 5. Distribution of $H_{\max}$ and $H_{\max(\text{avg})}$ values by months: *a* – for the South-Eastern Baltic; *b* – for the Western Kamchatka

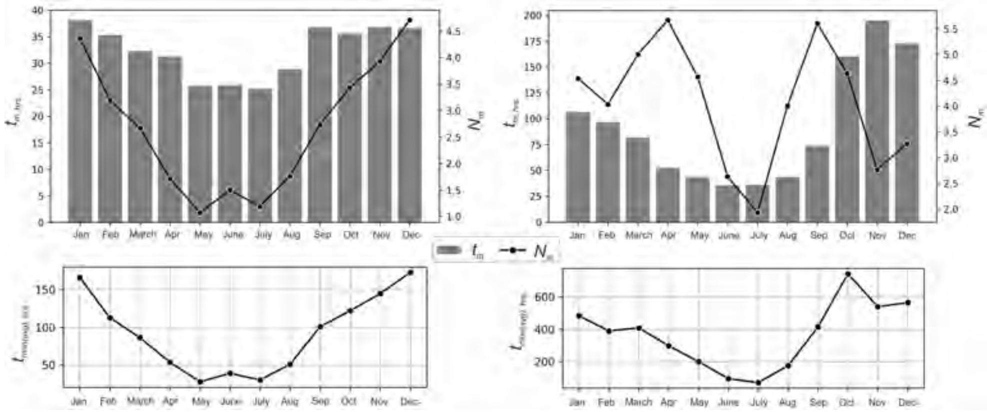

a *b*

F i g. 6. Distribution of t_m, N_m and $t_{\text{mon}(avg)}$ values by months: *a* – for the South-Eastern Baltic; *b* – for the Western Kamchatka

In the South-Eastern Baltic, similar seasonal variability is also characteristic of the indices that determine the occurrence of storms: t_m, N_m, $t_{\text{mon(avg)}}$ (Fig. 6). In Western Kamchatka, the maximum number of storms (N_m) is observed in April and September. In spring, the Western Kamchatka is characterized by the presence of ice on the beach, and our focus is on the summer and autumn periods. Following the peak in September, the average number of storms decreases against the background of increasing in their duration. Nevertheless, relatively high t_m and N_m values are observed in October, which, in conjunction with the elevated values of $H_{\max}$ and $H_{\max(avg)}$ allows us to characterize this month as the peak of storm activity. For the South-Eastern Baltic, all the studied indices exhibit a similar trend, with a peak in storm activity from November to January.

For quantitative characterization of wave variability during the year, we can use the index $\overline{\sigma}_{\Omega_{360}}/\overline{\sigma}_{\Omega_{30}}$ proposed in the work [5], where $\overline{\sigma}$ is the average value of the standard deviation of the Dean's parameter Ω for the specified years ($\overline{\sigma}_{\Omega_{360}}$) and months ($\overline{\sigma}_{\Omega_{30}}$). The higher the value of the index $\overline{\sigma}_{\Omega_{360}}/\overline{\sigma}_{\Omega_{30}}$, the more the studied coastal area is subject to seasonal fluctuations in wave steepness during the year. If $\overline{\sigma}_{\Omega_{360}}/\overline{\sigma}_{\Omega_{30}}$ index is close to one, the morphodynamics of a given coast are affected mostly by individual storms. The calculations performed indicate that the $\overline{\sigma}_{\Omega_{360}}/\overline{\sigma}_{\Omega_{30}}$ indices for the areas under study are approximately equal, with values of 1.06 for the Vistula Spit area and 1.006 for the water area of the Sea of Okhotsk. Thus, according to this index, the coast morphodynamics are mostly affected by individual storms, rather than by seasonal variation in wave intensity.

The R_t and R_H indices proposed in this study were calculated further. Their values were then compared with the seasonal variation of storm activity. Statistical processing of R_t values for each storm (Fig. 7) revealed that no visible seasonal differences in the dynamics of this index were indicated during the year. The median R_t value is close to 0.6 for each month for the two water areas under study.

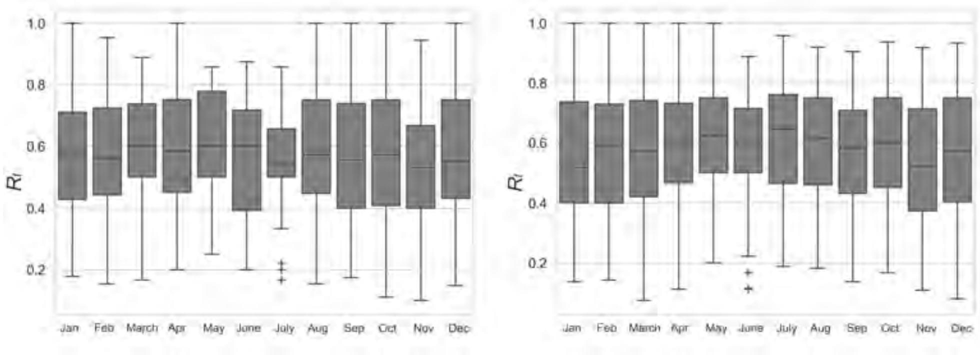

a *b*

F i g. 7. Statistical characteristics of the change in index R_t during a year for the parts of water areas of the South-Eastern Baltic (*a*) and the Western Kamchatka (*b*) under study

A statistical analysis of the R_H values (Fig. 8) showed that, for the waters of the South-Eastern Baltic, the differences in the median R_H values across each month are not statistically significant. The maximum value recorded was 0.86 in July, while the minimum value was 0.79 from January to March. A well-defined seasonal dynamic is observed for the Western Kamchatka waters, characterized by the median R_H values that approach one in June and July (~ 0.85) and decrease to a minimum by November (~ 0.54). In the Western Kamchatka, a correlation has been observed between the increase in wave intensity $Hs_{\max}$, $Hs_{\max(\text{avg})}$ (see Fig. 5), storm duration t_m, N_m (see Fig. 6) and the average number of hours with storms $t_{mon(\text{avg})}$ with a corresponding change in the nature of waves in the attenuation stage. Low R_H values in the autumn season determine the trend towards the final erosion of the coastal profile for the majority of storm events. This trend has not been identified in the South-Eastern Baltic region. At the same time, the interseasonal dynamics of the R_H index for the Western Kamchatka do not correspond to the result obtained when calculating the $\overline{\sigma}_{\Omega_{360}}/\overline{\sigma}_{\Omega_{30}}$ index (according to [5]). This indicates that coastal morphodynamics are predominantly affected by individual storms, rather than by the seasonal variation of wave intensity.

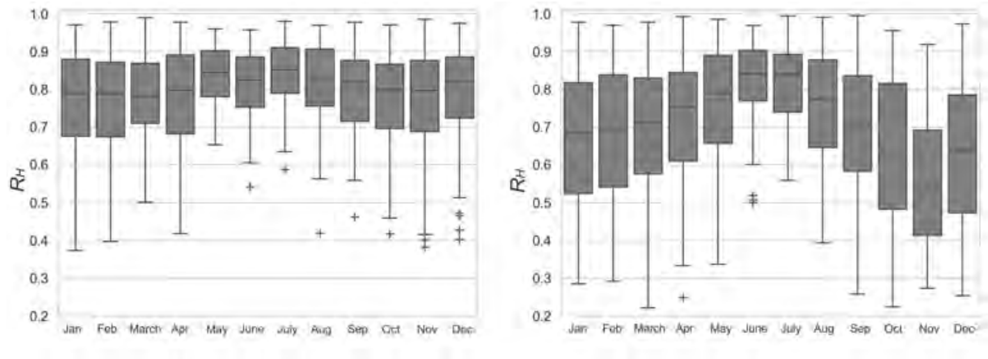

a *b*

F i g. 8. Statistical characteristics of the change in index *R* during a year for the parts of water areas of the South-Eastern Baltic (*a*) and the Western Kamchatka (*b*) under study

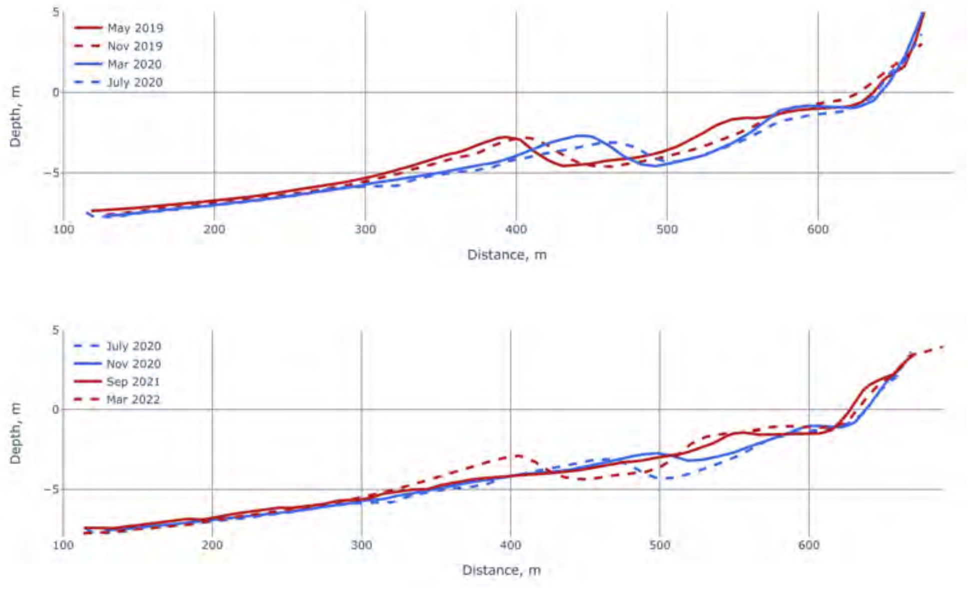

F i g. 9. Dynamics of the Vistula Spit coastal profile from May 2019 to March 2022

The results of the R_H statistical analysis for the water areas under study by month were compared with the data on the sand profile morphodynamics in different seasons. Over the course of three years (from May 2019 to March 2022), relief measurements were taken on the Vistula Spit. They revealed that there are no coastal profile deformations in this section of the coast that can be characterized as seasonal. Throughout the observation period, a cycle involving the evolution of the underwater bar from a straightened outer one (May 2019) to a crescent-shaped one with subsequent adjoining to the coast (September 2021) (Fig. 9) was documented. In March 2022, a new outer underwater bar was formed. However, the typical seasonal morphodynamic rhythm, characterized by the coast's retreat and the formation of an underwater bar during winter, followed by its subsequent adjoining to the coast in the form of an accumulative terrace during summer, remained unidentified.

On the Oktyabrskaya Spit, the relief was measured with less regularily and exclusively in the above-water portion of the coastal zone. The seaward boundary of the measurements passed above the waterline, approximately at the maximum wave run-up during the survey. Nevertheless, the seasonal rhythm of changes in the beach relief on this coast section was identifiable. The profile measured in June 2011 can be considered as summer one, since it is located higher in relation to other profiles and extends towards the sea (Fig. 10). Autumn brings an increase in waves, as well as beach erosion and the formation of a winter profile. This phenomenon is evident from the relative position of the profiles taken in November 2010 and September 2011. Thus, during storm seasons (November 2010 and September 2011), the average position of profile changes and a trend towards erosion is outlined. This corresponds to lower values of the R_H coefficient.

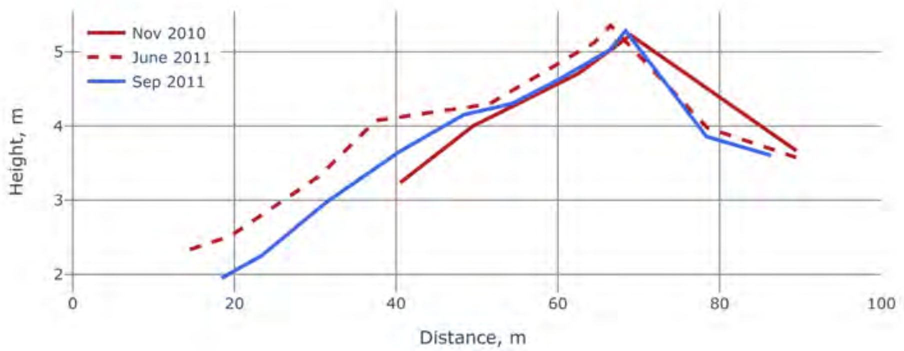

F i g. 10. Dynamics of the Oktyabrskaya Spit beach from November 2010 to September 2011

Conclusion

Using an example of two regions with different hydrodynamic characteristics (the waters of the South-Eastern Baltic and the eastern portion of the Sea of Okhotsk), it was found that seasonal fluctuations in the intensity of sea waves can be accompanied by varied features of storm events during the attenuation stage. It was revealed that the ratio of the median value of the storm wave height in the attenuation stage to its maximum height can vary for different seasons, as reflected by the proposed R_H index. In turn, the R_t index, which characterizes the relative duration of the storm attenuation stage, does not tend to seasonal variability.

A more "energetic" storm in the attenuation stage (R_H values are close to 1) can be regarded as a contributing factor to the post-storm recovery of the coastal profile.

Variations in this factor on a seasonal scale can be considered as one of the possible causes for seasonal deformations in the accumulative relief of the coastal zone.

In particular, the coastal profile deformations that can be characterized as seasonal were revealed for the sandy coast of the Oktyabrskaya Spit (Western Kamchatka). In contrast, no such deformations were revealed for the South-Eastern Baltic. The observed variations in morphodynamics between these two regions are accompanied by a regular seasonal variation in the R_H index for the wave conditions at the Oktyabrskaya Spit and the absence of seasonality in the R_H values for the Vistula Spit conditions.

It has been demonstrated that the change in wave intensity throughout the year does not always entail a change in the average position of the coastal profile. The key factor may be the seasonal trends in the variation of wave parameters within the storm cycle. In particular, the role of storm wave energy in the attenuation stage is indicated. The approach we proposed is a variation of approaches to storm structure analysis suggested by other authors. These approaches suggest that the duration of the storm and the wave energy amount in the attenuation stage determine the volume of sediment transported towards the coast.

The proposed approach to assessing individual storm events can be scaled up to a series of storms or down to an individual season. A group of storms following the maximum wave intensity can be considered as storms in the attenuation stage, which can be assessed using the R_t and R_H indices adapted to a different time scale. Thus, based on long-term wave data, we can forecast the coastal profile recovery after typical seasonal erosions.

REFERENCES

1. Yates, M.L., Guza, R.T., O'Reilly, W.C. and Seymour, R.J., 2009. Overview of Seasonal Sand Level Changes on Southern California Beaches. *Shore & Beach*, 77(1), pp. 39-46.
2. Katoh, K. and Yanagishima, S., 1988. Predictive Model for Daily Changes of Shoreline. In: B.L. Edge, ed., 1988. *Coastal Engineering 1988.* New York: American Society of Civil Engineers, pp. 1253-1264. https://doi.org/10.1061/9780872626874.094
3. Hansen, J.E. and Barnard P.L., 2010. Sub-Weekly to Interannual Variability of a High-Energy Shoreline. *Coastal Engineering*, 57(11-12), pp. 959-972. https://doi.org/10.1016/j.coastaleng.2010.05.011
4. Castelle, B., Marieu, V., Bujan, S., Ferreira, S., Parisot, J-P., Capo, S., Sénéchal, N. and Chouzenoux, T., 2014. Equilibrium Shoreline Modelling of a High-Energy Meso-Macrotidal Multiple-Barred Beach. *Marine Geology*, 347, pp. 85-94. https://doi.org/10.1016/j.margeo.2013.11.003
5. Splinter, K.D., Turner, I.L., Davidson, M.A., Barnard, P., Castelle, B. and Oltman-Shay, J., 2014. A Generalized Equilibrium Model for Predicting Daily to Interannual Shoreline Response. *Journal of Geophysical Research: Earth Surface*, 119(9), pp. 1936-1958. https://doi.org/10.1002/2014JF003106
6. Huguet, J.-R., Castelle, B., Marieu, V., Morichon, D. and de Santiago, I., 2016. Shoreline-Sandbar Dynamics at a High-Energy Embayed and Structurally-Engineered Sandy Beach: Anglet, SW France. *Journal of Coastal Research*, 75(sp1), pp. 393-397. https://doi.org/10.2112/SI75-079.1

7. Inman, D.L., Elwany, M.H.S. and Jenkins, S.A., 1993. Shorerise and Bar-Berm Profiles on Ocean Beaches. *Journal of Geophysical Research: Oceans*, 98(C10), pp. 18181-18199. https://doi.org/10.1029/93JC00996

8. Bernabeu, A.M., Medina, R. and Vidal, C., 2003. *A* Morphological Model of the Beach Profile Integrating Wave and Tidal Influences. *Marine Geology*, 197(1-4), pp. 95-116. https://doi.org/10.1016/S0025-3227(03)00087-2

9. Goodfellow, B.W. and Stephenson, W.J., 2005. Beach Morphodynamics in a Strong-Wind Bay: A Low-Energy Environment? *Marine Geology*, 214(1-3), pp. 101-116. https://doi.org/10.1016/j.margeo.2004.10.022

10. Elgar, S., Gallagher, E.L. and Guza, R.T., 2001. Nearshore Sandbar Migration. *Journal of Geophysical Research: Oceans*, 106(C6), pp. 11623-11627. https://doi.org/10.1029/2000JC000389

11. Price, T.D., Ruessink, B.G. and Castelle, B., 2014. Morphological Coupling in Multiple Sandbar Systems - A Review. *Earth Surface Dynamics*, 2(1), pp. 309-321. https://doi.org/10.5194/esurf-2-309-2014

12. Wright, L.D. and Short, A.D., 1984. Morphodynamic Variability of Surf Zones and Beaches: A Synthesis. *Marine Geology*, 56(1-4), pp. 93-118. https://doi.org/10.1016/0025-3227(84)90008-2

13. Dean, R.G., 1973. Heuristic Models of Sand Transport in the Surf Zone. In: *First Australian Conference on Coastal Engineering, 1973: Engineering Dynamics of the Coastal Zone*. Sydney, Australia: Institution of Engineers, pp. 215-221.

14. Castelle, B. and Masselink, G., 2023. Morphodynamics of Wave-Dominated Beaches. *Cambridge Prisms: Coastal Futures*, 1, e1. https://doi.org/10.1017/cft.2022.2

15. Grasso, F., Michallet, H., Certain, R. and Barthélemy, E., 2009. Experimental Simulation of Sandbar Dynamics. *Journal of Coastal Research*, 56(I), pp. 54-58.

16. Leont'yev, I.O., 2018. Modeling a Shore Profile Formed by Storm Cycle Impact. *Oceanology*, 58(6), pp. 892-899. https://doi.org/10.1134/S0001437018060085

17. Glukhovskii, B.Kh., Goptarev, N. and Terziev, F.S., eds., 1998. *Hydrometeorology and Hydrochemistry of Seas. Volume IX. The Sea of Okhotsk. Issue 1. Hydrometeorological Conditions*. Saint Petersburg: Gidrometeoizdat, 342 p. (in Russian).

18. Gorin, S.L., Ignatov, E.I., Kravchunovskaya, E.A., Kosonin, D.V. and Tembrel, I.I., 2012. The Morphodynamics of the Oktyabr'skaya Spit (Sea of Okhotsk Coast of Kamchatka). In: L. A. Zhindarev, 2012. "Sea Coasts" Working Group, 2012*. XXIV International Coastal Conference "Sea Coasts – Evolution, Ecology, Economy" for the 60-th Anniversary of the "Sea Coasts" Working Group: in 2 Volumes*. Vol. 1. Krasnodar: Yug Publishing, pp. 94-97 (in Russian).

19. Hersbach, H., Bell, B., Berrisford, P., Hirahara, S., Horányi, A., Muñoz-Sabater, J., Nicolas, J., Peubey, C., Radu, R. [et al.], 2020. The ERA5 Global Reanalysis. *Quarterly Journal of the Royal Meteorological Society*, 146(730), pp. 1999-2049. https://doi.org/10.1002/qj.3803

20. Shtremel, M., 2020. ERA5 Wave Data Verification with Buoy Field Measurements in the Nearshore Region of the Baltic Sea. In: M. Kalinowska, P. Rowiński, T. Okruszko and M. Nones, eds., 2020. *Abstract Book of 6th IAHR Europe Congress (Warsaw Poland 2020)*. Warsaw, Poland: IAHR, pp. 433-434.

21. Larson, M. and Kraus, N.C., 1989. *SBEACH: Numerical Model for Simulating Storm-Induced Beach Change. Report 1. Empirical Foundation and Model Development.* Washington: US Army Corps of Engineers, 256 p. https://doi.org/10.5962/bhl.title.47893

22. Leontiev, I.O., 2001. *Coastal Dynamics: Waves, Currents, Sediment Transport*. Moscow: GEOS, 272 p. (in Russian).

23. Bobykina, V.P. and Zhurakhovskaya, P.M., 2012. [Interannual Variations in the Composition of Beach Sediments of the Vistula Spit]. In: RGS, 2012. *Scientific Notes of the Russian Geographical Society (Kaliningrad Branch)*. Kaliningrad: BFU Publishing. Vol. 11, pp. 4B-1-4B-8. (CD-ROM) (in Russian).
24. Kobelyanskaya, J., Piekarek-Jankowska, H., Boldyrev, V.L., Bobykina, V. and Stępniewski, P., 2009. The Morphodynamics of the Vistula Spit Seaward Coast (Southern Baltic, Poland, Russia). *Oceanological and Hydrobiological Studies*, XXXVIII(I), pp. 1-16.
25. Lappo, D.D., Strekalov, S.S. and Zavyalov, V.K., 1990. *Loads and Effects of Wind Waves on Hydraulic Structures*. Leningrad: VNIIG, 432 p. (in Russian).
26. Atkinson, A., Shimamoto, T., Wu, S., Birrien, F. and Baldock, T.E., 2015. Beach Profile Evolution under Cyclic Wave Climates. In: Engineers Australia, 2015. *Australasian Coasts & Ports Conference 2015: 22nd Australasian Coastal and Ocean Engineering Conference and the 15th Australasian Port and Harbour Conference*. Aukland, New Zealand: Engineers Australia and IPENZ, pp. 18-23. https://search.informit.org/doi/10.3316/informit.700361621097694

Submitted 31.07.2024; approved after review 26.08.2024;
accepted for publication 20.11.2024.

About the author:

Dmitry V. Korzinin, Senior Research Associate, Shirshov Institute of Oceanology of RAS (36 Nakhimovskiy Ave., Moscow, 117997, Russian Federation), CSc (Geogr.), **ORCID ID: 0000-0002-7365-8386, ResearcherID: A-5093-2017, Scopus Author ID: 56829564800,** korzinin@ocean.ru

The author has read and approved the final manuscript.
The author declares that he has no conflict of interest.

ISSN 1573-160X, *PHYSICAL OCEANOGRAPHY*, VOL. 32, Iss. 1, pp. 32-45 (2025)
Original Russian Text © A. S. Kuznetsov, I. K. Ivashchenko, 2025,
published in *Morskoy Gidrofizicheskiy Zhurnal*, 2025, Vol. 41, Iss. 1, pp. 36–49

Original article

Long-Term Average Annual Spectral Characteristics of the Coastal Current Long-Period Oscillations off the Southern Coast of Crimea

A. S. Kuznetsov ✉, I. K. Ivashchenko

Marine Hydrophysical Institute of RAS, Sevastopol, Russian Federation
✉ *kuznetsov_as@mhi-ras.ru*

Abstract
Purpose. The main purpose of the study is to analyze the long-period variability of the circulation characteristics of coastal waters in the Black Sea when assessing their energy contribution based on the long-term contact monitoring data on coastal currents.
Methods and Results. The variability of kinetic energy of long-term oscillations of the coastal current off the Southern Coast of Crimea is analyzed based on the materials for 2002–2023 of the oceanographic database of Marine Hydrophysical Institute, RAS. The features of structure of the coastal water long-period oscillations are studied using the methods of statistical and spectral analysis of the energy variability of along-coastal current circulation in the 5–20 m layer over a 22-year measurement period. Within the intra-annual range of current variability, the energy contribution of seasonal oscillations is statistically reliably systematized for the periods 1.0, 0.5, 0.33 and ~ 0.2 years. The results of analyzing the vector-averaged data made it possible to identify the spectral composition both of long-term current oscillations for the periods ~ 2.7, 3.6, 5.3, 7.1 years and 11-year oscillations within the 22-year variability cycle. The spectral composition of coastal current inter-annual oscillations was compared to the North Atlantic Oscillation index. During the period of solar activity intensification in 2007–2020, a 1.5-fold increase in the values of velocity modulus of the coastal current inter-annual oscillations was noted.
Conclusions. The long-period oscillations of coastal current including a range of short-term climatic oscillations were identified and systematized based on the results of analyzing the long-term field data obtained off the Black Sea coast. The prospects for further investigating the relations between such current oscillations and long-term circulation processes in the atmosphere of the Black Sea region are shown.

Keywords: coastal current, long-period oscillations, short-term climate oscillations, energy spectrum of oscillations, contact measurements, Southern Coast of Crimea, Black Sea

Acknowledgments: The study was carried out within the framework of theme of state assignment of FSBSI FRC MHI FNNN-2024-0016 “Study of spatio-temporal variability of oceanographic processes in the coastal and shelf zones of the Black Sea under the influence of natural and anthropogenic factors based on contact measurements and mathematical modeling”.

For citation: Kuznetsov, A.S. and Ivashchenko, I.K., 2025. Long-Term Average Annual Spectral Characteristics of the Coastal Current Long-Period Oscillations off the Southern Coast of Crimea. *Physical Oceanography*, 32(1), pp. 32-45.

Introduction

A fundamental understanding of the local features of the dynamics of the Black Sea coastal waters in the areas of conjugation with land is imperative to ensure sustainable economic development of the coastal region concentrated near the sea. This includes the near water area of the continental shelf, gulfs, bays, and estuaries.

In the Black Sea shelf zone, the development of water dynamics is primarily caused by the formation of hydrodynamic disturbances of the Black Sea Rim Current (RC), particularly multi-scale anticyclonic and cyclonic eddy structures, including quasi-stationary ones [1–8]. At the same time, along-coastal currents have been observed everywhere under conditions of various geomorphological structures of land and bottom topography of the adjacent water area. According to the data systematized in the Black Sea Pilot [1], the currents adjacent to rectilinearly oriented coastal sections exhibit a cyclonic direction, as does the jet RC abeam of the adjacent coastal section.

At a relatively straight section of the coastline of Cape Kikineiz of the Southern Coast of Crimea (SCC), which has a smooth outline, where the Goluboy (Limensky) Gulf slightly juts into the land, in the sea at a distance of ~ 0.5 km and a depth of 28 m, the regime characteristics of a quasi-stationary along-coastal current and a number of its intra-annual oscillations were identified and studied [9, 10]. In this case, the elliptical orbital movements of the shelf waters [3] are transformed near the coast into reciprocating along-coastal current oscillations [11].

As is known [12–17], the seasonal variability of the Black Sea hydrosphere transforms regional circulation processes in the atmosphere, including the surface wind field in the zone underlying the atmosphere of the sea and land surface. The surface stress of the wind field and its vorticity significantly affect the physical processes in the coastal zone of the sea, as evidenced by the formation of multiscale variability of the along-coastal current, including regular generation of packets of anticyclonic inertial oscillations. Mesoscale disturbances in the circulation of coastal waters, interacting with intense inertial oscillations, form a bimodal distribution regime of the frequency of monomodal current directions throughout the coastal zone depth [10, 17]. The nature of the circulation and transport of coastal waters in the west-southwest direction along Cape Kikineiz is observed year-round, with average annual velocities ranging from 5.8 to 9.4 cm/s [9].

The objective of this study is to conduct an analytical investigation into the long-term variability of the circulation characteristics of coastal waters in the Black Sea based on the data obtained from long-term contact monitoring of coastal currents. The primary goal is to systematize the structure of long-term oscillations and assess their energy contribution. The study’s new empirical findings contribute to the development and verification of a model forecasting system for the dynamics of coastal waters at sub-satellite polygons in the Black Sea [18] and system modeling of marine ecological and economic processes in the coastal zone near the South Coast of Crimea [19].

Materials and methods

A study of the energy spectral characteristics of long-term oscillations of coastal waters was conducted using the materials from the oceanographic database of Marine Hydrophysical Institute (MHI) of RAS [20]. These materials were obtained over a 22-year period of contact measurements of the current field characteristics near Cape Kikineiz, SCC. Instrumental measurements of the variability of

[1] Lapin, M.N., 1954. [*The Black Sea Pilot*]. Leningrad: Izd-vo Gidrograficheskogo Upravleniya Voenno-Morskih Sil, 506 p. (in Russian).

the vertical structure of currents were carried out using a set of vector-averaging Eulerian meters installed in the active layer at hydrological horizons from the oceanographic platform of MHI Black Sea Hydrophysical Subsatellite Polygon [9–11]. A schematic map of the study area showing bathymetry, platform position, and arrangement of the vertical antenna of the cluster of meters is given in Fig. 1 in [11, p. 508]. The meters record chronological sequences of vector-averaged pairs of horizontal current components calculated over a 5-minute interval. The calculation is based on second-by-second readings of orthogonal projections of the current vector. The study uses current monitoring data collected from 2002 to 2023 at standard hydrological horizons (hereinafter referred to as “horizons”) of 5, 10, 15, and 20 m. Vector-averaged hourly averages and 8,035 pairs of mean daily readings for each measuring horizon are derived from the initial vector data arrays that have undergone a quality control procedure. The mean hourly database is presented in dbf-format and registered as the result of intellectual activity of MHI [9, 10]. The database volume for 8,035 days amounted to 771.4 thousand pairs of mean hourly values of the corresponding current vector components.

A long-term, full-scale experiment is carried out in open sea conditions, with continuous quality control of the functioning of domestic measuring complexes. Information technology is used for operational quality control of measurements, with a certain redundancy of the full data set from a set of meters installed from the pile foundation of a stationary oceanographic platform. This approach permitted to exclude the contribution of failures, significant methodological and systematic errors to the total error of current measurements. The metrological unity of a long-term set of vector data obtained under uniform conditions and means of instrumental measurements of currents, after averaging the original arrays, allowed minimizing their random errors to the sensitivity values of the corresponding primary measuring transducers of the complexes. In this case, the total error of the vector-averaged values of the velocity module does not exceed 0.1 cm/s, and the direction of the current – 3° [10, 17].

A software module has been developed at MHI for the purpose of spectral analysis. This module has been applied in the context of studies examining energy variability and spatiotemporal characteristics of wind fields, currents, long-wave motions, and internal waves [2] [9–10, 15–18]. The essence of the used filter (linear) estimate of the energy spectrum is described in the work [3]. When processing the statistical characteristics of the vertical distribution of horizontal components of the current velocity, the method of analytical filtering of vector data was used [21]. Vector filtering of time series is also employed to minimize distortions that arise when calculating spectral characteristics in the presence of intense multi-scale oscillations. These oscillations introduce distortions into the estimate of the actual level of spectral energy density in the studied variability range. The paper presents the results of the corresponding calculations of the components and full energy spectra of long-term oscillations of the current vectors. During the analytical

[2] Ivanov, V.A. and Yankovsky, A.E., 1992. [*Long-Wave Motions in the Black Sea*]. Kyiv: Naukova Dumka, 110 p. (in Russian).

[3] Konyaev, K.V., 1981. [*Spectral Analysis of Random Oceanological Fields*]. Leningrad: Gidrometeoizdat, 207 p. (in Russian).

processing of arrays of inter-annual variations in the mean annual vector values of currents, obtained synchronously at horizons in the 5–20 m layer, a procedure for centering the mean annual values of vector series was also used. This procedure entailed the component-wise exclusion from the realization of the corresponding values of the mathematical expectation vector, calculated over a 22-year measurement period.

Results and discussion

The results of the studies of the regime characteristics and features of long-term variability of the current were obtained on the basis of statistical and spectral analysis of the data of 22-year monitoring of currents in the 5–20 m layer at MHI Black Sea Hydrophysical Subsatellite Polygon. The new results enabled a methodical examination of the spectral density distributions of the total (kinetic) energy of coastal water oscillations, encompassing intra-annual and inter-annual variations in the values of coastal current characteristics within the 5–20 m layer.

Regime characteristics of the coastal current. The values of the mathematical expectation vector components of the current velocity of the west-southwest rhumbs and the standard deviations (SD) were calculated for 2002–2023. The table below shows estimates of the regime characteristics of the components of the current velocity vector and the corresponding SD at measurement horizons of 5, 10, 15, 20 m.

T a b l e

Estimates of the regime characteristics of coastal current in the 5–20 m layer

Depth, m	Velocity, cm/s	RMS_V, cm/s	Direction, °	RMS_D, °
5	8.1	0.8	254	3
10	8.0	0.8	240	3
15	7.7	0.8	234	3
20	6.9	0.8	217	3

The values of the regime characteristics of the along-coastal current, as presented in the table, practically coincide with the estimates obtained earlier in [10]. The reciprocating oscillations of the current at each measurement horizon, similar to [11], occur reversibly along the corresponding general west-southwest direction of the current. The vector-averaged current in the 5–20 m layer over the 22-year measurement period exhibits a velocity module of 7.5 cm/s and a direction of 237° along a straight section of the coastline oriented to the west-southwest. The values of the regime characteristics of the current, as presented in the table, are employed in the vector centering of the mean annual data for calculating the average long-term energy spectra of long-term inter-annual oscillations.

The analytical and spectral data processing results, as well as previously obtained estimates, has enabled the systematization and evaluation of the characteristics of long-term oscillations of the coastal current on the scales of intra-annual and inter-annual variability. Fig. 1 shows statistically reliable spectral maxima of the energy of intra-annual oscillations of the current in the 5–20 m layer in the variability range of 4 days to 6 years.

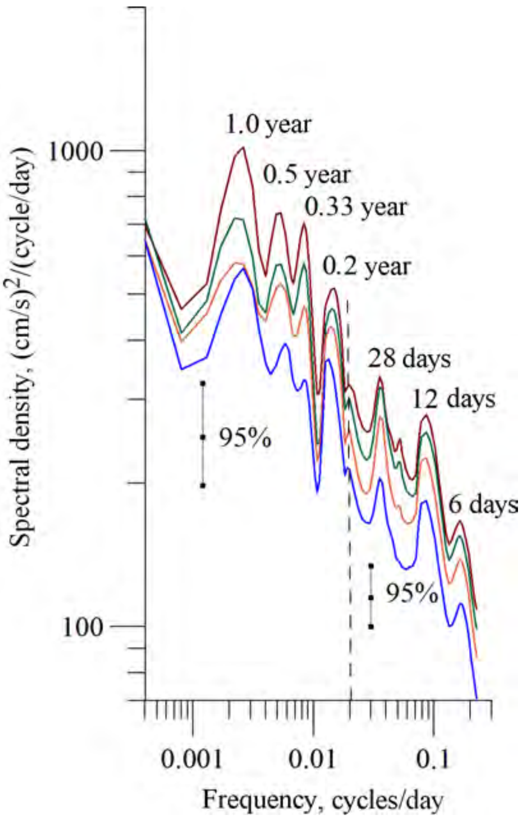

F i g. 1. Average long-term full energy spectra of the coastal current intra-annual variability in the range of periods 4 days – 6 years at horizons 5, 10, 15, 20 m (red, green, orange and blue lines, respectively) for 2002–2023 at the 95% confidence intervals for the ranges 4–50 days and 50 days – 6 years (vertical dashed line corresponds to the 50-day period)

A similar type of spectrum of seasonal sea surface level oscillations was previously obtained in the study of altimetry data of long-term remote satellite probes of the Black Sea level, with long-term level oscillations identified on an annual and semi-annual basis, caused by the corresponding seasonal variations in the tangential stress of wind friction [22]. In this study, it was observed that the spectral maxima of the level oscillations near the lowest annual harmonics correspond to the intrinsic variability of the Black Sea water circulation. The application of the analytical filtering procedure in the processing of time realizations enabled statistically reliable identification of the spectral peak of seasonal oscillations on a period of ~ 0.2 years (Fig. 1).

The range of long-term inter-annual oscillations of currents in the Black Sea remains the least studied both experimentally and theoretically, despite the development of such studies due to long-term contact measurements of currents carried out at MHI near the Southern Coast of Crimea. The availability of 22-year arrays of representative data from contact monitoring of the current field in the coastal zone has provided new empirical results on the problem under study. Fig. 2, a shows the energy spectra of inter-annual variability of the coastal current, calculated at each measurement horizon, where spectral peaks of close intensity are figured out at periods of ~ 2.7 and 3.6 years.

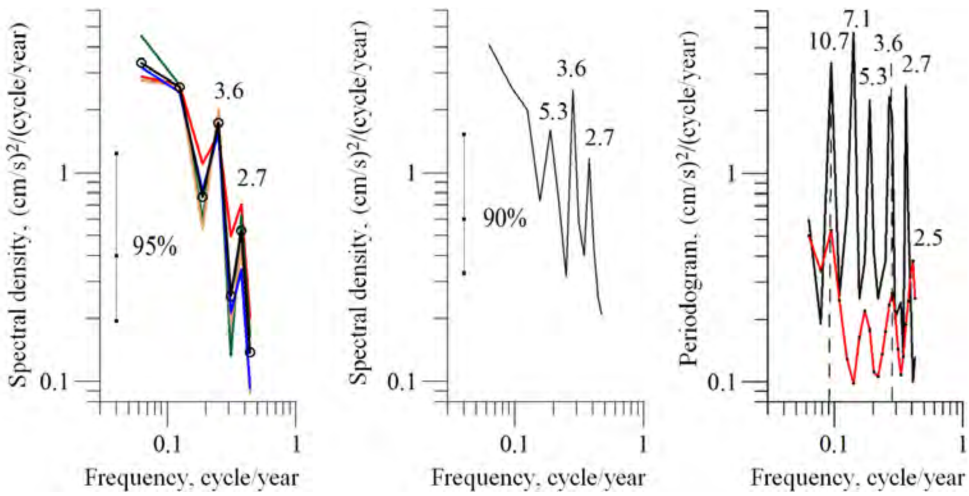

F i g. 2. Average long-term estimates of full energy spectra of the coastal current inter-annual variability in the range of periods 2–16 years (shown by the numbers at energy peaks): a – at horizons 5, 10, 15, 20 m (red, green, orange and blue lines, respectively) and on average over the layer (black line with circles) at the 95% confidence interval; *b* – in the 5–20 m layer at the 90% confidence interval; periodograms of current oscillations (black line) and the North Atlantic Oscillation index (red line) are shown in fragment *c*

When analyzing the relative variability of spectral density levels (Fig. 1; 2, *a*), it should be noted that the differences in their values between adjacent measurement horizons do not exceed the limits of the specified 95% confidence intervals. In fact, this is true over the entire variability range. Thus, the spectra calculated in the 15-m layer of coastal waters between the 5 m and 20 m horizons are similar and statistically homogeneous. This finding enables the utilization of the entire set of data obtained in this layer for integral estimates of the spectral characteristics of the layer oscillations as a whole. The spectrum of the stationary process (Fig. 2, *b*) is calculated based on the formed set of centered vector data obtained in the layer. The periodogram (Fig. 2, *c*, black line) is calculated to determine the full spectral composition and the values of the periods of coastal current oscillations contributing to the implementation under study. The spectrum estimate indicates that significant oscillations over periods of ~ 7.1 and 10.7 years contribute to the set of vector-centered mean annual variations obtained for 2002–2023, along with coastal current oscillations over periods of ~ 2.7, 3.6, and 5.3 years.

At present, scientific and theoretical studies of the relationships between long-term (climatic) oscillations of circulation processes in the World Ocean, atmosphere, and hydrosphere and actual variability of solar activity are being intensively developed [23–25]. The problem of assessing the role and characteristics of long-term variations in ocean and atmospheric waters in the formation of climate change has been discussed in domestic scientific publications since 1936. In [26], an analysis of auto-oscillations in the ocean – atmosphere – continent system was conducted to study the causes of long-term inter-annual oscillations in the Atlantic current regime. This analysis yielded an estimate of the period of oscillations under study, which was determined to be ~ 3.5 years. According to [27], the 5-year cyclicity is expressed in the Southern Oscillation (SO) and in the data on wind variability in the tropics, while 4–5-year oscillations in zonal temperatures were identified by statistical and spectral analysis of a set of long-term field data. As stated in [23], short-term climatic variations in the ocean – atmosphere system with typical periods ranging from 2 to 7–8 years are of global nature and can be reliably identified in different regions of the globe using various data types. The inter-annual variability of hydrometeorological fields in the Northern Hemisphere is most significantly reflected in the long-range climatic North Atlantic Oscillation (NAO) and the SO [23–25]. As demonstrated in [28], the analogue of the NAO index and the Black Sea level exhibit a 22-year cyclicity. The inter-annual variability of these characteristics is associated with the features of the phases of the 11-year solar cycle, resulting in noticeable differences in the formation of atmospheric circulation conditions. A stable trend emerges in the variability of the Rim Current intensity and the spatial structure of two macrocyclonic gyres of the Black Sea currents.

A comparison is made between the spectral composition of short-period climatic oscillations of the Black Sea coastal zone current (Fig. 2, *c*, black line) and inter-annual oscillations of the climatic NAO index (Fig. 2, *c*, red line). The data concerning the variability of monthly average NAO index can be accessed via https://origin.cpc.ncep.noaa.gov/products/precip/CWlink/pna/norm.nao.monthly.b5001.current.ascii.table. The inter-annual variation of the annual average NAO index values was computed from the sequence of monthly average values, and an estimate of the spectrum of these oscillations was calculated as well. When analyzing the spectral composition, significant climatic oscillations of the NAO index with periods of ~ 2.5, 3.6, 5.8 and 10.7 years (Fig. 2, *c*, red line) were identified. These periods exhibit close values with the corresponding periods (~ 2.7, 3.6, 5.3 and 10.7 years) of the coastal current oscillations in the Black Sea (Fig. 2, *c*, black line). It should be noted that despite the proximity of the compared values of the inter-annual oscillations' periods, in the studied range of variability of hydrometeorological fields in the NAO index oscillations, the spectral peak at a period of ~ 7 years is not manifested (Fig. 2, *c*).

Characteristic of the components of inter-annual current oscillations. As a result of applying the vector centering procedure to the 22-year inter-annual variations of smoothed annual average values of the velocity module (Fig. 3, *a*) and the direction of the current vector (Fig. 3, *b*), inter-annual variations in the velocity module (Fig. 3, *c*) and the direction (Fig. 3, *d*) of the centered current vector at 5–20 m layer horizons were formed. The smoothing procedure was performed in order to minimize the contribution of along-coastal current oscillations with periods of less than 3 years.

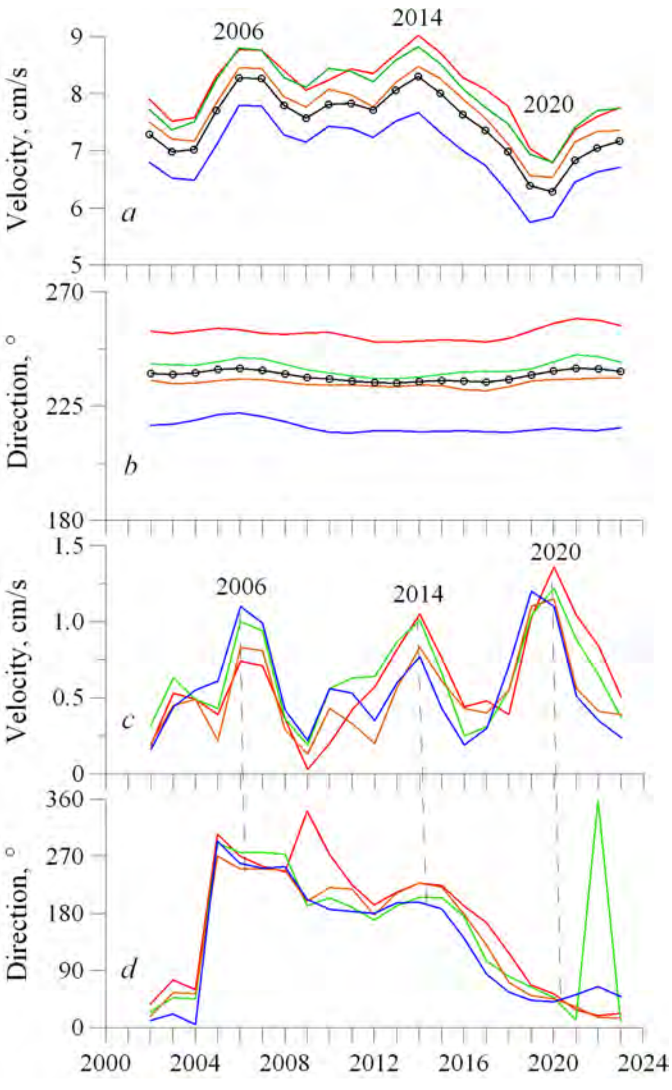

F i g. 3. Inter-annual variations of smoothed average annual values of current module (*a*) and direction (*b*) of the components of initial current vectors at horizons 5, 10, 15, 20 m (red, green, orange and blue lines, respectively) and their vector-averaged (in the 5–20 m layer) values (black lines with circles), as well as inter-annual variability of the components of corresponding centered current vectors: current module (*c*) and direction (*d*) in the 5–20 m layer

The inter-annual oscillations of velocity modules and directions of the centered current vectors over the periods of ~ 5 and 7 years have values that closely resemble those of each year at all measurement horizons. Vector averaging was performed on the components of the centered current vectors in the 5–20 m layer. Subsequently, smoothed estimates of their integral components were calculated (Fig. 4, *b*, *c*). The application of smoothing was implemented in order to minimize the contribution of current oscillations with 5-year periods.

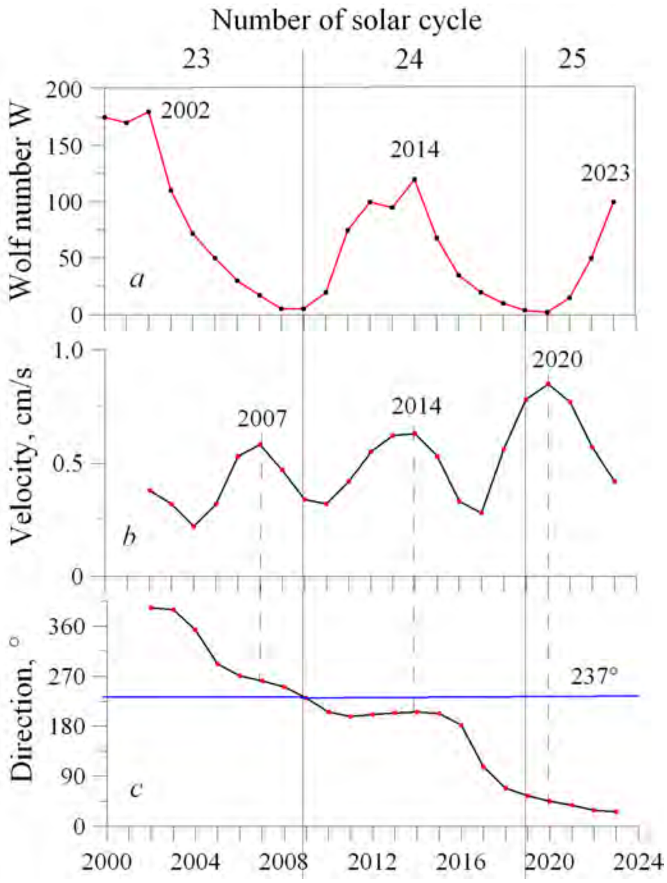

F i g. 4. Inter-annual variations in the smoothed annual average Wolf number (*a*), current module (*b*) and direction (*c*) of the vector-averaged (in the 5–20 m layer) centered current vector. Vertical solid lines are the boundaries of the 24th standard solar cycle, and blue horizontal line corresponds to the west-southwest direction (237°) of the stationary along-coastal current

The data on inter-annual variations in the annual mean Wolf number are available at https://www.side.be/SILSO/ssngraphics. Three full periods of 7-year oscillations of the centered current vector, corresponding in time to certain phases of the 23rd, 24th, 25th solar activity cycles (Fig. 4, *a*), are identified explicitly in Fig. 4, *b* due to smoothing. Fig. 4, *c* shows a smoothed realization of a complete cyclonic reversal of the current oscillation direction over a 22-year measurement period. At the same time, during 2006–2015, the along-coastal water movement during 7-year oscillations of the coastal current occurs practically in phase, and in the years 2002–2003 and 2020–2023, it displays an antiphase relationship with the general direction of the along-coastal current (solid blue line at 237°). Thus, the along-coastal current composition contains a directionally changing contribution of the 7-year oscillation vector, which leads to periodic changes in the velocity module of the stationary current. In the initial current variations shown in Fig. 3, *a*, the average annual velocity modulus in 2014 reached a maximum value of 9.4 cm/s, and subsequently decreasing to 5.8 cm/s in 2020. This phenomenon can be attributed to the periodic variability of the contribution of the identified long-term current oscillations. The identified long-term oscillations of coastal waters are synchronized with short-period climatic variations in their temporal scales. They are actively studied in the atmosphere and ocean due to their special role in the formation of changes in the climate system.

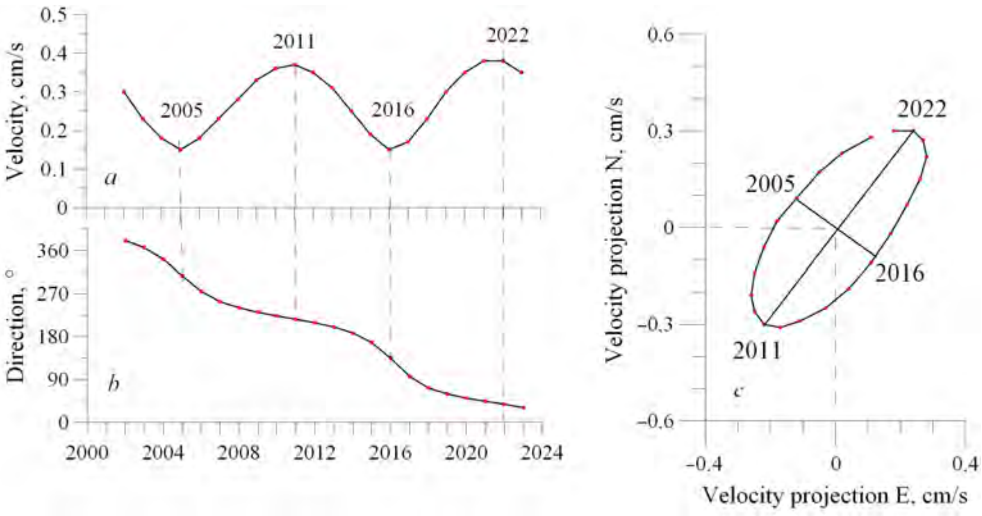

F i g. 5. Inter-annual variations in the smoothed annual average values of the current module (*a*), direction (*b*) and hodograph (*c*) corresponding to a 22-year circulation cycle of the vector-averaged (in the 5–20 m layer) centered current vector with minimization of the oscillation (with periods < 7 years) contributions

During the vector filtering of 7-year current oscillations in inter-annual variations of smoothed annual average values of velocity module (Fig. 5, *a*), 11-year oscillations with a complete 360° reversal of the direction (Fig. 5, *b*) of the centered current vector were identified upon completion of the 22-year measurement cycle. Figure 5, *c* shows the corresponding ellipse-shaped hodograph with cyclonic rotation of the annual average velocity of the centered current vector. The hodograph, constructed in the right-hand orthogonal coordinate system oriented to the north, demonstrates an almost complete 22-year cycle of current velocity vector rotation for the 2002–2023 period. Axial lines of the ellipse in Fig. 5, *c* indicate the orientation of the current vector in 2005, 2011, 2016 and 2022 in accordance with the extreme values of the velocity module oscillations (Fig. 5, *a*).

The results of the study on the variability characteristics of long-term current fluctuations in the coastal zone serve as an informative indicator of climatic variability of the Black Sea current system. Fig. 4, a demonstrates the inter-annual variations in the average annual values of the Wolf number, according to which the performed studies of currents are confined to the second half of the 23rd (odd), the first and second halves of the 24th (even) and the first half of the current 25th (odd) standard 11-year solar cycle. As demonstrated in [29–31], odd and even solar cycles play a distinctive role in the formation of inter-annual variability within hydrometeorological fields. At the same time, [29] observes that the time periods (with increased solar activity) that include the second half of the even and the first half of the odd standard solar cycles are particularly intense. The intensification of solar activity during the second half of the 24th even and the first half of the 25th odd current solar cycle (Fig. 4, *a*) from 2007 to 2020 resulted in a gradual increase of 1.5 times in the velocity module of inter-annual current oscillations (Fig. 3, *c*; 4, *b*). The previous phase of solar activity decline was observed in the second half of the 23rd solar cycle from 2002 to 2008, and the next phase of decline, according to [29], occurs in the second half of the 25th cycle after 2023.

As indicated in [30], the long-term oscillations of hydrometeorological fields are possible due to the combined influence of solar activity effects with periods of ~ 11 years and the dynamics of the underlying atmosphere with periods of ~ 2–7 years. The findings presented in this study and the availability of the necessary materials for long-term complex monitoring of currents and hydrometeorological conditions at MHI, make it possible to continue field studies of the long-term dynamics of coastal waters and circulation processes within the Black Sea region atmosphere, encompassing the spectrum of inter-annual (intradecadal) and interdecadal variability.

Conclusion

Marine Hydrophysical Institute of RAS has identified the study of the variability features of the Black Sea's long-period oscillations near the coastline as a priority task. These oscillations directly affect the dynamics of marine ecological and economic processes in the coastal zone near the Southern Coast of Crimea. The use of verified informational technology for contact monitoring ensured the metrological unity of the recorded values of vertical structure characteristics of the coastal current horizontal components with the utmost accuracy of instrumental measurements of their vector-averaged values. In a novel approach to the full-scale experimentation in the Black Sea coastal zone, the characteristics of long-period (seasonal and inter-annual) oscillations of quasi-stationary coastal currents have been identified, studied, and systematized. The structure and composition of short-period climatic variations of the coastal current, concentrated in the variability range of 2.7–7.1 years, as well as 11-year oscillations of the current within a 22-year variability cycle, are studied. A comparison of the spectral composition of inter-annual oscillations of the Black Sea coastal current and the corresponding NAO index oscillations reveals several periods of significant similarity. It is determined that an increase in the velocity module and a reversible change in the phase of the current inter-annual oscillations in the period 2007–2020 occur simultaneously with the intensification of solar activity. These analytical results provide a foundation for further investigation into the long-period variability characteristics of the Black Sea coastal current system.

REFERENCES

1. Ivanov, V.A. and Belokopytov, V.N., 2013. *Oceanography of the Black Sea***.** Sevastopol: ECOSI-Gidrofizika, 210 p.
2. Korotaev, G., Oguz, T., Nikiforov, A. and Koblinsky, C., 2003. Seasonal, Inter-annual, and Mesoscale Variability of the Black Sea Upper Layer Circulation Derived from Altimeter Data. *Journal of Geophysical Research: Oceans,* 108(C4), 3122. https://doi.org/10.1029/2002JC001508
3. Ovchinnikov, I.M., Titov, V.B. and Krivosheia, V.G., 1986. New Data on the Time Variability of Currents According to the Results of Perennial Measurements from a Stabilized Buoy of the Black Sea Shelf. *Doklady Akademii Nauk SSSR*, 286(5), pp. 1250-1254 (in Russian).
4. Krivosheya, V.G., Moskalenko, L.V. and Titov, V.B., 2004. On the current regime over the shelf near the North Caucasian coast of the Black Sea. *Oceanology*, 44(3), pp. 331-336.
5. Serebryany, A. and Lavrova, O., 2008. [Anticyclonic Eddy on the Northeastern Black Sea Shelf: Joint Analysis of Satellite Images and Acoustic Probing Data of the Water Column]. *Sovremennye Problemy Distantsionnogo Zondirovaniya Zemli iz Kosmosa*, 5(2), pp. 206-215 (in Russian).
6. Demyshev, S.G. and Evstigneeva, N.A., 2016. Modeling Meso- and Submesoscale Circulation along the Eastern Crimean Coast Using Numerical Calculations. *Izvestiya Atmospheric and Oceanic Physics*, 52(5), pp. 560-569. https://doi.org/10.1134/S0001433816050042
7. Zatsepin, A.G., Elkin, D.N., Korzh, A.O., Kuklev, S.B., Podymov, O.I., Ostrovskii, A.G. and Soloviev, D.M., 2016. On Influence of Current Variability in the Deep Black Sea upon Water Dynamics of Narrow North Caucasian Continental Shelf. *Physical Oceanography*, (3), pp. 14-22. https://doi.org/10.22449/1573-160X-2016-3-14-22
8. Belokopytov, V.N. and Nikol´sky, N.V., 2015. Stationary Anticyclonic Eddies Near the South and West Coasts of Crimea. *Ecological Safety of Coastal and Shelf Zones of Sea*, (1), pp. 47-53 (in Russian).
9. Kuznetsov, A.S., 2022. Mean Long-Term Seasonal Variability of the Coastal Current at the Crimea Southern Coast in 2002-2020. *Physical Oceanography*, 29(2), pp. 139-151.
10. Kuznetsov, A.S. and Ivashchenko, I.K., 2023. Features of Forming the Alongcoastal Circulation of the Coastal Ecotone Waters nearby the Southern Coast of Crimea. *Physical Oceanography*, 30(2), pp. 171-185.
11. Ivanov, V.A., Kuznetsov, A.S. and Morozov, A.N., 2019. Monitoring Coastal Water Circulation along the South Coast of Crimea. *Doklady Earth Sciences*, 485(4), pp. 405-408. https://doi.org/10.1134/S1028334X19040044
12. Koveshnikov, L.A., Ivanov, V.A., Boguslavsky, S.G., Kazakov, S.I. and Kaminsky, S.T. 2001. Problems of Heat and Dynamic Interaction in a Sea–Atmosphere–Land System of the Black Sea Region. In: MHI, 2001. *Ecological Safety of Coastal and Shelf Zones and Complex Use of Shelf Resources*. Sevastopol: MHI. Iss. 3, pp. 9-52 (in Russian).
13. Efimov, V.V., Shokurov, M.V. and Barabanov, V.S., 2002. Physical Mechanisms of Wind Circulation Forcing over the Inland Seas. *Izvestiya Atmospheric and Oceanic Physics*, 38(2), pp. 217-227.

14. Efimov, V.V., Barabanov, V.S. and Krupin, A.V., 2012. Simulation of Mesoscale Features of Atmospheric Circulation in the Crimean Black Sea Region. *Morskoy Gidrofizicheskiy Zhurnal*, (1), pp. 64-74 (in Russian).

15. Ivanov, V.A. and Yankovsky, A.E., 1993. Local Dynamic Experiment in the Shelf Zone of Southern Crimean Coast. *Okeanologiya*, 33(1), pp. 49-56 (in Russian).

16. Kuznetsov, A.S., 2023. Spectral Characteristics of Wind Variability in the Coastal Zone of the South Coast of Crimea 1997–2006. *Ecological Safety of Coastal and Shelf Zones of Sea*, (2), pp. 6-20.

17. Kuznetsov, A.S., 2024. Peculiarities of Interseasonal Variability of Alongshore Wind Circulation and Coastal Currents off the Southern Coast of Crimea. *Ecological Safety of Coastal and Shelf Zones of Sea*, (1), pp. 31-44.

18. Ivanov, V.A. and Dulov, V.A., eds., 2014. *Monitoring of the Coastal Zone in the Black Sea Experimental Sub-Satellite Testing Area*. Sevastopol: ECOSI-Gidrofizika, 526 p. (in Russian).

19. Timchenko, I.E. and Igumnova, E.M., 2011. Control over the Ecological-Economic Processes in the Integral Model of the Coastal Zone of the Sea. *Physical Oceanography*, 21(1), pp. 45-62. https://doi.org/10.1007/s11110-011-9103-9

20. Bayankina, T.M., Godin, E.A., Zhuk, E.V., Ingerov, A.V., Isaeva, E.A. and Vetsalo, M.P., 2021. Information Resources of Marine Hydrophysical Institute, RAS: Current State and Development Prospects. In: T. Chaplina, ed., 2021. *Processes in GeoMedia – Volume II.* Cham: Springer, pp. 187-197. https://doi.org/10.1007/978-3-030-53521-6_22

21. Ozmidov, R.V., 1964. Some Data on Large-Scale Field Characteristics of Horizontal Velocity Components in the Ocean. *Izvestiya AN SSSR. Seriya Geofizicheskaya*, (11), pp. 1708-1719 (in Russian).

22. Korotaev, G.K., Saenko, O.A. and Koblinsky, C.J., 2001. Satellite Altimetry Observations of the Black Sea Level. *Journal of Geophysical Research: Oceans,* 106(C1), pp. 917-933. https://doi.org/10.1029/2000JC900120

23. Polonsky, A.B., 2019. *The Ocean's Role in Climate Changes*. Newcastle upon Tyne: Cambridge Scholars Publishing, 270 p.

24. Palmén, E. and Newton, C.W., eds., 1969. *Atmospheric Circulation Systems: Their Structure and Physical Interpretation*. New York, London: Academic Press, 603 p.

25. Bigg, G.R., Jickells, T.D., Liss, P.S. and Osborn, T.J., 2003.The Role of the Oceans in Climate. *International Journal of Climatology*, 23(10), pp. 1127-1159. https://doi.org/10.1002/joc.926

26. Shuleikin, V.V. and Ershova, N.D., 1936. [The Reason for Periodic Fluctuations in the Regime of the Atlantic Currents]. *Doklady Akademii Nauk SSSR*, I(5), pp. 217-222 (in Russian).

27. Monin, A.S. and Shishkov, Yu.A., 1998. The 5-Year Cyclicity of Global Weather. *Doklady Earth Sciences*, 358(1), pp. 128-131.

28. Sizov, A.A. and Belokopytov, V.N., 2004. Peculiarities of Hydrometeorological and Hydrological Fields of the Black Sea at a Decline Phase of 11-Year Solar Activity Cycle. *Ecological Safety of Coastal and Shelf Zones and Complex Use of Shelf Resources*, 10, pp. 109-118 (in Russian).

29. Cliver, E.W., Boriakoff, V. and Bounar K.H., 1996. The 22-Year Cycle of Geomagnetic and Solar Wind Activity. *Journal of Geophysical Research: Space Physics,* 101(A12), pp. 27091-27109. https://doi.org/10.1029/96JA02037

30. Mikhalev, A.V. and Medvedeva, I.V., 2009. Solar Cycles in Variations of the 557.7 nm Emission. *Optika Atmosfery i Okeana*, 22(9), pp. 896-900 (in Russian).

31. Apostolov, E.M., Altadill, D. and Todorova, M., 2004. The 22-Year Cycle in the Geomagnetic 27-Day Recurrences Reflecting on the F2-Layer Ionization. *Annales Geophysicae,* 22(4), pp. 1171-1176. https://doi.org/10.5194/angeo-22-1171-2004

Submitted 30.05.2024; approved after review 09.08.2024;
accepted for publication 20.11.2024.

About the authors:

Alexandr S. Kuznetsov, Leading Research Associate, Marine Hydrophysical Institute of RAS (2 Kapitanskaya Str., Sevastopol, 299011, Russian Federation), CSc (Tech. Sci.), **ORCID ID: 0000-0002-5690-5349**, **Scopus Author ID**: **57198997777**, kuznetsov_as@mhi-ras.ru

Igor K. Ivashchenko, Research Associate, Marine Hydrophysical Institute of RAS (2 Kapitanskaya Str., Sevastopol, 299011, Russian Federation), CSc (Econ.), journal@mhi-ras.ru

Contribution of the co-authors:

Alexandr S. Kuznetsov – formulation of research goals and objectives, processing and analysis of in situ experiment data, discussion of the paper materials and results, preparation of paper text

Igor K. Ivashchenko – analysis of the research problem materials, discussion of the paper materials and results, preparation of paper text, editing of the manuscript

The authors have read and approved the final manuscript.
The authors declare that they have no conflict of interest.

ISSN 1573-160X, *PHYSICAL OCEANOGRAPHY*, Vol. 32, Iss. 1, pp. 46-62 (2025)

Original article

Geospheric Disturbances on Recordings of Laser Interference Devices

S. G. Dolgikh ✉, G. I. Dolgikh

V.I. Il'ichev Pacific Oceanological Institute, Far Eastern Branch of RAS, Vladivostok, Russian Federation
✉ *sdolgikh@poi.dvo.ru*

Abstract
Purpose. The purpose of the work is to investigate the meteotsunami phenomenon, search for its occurrences in the atmosphere, lithosphere and hydrosphere, and evaluate the characteristics of the oscillations caused by this phenomenon.
Methods and Results. Since 2000, measurements have been carried out at the Cape Schultz Marine Experimental Station using a seismoacoustic hydrophysical complex consisting of laser strainmeters, a laser nanobarograph, laser meters of hydrosphere pressure variations, a broadband seismograph, a weather station, a laboratory room and auxiliary equipment. All laser meters are based on Michelson interferometers. Data from all equipment are pre-processed and entered into the experimental database. To achieve this goal, synchronous data obtained during the meteotsunami in May 2015 were processed and analyzed. To compare the oscillations, registered in neighboring geospheres, filtering in the specified frequency ranges was performed in each case of comparison (Hamming filter was used for this purpose). The analysis of the data of the seismo-acoustic hydrophysical complex revealed several solitary waves corresponding in their characteristics to meteotsunami. The laser nanobarograph recorded a sharp change in the atmospheric pressure, which led to the occurrence of waves in the hydrosphere with an amplitude several times greater than the amplitude of the irregular semidiurnal tide, which was recorded by the laser meter of hydrospheric pressure variations. The moment of wave arrival in the hydrosphere was accompanied by powerful deformation perturbations, which were recorded by a laser strainmeter and a broadband seismograph. After a while, the laser nanobarograph and the laser strainmeter recorded strong oscillations.
Conclusions. As a result of a comprehensive analysis, a sharp increase in atmospheric pressure was recorded, which led to the appearance of waves in the hydrosphere, exceeding the amplitudes of the daily tide in the studied region, an increase in the amplitude of microdeformations of the Earth's crust with periods from 2 to 2.5 min was detected. A sharp change in atmospheric pressure caused an increase in the amplitudes of infragravity wave oscillations. A few hours after the passage of the last wave, the registration of vibrations and waves with a period of 1 hour 37 minutes in all geospheres began simultaneously on all records of laser interference devices. The analysis of the data obtained with the laser interference devices showed that the main source of these vibrations was in the atmosphere.

Keywords: meteotsunami, laser strainmeter, laser nanobarograph, laser meters of hydrosphere pressure variations, broadband seismograph

Acknowledgments: The work was supported in part by the State Assignment under Grant 124022100074-9 "The study of the nature of linear and nonlinear interaction of geospheric fields of the transition zones of the World Ocean and their consequences" (instrumentation setup, physical measurements) and in part by the Laboratory of Nonlinear Hydrophysics and Natural Hazards of V.I. Il'ichev Pacific Oceanological Institute, Far Eastern Branch Russian Academy of Sciences, Ministry of Science and Education of Russia, Project Agreement No. 075-15-2022-1127 from July 1, 2022 (processing and interpretation of the obtained data).

For citation: Dolgikh, S.G. and Dolgikh, G.I., 2025. Geospheric Disturbances on Recordings of Laser Interference Devices. *Physical Oceanography*, 32(1), pp. 46-62.

Introduction

Atmospheric pressure variations significantly contribute to the oscillations and waves that occur in the hydrosphere. Passage of tropical cyclones and typhoons over small bays leads to an increase in the amplitudes of eigen oscillations of seas and their separate parts [1–3].

Amplitudes of seiches in bays and seas can increase when acoustic-gravity waves pass over a water area. This phenomenon occurred during the explosion of the volcano in January 2022, when the eruption on Hunga Tonga-Hunga Ha'apai Island in the Tonga archipelago escalated to the active explosive phase. An acoustic-gravity Lamb wave was formed, which circled the Earth several times [4]. Analysis of data from wave recorders installed in the Sea of Japan revealed an increase in the amplitudes of seiches both in the sea itself and in the bays where the recorders were installed [5]. The reason for the growth of seish was the disturbance that occurred in the atmosphere. An abrupt change in atmospheric pressure in some cases leads to the formation of a wave with characteristics similar to a tsunami. This is a meteorological tsunami, or meteotsunami, caused not by underwater earthquakes and landslides, but by atmospheric processes passing over the ocean [6]. Sometimes, a meteorological tsunami occurs during the passage of a thunderstorm front, which can be caused by atmospheric gravity waves or an abrupt change in wind direction over the water surface.

Resonance effects play an important role in the generation of meteotsunamis when the period of eigen oscillations of the water area and their propagation velocity are close to the period and propagation velocity of atmospheric disturbances. However, not every atmospheric front or atmospheric disturbance leads to the generation of a meteorological tsunami. The most important is the atmospheric pressure gradient, which directly affects the ocean [7].

As observations show, the consequences of meteorological tsunamis can be serious and, in some regions, even catastrophic. For example, in June 2014 in Croatia, the water level in the harbor began to rise, resulting in flooding of the roads, displacement of cars and landing of boats onshore. Over time, the water receded from the streets. However, there were no strong underwater earthquakes at the time. Similar destructive meteorological tsunamis have been observed on the shores of the Yellow and Black Seas. The majority of cases of destructive waves, not associated with seismic events, have been recorded along the coasts of Japan, Europe and North America.

There is no periodicity in the occurrence of meteorological tsunamis, in some areas they occur only in spring and summer months, while in others, they occur once every 3–5 years [8–12]. During the registration of a meteotsunami, increases in the amplitude of sea excitement are also observed in the range of periods from 2 minutes to 3 hours [13]. Water levels rise very slowly during a meteorological tsunami, within tens of minutes or even hours. The water can rise by a few decimeters or even several meters, flooding areas close to the basin and altering the coastline [14]. The consequences of such natural disasters can be enormous, although not comparable to ordinary tsunamis. The development of measuring equipment over the past 30 years has almost doubled the proportion of meteotsunamis recorded. In order to assess and prevent the consequences of meteorological tsunamis, the databases are used to develop numerical models to evaluate the impact of an abrupt change in atmospheric pressure on the water surface [15–17].

According to the data of experimental observations of near-bottom hydrostatic pressure conducted by Russian scientists from the Institute of Marine Geology and Geophysics of the Far Eastern Branch of the Russian Academy of Sciences in the shelf area of the southern part of Sakhalin Island and the Kuril Islands, sea level fluctuations corresponding to tsunami waves were identified. Analysis of the seismic situation in this area showed that there were no strong underwater earthquakes on these days, and these fluctuations were attributed to meteorological tsunamis [18].

Meteotsunami phenomena are actively studied by scientists around the world. In most cases, meteorological stations and tide sensors are used to register meteotsunamis. In some cases, wave gauges and mareographs are used. Based on data from meteorological stations and tide sensors in the Yellow Sea, scientists identified 42 events from 2010 to 2019 that can be attributed to a meteotsunami [16, 19]. This phenomenon is often found off the coast of Japan, which is recorded by deep-sea sensors of the DART (Deep-ocean Assessment and Reporting of Tsunamis) type. Based on measurements from meteorological stations, wave detectors and deep-sea sensors, the trajectory of the meteotsunami wave and possible consequences are calculated [20, 21]. This approach is essential for reducing possible consequences when a meteotsunami wave comes ashore.

In the south of the Primorsky Territory, in Posyet Bay, according to the data of laser-interference devices and a broadband seismograph, a natural phenomenon was recorded. This phenomenon exhibited characteristics consistent with meteotsunami. Specifically, the data from the laser nanobarograph indicated an atmospheric disturbance of several hPa, which led to the emergence of anomalous solitary hydrosphere waves with amplitudes several times higher than the amplitudes of irregular semi-diurnal fluctuations typically observed in this region [22]. These waves were recorded by the laser meter of hydrosphere pressure variations, which was installed on the shelf of the Sea of Japan. During the solitary wave recordings, an increase in the amplitude of oscillations with periods ranging from 2 to 2.5 minutes was observed in the recordings of laser strainmeters. A few hours after the registration of waves in the hydrosphere, fluctuations with a period of approximately one and a half hours were detected in the recordings of the laser strainmeter and the laser nanobarograph. The present article describes this phenomenon and offers a probable assessment of its manifestation in the neighboring geospheres (atmosphere, hydrosphere, lithosphere).

Materials and methods

Since the year 2000, a seismoacoustic hydrophysical complex has been operating continuously on the base of the Cape Schultz Marine Experimental Station of the V.I. Il'ichev Pacific Oceanological Institute of FEB of RAS. The complex includes laser strainmeters, a laser nanobarograph, laser meters of hydrosphere pressure variations, a broadband seismograph, a weather station, a laboratory room, and auxiliary equipment.

All laser meters are based on Michelson interferometers using a frequency-stabilized helium-neon laser with a long-term stability frequency of 10^{-9} as a light source. The laser strainmeters are based on Michelson unequal-arm interferometers with measuring arm lengths of 52.5 and 17.5 m and North-South and West-East orientations, respectively. Both strainmeters are capable of detecting microdeformations of the Earth's crust in the frequency range from 0 (conditionally) to 1000 Hz, with an accuracy of 0.3 nm and an almost unlimited dynamic range [23]. The laser nanobarograph is based on Michelson equal-arm interferometer, where the aneroid box is the sensitive element. The device is capable of detecting atmospheric pressure variations in the frequency range from 0 (conditionally) to 1000 Hz with an accuracy of 1 μPa and in an almost unlimited dynamic range [24]. The laser meter of hydrosphere pressure variations is made on the basis of a nonequal-arm Michelson interferometer using a thin membrane fixed at the edges as a sensitive element. The meter is capable of detecting hydrosphere pressure variations in the frequency range from 0 (conditionally) to 1000 Hz with an accuracy of 1 μPa and in an almost unlimited dynamic range [25]. The complex also includes a Guralp CMG-3ESPB broadband seismograph with an operating frequency range f 0.003–50 Hz per sensor. Data from all devices are transmitted via cable lines to the laboratory room, where a database of experimental data is created after preliminary processing.

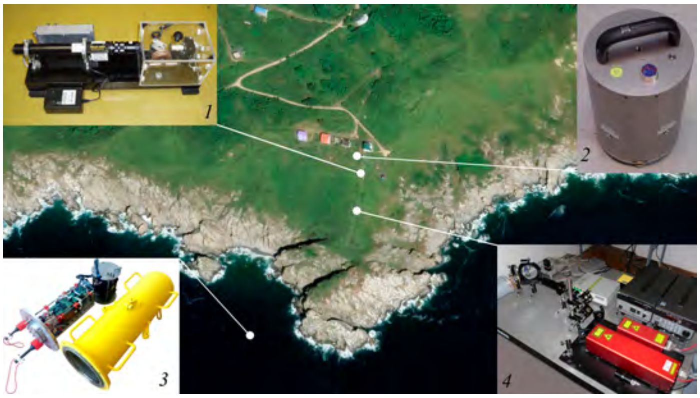

F i g. 1. Device arrangement scheme: *1* – laser nanobarograph; *2* – broadband seismograph; *3* – laser meter of hydrosphere pressure variations; *4* – laser strainmeter

Figure 1 shows the arrangement of the devices included in the complex. Laser strainmeters are installed under the Earth's surface at a distance of 80 m from each other. Optical parts of the interferometers are installed in thermally insulated rooms to eliminate the influence of temperature variations on the instrument measurements. The broadband seismograph is installed below the surface in a thermally insulated chamber between two laser strainmeters. The laser nanobarograph is installed in a thermally insulated room 50 m from the laser strainmeter with North-South orientation and about 30 m from the laser strainmeter with West-East orientation.

The laser meter of hydrosphere pressure variations is installed on the shelf of the Sea of Japan at a distance of 200 m from the coast and 300 m from the 52.5 m laser strainmeter at a depth of 33 m.

In the course of solving the aforementioned problems, we performed processing and analysis of synchronous experimental data obtained during the registration of atmospheric pressure variations by laser nanobarographs, hydrostatic pressure variations by laser hydrosphere pressure meters and microdeformations of the upper layer of the Earth's crust by laser strainmeters. To assess the meteotsunami manifestation in neighboring geospheres, we shall consider synchronous data for May 2015. The data records of all laser interference meters were obtained with a duration of 1 hour and a sampling rate of 1000 Hz. For convenience, the data were filtered with a low-frequency Hamming filter up to 1 Hz and diluted 1000-fold. As a result, we obtain a set of data from laser strainmeters, the laser nanobarograph and the laser meter of hydrosphere pressure variations with a sampling rate of 1 Hz. The measurement of the main parameters of oscillations and waves in all geospheres is carried out simultaneously, which, with their subsequent processing, makes it possible to determine more accurately the primary source in the "atmosphere-hydrosphere-lithosphere" system.

Results and discussion

Registration and analysis of atmospheric-hydrosphere oscillations. Processing the data of atmospheric pressure variations obtained by the laser nanobarograph and hydrostatic pressure obtained by the laser hydrosphere pressure change meter, several events of abnormal hydrosphere behavior were detected on May 25–26, 2015. The laser nanobarograph recorded an abrupt change in atmospheric pressure (Fig. 2) with a magnitude of 13.5 hPa. The abrupt change in atmospheric pressure was recorded at 15:20 on May 25, 2015. The abrupt change in atmospheric pressure was also accompanied by an increase in oscillations with periods of 2 to 2.5 min.

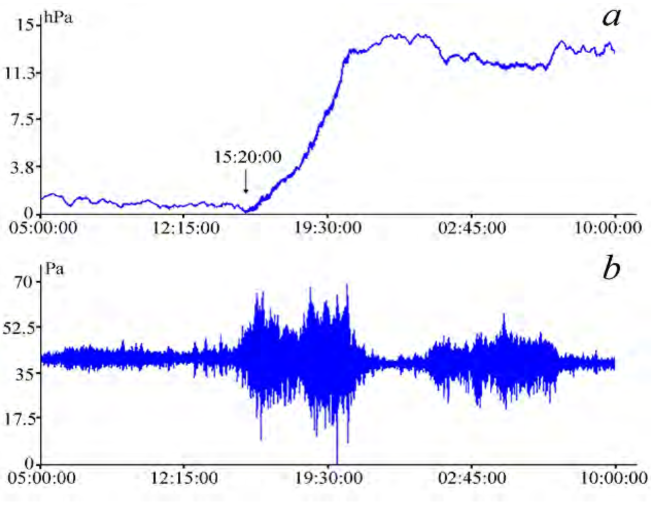

F i g. 2. Fragment of the laser nanobaroghraph recording for May 25–26, 2015, UTC (*a*) (adapted from [22]) and filtered fragment of the laser nanobaroghraph recording (*b*)

To identify these oscillations, we filter the laser nanobarograph recording with a bandpass filter. The recording clearly shows an increase in the amplitudes of these oscillations at the time of registration of the atmospheric pressure increase (Fig. 2, *b*). The amplitudes of oscillations with periods of 2 to 2.5 min increased almost tenfold. After the atmospheric pressure stabilized, these oscillations also decreased. Such an increase in atmospheric pressure could be attributed to the arrival of a typhoon or cyclone at the site where the instruments were installed. However, according to the Meteorological Service of the Russian Academy of Sciences, no cyclones or, especially, typhoons were recorded in the region at that time. The weather over the region was clear with moderate northeasterly winds.

Let us look at the records of the laser meter of hydrosphere pressure variations at the time of registration of the atmospheric pressure increase and after this increase. Figure 3 shows a record of the laser interference meter installed on the bottom in the shelf zone of the Sea of Japan at a depth of 33 m on May 25–26, 2015. The initial disturbance was recorded almost an hour and a half after the start of registration of the atmospheric pressure jump. The registration of the initial disturbance began at 16:44 on May 25, 2015, and almost 12 hours later, at 04:20 on May 26, 2015, the second disturbance was recorded.

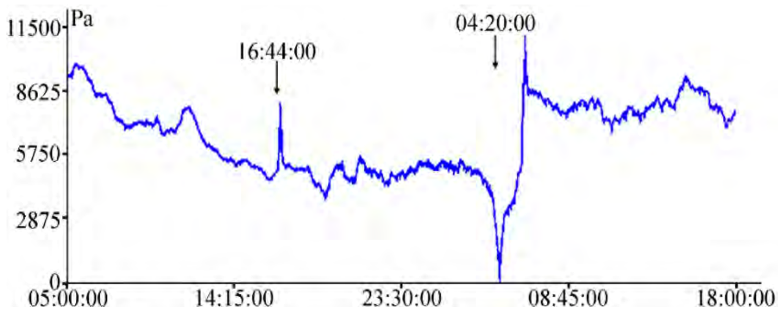

F i g. 3. Fragment of the recording of the laser meter of hydrosphere pressure variations for May 25–26, 2015, UTC (adapted from [22])

The two disturbances were inherently different. If the first was a solitary wave of almost soliton-like shape (Fig. 4, *a*), the second was a wave accompanied by an outflow of water masses (Fig. 4, *b*). The first wave caused only an inflow of water masses (increase of hydrostatic pressure) and its characteristics were very similar to a tsunami wave. The height of the recorded wave was four times higher than the amplitude of the irregular semi-diurnal tide in this region. The amplitude of the 9irregular semi-diurnal tide according to the sea level station monitoring facility was 0.1 m [1]. The wave propagation time through the point, where the laser meter of hydrosphere pressure variations was installed was about 14.5 min. During the arrival

[1] UNESCO. *Sea Level Station Monitoring Facility.* [online] Available at: https://ioc-sealevelmonitoring.org [Accessed: 25 May 2023].

of the second wave, the first outflow of water masses was recorded (decrease of hydrostatic pressure). The depth of the sea at the location of the device decreased by a value approximately equal to five amplitudes of the irregular semi-diurnal tide. The outflow of water masses lasted 25.5 min, and then the sea level returned to its previous position within 16 min. The third wave was recorded by the laser meter of hydrosphere pressure variations in about an hour. As with the arrival of the first wave, an influx of water masses was observed. However, their shapes were different, and the wave height was almost double that of the height of the first wave. The graph shows that the sea level began to rise sharply, and in 5 min, a decrease of one third of this value began. Nevertheless, with the arrival of another wave, the hydrostatic pressure begins to rise again. The total time of wave propagation through the installation point of the laser meter of hydrosphere pressure variations was 23 min.

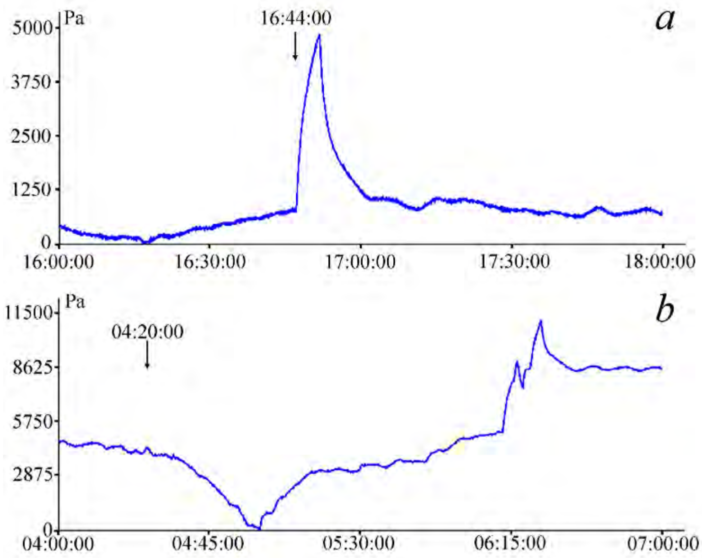

F i g. 4. Enlarged fragments of the recordings of the laser meter of hydrosphere pressure variations for May 25, 2015, UTC (*a*) and May 26, 2015, UTC (*b*) (adapted from [22])

Hen recording these solitary waves, the initial sea level did not change until after the arrival of the third wave. If the sea level recovered immediately after the first wave, it returned to its initial position 40 min after the second wave. After the third wave, the sea level rose, and it took several days for the sea level to return to its initial state. Considering that the time of the first disturbance passage was 14.5 min, the total period of the wave should be approximately 29 min. This is close to the period of seiches of the Sea of Japan, recorded in the region, which is 30.5 min [26]. However, upon analyzing the second and the third disturbances, it is evident that the total period of the waves is 51 and 46 min respectively, which is much longer than the seiche period observed in the region. In terms of their shape, the second and the third waves differ from the first, as they are not as well defined. In the third case, there is an apparent overlap of the waves. The registration of solitary waves, instead of the increase in the amplitudes of the Sea of Japan seiches, testifies to the fact that the increase in atmospheric pressure did not take place over the entire area of the sea, but formed in its certain part and then moved towards the site of installation of the laser interference devices. Taking into account that the registration of the atmospheric disturbance began 1 hour 24 min earlier than the disturbance in the hydrosphere, we can say that it caused solitary waves in the hydrosphere.

Similar behavior of water masses was recorded in 1978 in Vela Luka, Croatia. Early in the morning, the water began to come into the streets of the city, flooding everything in its path, and after 10 min it began to move back. After some time, the phenomenon repeated itself. The flood in Vela Luka is considered one of the most striking examples of the phenomenon, which has been called a "meteorological tsunami" (or simply "meteotsunami") [2]. In this context, the solitary waves recorded by the laser meter of hydrosphere pressure variations, along with the increase in atmospheric pressure, recorded by the laser nanobarograph, can be associated with a meteorological tsunami.

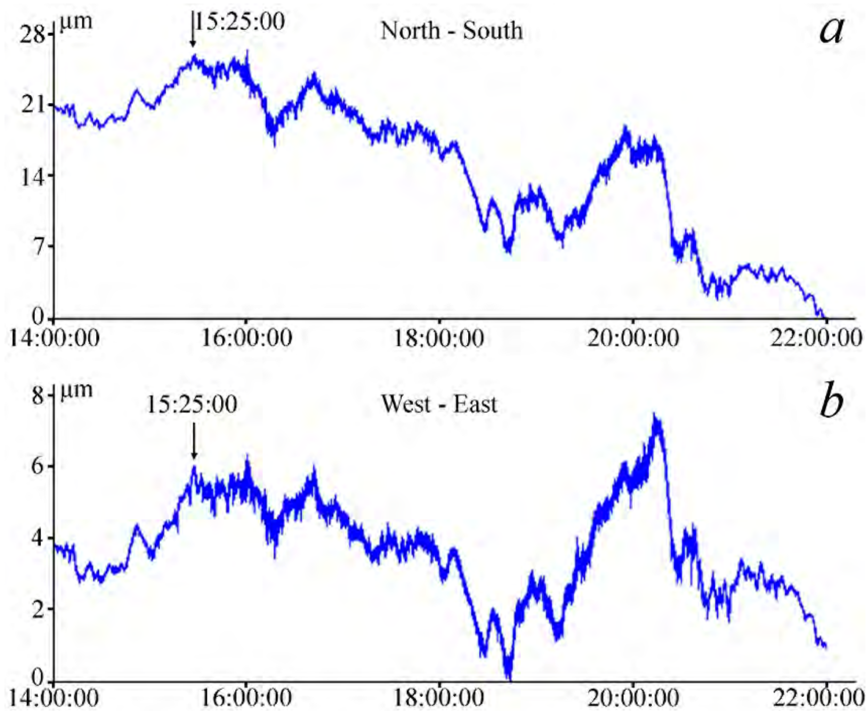

F i g. 5. Fragments of the laser strainmeter recordings, North-South orientation (*a*), West-East orientation (*b*) for May 25, 2015, UTC (adapted from [22])

---

[2] Hodzić, M., 1979. Occurrences of Exceptional Sea Level Oscillations in the Vela Luka Bay. *Priroda*, 68(2-3), pp. 52-53 (in Croatian).

Registration and analysis of lithospheric oscillations. During the arrival of atmospheric disturbance recorded by the laser nanobarograph, oscillations of the earth crust with periods from 2 to 2.5 min are observed on the recordings of laser strainmeters and the broadband seismograph. Figure 5 shows fragments of recordings of the laser strainmeter with measuring arm length of 52.5 m and North-South (a) orientation and the laser strainmeter with measuring arm length of 17.5 m and West-East orientation (b). Both graphs show that at approximately 3:20 p.m. on May 25, 2015, micro deformations of the earth crust begin to appear with periods from 2 to 2.5 min, and their amplitude increases. And at the moment of termination of short-period oscillations in the atmosphere, the amplitude of these oscillations in the upper layer of the earth's crust drops to the background level.

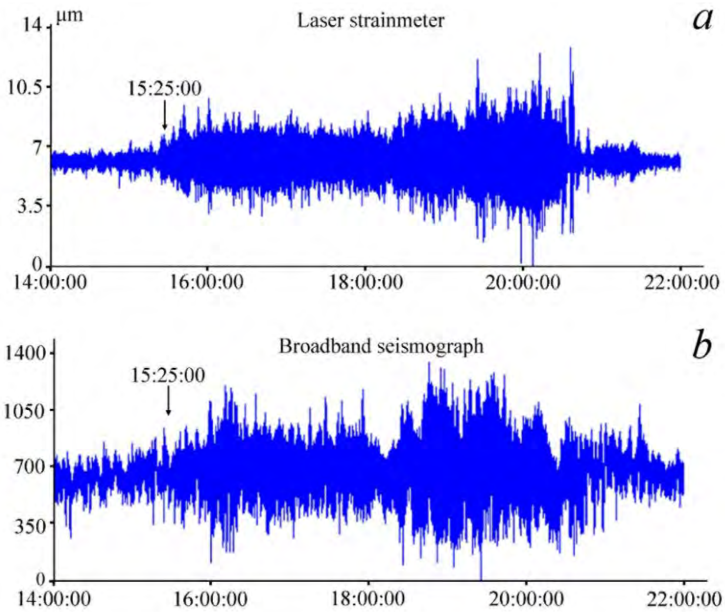

F i g. 6. Filtered fragment of the recording of the laser strainmeter of North-South orientation (*a*) and fragment of the broadband seismograph recording (*b*) for May 25, 2015, UTC (adapted from [22])

When analyzing the broadband seismograph data, an increase in the amplitude of crustal oscillations with periods of 2 to 2.5 min is also observed. Thus, Fig. 6 shows a fragment of the broadband seismograph recording of the North-South arm (bottom), where an increase in the amplitude of these oscillations is observed. To compare the laser strainmeter and broadband seismograph records, we filter out the laser strainmeter recording in the frequency range of the seismograph. We use a Hamming bandpass filter with boundaries from 0.003 to 50 Hz. After filtering the fragment of the laser strainmeter recording with North-South orientation, the manifestation of microdeformations within the Earth's crust with periods from 2 to 2.5 min becomes more pronounced (Fig. 6, *a*). After filtering, the laser strainmeter and broadband seismograph recordings became similar. A similar manifestation of the crustal oscillations is observed on the horizontal laser strainmeter with West-East orientation and a measuring arm length of 17.5 m, as well as a component of the West-East arm of the broadband seismograph (Fig. 7).

Let us analyze the records of the laser nanobarograph, laser strainmeters, and the broadband seismograph during registration of infragravity oscillations with periods from 2 to 2.5 min. In the laser nanobarograph records, the amplitude of the excited oscillations is 9.3 times greater than the amplitudes of the same oscillations before the atmospheric disturbance. In the records of the laser strainmeters at the moment of the atmospheric disturbance, the amplitude of the oscillations is 9.2 times greater than the amplitudes of the oscillations before the disturbance. Similar values of the ratio of the amplitudes of the oscillations before the atmospheric disturbance and at the time of its registration are observed on the records of the broadband seismograph, the ratio of the amplitudes is 9.4. The atmospheric disturbance, registered by the laser nanobarograph, caused an almost 10-fold increase in the amplitudes of infragravity oscillations in the atmosphere and lithosphere. The similarity of the amplitude ratio of these oscillations does not allow to unambiguously identify their primary source, whether in the atmosphere or in the lithosphere.

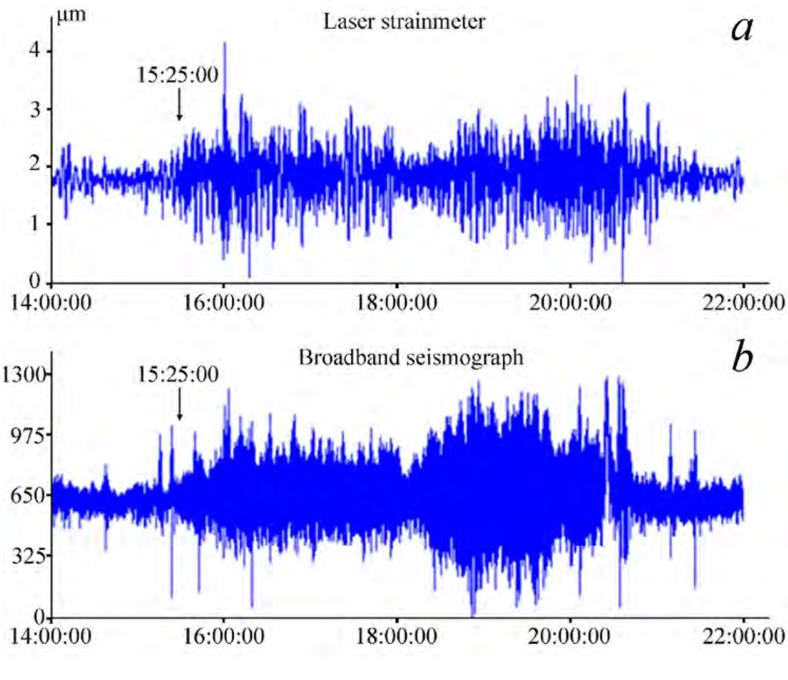

F i g. 7. Filtered fragment of the recording of the laser strainmeter with West-East orientation (*a*) and fragment of the broadband seismograph recording (*b*) for May 25, 2015, UTC

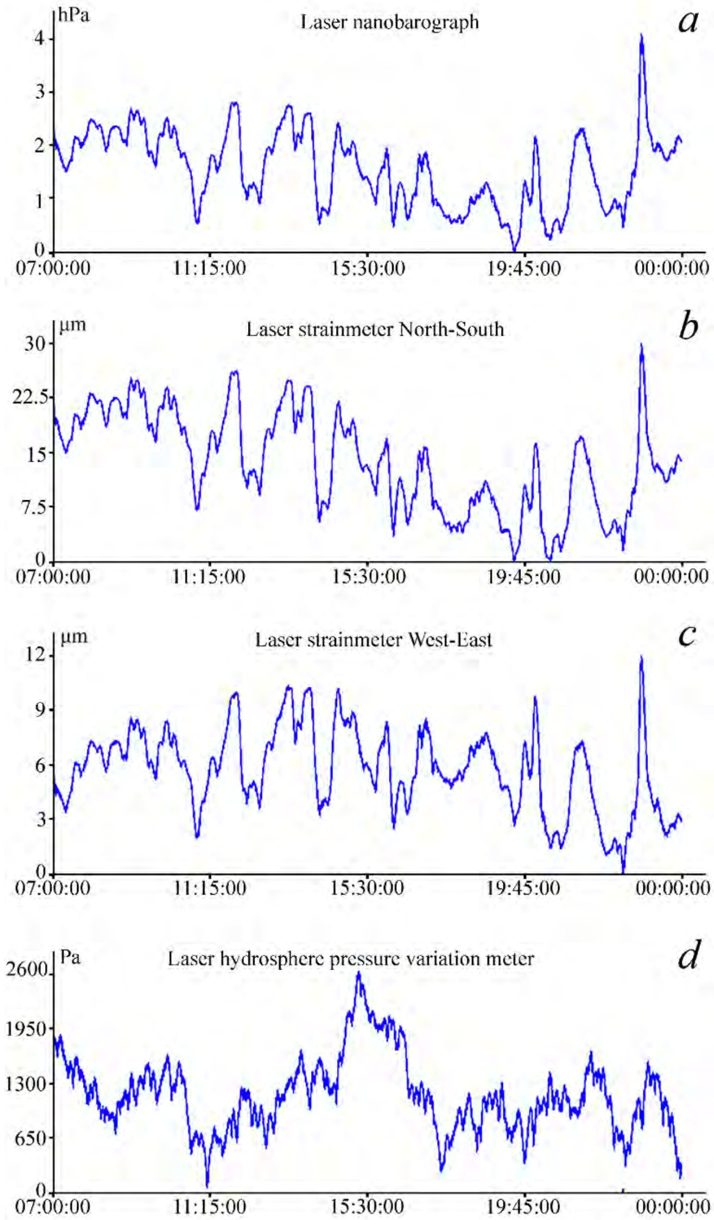

F i g. 8. Fragments of the recordings of laser nanobarograph (*a*), laser strainmeter with North-South orientation (*b*), laser strainmeter with West-East orientation (*c*) and laser meter of hydrosphere pressure variations for May 26–27, 2015, UTC (adapted from [22])

Registration of one and a half hour fluctuations in geospheres. When analyzing the data from the laser-interference devices, oscillations with a period of about one and a half hours were recorded. Consequently, on the recordings of laser strainmeters for May 26 and 27, 2015, oscillations with a period of 1 h 37 min were detected. Figure 8 shows fragments of recordings obtained with laser strainmeters, with measuring arm lengths of 52.5 m (*b*) and 17.5 m (*c*). Powerful hour-and-a-half oscillations are observed in both graphs. When processing recordings of the laser nanobarograph installed in close proximity to laser strainmeters, oscillations with similar periods were also identified (Fig. 8, *a*). A subsequent analysis of hydrostatic pressure data obtained using the laser meter of hydrosphere pressure variations showed the presence of oscillations with similar periods. However, these oscillations are less pronounced in the neighboring geospheres (Fig. 8, *d*). The correlation coefficient of variations in the pressure of the hydrosphere and the atmosphere is 0.14, and between variations in the pressure of the hydrosphere and microdeformations of the upper layer of the Earth's crust is 0.22. A more pronounced correlation, with a coefficient of 0.89, is observed between atmospheric pressure variations and micro-deformations of the Earth's crust. The presence of oscillations with a period of 1 h 37 min in the atmosphere, lithosphere, and hydrosphere indicates their common origin associated with one of the geospheres. The use of complex research methods, integrating laser-interference meters across three distinct geospheres, allows us to determine the primary source of these oscillations. The analysis of the data from the laser nanobarograph, laser strainmeters and the laser meter of hydrosphere pressure variations revealed that the maximum ratio of the amplitude of the hour-and-a-half oscillations to background oscillations in the atmosphere is greater than in other geospheres. The most important factor in determining the primary source is the abrupt change in atmospheric pressure that preceded the arrival of solitary long waves in the hydrosphere. Consequently, it can be concluded that the atmosphere is the primary source of all observed oscillations and waves.

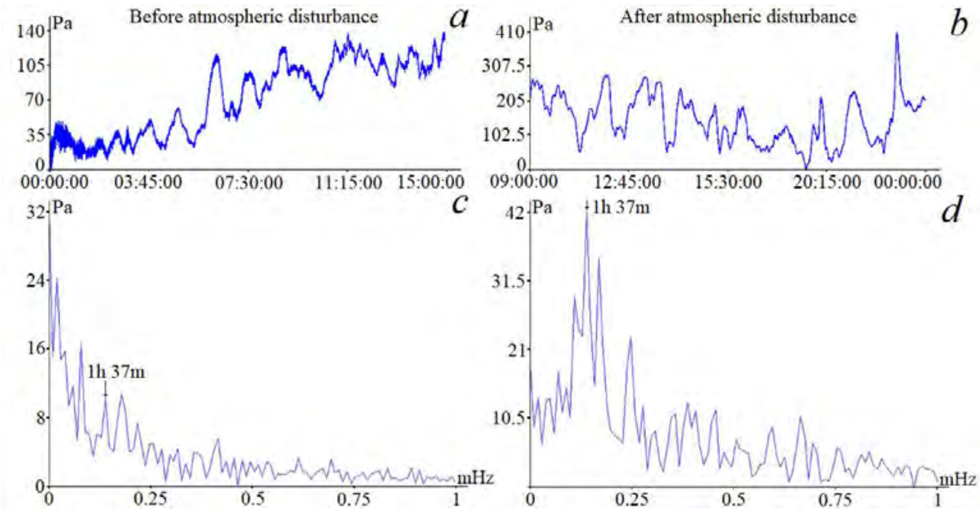

F i g. 9. Fragments and spectra of the laser nanobarograph recordings for May 25 and 26, 2015, UTC

In order to estimate the amplitudes of these oscillations, the spectra of the recordings of the laser nanobarograph and the horizontal laser strainmeters with North-South and West-East orientations must be considered. Figures 9, 10 and 11 illustrate fragments of the recordings and spectra. The left side exhibits the curves prior to the oscillations, while the right side displays the curves at the moment of their arrival.

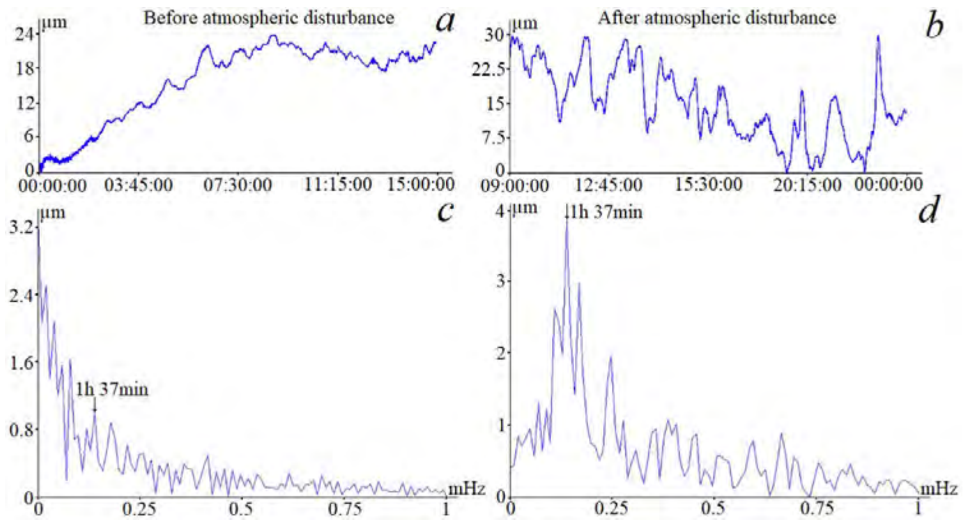

F i g. 10. Fragments and spectra of the recordings of the laser strainmeter with North-South orientation for May 25 and 26, 2015, UTC

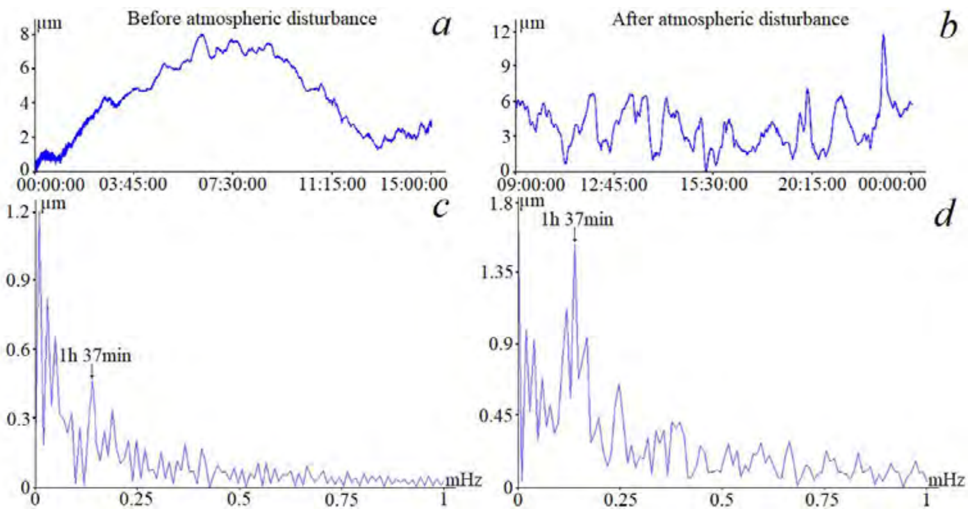

F i g. 11. Fragments and spectra of the recordings of the laser strainmeter with West-East orientation for May 25 and 26, 2015, UTC

Spectra were calculated using sections of recordings of laser interference devices with a duration of 15 h. The recording was made at a frequency of 10 Hz. This results in a duration of 540,000 points for each section. The spectrum of the recording area prior to the atmospheric disturbance exhibited a classical form, accompanied by a few prominent peaks. This spectrum can be attributed to background fluctuations that are constantly present on the instrument recordings.

Three peaks with periods of 1 h 23 min, 1 h 37 min and 1 h 49 min are clearly distinguished in the right spectra. The amplitude of the oscillations with a period of 1 h 37 min is the largest, as evidenced by both the instrument recordings and the spectra. A visual analysis of the spectra shows that the amplitudes of these oscillations have increased by more than threefold compared to the background oscillations, thereby becoming more pronounced. Furthermore, the amplitude of these oscillations increased with a period of about 1 h, manifesting as a peak positioned to the right of the group of peaks described above.

Let us compare the oscillations amplitudes with a period of 1 h 37 min before and after the arrival of the atmospheric disturbance. The following Table presents the values of the amplitudes of these oscillations based on the data collected by laser interference devices. The analysis of the data reveals that the maximum ratio of the amplitudes of these oscillations in the spectra of the laser nanobarograph records is nearly 15% higher than in the spectra of the laser strainmeter records. In the context of baro-deformation interaction, atmospheric pressure variations predominantly influence the microdeformations of the Earth’s crust [25]. Consequently, the primary source of the oscillations with a period of 1 h 37 min, as recorded by laser interference devices, is attributed to atmospheric fluctuations. The oscillations with similar periods were identified in the atmosphere several hours after the meteotsunami occurrence in other regions [8].

T a b l e

Value of oscillation amplitudes with a period of 1 h 37 min on laser interference devices

Devices	Before atmospheric disturbance	After atmospheric disturbance	Ratio of amplitudes
Laser nanobarograph, Pa	10.37	42.98	4.14
North-South laser strainmeter, μm	1.04	3.75	3.61
West-East laser strainmeter, μm	0.49	1.67	3.41

Conclusion

An abrupt increase in atmospheric pressure resulted in the generation of solitary long waves in the hydrosphere, as recorded at 15:20 on May 25. Several waves were recorded by the laser meter of hydrosphere pressure variations. The first wave exhibited a shape resembling a soliton. The first wave’s registration occurred at 16:44 on May 25, while the second wave was recorded at 04:20 on May 26. The time difference between the arrivals of these waves was about 13 hours, and the height of these waves was several times greater than the amplitude of the daily tide in this region. The height of the first wave, which was smaller than the subsequent ones, and its smoother shape indicate that it formed closer to the location of the device. An abrupt change in atmospheric pressure caused an increase in the amplitudes of the oscillations of the infragravity waves. A study of the data from the laser strainmeters and the broadband seismograph revealed an increase in the amplitude of microdeformations of the Earth's crust with periods ranging from 2 to 2.5 min coinciding with the abrupt change in atmospheric pressure. The registration of changes in the amplitude of these upper layer crust oscillations occurred at 15:25 on May 25. The duration of this change was approximately 6.5 h. Several hours after the passage of the last wave, the records of all laser interference devices revealed the presence of oscillations with a period of approximately one and a half hours. Concurrently, at about 07:00 on May 26, the registration of vibrations and waves with a period of 1 h 37 min commenced simultaneously in all geospheres. However, the largest ratio of the amplitudes of these oscillations before and after the atmospheric disturbance was observed in the atmosphere.

A comprehensive analysis of the data from the laser nanobarograph, laser meter of hydrosphere pressure variations, laser strainmeters, and the broadband seismograph showed that all these disturbances were associated with the passage of meteorological tsunamis in the southern region of the Russian Far East. An abrupt increase in atmospheric pressure, formation of solitary waves in the hydrosphere, an increase in the amplitude of waves with periods from 2 to 120 min are the cause and effect of the passage of meteotsunamis at the location of laser interference devices.

REFERENCES

1. Deng, G., Xing, J., Sheng, J. and Chen, S., 2022. A Process Study of Seiches over Coastal Waters of Shenzhen China after the Passage of Typhoons. *Journal of Marine Science and Engineering*, 10(3), 327. https://doi.org/10.3390/jmse10030327
2. Fan, G. and Xu, Y., 2014. Seiche Phenomenon and the Cause Analysis in the Sea Area of Laohutan of Dalian. *Transactions of Oceanology and Limnology*, 4, pp.139-143.
3. Dolgikh, S., Dolgikh, G., Zaytsev, A. and Pelinovsky, E., 2023. The Long Wave Height Distribution at the Sea of Japan Caused by Hinnamnor Typhoon Passage: Observations and Modeling. *Physical Oceanography*, 30(6), pp. 747-759.
4. Xu, J., Li, D., Bai, Z., Tao, M. and Bian, J., 2022. Large Amounts of Water Vapor Were Injected into the Stratosphere by the Hunga Tonga–Hunga Ha'apai Volcano Eruption. *Atmosphere*, 13(6), 912. https://doi.org/10.3390/atmos13060912
5. Dolgikh, G.I., Dolgikh, S.G. and Ovcharenko, V.V., 2022. Initiation of Infrasonic Geosphere Waves Caused by Explosive Eruption of Hunga Tonga-Hunga Haʻapai Volcano. *Journal of Marine Science and Engineering*, 10(8), 1061. https:// doi.org/10.3390/jmse10081061
6. Rabinovich, A.B. and Monserrat, S., 1998. Generation of Meteorological Tsunamis (Large Amplitude Seiches) near the Balearic and Kuril Islands. *Natural Hazards*, 18(1), pp. 27-55. https://doi.org/10.1023/A:1008096627047
7. Ranguelov, B.K., 2011. *Natural Hazards-Nonlinearities and Risk Assessment*. Sofia, Bulgaria: Prof. Marin Drinov Academic Publishing House, 326 p.
8. Monserrat, S., Vilibić, I. and Rabinovich, A.B., 2006. Meteotsunamis: Atmospherically Induced Destructive Ocean Waves in the Tsunami Frequency Band. *Natural Hazards and Earth System Sciences*, 6(6), pp. 1035-1051. https://doi.org/10.5194/nhess-6-1035-2006
9. Rabinovich, A.B., 2009. Seiches and Harbor Oscillations. In: Young C. Kim, ed., 2009. *Handbook of Coastal and Ocean Engineering*. Los Angeles, USA: California State University, pp. 193-236. https://doi.org./10.1142/9789812819307_0009
10. Pattiaratchi, C.B. and Wijeratne, E.M.S., 2015. Are Meteotsunamis an Underrated Hazard? *Philosophical Transactions of the Royal Society A*, 373(2053), 20140377. https://doi.org/10.1098/rsta.2014.0377
11. Picco, P., Schiano, M.E., Incardone, S., Repetti, L., Demarte, M., Pensieri, S. and Bozzano, R., 2019. Detection and Characterization of Meteotsunamis in the Gulf of Genoa. *Journal of Marine Science and Engineering*, 7(8), 275. https://doi.org/10.3390/jmse7080275

12. Maramai, A., Brizuela, B. and Graziani, L., 2022. A Database for Tsunamis and Meteotsunamis in the Adriatic Sea. *Applied Sciences*, 12(11), 5577. https://doi.org/10.3390/app12115577

13. Anarde, K., Figlus, J., Sous, D. and Tissier, M., 2020. Transformation of Infragravity Waves during Hurricane Overwash. *Journal of Marine Science and Engineering*, 8(8), 545. https://doi.org/10.3390/jmse8080545

14. Kilibarda, Z. and Kilibarda, V., 2022. Foredune and Beach Dynamics on the Southern Shores of Lake Michigan during Recent High Water Levels. *Geosciences*, 12(4), 151. https://doi.org/10.3390/geosciences12040151

15. Heo, K.-Y., Yoon, J.-S., Bae, J.-S. and Ha, T., 2019. Numerical Modeling of Meteotsunami–Tide Interaction in the Eastern Yellow Sea. *Atmosphere*, 10(7), 369. https://doi.org/10.3390/atmos10070369

16. Kwon, K., Choi, B.-J., Myoung, S.-G. and Sim, H.-S., 2021. Propagation of a Meteotsunami from the Yellow Sea to the Korea Strait in April 2019. *Atmosphere*, 12(8), 1083. https://doi.org/10.3390/atmos12081083

17. Kakinuma, T., 2022. Tsunamis Generated and Amplified by Atmospheric Pressure Waves Due to an Eruption over Seabed Topography. *Geosciences*, 12(6), 232. https://doi.org/10.3390/geosciences12060232

18. Kovalev, P.D., Shevchenko, G.V., Kovalev, D.P. and Shishkin, A.A., 2017. Meteotsunamis on Sakhalin and the South Kuriles. *Vestnik of Far Eastern Branch of Russian Academy of Sciences*, 1, pp. 79-87 (in Russian).

19. Kim, M.-S., Woo, S.-B., Eom, H. and You S.H., 2021. Occurrence of Pressure-Forced Meteotsunami Events in the Eastern Yellow Sea during 2010-2019. *Natural Hazards and Earth System Science*, 21(11), pp. 3323-3337. https://doi.org/10.5194/nhess-21-3323-2021

20. Asano, T., Yamashiro, T. and Nishimura, N., 2012. Field Observations of Meteotsunami Locally Called "Abiki" in Urauchi Bay, Kami-Koshiki Island, Japan. *Natural Hazards*, 64(2), pp. 1685-1706. https://doi.org/10.1007/s11069-012-03330-2

21. Kubota, T., Saito, T., Chikasada, N.Y. and Sandanbata, O., 2021. Meteotsunami Observed by the Deep-Ocean Seafloor Pressure Gauge Network off Northeastern Japan. *Geophysical Research Letters*, 48(21), e2021GL094255. https://doi.org/10.1029/2021GL094255

22. Dolgikh, S.G. and Dolgikh, G.I., 2019. Meteotsunami Manifestations in Geospheres. *Izvestiya, Physics of the Solid Earth*, 55(5), pp. 801-805. https://doi.org/10.1134/S1069351319050045

23. Dolgikh, G.I., Valentin, D.I., Dolgikh, S.G., Kovalev, S.N., Koren, I.A., Ovcharenko, V.V. and Fishchenko, V.K., 2002. Application of Horizontally and Vertically Oriented Strainmeters in Geophysical Studies of Transitional Zones. *Izvestiya, Physics of the Solid Earth*, 38(8), pp. 686-689.

24. Dolgikh G.I., Dolgikh, S.G., Kovalev, S.N., Koren, I.A., Novikova, O.V., Ovcharenko, V.V., Okuntseva, O.P., Shvets, V.A., Chupin, V.A. [et al.], 2004. A Laser Nanobarograph and Its Application to the Study of Pressure-Strain Coupling. *Izvestiya, Physics of the Solid Earth*, 40(8), pp. 683-691.

25. Dolgikh, G.I., Dolgikh, S.G., Kovalev, S.N., Chupin, V.A., Shvets, V.A. and Yakovenko, S.V., 2009. Super-Low-Frequency Laser Instrument for Measuring Hydrosphere Pressure Variations. *Journal of Marine Science and Technology*, 14(4), pp. 436-442. https://doi.org/10.1007/s00773-009-0062-5

26. Fischenko, V.K., Goncharova, A.A., Dolgikh, G.I., Zimin, P.S., Subote, A.E., Klescheva, N.A. and Golik, A.V., 2021. Express Image and Video Analysis Technology QAVIS: Application in System for Video Monitoring of Peter the Great Bay (Sea of Japan/East Sea). *Journal of Marine Science and Engineering*, 9(10), 1073. https://doi.org/10.3390/jmse9101073

Submitted 21.05.2024; approved after review 05.08.2024;
accepted for publication 20.11.2024.

About the authors:

Stanislav G. Dolgikh, Head of the Laboratory of Nonlinear Hydrophysics and Natural Disasters, V.I. Il'ichev Pacific Oceanological Institute, Far Eastern Branch of RAS (43 Baltiyskaya Str., Vladivostok, 690041, Russian Federation), DSc (Tech.), **ORCID ID: 0000-0001-9828-5929, Scopus Author ID: 6604069353, WoS ResearcherID: A-7684-2014,** sdolgikh@poi.dvo.ru

Grigory I. Dolgikh, Director, V.I. Il'ichev Pacific Oceanological Institute, Far Eastern Branch of RAS (43 Baltiyskaya Str., Vladivostok, 690041, Russian Federation), DSc (Phys.-Math.), Academician of RAS, **ORCID ID: 0000-0002-2806-3834, Scopus Author ID: 7003888822, WoS ResearcherID: A-7685-2014**, dolgikh@poi.dvo.ru

Contribution of the co-authors:
Stanislav G. Dolgikh – data processing, analysis of results, writing the paper

Grigory I. Dolgikh – formulation of the problem, analysis of results, writing the paper

The authors have read and approved the final manuscript.
The authors declare that they have no conflict of interest.

Original article

Methods and Errors of Wave Measurements Using Conventional Inertial Motion Units

Yu. Yu. Yurovsky ✉, O. B. Kudinov

Marine Hydrophysical Institute of RAS, Sevastopol, Russian Federation
✉ *y.yurovsky@mhi-ras.ru*

Abstract
Purpose. The purpose of the work is to assess the impact of the characteristics of modern conventional microelectromechanical inertial motion units on the errors in measuring the energy characteristics of surface waves by wave buoys.
Methods and Results. Several methods are considered for estimating the wave energy spectrum based on inertial measurements, including accelerometer/gyroscope/magnetometer data. Four algorithms for reconstructing vertical acceleration were analyzed for further assessment of the spectrum of sea surface elevations. Based on the data obtained in a field experiment from the MHI Stationary Oceanographic Platform, differences in estimates of wave heights using one or another algorithm are shown. The performed numerical experiment qualitatively reproduces the features of inertial measurements and their respective spectra observed in field conditions.
Conclusions. It has been shown that the accelerometer noise level of typical sensors is 3–4 orders of magnitude lower than the signal from surface waves, and the accuracy characteristics of such sensors provide measurement of wave heights with an error not exceeding the specification values, which is usually no more than 3%. The noise below the spectral peak frequency can be a serious problem in wave height estimation, as it hinders the reliable isolation of the spectral peak. A sufficient condition for the occurrence of such noise is nonlinearity in the “sea surface-sensor” system. The strongest low frequency noise is observed when using an algorithm based on the Kalman filter. Thus, for minimizing wave height measurement errors, the choice of an inertial data processing algorithm seems to be more significant than the choice of a specific sensor model.

Keywords: buoy, wave gauge, inertial measurements, Kalman filter, wind waves, wave height, measurement errors, oceanographic platform, numerical experiment

Acknowledgments: The work was supported by the Russian Scientific Foundation grant 24-27-00153 “Measuring waves with small buoys: methods, validation, prospects of miniaturization”.

For citation: Yurovsky, Yu.Yu. and Kudinov, O.B., 2025. Methods and Errors of Wave Measurements Using Conventional Inertial Motion Units. *Physical Oceanography*, 32(1), pp. 63-83.

Introduction

Wave buoys represent a prevalent means for *in situ* measuring sea surface wave characteristics in both the world’s oceans [1, 2] and the Russian seas [1] [3, 4]. The operational principle of wave buoys is based on tracking the motion of a floating body assumed to perfectly follow the sea surface [5]. The measurement of motion can be achieved through various methods, all of which are generally based on two

[1] Saprykina, Y., Kuznetsov, S. and Divinskiy, B., 2020. *Real Time History of Wave Parameters in Black Sea Based on Wave Buoy Measurements. Dataset.* https://doi.org/10.6084/M9.FIGSHARE.12765407.V1

primary types of measurements: inertial measurements (typically include measurements of the geomagnetic field) [2] [5, 6] and global navigation satellite system (GNSS) measurements [7–9]. This paper focuses on the first type of measurements due to the progress in microelectromechanical systems (MEMS) over the past few decades. The development of MEMS has led to the widespread availability of inertial motion units (IMUs), which have become increasingly attractive due to their low cost, lightweight, compact size, energy efficiency, and immunity to radio interference when compared to analogous GNSS-based sensors.

In the early versions of wave buoys, the IMU measured linear acceleration along the vertical direction [10]. To stabilize the vertical axis, mechanically damped gimbals were used, thereby providing a direct estimate of the vertical accelerations of the hull. Consequently, this approach resulted in a non-directional elevation spectrum, significant wave height (SWH), and the period of dominant waves [1, 11]. When combined with magnetic sensors, such systems are capable of tracking the hull tilt with reference to the magnetic north, enabling the estimation of directional wave spectra.

With the development of MEMS technologies, the use of inertial sensors rigidly attached to the hull, often referred to as strapped-down IMUs, has become more suitable for wave measurements [12, 13]. The lack of mechanical stabilization is compensated by the simultaneous measurement of three components: acceleration (accelerometer), rotation rate (gyroscope), and geomagnetic field (magnetometer).

In theory, given the initial conditions are known, these measurements are sufficient to unambiguously determine the position and orientation of the hull, which is necessary to calculate the wave parameters. However, the presence of noise makes the estimation of the hull orientation unreliable due to the accumulation of errors over time. It should be noted that this is a standard navigation problem, the solution of which is especially important for unmanned aircraft technology, robotics, entertainment industry, etc.

The early strapped-down navigation systems used an approach based on the ability to estimate orientation using two reference vectors [14, 15], such as the gravity vector and the geomagnetic field. This deterministic approach was called the TRIAD method, since the rotation matrix determining the orientation of a body in a fixed reference frame is a combination of three vectors, two reference vectors and their cross product. The main drawback of the TRIAD method is the errors associated with the distortion of the gravity vector by inertial forces arising due to the accelerated motion of the moving reference frame.

Today, the traditional solution for wave buoys is a recursive Kalman filter [16–18], aimed at assimilating all possible types of measurements to estimate the true orientation of the sensor, its acceleration, velocity, and position in a fixed reference frame [6, 18–27].

The Kalman filtering provides a weighted estimate of the current state of a dynamic system based on the previous state history and current measurements, the process also known as "data fusion". The choice of weighting factors depends on the estimated measurement errors. This approach is useful when a series of generally "precise" measurements is interrupted by "erroneous" readings. In the case of inertial measurements, the "precise" measurements can be obtained for uniform

[2] Barber, N.F., 1946. *Measurement of Sea Conditions by the Motion of a Floating Buoy*. Admiralty Research Laboratory, Tech. Note A.R.L./103.40/N.2/w., 8 p.

rectilinear (non-accelerated) motion. The "erroneous" measurements occur during accelerated motion of the sensor, when the measured gravity vector is distorted by additional inertial forces. A typical example of such a system is a vehicle that generally moves uniformly but experiences interruptions due to accelerations/stops and course changes. When measuring waves, the gravity vector is always distorted by inertial forces, since the buoy continuously follows the orbital motion of the surface waves. Therefore, the efficiency of using standard IMU data assimilation algorithms for wave measurement seems unclear.

This paper analyzes the errors that can potentially occur in wave measurements using conventional commercially available IMUs. This issue is important because the possibility of using simple and cheap sensors in wave buoys allows to create expendable buoy fleets for specialized scientific experiments that are unrealistic with traditional buoys due to their much higher cost [28]. On the other hand, the use of small sensors allows a significant miniaturization of the buoy hulls, thus extending their bandwidth to shorter waves, which are important for several geophysical applications.

This study considers the noise characteristics of typical IMUs. Various methods for estimating buoy motion are analyzed, including a standard algorithm using the Kalman filter, as well as earlier methods based on the TRIAD method. The differences in the algorithm performance are demonstrated using the field data obtained from a wave buoy prototype. To illustrate the characteristics of the algorithms, a numerical simulation of an idealized buoy motion (the buoy that perfectly follows the waves) is performed. For the sake of brevity, we focus only on the retrieval of omnidirectional spectra and their two basic integral parameters, SWH and peak frequency, leaving the discussion of directional wave properties to other studies.

Materials and methods

General considerations. Let us consider a free-floating body perfectly following the local slope of the sea surface. The height of the wave ζ is given by a plane sinusoidal wave $\zeta(t,x) = A\sin(\Omega t + Kx)$, where A is the wave amplitude, $\Omega = 2\pi F$ is the radial frequency of the wave, F is the wave frequency, K is the wave number, x is the spatial coordinate, t is the time (Fig. 1). Usually, the most interesting wave parameter is the amplitude A, which cannot be obtained directly from the measurement of acceleration, rotation rate or magnetic field (combined accelerometer/gyroscope/magnetometer).

In the moving sensor reference frame $x'y'z'$, the deviation of the measured magnetic field vector from the x'-axis can be interpreted as the local slope of the sea surface $\xi = \partial\zeta/\partial x$. The gyroscope readings corresponding to the rate of rotation around the y'-axis represent the rate of the slope change, $\eta = \partial^2\zeta/\partial x\,\partial t$. The acceleration along the moving z'-axis is equal to the vertical acceleration in the fixed reference frame modified by the acceleration due to gravity, $g = 9.8$ m/s^2.

Therefore,

$$g' = \partial^2\zeta/\partial t^2 + g, \tag{1}$$

since the vector measured by the accelerometer is always normal to the surface. Indeed, the vector change of a stationary accelerometer reading, $g \cdot \widehat{e_z}$, is equal to the centrifugal acceleration of the sensor, $A\Omega^2(\sin\theta \cdot \widehat{e_x} + \cos\theta \cdot \widehat{e_z})$, where θ is the wave phase, and $\widehat{e_x}, \widehat{e_y}, \widehat{e_z}$ are the unit vectors of the fixed reference frame.

Obviously, the maximum tangent of the angle between the measured acceleration and the gravity vector is $A\Omega^2/g$, which is exactly equal to the magnitude of the surface slope AK, if the deep-water linear dispersion relation, $\Omega^2 = gK$, is accepted. Thus, for linear waves, the acceleration measured in the moving reference frame is always directed along the z'-axis, and its variations are equal to the vertical acceleration of the fluid particles in the wave, as noted, for example, in [29].

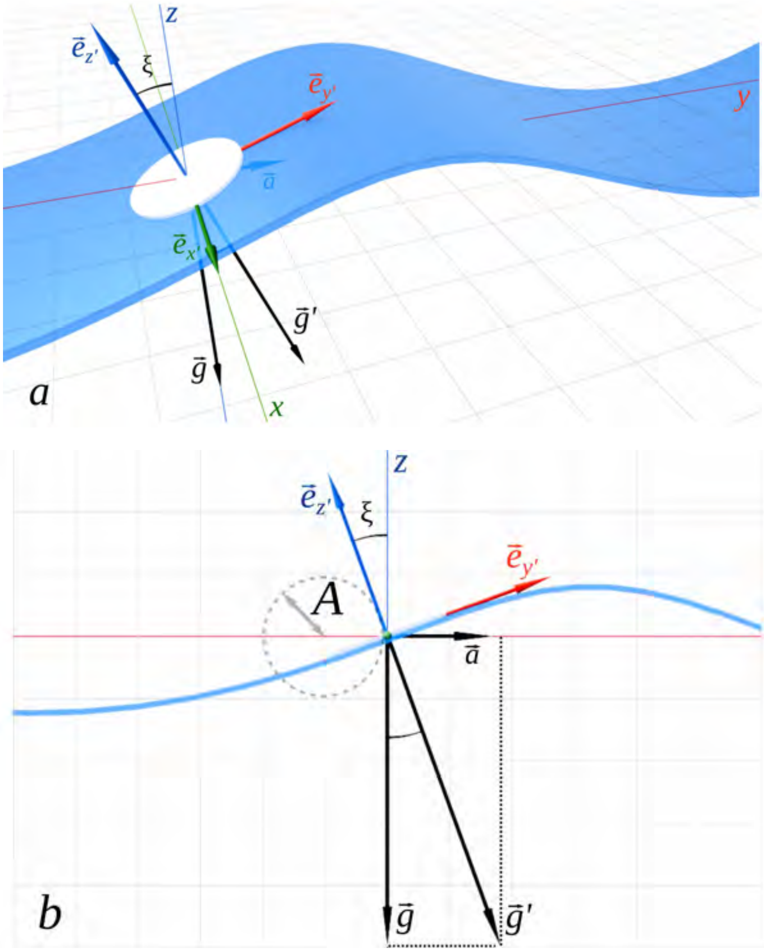

F i g. 1. Sketch explaining the accepted notation and the principle of inertial measurement of waves in the *x'y'z'* frame moving with liquid particles: general view (*a*), side view along the *x*-axis (*b*). The wave propagates in the positive direction of the *x*-axis of the right fixed reference frame

Therefore, an estimate of the wave height can be obtained by double integration of the measured accelerations, or, equivalently, in the spectral domain, by relating the spectra of the heights and accelerations. Therefore,

$$S_z(\omega) = \omega^{-4} S_a(\omega), \qquad (2)$$

where S_z is the elevation spectrum, S_a is the acceleration spectrum, $\omega = 2\pi f$ is the radial frequency representing the Fourier frequency domain (not the single harmonic Ω). Similar estimates can also be written for slope spectra (or magnetic measurements) S_ξ and rotation rate spectra (or gyroscope measurements) S_η, taking into account the linear dispersion relation:

$$S_z(\omega) = g^2\omega^{-4}S_\xi(\omega),$$

$$S_z(\omega) = g^2\omega^{-6}S_\eta(\omega). \quad (3)$$

All three estimates have a singularity, $S_z \to \infty$ for $\omega \to 0$, which distorts the integral estimates such as SWH, $H_s = 4\sqrt{\int S_z(\omega)d\omega}$. To avoid uncertainty, the low-frequency oscillations are usually suppressed by a high-pass filter. The characteristic frequency of this filter must be explicitly specified, e.g., empirically based on the typical or minimum possible frequency observed in a given water body, or can be a tuning parameter of the filter that separates signal from noise [13, 30–32].

Equipment. In this work, conventional commercial off-the-shelf IMUs were used. Table lists some parameters of the most accessible models on the market, including Russian devices. Based on the chip package size and typical parameters of the measured waves, the applicability of these modules for wave measurements can be assessed.

In particular, the magnitude of the liquid particle wave acceleration, $a = A\Omega^2 = (AK)g$, is usually smaller than the acceleration of gravity, because waves break when $(AK) > 0.44 \ldots 0.55$ [33]. Therefore, it is optimal to select the acceleration measurement range within $(1 \ldots 2)g$, both for the most efficient use of the analog-to-digital converter dynamic range and for possible wave breaking moments filtering and/or analysis.

Unlike acceleration, the rotation rate measured by a gyroscope depends not only on the steepness of the wave, but also on its frequency, $\eta = (AK)\Omega$. The maximum recorded frequency, which has a practical meaning, is determined by the geometry of the buoy hull, i.e., the frequencies of the resonant oscillations and the cut-off frequency of the hull. For example, for the Datawell [34] and Spotter [22] buoys, both 40 cm in diameter, this frequency is set to 0.6 Hz and 1 Hz, respectively. These frequencies correspond to ~ 120 and ~ 200 °/s rotation rates, falling within the first two ranges that can be selected with most sensors.

Magnetometer measurements in wave sensing applications are usually limited to recording the geomagnetic field with typical values of (25...65) μT, which is a standard task for most sensors.

Thus, the measurement ranges of the simplest (cheapest) sensors provide the means to confidently use them for wave measurements. It should also be noted that the bandwidths of the accelerometer and gyroscope are in the order of tens to hundreds of Hz (nominally for vibration measurements). This is particularly important for shortest wave measurements [29] and wind speed estimates [35]. The nonlinearity and calibration coefficient errors are typically less than 1%, a very good relative error for *in situ* wave height measurements. Many IMUs (e.g. BNO-055 and MG-10 in Table) are equipped with a built-in algorithm for processing inertial measurements. However, such algorithms are usually not documented, and the only tuning parameter available to the user is the sensor sampling frequency.

Therefore, it is preferable to implement a specialized data processing algorithm that takes into account the characteristics inherent in sea wave motion.

Characteristics of some commercial IMUs

Parameters	MPU-9250 (Invensense)[3]	BNO-055 (Bosch)[4]	ADXL345 (Analog Devices)[5]	MMA8452 (NXP Semiconductors)[6]	MA-10 (Laboratoria Micropriborov)[7]	MG-10 (Laboratoria Micropriborov)[8]
Accelerometer						
Range, *g*	±2, ±4, ±8, ±16	±2, ±4, ±8, ±16	±2, ±4, ±8, ±16	±2, ±4, ±8	±50 *	±10
Bandwidth, Hz	< 260	< 1000	< 1600	0 < 400	45	< 500
Spectral noise density, μg/Hz$^{1/2}$	300	150	290–430	99–126	300	75
Nonlinearity, %	0.5	0.5	0.5	–	0.1	0.1
Gyroscope						
Range, °/sec	±250, ±500, ±1000, ±2000	±125, ±250, ±500, ±1000, ±2000	–	–	–	±75, ±150, ±300
Bandwidth, Hz	< 250	< 523	–	–	–	<160
Spectral noise density, °/Hz$^{1/2}$	0.01	0.014	–	–	–	0.02
Nonlinearity, %	0.1	0.05	–	–	–	0.1
Magnetometer						
Range, μT	±4800	±1300, ±2500	–	–	–	±800
Bandwidth, Hz	4	10	–	–	–	–

* The range can be adjusted upon request.

[3] Invensense. *MPU-9250*. Product Specification. 2014. [online] Available at: https://invensense.tdk.com/wp-content/uploads/2015/02/PS-MPU-9250A-01-v1.1.pdf [Accessed: 30 January 2025].

[4] BOSCH. *BNO055. Intelligent 9-Axis Absolute Orientation Sensor.* Data Sheet. 2014. [online] Available at: https://cdn-shop.adafruit.com/datasheets/BST_BNO055_DS000_12.pdf [Accessed: 30 January 2025].

[5] Analog Devices. *ADXL345*. Data Sheet. 2022. [online] Available at: https://www.analog.com/media/en/technical-documentation/data-sheets/adxl345.pdf [Accessed: 30 January 2025].

[6] NXP Semiconductors. *MMA8452Q*. Data Sheet: Technical Data. 2016. [online] Available at: http://www.nxp.com/docs/en/data-sheet/MMA8452Q.pdf [Accessed: 30 January 2025].

[7] Laboratoria Mikropriborov. *MEMS-accelerometer MA-10*. Brief Information. 2022. [online] Available at: https://mp-lab.ru/wp-content/uploads/2022/10/Brif-MA-10-3.pdf [Accessed: 30 January 2025] (in Russian).

[8] Laboratoria Mikropriborov. *MG-10 Inertial Module*. Brief Information. 2022. [online] Available at: https://mp-lab.ru/wp-content/uploads/2022/08/Brif-MG-10.pdf [Accessed: 30 January 2025] (in Russian).

A critical parameter for wave measuring is the intrinsic noise of the sensors. In fact, according to (2–4), spectral estimates at low-frequencies are artificially "amplified" by multiplying the spectrum by a rather high negative frequency power (−4 or −6) – in the spectral domain – or by integrating it twice or thrice – in the time domain. Obviously, the presence of broadband inherent noise can lead to critical errors in the estimation of wave parameters, as will be discussed below.

In general, the sensors listed in Table have noise characteristics that are similar in magnitude. The MPU-9250 sensor, which combines an accelerometer/gyroscope/magnetometer, was chosen as a sample for more detailed testing. On the one hand, this is the most affordable model on the Russian market at the time of the study. On the other hand, a sensor of this model was already available to us as part of a wave buoy prototype that has been operating episodically for five years [20, 29]. This helps to evaluate the effects of MEMS aging for this model. In addition to this sample, five similar IMUs from different production series were used in the tests.

The intrinsic noise characteristics were evaluated in static mode (the sensor is stationary) at various ambient temperatures ranging from −10 to 50 ºC.

IMU data processing. The sea surface elevation spectra were calculated from the vertical accelerations according to the formula (2). Vertical accelerations in the fixed reference frame can be estimated from inertial data in different ways. Four algorithms based on different approaches are considered.

<u>Algorithm A1.</u> It is assumed that the vertical acceleration variations of the sensor in the fixed reference frame coincide with the vertical acceleration variations measured in the moving reference frame according to the formula (1). This assumption is valid for the buoy perfectly following the wave slopes, which must be small (no resonance oscillations of the buoy, waves are linear).

<u>Algorithm A2/A3.</u> The vertical accelerations of liquid particles can also be obtained by knowing the instantaneous orientation of the moving reference frame. The orientation of one reference frame relative to another can be uniquely determined if the coordinates of two non-collinear vectors in each of these systems are known. Based on this statement, the so-called TRIAD method was developed [14, 15]. If $\vec{p}$ and $\vec{q}$ are the vector pair in the xyz reference frame, while $\vec{p}'$ and $\vec{q}'$ are the corresponding vector pair in the $x'y'z'$ reference frame, then the rotation matrix between xyz and $x'y'z'$ can be written as $R = [\overrightarrow{r_1}\,\overrightarrow{r_2}\,\overrightarrow{r_3}] \cdot [\overrightarrow{s_1}\,\overrightarrow{s_2}\,\overrightarrow{s_3}]^T$, where $[\overrightarrow{r_1}\,\overrightarrow{r_2}\,\overrightarrow{r_3}]$ and $[\overrightarrow{s_1}\,\overrightarrow{s_2}\,\overrightarrow{s_3}]$ are the matrices obtained by the horizontal concatenation of the following vector triads: $\overrightarrow{r_1} = \vec{p}'$, $\overrightarrow{r_2} = \vec{p}' \times \vec{q}'$, $\overrightarrow{r_3} = \overrightarrow{r_1} \times \overrightarrow{r_2}$, and $\overrightarrow{s_1} = \vec{p}$, $\overrightarrow{s_2} = \vec{p} \times \vec{q}$, $\overrightarrow{s_3} = \overrightarrow{s_1} \times \overrightarrow{s_2}$.

For standard inertial measurements, only two vectors can be used as a reference: the acceleration of gravity, $\vec{g}$, and the geomagnetic field, $\vec{m}$. The TRIAD method provides an exact solution only in the case of uniform rectilinear motion. In the case of accelerated motion, i.e., wave orbital motion, the measured acceleration does not coincide with the gravity force in the moving reference frame. Therefore, the TRIAD method requires the sensor accelerations to be much smaller than the acceleration of gravity, $a \ll g$, or $(AK) \ll 1$, the same condition as for the A1 algorithm. However, unlike A1, the resonant buoy oscillations can be accounted for.

The TRIAD transform is invariant with respect to the permutation of $\vec{p}$ and $\vec{q}$ only if the angle between them is constant. Otherwise, if $\angle(\vec{p},\vec{q}) - \angle(\vec{p}',\vec{q}') = \varepsilon$, the estimated rotation transform R exactly matches only $\vec{p}$ and $\vec{p}'$, but not $\vec{q}$ and $\vec{q}'$, i.e., $\angle(\vec{p},\vec{p}' \cdot R) = 0$ and $\angle(\vec{q},\vec{q}' \cdot R) = \varepsilon$. Thus, for accelerated (wave) motion, the order of the reference vectors is important: $\vec{p} = \vec{g}$, $\vec{q} = \vec{m}$ or $\vec{p} = \vec{m}$, $\vec{q} = \vec{g}$. Depending on this choice, the priority vector, $\vec{p}$, will be either the acceleration vector or the magnetic field vector. In our notations, the A2 algorithm corresponds to $\vec{p} = \vec{g}$ (gravity priority), while the A3 algorithm corresponds to $\vec{p} = \vec{m}$ (magnetic field priority).

Algorithm A4 is based on the Kalman filter, which assimilates all three types of inertial data [16, 17]. We use the open-source implementation of this algorithm, which is documented in (https://github.com/memsindustrygroup/Open-Source-Sensor-Fusion). Unlike the A2/A3 algorithms, which provide the orientation directly, the Kalman filter recursively assimilates the estimation errors of the acceleration, rotation rates and magnetic field, and improves the current estimate of the orientation based on the error model. Note that such a filtering is used in the most advanced IMU-based wave buoys [18, 21, 24, 25, 36].

Field data were obtained in an experiment from the Stationary Oceanographic Platform of Marine Hydrophysical Institute using a wave buoy prototype (float diameter is 15 cm) built on the basis of the MPU-9250 sensor [29]. Simultaneously with the buoy measurements, vertical elevations of the sea surface were recorded by a six-channel resistive wave gauge at a distance of 100–150 m from the buoy [37, 38]. The accuracy of the wave gauge measurement is 1 cm in the 0.1–5 Hz frequency band (sampling frequency is 10 Hz).

Two time series of 30 min each, obtained under different wind and wave conditions, are used. The first case corresponds to a developing sea: wind speed was 13.1 m/s; SWH was 0.7 m; the spectrum measured by the wave gauge had a peak at 0.25 Hz (inverse wave age is 2.1). In the second case, a mixed sea was observed: wind speed was 5.2 m/s; SWH was 0.2 m; the spectrum had two peaks, one corresponding to the wind waves at a frequency of 0.5 Hz and the second swell peak at a frequency of 0.15–0.2 Hz.

Results and discussion

Sensor static noise. The noise characteristics for the selected IMU samples are shown in Fig. 2. The standard deviation (STD) of the accelerometer static noise signals depends almost linearly on the sensor temperature, with the *z*-component noise being 1.5–2 times higher than the *x*- and *y*-component noise. At the same time, even the maximum observed value of ~ 2 mg is approximately 4 times lower than the STD value of 8 mg declared in the sensor specification. A similar trend is observed for the spectral noise density measured at a sensor temperature of (20 ± 2) °C (Fig. 2, *b*). At frequencies above 0.1 Hz, the noise spectrum level for the *z*-component is higher, but not higher than the specification value (shown by the dotted line).

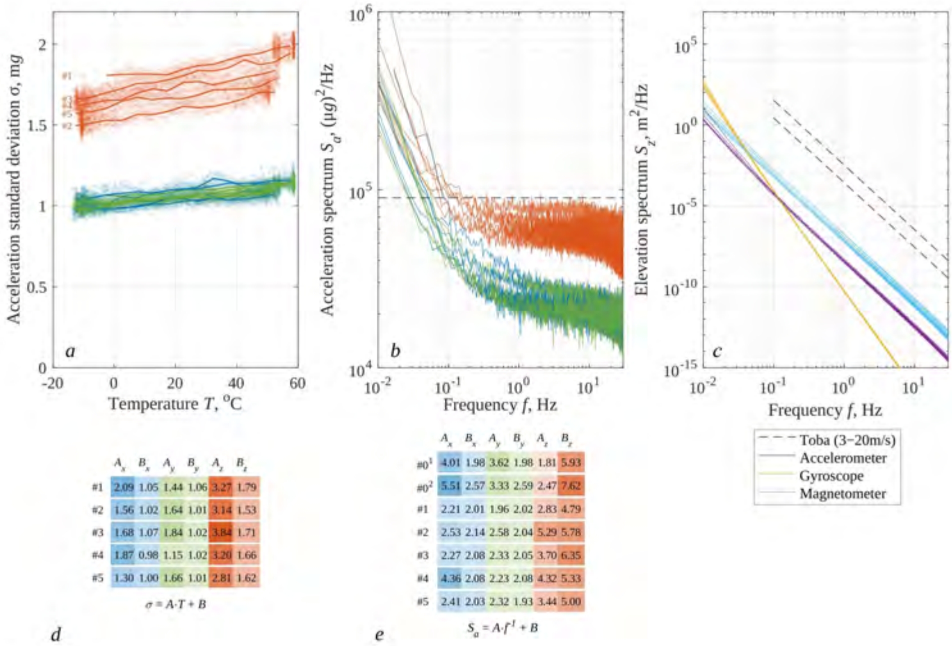

F i g. 2. Measured intrinsic noise of accelerometer channels for the MPU-9250 inertial motion unit: the acceleration standard deviation versus temperature (*a*), acceleration noise spectrum (*b*), equivalent elevation spectra estimated from accelerometer, gyroscope, and magnetometer data (*c*); heat map of fitting coefficients for the curves shown in panel *a* (*A* – in [μg/°C], *B* – in [mg]) (*d*); heat map of fitting coefficients for the curves shown in panel *b* (*A* – in [(μg)^2 · 10^{-3}], *B* – in [(μg)^2/Hz · 10^{-4}]) (*e*)

At frequencies below 0.1 Hz, the noise spectrum becomes higher than the specification level and has a 1/f slope indicating its non-thermal nature (flicker noise [39]). Sample #0, used periodically for five years (curves #0^1 and #0^2), shows an increase in spectral noise density by a factor of ~ 1.3, but this value does not exceed the specification values.

The similar behavior, a good agreement with the specification levels, is also observed for the noise of the gyroscope and magnetometer channels, which are not shown in the figures for brevity. Instead, Fig. 2, *c* shows the equivalent elevation spectra estimated from (2–4) for all three types of inertial measurements. As can be seen from the Figure, the most noise is expected in the spectra obtained from the magnetometer channel (blue lines). With the same f^{-4} slope, these spectra are ~ 1–1.5 orders of magnitude higher than the corresponding noise spectra estimated from accelerometer measurements (purple lines). The noise spectra estimated from rotation rates (yellow lines), in accordance with the formula (3), have a f^{-6} slope, resulting in a much higher spectral noise density at frequencies below 0.1 Hz. Note, however, that the expected elevation spectra for the real sea surface (the Toba spectrum [40] at 3–20 m/s wind speed shown for reference in Fig. 2, *c* by dashed lines) are 4–5 orders of magnitude higher than any equivalent noise spectra. Thus, the intrinsic noise of the sensors can be neglected when estimating the real wind wave elevation spectra.

Field measurements. To estimate the elevation spectra from *in situ* data, the A1–A4 algorithms were applied to the raw accelerometer/gyroscope/ /magnetometer records. An example of such processing for typical conditions (developing sea, wind speed is 13.1 m/s) is shown in Fig. 3, which demonstrates a fragment of the vertical acceleration record in a moving reference frame (A1) in comparison with the results of processing by the TRIAD method (A2/A3) and the Kalman filter (A4).

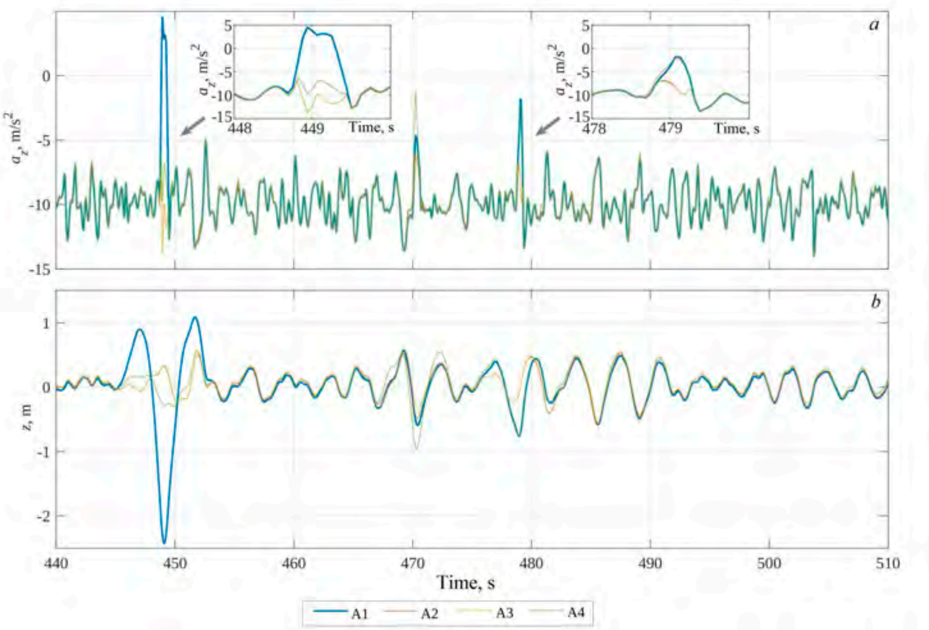

F i g. 3. Vertical acceleration time series (*a*) and vertical displacement after 5 s high-pass filtering (*b*) estimated using algorithms A1–A4. The subpanels show the wave breaking events at 449 s and 479 s in more detail

In general, the corrections introduced by the A2–A4 algorithms are not large, indicating the smallness of the slopes. The exception is the case of sharp spikes associated with wave breaking. In Fig. 3, a fragment with three such events (at 448 s, 470 s, 478 s) occurring within 30 s was deliberately selected. The TRIAD method (A2/A3) smooths such spikes, whereas the use of the Kalman filter (A4) can lead to an increase of the burst (events at 470 s, 478 s). We also note the presence of a certain relaxation time for the A4 algorithm, which is required to readjust the Kalman filter after a sharp jump in all measured parameters (interval 450–470 s).

The sea surface elevations obtained by integrating the accelerations are shown in Fig. 3, *b*. The low-frequency components of the accelerations introduce unacceptable errors into this signal, so for this Figure the original series are high-pass filtered with a time constant equal to the period of the peak waves, 5 s. During the event at 449 s, the height difference according to algorithm A1 is unrealistically large, more than 3 m, while the SWH is about 0.7 m. The reason is obviously the penetration of horizontal accelerations into the vertical acceleration signal due to the fact that the hull orientation is not taken into account by the A1 algorithm.

The corrections introduced by the A2–A4 algorithms allow the smoothing of such spikes, as can be seen in Fig. 3, *b*

Figure 4 *a*, *c* shows the elevation spectra calculated from 30-min records under developing and mixed sea conditions, with the initial time series divided into successive 1-min intervals and further averaging over them. These estimates are based on vertical accelerations obtained using the A1–A4 algorithms (colored lines). The elevation spectra measured by the wave gauge (black lines) are given as a reference. In the operating frequency range (0.2–1 Hz), all spectral estimates agree within the confidence intervals, as well as with the empirical level of the Toba spectrum [40], regardless of the choice of the processing algorithm. At frequencies above 1 Hz, the possible deviations are related to the transfer function of the buoy hull and to Doppler distortions of the reference wave gauge spectra [41].

The main differences between the algorithms are observed at frequencies below the peak frequency f_p. For the case of the developing sea (Fig. 4, *a*), the contrast of the spectral peak to the low frequency noise background is ~ 7 for the moving frame vertical accelerations (A1), ~ 16 for the TRIAD method (A2/A3), and ~ 1.5 for the Kalman filter (A4). Hereinafter, the "low-frequency" corresponds to the oscillations with frequencies below the peak frequency, $0 < f < f_p$. In the case of the mixed sea (Fig. 4, *c*), a similar tendency remains, but the contrast is several times smaller, about 2–4.

The low frequency noise is critically important when estimating the SWH. The elevation spectrum decreases rather rapidly with frequency (f^{-4}), so that the main contribution to the SWH comes from the longest waves, which, as follows from the results presented, are measured quite well up to the spectral peak. However, the presence of low frequency noise below the peak requires the correct choice of the lower integration limit when estimating the SWH. This statement is illustrated in Figure 4 *b*, *d*, which shows the cumulative values of SWH depending on the lower integration limit (plotted along the horizontal frequency axis):

$$H_s(f) = 4\sqrt{\int S\,(f')df'}.$$

For instance, if the lower limit is 0, then the SWH (left axis in Fig. 4 *b*, *d*) and its relative error $1 - H_s\left(f_p\right)/H_s$ (right axis in the same plot) tend to infinity (the colored lines bend upwards at $f \to 0$), see (2).

If the lower limit is equal to the frequency of the first inflection of the spectrum to the left of the spectral peak (shown by vertical dashed dotted lines), the relative measurement error will not exceed 2% for A2/A3 algorithms and 10% for A1, A4 algorithms. However, this method of searching for the lower integration boundary has its limitations, since a swell signal can also be observed below f_p. For example, if the wind peak in the situation shown in Fig. 4, *c* was higher than the swell peak.

An alternative signal/noise boundary can be a frequency identified by the first (from the $f = 0$ side) minimum in the spectrum. These points for all four algorithms are shown as encircled crosses in Fig. 4. In the case of such an automated search, the relative SWH error also lies within 10%. However, this method is not always efficient, since the first local minimum can be at a significantly lower frequency due to the random nature of the wave signal, while the errors become unacceptable at $f \to 0$ due to the f^{-4}-slope of the spectrum.

The issue of filtering low-frequency noise is traditional for buoy data processing. For example, it has been proposed to use a priori information about the shape of the spectrum [30, 42], the ratio of the amplitudes of vertical and horizontal motions [10], and various empirical corrections [11, 13]. However, the origin of the low-frequency noise does not seem to be related to the internal characteristics of the sensor, because, firstly, the measured intrinsic noise is 3–4 orders weaker, as follows from the comparison of Fig. 4 and Fig. 2, and, secondly, it depends significantly on the signal processing method (Fig. 4). Therefore, the origin of this noise requires additional discussion.

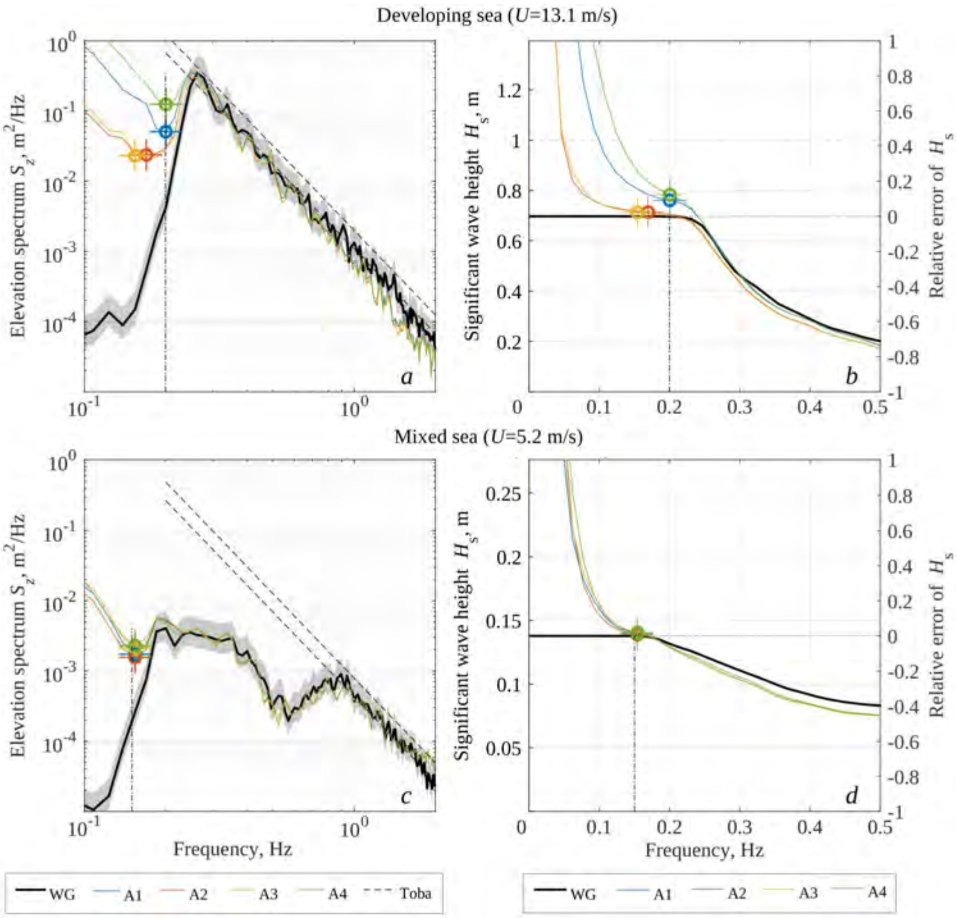

F i g. 4. Sea surface elevation spectra (*a*, *c*) and significant wave height relative error (*b*, *d*) measured in the field experiment. The colored lines show the results of the processing by the A1–A4 algorithms, the thick black line shows the reference measurements by wire wave gauge. Symbols (+) indicate the first local minimum in the spectrum. The vertical dash-dotted line shows the frequency corresponding to the inflection point in the spectrum

Numerical simulation. The following numerical simulation was performed to illustrate the features of the data processing algorithms. The initial unperturbed sea surface, defined as a flat uniform grid, is deformed by a superposition of N Gerstner waves,

$$X_m = \sum \mathrm{Real}\{A_{mn}\}\sin\theta_n,$$
$$Y_m = \sum \mathrm{Real}\{A_{mn}\}\cos\theta_n,$$
$$Z_m = \sum \mathrm{Imag}\{A_{mn}\},$$
$$A_{mn} = \sqrt{2 \cdot S(f_n) \cdot \Delta f / N} \cdot \exp\{i(K_{xn} \cdot x_m + K_{yn} \cdot y_m - 2\pi f_n t + \phi_n)\},$$

where $S(f_n)$ is the Toba spectrum, $\Delta f = f_N - f_1$ is the frequency band in which the simulation is performed, the frequency limits are $f_1 = 0.2$ Hz, $f_N = 4$ Hz, ϕ_n is the random phase uniformly distributed within $[0,2\pi]$, θ_n is the random wave direction normally distributed around zero mean (waves travel along the y-axis). The complex amplitude, A_{mn}, reproduces the target spectrum $S(f_n)$ for which the Toba spectrum is adopted again. The angular width is set to 45° in accordance with typical values of this parameter for the real sea surface [43]. The grid size is $\delta x = \delta y = 0.01$ m, the time step is $\delta t = 0.1$ s, the simulation domain is $\Delta x = \Delta y = 2$ m, the simulation duration is $\Delta t = 1800$ s, the number of harmonics is $N = \Delta f \cdot \Delta t$. The magnetic field is directed along the x- or y-axis, depending on the simulation run.

Despite some issues regarding the feasibility of Gerstner waves on the real sea surface [44], this approach has become widespread due to the possibility of taking into account the nonlinearity of waves [45–47]. In the present study, it is particularly convenient because it allows to simulate the motion of liquid particles, and thus the motion of a free-floating body "attached" to them, without numerically solving the hydrodynamic equations. In particular, it is assumed that a flat round buoy (15 cm in diameter, as in the field experiment) equipped with an IMU "lies" on the simulated surface without experiencing its own resonant oscillations (the buoy thickness is zero). The position of such a virtual buoy is determined at each moment by fitting the liquid particles under the buoy with a plane. Based on the known positions of the buoy center and its orientations, the inertial sensor measurements are simulated, i.e., accelerations, rotation rates, and magnetic field components in a moving reference frame.

With this simulation data set, it is possible to check how adequately the inverse problem of estimating wave parameters from inertial measurements is solved by one or another algorithm. Figure 5 shows an example of a simulation for a five-second interval, corresponding to one period of peak waves. The buoy orientation is shown by colored arrows in different scales: the long arrows are the true (estimated) orientation, the medium-length arrows show the TRIAD method estimate, the short arrows are the Kalman filter estimates (A4). Note that the A1 algorithm does not include an orientation estimate.

As can be seen from this example, all the considered methods provide generally reliable orientation in the direction of the x-axis (red unit vectors). This is explained by the small variability of the slope in this direction, since the waves in this simulation propagate along the y-axis. Accordingly, the main differences from the true values are observed in the yz-plane (blue and green unit vectors). The errors of the Kalman filter algorithm (A4) are generally smaller than those of the TRIAD method. But for the latter, the choice of the priority vector is crucial. If the magnetic field is chosen (in this example it is aligned with the direction of the waves), then the orientation retrieval is perfect. If the gravity vector is chosen, then the errors are larger than for the Kalman filter.

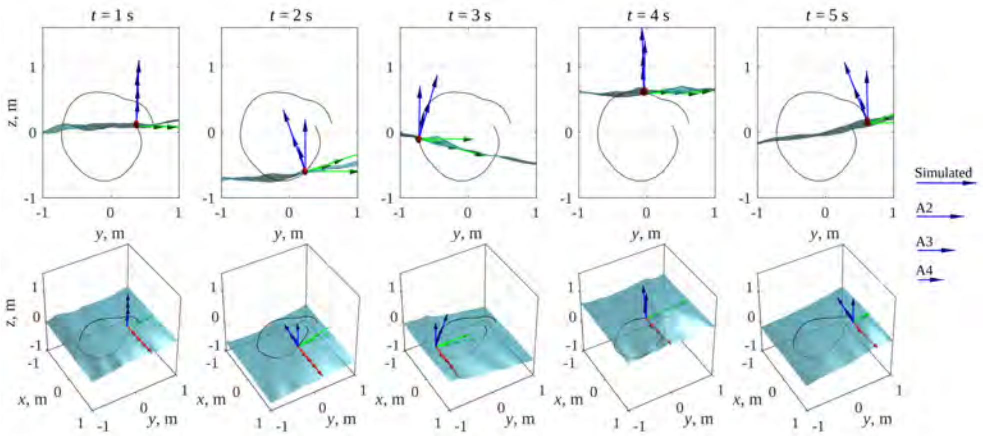

F i g. 5. An example showing a numerical simulation of the sea surface during a peak wave period for five equally spaced instants: side view – *on the top*, general view – *on the bottom*. The colored arrows show the orientations of the virtual buoy estimated by algorithms A2–A4, the black line is the trajectory of the buoy

These features are illustrated in more detail in Fig. 6, where the instantaneous orientations are shown as Euler angle time series, roll/pitch/azimuth, where roll is the slope angle along the y-axis, pitch is the slope angle along the x-axis, and azimuth angle is the rotation around the z-axis. In particular, pitch and azimuth are reproduced equally poorly by the TRIAD method (the curves A2 and A3 completely coincide), while true roll (blue thick line) is reproduced perfectly by the A3 algorithm (the red curve completely coincides with the blue thick line), contrary to the A2 algorithm. Thus, the main disadvantage of the TRIAD method is its sensitivity to the direction of the waves relative to the magnetic field vector, as well as to the choice of the priority vector (gravity or acceleration).

As with the Kalman filter, the roll and pitch are reproduced with approximately the same accuracy, but with a small delay relative to the true signal. Of critical importance to this study is the "stray" noise, which is clearly visible in the azimuth signal in Fig. 6. The true value of the azimuth angle is virtually constant, while the A4 curve randomly deviates from the mean value within ±10º, and, most importantly, with a period exceeding the period of the wave peak. Note also that the same low frequency oscillations are present, although less distinguishable, in the roll and pitch angles. For example, the A4 curve (green) is slightly higher than the true curve (blue) before ~ 13 s of the simulation, but later it becomes lower. At first glance, such a small error < 5º may seem insignificant. However, it can be a strong artifact in the elevation spectra, as shown below in the same way as for the field data analysis.

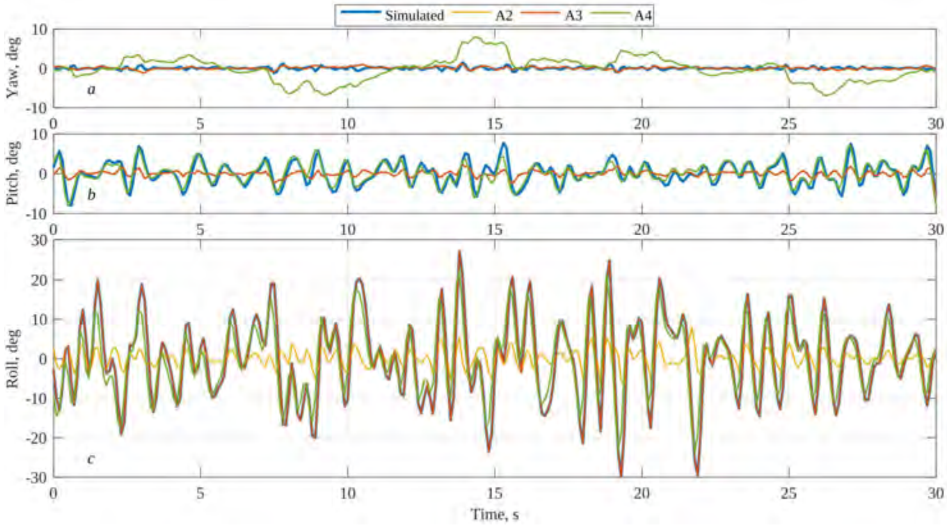

F i g. 6. Euler angles (roll/pitch/yaw) estimated using algorithms A2–A4 based on model calculations

Three different wave situations with peak frequencies $f_p = 0.3, 0.2, 0.1$ Hz are considered in Fig. 7 (left, middle and right columns, respectively). The wind speed, which determines the spectral level in the target Toba spectrum, is chosen to be equal to $U = 5.2, 7.8, 15.6$ m/s, respectively, based on the condition for the wave age $c_p/U = 1$, where U is the wind speed, $c_p = g/2\pi f_p$ is the phase velocity of the spectral peak waves. For these three situations, two cases are analyzed, the waves are co-aligned with the magnetic field (top row in Fig. 7) and perpendicular to the magnetic field (bottom row).

Comparing the simulation results with the field measurements (Fig. 7 and Fig. 4), one can note their close similarity. Despite the rather primitive simulation scheme (no resonant hull oscillations, perfect wave following, representation of the surface by a set of Gerstner waves), the numerical simulations exhibit the same characteristics as for the real sea. Particularly, an almost complete agreement of the estimates with the true value in the operating frequency range $f_p < f < 1$ Hz; a “fall-off” of the spectral density in the higher frequency range in accordance with the transfer function of the hull; the presence of low frequency noise. Regarding the latter, the level of low frequency noise may differ by a factor of 3–4, depending on the choice of data processing algorithm.

The strongest low frequency noise is introduced by the Kalman filter (A4). For example, at the wind speeds above 15 m/s, the spectral peak becomes barely distinguishable (Fig. 7, *f*) or indistinguishable (Fig. 7, *c*) depending on the direction of the waves relative to the magnetic field. The dependence on the wave azimuth is much greater for algorithms based on the TRIAD method (A2/A3). The worst performance is obtained with the A3 algorithm (magnetic field priority) when the orientation of the waves and the magnetic field are perpendicular to each other. The A2 algorithm (gravity priority) produces a level of low frequency noise comparable to the A1 algorithm, which assumes that the buoy perfectly follows the wave slopes (the default option in these simulations).

Thus, the conducted numerical simulation clearly demonstrates that the level of the intrinsic noise of modern inertial sensors (e.g., the noise of the MPU-9250 sensor is shown by the blue lines in Fig. 7) is negligibly small, compared to both the wave signal and the low frequency noise. The latter, based on the problem formulation, can only be generated by the nonlinearity in the response of the measuring device to wave surface. Particularly, the average slope and elevation of the buoy in this simulation is based on always changing ensembles of liquid particles.

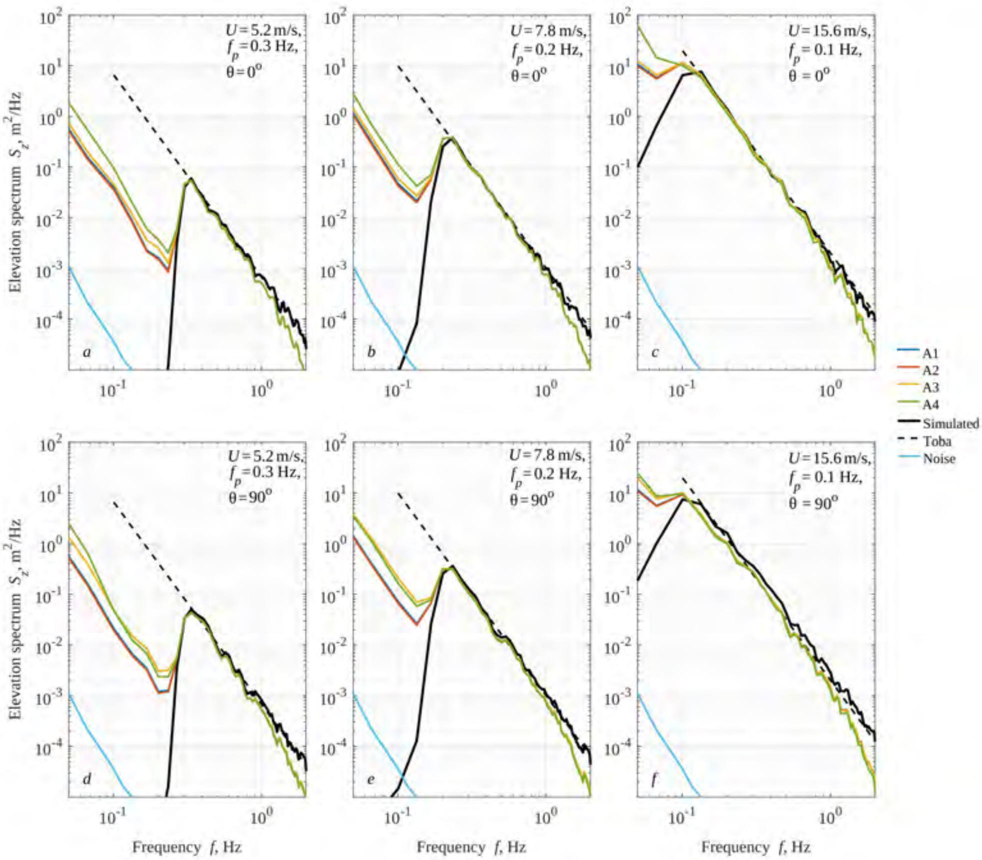

F i g. 7. Elevation spectra estimated from virtual buoy measurements (colored lines) compared to the true spectrum (thick black line). The direction of the waves in the numerical experiment is along the magnetic field – *on the top*, across the magnetic field – *on the bottom.* The peak wave frequency is 0.3 Hz (*on the left*), 0.2 Hz (*in the middle*), 0.1 Hz (*on the right*) with a constant wave age equal to 1

Similar non-linear effects are manifested as low frequency noise in various dynamic systems, such as infra-gravity waves [48], acoustic noise of the sea [49], etc. In the considered sea surface-buoy system, the nonlinearity is inherent both in the surface itself and in the estimation of the surface slope. In the case of the Kalman filter, the recursive transform is ambiguous, i.e., the estimate in the current step depends on the result of the calculation in the previous step.

It should also be noted that in the real conditions there are usually many more sources of noise. These include the hull resonance oscillations, which are generally non-linear because the dependence of the buoyancy force and the restoring moment on the current draft and tilt of the buoy is determined by the shape of the hull and the mass distribution within it. The holding line response (if present) can also be important [11], as can biofouling [50] and the interaction of the buoy hull with wind [51] and currents [52]. Obviously, all these factors may impact the measurement errors. At the same time, the technical characteristics of modern inertial sensors play a minor role, as can be seen from the present results.

Conclusion

This paper presents the results of laboratory, field, and numerical experiments to assess the applicability of the modern conventional MEMS inertial motion units (IMUs) in wave buoys. The main conclusions are as follows:

– various methods of estimating wave heights based on measurements from standard IMUs (accelerometer/gyroscope/magnetometer) are considered. The most suitable method is based on the analysis of the vertical accelerations of the sensor in a fixed reference frame. Four algorithms are considered for estimating vertical accelerations, based on (a) the assumption of perfect wave following, (b) the so-called TRIAD method, which is an exact solution only for uniform motion, and (c) the recursive Kalman filter, which is the most popular solution in navigation problems;

– laboratory tests have shown that the static accelerometer noise of a typical IMU is 3-4 orders of magnitude lower than the surface wave signal, and the accuracy characteristics of such sensors ensure that wave heights are measured with an error not exceeding the specification values, which is typically no more than 3%. The error in estimated wave height from the field wave buoy measurements is within 2% in the spectral peak band ranging from 0.2 to 0.25 Hz;

– the noise at frequencies below the spectral peak can be a serious problem for wave height estimation as it prevents the wave signal from being confidently distinguished. For example, the error in estimating the significant wave height increases to 10% when the spectrum is integrated from the signal/noise separating frequency estimated from the first local minimum condition. The error can become unacceptable when a low frequency spectral peak is mistakenly detected due to the “gain factor” f^{-4} that relates the acceleration and elevation spectra;

– in order to determine the origin of the low frequency noise, a numerical experiment was performed to simulate the signals of an idealized IMU-based buoy and to retrieve the wave parameters from them. A sufficient condition for the occurrence of such noise is the nonlinearity of the sea surface, which is present in the simulated superposition of Gerstner waves. Even without taking into account the resonant oscillations of the hull (a zero-thickness buoy), the results of the numerical experiment reproduce almost all the details of the field measurements, including the low frequency noise;

– the highest level of low frequency noise, both in the field and in the numerical experiments, is observed when the Kalman filter is used to determine the buoy current orientation. Thus, the minimization of the wave height measurement error is more sensitive to the choice of the data processing algorithm than to the choice of a specific sensor model.

REFERENCES

1. Earle, M.D. and Bishop, J.M., 1984. A *Practical Guide to Ocean Wave Measurement and Analysis*. Marion, MA, USA: Endeco Inc., 78 p.
2. McCall, J.C., 1998. Advances in National Data Buoy Center Technology. In: IEEE Oceanic Engineering Society, 1998. *OCEANS'98. Conference Proceedings (Cat. No. 98CH36259)*. Nice, France: IEEE. Vol. 1, pp. 544-548. https://doi.org/10.1109/OCEANS.1998.72806
3. Lobanov, V.B., Lazaryuk, A.Yu., Ponomarev, V.I., Sergeev, A.F., Marina, E.N., Starjinskii, S.S., Kharlamov, P.O., Shkorba, S.P. [et al.], 2020. The Results of Hydrometeorological Measurements by the WAVESCAN Buoy System on the Southwestern Shelf of the Peter the Great Bay in 2016. *Journal of Oceanological Research*, 48(4), pp. 5-31. https://doi.org/10.29006/1564-2291.JOR-2020.48(4).1
4. Divinsky, B.V. and Kuklev, S.B., 2022. Experiment of Wind Wave Parameter Research in the Black Sea Shelf. *Oceanology*, 62(1), pp. 8-12. https://doi.org/10.1134/S0001437022010040
5. Longuet-Higgins, M.S., Cartwright, D.E. and Smith, N.D., 1963. Observations of the Directional Spectrum of Sea Waves Using the Motions of a Floating Buoy. In: National Academy of Sciences, 1963. *Ocean Wave Spectra: Proceedings of a Conference*. Prentice-Hall, Englewood Cliffs, N.J., pp. 111-132.
6. Gryazin, D. and Gleb, K., 2022. A New Method to Determine Directional Spectrum of Sea Waves and Its Application to Wave Buoys. *Journal of Ocean Engineering and Marine Energy*, 8(3), pp. 269-283. https://doi.org/10.1007/s40722-022-00228-z
7. Herbers, T.H.C., Jessen, P.F., Janssen, T.T., Colbert, D.B. and MacMahan, J.H., 2012. Observing Ocean Surface Waves with GPS-Tracked Buoys. *Journal of Atmospheric and Oceanic Technology*, 29(7), pp. 944-959. https://doi.org/10.1175/JTECH-D-11-00128.1
8. Shimura, T., Mori, N., Baba, Y. and Miyashita, T., 2022. Ocean Surface Wind Estimation from Waves Based on Small GPS Buoy Observations in a Bay and the Open Ocean. *Journal of Geophysical Research: Oceans*, 127(9), e2022JC018786. https://doi.org/10.1029/2022JC018786
9. Collins, C.O., Dickhudt, P., Thompson, J., de Paolo, T., Otero, M., Merrifield, S., Terrill, E., Schonau, M., Braasch, L. [et al.], 2024. Performance of Moored GPS Wave Buoys. *Coastal Engineering Journal*, 66(1), pp. 17-43. https://doi.org/10.1080/21664250.2023.2295105
10. Stewart, R.H., 1977. A Discus-Hulled Wave Measuring Buoy. *Ocean Engineering*, 4(2), pp. 101-107.
11. Earle, M.D., 1996. *Nondirectional and Directional Wave Data Analysis Procedures.* NDBC Technical Document 96-01. Slidell, USA: Stennis Space Center, 43 p.
12. Earle, M. and Bush, K., 1982. Strapped-Down Accelerometer Effects on NDBO Wave Measurements. In: Marine Technology Society, IEEE, 1982. *OCEANS 82 Conference Record*. Washington, DC, USA, pp. 838-848. https://doi.org/10.1109/OCEANS.1982.1151908
13. Earle, M., Steele, K. and Hsu, Y.-H., 1984. Wave Spectra Corrections for Measurements of Hull-Fixed Accelerometers. In: Marine Technology Society, IEEE, 1984. *OCEANS 84 Conference Record*. Washington, DC, USA, pp. 725-730. https://doi.org/10.1109/OCEANS.1984.1152234
14. Black, H.D., 1964. A Passive System for Determining the Attitude of a Satellite. *AIAA Journal*, 2(7), pp. 1350-1351. https://doi.org/10.2514/3.2555
15. Shuster, M.D. and Oh, S.D., 1981. Three-Axis Attitude Determination from Vector Observations. *Journal of Guidance and Control*, 4(1), pp. 70-77. https://doi.org/10.2514/3.19717
16. Sabatini, A.M., 2011. Kalman-Filter-Based Orientation Determination Using Inertial/Magnetic Sensors: Observability Analysis and Performance Evaluation. *Sensors*, 11(10), pp. 9182-9206. https://doi.org/10.3390/s111009182

17. Wang, L., Zhang, Z. and Sun, P., 2015. Quaternion-Based Kalman Filter for AHRS Using an Adaptive-Step Gradient Descent Algorithm. *International Journal of Advanced Robotic Systems*, 12(9), 131. https://doi.org/10.5772/61313

18. Rabault, J., Nose, T., Hope, G., Muller, M., Breivik, O., Voermans, J., Hole, L.R., Bohlinger, P., Waseda, T. [et al.], 2022. OpenMetBuoy-v2021: An Easy-to-Build, Affordable, Customizable, Open Source Instrument for Oceanographic Measurements of Drift and Waves in Sea Ice and the Open Ocean. *Geosciences*, 12(3), 110. https://doi.org/10.13140/RG.2.2.15826.07368

19. MacIsaac, C. and Naeth, S., 2013. TRIAXYS Next Wave II Directional Wave Sensor the Evolution of Wave Measurements. In: IEEE, 2013. *OCEANS 2013*. San Diego, California, USA, pp. 2002-2010.

20. Yurovsky, Y.Y. and Dulov, V.A., 2017. Compact Low-Cost Arduino-Based Buoy for Sea Surface Wave Measurements. In: IEEE, 2017. *2017 Progress in Electromagnetics Research Symposium – Fall (PIERS – FALL)*. Singapore, pp. 2315-2322. https://doi.org/10.1109/PIERS-FALL.2017.8293523

21. Veras Guimarães, P., Ardhuin, F., Sutherland, P., Accensi, M., Hamon, M., Pérignon, Y., Thompson, J., Benetazzo, A. and Ferrant, P., 2018. A Surface Kinematics Buoy (SKIB) for Wave–Current Interaction Studies. *Ocean Science*, 14(6), pp. 1449-1460. https://doi.org/10.5194/os-14-1449-2018

22. Raghukumar, K., Chang, G., Spada, F., Jones, C., Janssen, T. and Gans, A., 2019. Performance Characteristics of "Spotter," a Newly Developed Real-Time Wave Measurement Buoy. *Journal of Atmospheric and Oceanic Technology*, 36(6), pp. 1127-1141. https://doi.org/10.1175/JTECH-D-18-0151.1

23. Houghton, I.A., Smit, P.B., Clark, D., Dunning, C., Fisher, A., Nidzieko, N.J., Chamberlain, P. and Janssen, T.T., 2021. Performance Statistics of a Real-Time Pacific Ocean Weather Sensor Network. *Journal of Atmospheric and Oceanic Technology*, 38(5), pp. 1047-1058. https://doi.org/10.1175/JTECH-D-20-0187.1

24. Rainville, E., Thompson, J., Moulton, M. and Derakhti, M., 2023. Measurements of Nearshore Ocean-Surface Kinematics through Coherent Arrays of Free-Drifting Buoys. *Earth System Science Data*, 15(11), pp. 5135-5151. https://doi.org/10.5194/essd-15-5135-2023

25. Zhong, Y.-Z., Chien, H., Chang, H.-M. and Cheng, H.-Y., 2022. Ocean Wind Observation Based on the Mean Square Slope Using a Self-Developed Miniature Wave Buoy. *Sensors*, 22(19), 7210. https://doi.org/10.3390/s22197210

26. Alari, V., Björkqvist, J.-V., Kaldvee, V., Mölder, K., Rikka, S., Kask-Korb, A., Vahter, K., Pärt, S., Vidjajev, N. [et al.], 2022. LainePoiss® – A Lightweight and Ice-Resistant Wave Buoy. *Journal of Atmospheric and Oceanic Technology*, 39(5), pp. 573-594. https://doi.org/10.1175/JTECH-D-21-0091.1

27. Mironov, A.S. and Charron, L., 2023. Miniaturized Drifting Buoy Platform for the Creation of Undersatellite Calibration and Validation Network. In: IEEE, 2023. *OCEANS 2023 – Limerick*. Limerick, Ireland: IEEE, pp. 1-10.

28. Thomson, J., Bush, P., Contreras, V.C., Clemett, N., Davis, J., de Klerk, A., Iseley, E. and Rainville, E.J., 2024. Development and Testing of MicroSWIFT Expendable Wave Buoys. *Coastal Engineering Journal*, 66(1), pp. 168-180. https://doi.org/10.1080/21664250.2023.2283325

29. Yurovsky, Y.Yu. and Dulov, V.A., 2020. MEMS-Based Wave Buoy: Towards Short Wind-Wave Sensing. *Ocean Engineering*, 217, 108043. https://doi.org/10.1016/j.oceaneng.2020.108043

30. Ashton, I.G.C. and Johanning, L., 2015. On Errors in Low Frequency Wave Measurements from Wave Buoys. *Ocean Engineering*, 95, pp. 11-22. https://doi.org/10.1016/j.oceaneng.2014.11.033

31. Ding, Y., Taylor, P.H., Zhao, W., Dory, J.-N., Hlophe, T. and Draper, S., 2023. Oceanographic Wave Buoy Motion as a 3D-Vector Field: Spectra, Linear Components and Bound Harmonics. *Applied Ocean Research*, 141, 103777. https://doi.org/10.1016/j.apor.2023.103777

32. Amarouche, K., Akpinar, A., Rybalko, A. and Myslenkov, S., 2023. Assessment of SWAN and WAVEWATCH-III Models Regarding the Directional Wave Spectra Estimates Based on Eastern Black Sea Measurements. *Ocean Engineering*, 272, 113944. https://doi.org/10.1016/j.oceaneng.2023.113944

33. Toffoli, A., Babanin, A., Onorato, M. and Waseda, T., 2010. Maximum Steepness of Oceanic Waves: Field and Laboratory Experiments. *Geophysical Research Letters*, 37(5), L05603. https://doi.org/10.1029/2009GL041771

34. Jeans, G., Bellamy, I., de Vries, J.J. and van Weert, P., 2003. Sea Trial of the New Datawell GPS Directional Waverider. In: J. A. Rizoli, ed., 2003. *Proceedings of the IEEE-OES Seventh Working Conference on Current Measurement Technology*. San Diego, CA, USA, pp. 145-147. https://doi.org/10.1109/CCM.2003.1194302

35. Rybalko, A., Myslenkov, S. and Badulin, S., 2023. Wave Buoy Measurements at Short Fetches in the Black Sea Nearshore: Mixed Sea and Energy Fluxes. *Water*, 15(10), 1834. https://doi.org/10.3390/w15101834

36. Kodaira, T., Katsuno, T., Nose, T., Itoh, M., Rabault, J., Hoppmann, M., Kimizuka, M. and Waseda, T., 2023. An Affordable and Customizable Wave Buoy for the Study of Wave-Ice Interactions: Design Concept and Results from Field Deployments. *Coastal Engineering Journal*, 66(1), pp. 74-88. https://doi.org/10.1080/21664250.2023.2249243

37. Bondur, V.G., Dulov, V.A., Murynin, A.B. and Yurovsky, Yu.Yu., 2016. A Study of Sea-Wave Spectra in a Wide Wavelength Range from Satellite and In-Situ Data. *Izvestiya, Atmospheric and Oceanic Physics*, 52(9), pp. 888-903. https://doi.org/10.1134/S0001433816090097

38. Smolov, V.E. and Rozvadovskiy, A.F., 2020. Application of the Arduino Platform for Recording Wind Waves. *Physical Oceanography*, 27(4), pp. 430-441. https://doi.org/10.22449/1573-160X-2020-4-430-441

39. Mohd-Yasin, F., Korman, C.E. and Nagel, D.J., 2003. Measurement of Noise Characteristics of MEMS Accelerometers. *Solid-State Electronics*, 47(2), pp. 357-360. https://doi.org/10.1016/S0038-1101(02)00220-4

40. Toba, Y., 1972. Local Balance in the Air-Sea Boundary Processes. *Journal of the Oceanographical Society of Japan*, 28, pp. 109-120. https://doi.org/10.1007/BF02109772

41. Korotkevich, A.O., 2008. On the Doppler Distortion of the Sea-Wave Spectra. *Physica D: Nonlinear Phenomena*, 237(21), pp. 2767-2776. https://doi.org/10.1016/j.physd.2008.04.005

42. Björkqvist, J.-V., Pettersson, H., Laakso, L., Kahma, K.K., Jokinen, H. and Kosloff, P., 2015. Removing Low-Frequency Artefacts from Datawell DWR-G4 Wave Buoy Measurements. *Geoscientific Instrumentation Methods and Data Systems*, 5(1), pp. 17-25. https://doi.org/10.5194/gid-5-363-2015

43. Donelan, M.A., Hamilton, J., Hui, W.H. and Stewart, R.W., 1985. Directional Spectra of Wind-Generated Ocean Waves. *Philosophical Transactions of the Royal Society of London. Series A, Mathematical and Physical Sciences*, 315(1534), pp. 509-562. https://doi.org/10.1098/rsta.1985.0054

44. Abrashkin, A.A. and Pelinovsky, E.N., 2022. Gerstner Waves and Their Generalizations in Hydrodynamics and Geophysics. *Physics–Uspekhi*, 65(5), pp. 453-467. https://doi.org/10.3367/UFNe.2021.05.038980

45. Creamer, D.B., Henyey, F., Schult, R. and Wright, J., 1989. Improved Linear Representation of Ocean Surface Waves. *Journal of Fluid Mechanics*, 205(1), pp. 135-161. https://doi.org/10.1017/s0022112089001977

46. Deusen, O., Ebert, D.S., Fedkiw, R., Musgrave, F.K., Prusinkiewicz, P., Roble, D., Stam, J. and Tessendorf, J., 2004. The Elements of Nature: Interactive and Realistic Techniques. In: Association for Computing Machinery, 2004. *ACM SIGGRAPH 2004 Course Notes*. Los Angeles, CA, USA: ACM, 32 p. https://doi.org/10.1145/1103900.1103932

47. Nouguier, F., Guérin, C.-A. and Chapron, B., 2009. "Choppy Wave" Model for Nonlinear Gravity Waves. *Journal of Geophysical Research: Oceans*, 114(C9), 2008JC004984. https://doi.org/10.1029/2008JC004984

48. Dolgikh, G. and Dolgikh, S., 2023. Nonlinear Interaction of Infragravity and Wind Sea Waves. *Journal of Marine Science and Engineering*, 11(7), 1442. https://doi.org/10.3390/jmse11071442

49. Ardhuin, F., Stutzmann, E., Schimmel, M. and Mangeney, A., 2011. Ocean Wave Sources of Seismic Noise. *Journal of Geophysical Research: Oceans*, 116(C9), C006952. https://doi.org/10.1029/2011JC006952

50. Thomson, J., Talbert, J., de Klerk, A., Brown, A., Schwendeman, M., Goldsmith, J., Thomas, J., Olfe, C., Cameron, G. [et al.], 2015. Biofouling Effects on the Response of a Wave Measurement

Buoy in Deep Water. *Journal of Atmospheric and Oceanic Technology*, 32(6), pp. 1281-1286. https://doi.org/10.1175/JTECH-D-15-0029.1

51. Voermans, J.J., Smit, P.B., Janssen, T.T. and Babanin, A.V., 2020. Estimating Wind Speed and Direction Using Wave Spectra. *Journal of Geophysical Research: Oceans*, 125(2), e2019JC015717. https://doi.org/10.1029/2019JC015717
52. Herrera-Vázquez, C.F., Rascle, N., Ocampo-Torres, F.J., Osuna, P. and García-Nava, H., 2023. On the Measurement of Ocean Near-Surface Current from a Moving Buoy. *Journal of Marine Science and Engineering*, 11(8), 1534. https://doi.org/10.3390/jmse11081534

Submitted 07.05.2024; approved after review 23.08.2024;
accepted for publication 20.11.2024.

About the authors:

Yury Yu. Yurovsky, Leading Researcher, Head of the Applied Marine Physics Laboratory, Marine Hydrophysical Institute of RAS (2 Kapitanskaya Str., Sevastopol, 299011, Russian Federation), CSc (Phys.-Math.), **Scopus Author ID: 24377122700, ORCID ID: 0000-0002-9995-3965, ResearcherID: F-8907-2014,** y.yurovsky@mhi-ras.ru

Oleg B. Kudinov, Researcher, Marine Hydrophysical Institute of RAS (2 Kapitanskaya Str., Sevastopol, 299011, Russian Federation), CSc (Tech.), **Scopus Author ID: 57201072321**, obk91@mail.ru

Contribution of the co-authors:

Yury Yu. Yurovsky – development of methodology and conducting experimental research, data processing, analysis, and description of research results, writing original draft

Oleg B. Kudinov – development and manufacturing of measuring devices, conducting experimental research, reviewing and editing the text

The authors have read and approved the final manuscript.
The authors declare that they have no conflict of interest.

ISSN 1573-160X, *PHYSICAL OCEANOGRAPHY*, Vol. 32, Iss. 1, pp. 84-98 (2025)
Original Russian Text © A. V. Varenik, 2025,
published in *Morskoy Gidrofizicheskiy Zhurnal*, 2025, Vol. 41, Iss. 1, pp. 50–65

Original article

Nitrogen and Phosphorus Compounds in Atmospheric Deposition in Sevastopol, 2015–2023

A. V. Varenik

Marine Hydrophysical Institute of RAS, Sevastopol, Russian Federation
alla.varenik@mhi-ras.ru

Abstract
Purpose. The purpose of the work is to estimate the long-term variations in concentration and flux of nutrients (inorganic nitrogen and inorganic phosphorus) in atmospheric deposition in Sevastopol.
Methods and Results. During 2015–2023, the samples of atmospheric deposition in Sevastopol were collected to analyze the concentration of dissolved forms of inorganic nitrogen (nitrate, nitrite and ammonium) and phosphorus. For each precipitation event, two types of samplers were used – the open and wet-only ones. Laboratory analysis of the collected samples was carried out in FSBSI FRC "Marine Hydrophysical Institute". A total of 1264 samples of atmospheric deposition were analyzed. The maximum content of nutrients was determined in the samples with minimum precipitation amount, or after a long dry period. The concentrations of inorganic forms of nitrogen in the samples from the open sampler were 1.3 times higher than those from the wet-only one. The phosphorus content in the open sampler exceeded that in the wet-only one by 3 times. The increased concentrations of ammonium in atmospheric deposition were revealed in spring, while those of nitrates – in fall-winter. The phosphorus flux in the samples from the open sampler reached its maximum value in fall and exceeded the winter flux by 2.3 times.
Conclusions. The long-term variation in inorganic nitrogen flux is of a quasi-periodic pattern: its maximum flux was observed in 2017, and the minimum one – in 2019–2020. The maximum phosphorus flux in the samples from the wet-only sampler was noted in 2017–2018, whereas the phosphorus flux in the samples from the open sampler in 2021–2022 exceeded the flux in 2017–2018 by 1.5 times. As for inorganic nitrogen, its annual contribution to atmospheric deposition amounted 9.4–11.5% of a river runoff, and as for phosphorus – 16.7–55.6%. During the low-water period, these values were 12–14% and 20–65%, respectively.

Keywords: atmospheric deposition, nutrients, inorganic nitrogen, nitrates, ammonium, phosphorus

Acknowledgements: The investigation was carried out within the framework of a state assignment of FSBSI FRC MHI on the theme FNNN 2024-0001 "Fundamental studies of the processes which determine the fluxes of matter and energy in the marine environment and at its boundaries, the state and evolution of the physical and biogeochemical structure of marine systems in modern conditions". The author is grateful to M.A. Myslina and D.V. Tarasevich for their assistance in obtaining the data.

For citation: Varenik, A.V., 2025. Nitrogen and Phosphorus Compounds in Atmospheric Deposition in Sevastopol, 2015–2023. *Physical Oceanography*, 32(1), pp. 84-98.

Introduction

Atmospheric precipitation serves as a primary source of various chemical components for many ecosystems. Yet, the composition of precipitation is found to be significantly affected by anthropogenic activity. Rainwater composition plays an important role in the absorption of soluble components from the atmosphere, thereby contributing to our understanding of the relative contribution of different sources of atmospheric pollutants [1]. Urban areas are more susceptible to problems associated with atmospheric deposition of coarse and fine particles, largely due to the high density of vehicles and the presence of large industrial enterprises [2]. According to [1], the increase in atmospheric emissions of pollutants, including sulfur dioxide, nitrogen oxides, volatile organic compounds and aerosols, is predominantly associated with the growth of urban population and the subsequent increase in traffic.

A variety of factors contribute to the presence of air pollutants in urban environments. Among these are industrial activity, dust from roads and construction sites, combustion of fossil fuels, etc. Studies have shown a link between urbanization and increased rates of atmospheric deposition of both inorganic nitrogen [3] and inorganic phosphorus [4]. The findings of [4] revealed that phosphate deposition in Rio Grande exhibited higher levels in comparison to adjacent rural regions. The observed differences were attributed to the anthropogenic influence of a large fertilizer manufacturing facility located in the city.

Human activities, particularly the combustion of fossil fuels and the synthesis and utilization of nitrogen fertilizers, have led to an increase in atmospheric emissions of sulfur oxide (SO_x), nitrogen oxides (NO_x), and ammonia (NH_3). Consequently, this has led to increased levels of atmospheric deposition of sulfur and nitrogen in terrestrial and aquatic ecosystems [5–7]. In terrestrial ecosystems, excess atmospheric deposition of sulfur and nitrogen can lead to soil acidification, depletion of essential cations, changes in soil nutrients availability, nutrients imbalances in vegetation, loss of biodiversity, acidification, and eutrophication of nearby aquatic ecosystems [8, 9].

The primary sources of nitrogen in the air and atmospheric deposition include emissions from livestock farming, resulting from the application of manure and mineral fertilizers on agricultural fields, as well as catalysts in vehicles (ammonium), nitrogen oxides emissions from various combustion processes, the chemical industry, shipping, and other activities (nitrate) [10]. Owing to the surge in anthropogenic activities, such as deforestation, combustion of fossil fuels, and industrialization, there has been a marked increase in global nitrogen emissions since the pre-industrial era [11].

It has been established that the phosphorus content in the atmosphere is generally proportional to the total air dustiness and subject to significant fluctuations [12]. The primary natural sources of phosphorus in the atmosphere are wind erosion of the soil cover and the generation of biogenic aerosols by vegetation (spores, pollen and plant residues). Additionally, the presence of phosphorus in the atmosphere is known to occur during volcanic eruptions, the destruction of air bubbles on the surface of water bodies, and during vegetation combustion. Anthropogenic sources of phosphorus include the production of phosphorus fertilizers and agricultural work associated with the introduction of these fertilizers into the soil, metallurgical production, combustion of fossil fuels, fire retardants, industrial waste, construction dust, and road debris [8, 12–14]. Furthermore, cities tend to have a greater number of these sources in comparison to rural areas [15, 16]. The authors of [17] observed higher levels of inorganic phosphorus deposition in the Indian city Rajghat compared to rural areas, which was attributed to urban land use and biomass burning. In other studies [18], scientists attributed the increased phosphorus input to the urban atmosphere to the use of phosphate-containing fertilizers, weathering from mined rocks, and the burning of fossil fuels and plant biomass.

Significant quantities of particulate matter, including inorganic nitrogen and phosphorus, are introduced into the atmosphere due to industrial and transportation activities, as well as forest fires. Of particular concern in central and northern Brazil are forest fires, which are the primary sources of anthropogenic emissions of gases and aerosols during the dry season [19]. These fires have detrimental effects on ecosystems and air quality.

The study of the chemical composition of atmospheric precipitation is an important approach to assessing air pollution levels. This is due to the effective purification process of precipitation, which results in the removal of pollutants from the atmosphere and their transfer to other ecosystems, such as soil, water bodies (lakes, rivers, groundwater), forests, etc.

The present paper aims to study the long-term variations in concentration and flux of nutrients (inorganic nitrogen and inorganic phosphorus) with atmospheric precipitation in Sevastopol and estimate their impact on the Sevastopol Bay waters.

Methods

Atmospheric precipitation sampling area

The atmospheric precipitation sampling site is located in Sevastopol (Fig. 1) on the shore of Sevastopol Bay.

F i g. 1. Location of the atmospheric precipitation sampling site (Available at: https://arch-sochi.ru/2021/04/konczepcziya-razvitiya-infrastruktury-yahtinga-i-pribrezhnogo-morskogo-passazhirskogo-soobshheniya-na-azovo-chernomorskom-poberezhe-krasnodarskogo-kraya-2/)

The city of Sevastopol is located on the Black Sea coast in the southwestern part of the Crimean Peninsula. According to the Main Directorate of Natural Resources and Ecology of the city of Sevastopol (Sevprirodnadzor), the climate in Sevastopol is classified as relatively mild, with characteristics of a marine climate that is moderately continental in the foothills and subtropical Mediterranean in nature along the southeastern coast. The precipitation in Sevastopol exhibits variability, with annual rainfall from 300 to 500 mm/year. The amount of precipitation in the cold period is greater than in the warm period. The driest month is July.

Atmospheric precipitation sampling

The samples were collected in two types of samplers: wet-only and closed. To collect samples of wet precipitation without the influence of dry precipitation on the concentration of nutrients, an automatic sampler with a precipitation sensor was utilized. This device was developed and manufactured at the V.E. Zuev Institute of Atmospheric Optics of Siberian Branch of RAS (Tomsk), and it meets the requirements of the World Meteorological Organization (WMO). A Tretyakov precipitation gauge was utilized as an open sampler to assess the contribution of dry precipitation.

Individual samples of atmospheric precipitation were collected for each precipitation event. According to the requirements of the guidance document [1], samples were collected under the following conditions: if precipitation fell with a short interval (no more than 1 hour) and under consistent cloud cover, the samples were collected into a single container. If the interval exceeded 1 hour, the precipitation was collected as individual samples. The collected samples were transferred from the precipitation samplers into polyethylene containers and frozen for subsequent analysis. Each container was accompanied by the necessary information (indicated on the label), including the sampler type, the date of precipitation, air temperature, wind speed and direction, atmospheric pressure, relative air humidity at the time of the precipitation onset, and the precipitation amount.

Chemical analysis methods

Laboratory analysis of the samples was carried out at FSBSI FRC "Marine Hydrophysical Institute of RAS". The content of inorganic forms of nitrogen (nitrate, nitrite and ammonium) and inorganic phosphorus was determined in the samples, which had a sufficient volume for chemical analysis.

The concentration of ammonium ions was determined using a modified Sagi-Solorzano method based on the phenol-hypochlorite reaction with the formation of indophenol [20]. The concentration range, as defined by the method, was 0.1–15.0 μM, with an error margin of ±12%. The content of nitrites and the sum of nitrites and nitrates were determined according to the method (RD 52.10.745-2020) by the spectrophotometric method on a Scalar San^{++} continuous flow automatic analyzer of nutrients (Netherlands). The minimum detectable concentration, as

[1] The USSR State Committee for Hydrometeorology and the Ministry of Health of the USSR, 1991. *Atmospheric Pollution Control Guidelines: RD 52.04.186-89*. Moscow, 694 p. (in Russian).

determined by the method, is 0.07 μM, with an error margin of ±20%. The phosphorus content was determined photometrically according to the method based on the formation of a blue phospho-molybdic complex. The minimum detectable concentration of phosphates is 0.05 μM, with an error margin of ±10%.

The concentration of nutrients in precipitation samples was processed using mathematical statistics methods based on the RD 52.04.186-89 requirements. In the selected atmospheric precipitation, nitrites were found in much lower concentrations than nitrates and ammonium. Their contribution to the total inorganic nitrogen input was approximately 2%. Consequently, in the present study, the total concentration of nitrates and ammonium is regarded as inorganic nitrogen.

Calculation of the nutrient input

In this study, the volume weighted mean concentration (C_{vwm}) value, as calculated using the specified formula, is employed as an average characteristic of the input of inorganic nitrogen and phosphorus:

$$C_{\text{vwm}} = \sum C_{\text{i}} \cdot R_i / \sum R_i,$$

where C_{vwm} is the volume weighted mean concentration, μM; C_i is the measured concentration in one sample, μM; R_i is the measured amount of precipitation for each individual rain event, mm.

The flux of dissolved nutrients was calculated as the product of the volume weighted mean concentration for a specified period and the precipitation amount. The calculation method is outlined in the following equation:

$$F = C_{\text{vwm}} \cdot R,$$

where F is the flux of the element under consideration with precipitation over a specified period (month, season, year), $\text{mM} \cdot \text{m}^{-2} \cdot \text{season}^{-1}$, $\text{mM} \cdot \text{m}^{-2} \cdot \text{year}^{-1}$; R is the total precipitation amount for the specified calculation period, mm.

Results and discussion

Number of the samples selected

Samples from Sevastopol were obtained from a 24-hour weather station, thus yielding a data set comprising 1,264 samples. The histogram illustrating the distribution of the analyzed samples' amount by year is presented in Fig. 2.

Precipitation amount

Figure 3 shows the distribution of total precipitation by year and season, obtained on the basis of the samples collected.

The average annual precipitation in Sevastopol was 350.5 mm. The year 2020 was the driest. A seasonal pattern is evident in the precipitation data, with a decline observed in the spring-summer period, and an increase observed in the winter-fall period. The least amount of precipitation was observed in August, with a total of 100.6 mm recorded from 2015 to 2023. The maximum total precipitation for the period 2015–2023 was recorded in July and November, with values of 362.2 and 358.9 mm, respectively.

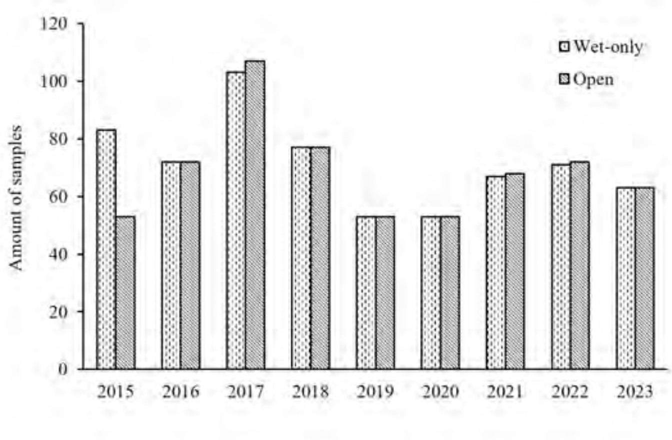

F i g. 2. Amount of atmospheric deposition samples collected in the open and wet-only samplers in Sevastopol

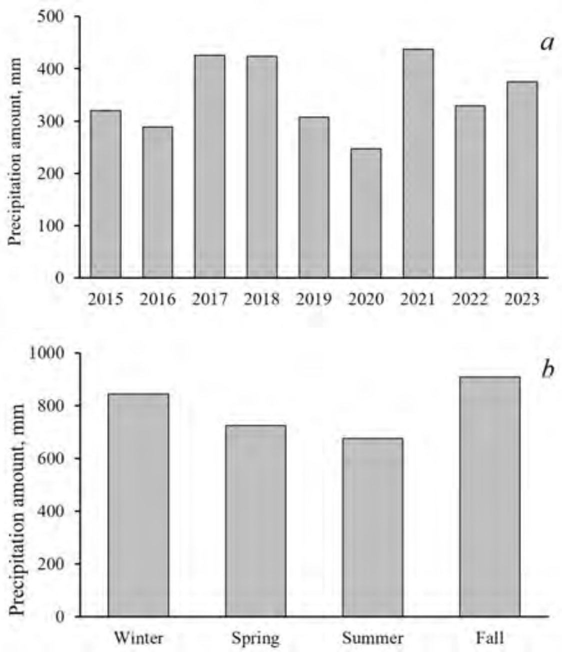

F i g. 3. Cumulative interannual (*a*) and seasonal (*b*) distribution of precipitation amount in Sevastopol during the study period

Concentration of nutrients

Our results show that atmospheric deposition plays an important role in the input of inorganic nitrogen and phosphorus to the underlying surface. Table 1 presents generalized data on the volume weighted mean concentrations of the considered nutrients for different types of samplers.

Table 1

Concentrations of dissolved nutrients C_{vwm}, μM, in atmospheric deposition in Sevastopol

Indicator	Wet-only Sampler	Open Sampler
Nitrates	40.51	53.65
Ammonium	34.38	36.03
Phosphorus	0.38	1.21

The maximum concentrations of the considered nutrients were determined in samples with minimal precipitation or following an extended dry period. In drier months, the atmosphere contains increased levels of dust, originating from the dry underlying surface and through dust transfer processes. Consequently, the combination of minimal precipitation, which dilutes pollutants, and increased dust levels could result in increased nutrient concentrations in these samples.

The volume weighted mean concentration of nitrates in atmospheric precipitation exceeded the ammonium concentration, with an excess of 18% for samples collected using a wet-only sampler and 49% for those collected using an open sampler.

In general, the concentrations of nutrients in the samples from the open sampler were higher than those from the wet-only one. However, for inorganic forms of nitrogen, this excess was insignificant – 1.3 times for nitrates and 1.05 times for ammonium. The concentration of phosphorus in the open sampler showed a threefold increase over the wet-only sampler. This discrepancy can be attributed to various origins and sources of these elements. Nitrogen is a soluble gas, while phosphorus is derived from terrigenous particles. This is significant because the gaseous form of phosphorus compounds plays a minimal role in the biogeochemical cycle of phosphorus. Therefore, the effect of dry aerosols on the total phosphorus supply is greater than that of inorganic nitrogen.

Flux of nutrients

For the designated sampling area, seasonal and annual values of fluxes of dissolved nutrients with atmospheric deposition were calculated.

Seasonal variation of nutrients input

A specific seasonal pattern is observed in the intra-annual fluctuation of nitrate input with atmospheric precipitation from both open and wet-only samplers.

The flux increases in the fall-winter period and decreases in the spring-summer one. At the same time, the influx of ammonium reaches its peak during the spring season (Table 2).

T a b l e 2

Seasonal flux of dissolved nutrients, mM·m^{-2}·season^{-1} in atmospheric deposition in Sevastopol

Season	Nitrates		Ammonium		Phosphorus	
	Wet-only sampler	Open sampler	Wet-only sampler	Open sampler	Wet-only sampler	Open sampler
Winter	37.56	44.98	26.82	29.33	0.30	0.56
Spring	28.25	36.59	31.42	32.27	0.33	1.08
Summer	23.64	31.39	21.43	20.86	0.27	0.91
Fall	30.67	44.51	22.05	23.54	0.28	1.32

The increase in the ammonium concentration during the warm period is likely due to the vital activity of animals and plants, as evidenced by the breakdown of urea and denitrification reactions [2] [21]. The observed phenomenon is also likely associated with the seasonal intensification of recreational loads.

The input of phosphorus with atmospheric deposition in Sevastopol was an order of magnitude lower than the input of inorganic nitrogen. However, as with ammonium, the inorganic phosphorus flux increased from winter to spring. This may be attributed to a combination of factors that have a maximum effect in late spring, including pollen deposits, microbial activity, insect sedimentation, and the utilization of fertilizers that can enter the atmosphere as aerosols and subsequently settle [22, 23]. Furthermore, the input of phosphorus, as measured by samples from an open sampler, reached its maximum in fall and exceeded the input observed in winter by a factor of 2.3.

Interannual variation in the nutrients input

The annual flux of nutrients varied during the study period depending on precipitation amount and the average annual concentration. The average annual value of the nitrate flux for the wet-only sampler was 13.2 mM·m^{-2} per year, whereas for the open sampler, it was 17.5 mM·m^{-2} per year. For ammonium, the average annual flux values were 11.2 and 11.8 mM·m^{-2} per year for the wet-only and open samplers, respectively.

Figure 4 shows the interannual variation in the input of nitrate and ammonium, as well as phosphorus resulting from atmospheric deposition.

[2] Brimblecombe, P., 1986. *Air Composition and Chemistry*. Cambridge: CUP Publishing, 240 p. (Cambridge Environmental Chemistry Series. Book 6).

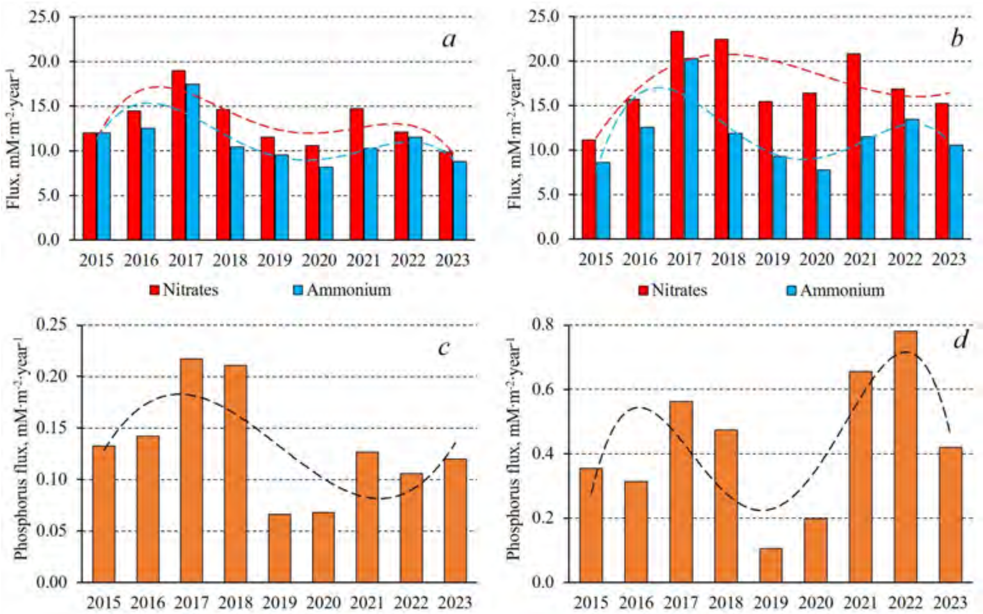

F i g. 4. Interannual variation of inorganic nitrogen flux in Sevastopol based on the wet-only (*a*) and open (*b*) samplers, and that of phosphorus based on the wet-only (*c*) and open (*d*) samplers. The dotted lines show trend lines

For samples collected using a wet-only sampler, a quasi-periodic variation in the flux of inorganic forms of nitrogen (both nitrate and ammonium) is observed, with a maximum input occurring in 2017 (Fig. 4, *a*). The nitrate input showed a lack of clear trend in the data collected using a permanently open sampler (Fig. 4, *b*). However, ammonium input demonstrated a consistent quasi-periodic variation. Concurrently, the difference between the maximum and minimum annual input of inorganic forms of nitrogen reached almost twofold.

The average annual values of the inorganic phosphorus flux for wet-only and open samplers were 0.13 and 0.43 $mM \cdot m^{-2}$ per year, respectively. The interannual change in the phosphorus flux with atmospheric deposition (Fig. 4, *c*, *d*) also generally shows some quasi-periodicity with minimum values in 2019–2020. For samples from the wet-only sampler, the maximum phosphorus flux was observed in 2017–2018, but for samples from the open sampler, the flux in 2021–2022 exceeded the flux in 2017–2018 by almost 1.5 times. At the same time, the minimum and maximum element fluxes for the wet-only sampler differ by about three times, and for the open sampler by seven times, although the amount of precipitation during these periods (Fig. 3, *a*) did not differ so significantly. This difference may be due to the influence of long-range dust transport contributing to an increased phosphorus content in the air.

In addition to urbanization, climatic conditions influence atmospheric phosphorus concentrations. For instance, [24] showed a positive relationship between air temperature and total atmospheric phosphorus concentrations in Hamilton, Canada. However, no significant relationship was identified between average annual precipitation and phosphorus concentrations. Furthermore, the authors of [25] found that the difference between the rates of atmospheric phosphorus deposition in urban and rural areas was positively associated with average annual temperature.

In our work the dependence of interannual variation in phosphorus and inorganic nitrogen flux on mean annual air temperature was also analyzed. The findings revealed a statistically insignificant relationship between the fluxes of nutrients and atmospheric precipitation, as well as air temperature. Yet, a statistically significant positive correlation was observed between the flux of nutrients and the amount of precipitation, while a significant negative correlation was identified between the concentration of elements and the precipitation amount. These findings confirm the previously obtained results [26].

Nitrate/ammonium ratio

Despite the generally negligible excess of nitrate content over ammonium in atmospheric precipitation, seasonal variations in their concentrations are clearly visible (Fig. 5).

An increased ratio of nitrate to ammonium in atmospheric precipitation is observed during the cold season, which may be attributable to additional emissions of nitrogen oxides into the air coinciding with the beginning of the heating season [27]. In spring-summer period, the NO_3^-/NH_4^+ ratio in precipitation is observed to be less than one or slightly exceeds one in samples collected from a wet-only sampler. This can be explained by a slight decrease in the concentration of nitrate and an increase in the input of ammonium. Starting in fall, this ratio reaches 1.4 and remains at this level in winter. For samples obtained from an open sampler, a similar trend is observed, although the ratio value in fall reaches 1.9.

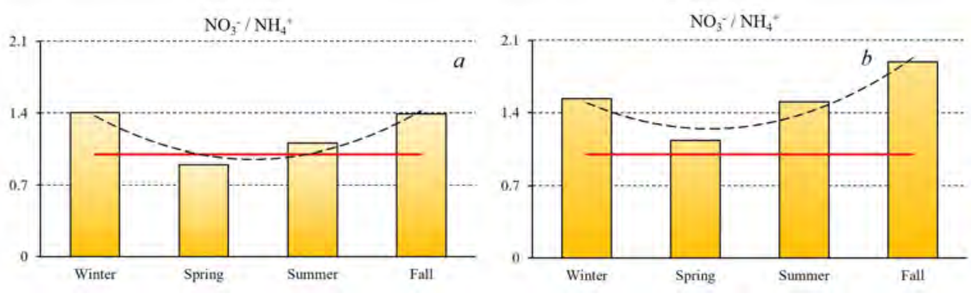

F i g. 5. Seasonal variation of the ratio of mineral forms of nitrogen in Sevastopol based on the samples from the wet-only (*a*) and open (*b*) samplers. Red line shows the ratio value equal to 1. The dotted lines show trend lines

Input of nutrients with atmospheric precipitation to the Sevastopol Bay waters

According to [28, 29], atmospheric precipitation is an important component of the cycle and redistribution of various chemical substances across water bodies, thereby playing a fundamental role in coastal biogeochemical processes. The input of nutrients from the atmosphere constitutes a significant source of income for the balance of seas and oceans. Moreover, the input from this source often exceeds the removal through river runoff [30]. In turn, the hydrochemistry of precipitation is largely determined by atmospheric emissions, thereby showing a direct correlation with both natural and anthropogenic activities [31]. Consequently, quantitative and qualitative assessments of precipitation and associated impurities are crucial for a better understanding of the anthropogenic impact on these biogeochemical processes. This is of practical importance as well, given that polluted atmospheric precipitation can have a negative impact on local fauna and flora, human health, etc. [31].

The majority of cities are located in coastal areas and along river banks [32], making coastal aquatic ecosystems vulnerable to runoff of various substances. As urban development expands, it becomes imperative to understand how urbanization influences the atmospheric input of nutrients. Therefore, we have determined the impact of inorganic nitrogen and phosphorus inputs from atmospheric precipitation on Sevastopol Bay.

The amount of inorganic nitrogen and phosphorus entering Sevastopol Bay with precipitation can be estimated based on the bay's area (7.96 km^2) and the calculated fluxes of these elements.

The average annual flux of inorganic nitrogen resulting from atmospheric deposition is 24.4 $mM \cdot m^{-2}$ per year for a wet-only sampler and 29.7 $mM \cdot m^{-2}$ per year for an open sampler. The average phosphorus flux values are 0.13 and 0.43 $mM \cdot m^{-2}$ per year for wet-only and open samplers, respectively. Consequently, the inorganic nitrogen input to the bay water area, calculated according to the data obtained, will be 2.6–3.2 $t \cdot year^{-1}$, and the phosphorus will be 0.03–0.1 $t \cdot year^{-1}$.

According to the data presented in [33], the average long-term removal of nutrients into Sevastopol Bay from the Chernaya River is 27.8 $t \cdot year^{-1}$for inorganic nitrogen and 0.18 $t \cdot year^{-1}$for inorganic phosphorus. Consequently, the contribution of atmospheric precipitation constitutes 9.4–11.5% of the river runoff for nitrogen and 16.7–55.6% for phosphorus. However, the removal of nutrients with river runoff during the low-water period is significantly less – 10.16 $t \cdot year^{-1}$ of inorganic nitrogen and 0.08 $t \cdot year^{-1}$ of inorganic phosphorus. Consequently, the influence of atmospheric precipitation as a source of nutrients will be more significant. According to our calculations, atmospheric precipitation contributes 12–14% of the inorganic nitrogen and 20–65% of the phosphorus, when compared to river runoff during the low-water period.

It has been increasingly recognized that atmospheric phosphorus input constitutes a significant source of phosphorus for terrestrial, freshwater, and marine ecosystems [8]. The results obtained in the present paper confirm these observations. Despite the reduced content of phosphorus in atmospheric deposition compared to inorganic nitrogen, their contribution to the inorganic phosphorus budget in Sevastopol Bay exceeds that of nitrogen. At the same time, phosphorus is an essential element for all organisms and can limit primary productivity. However, in excess, phosphorus can leak from terrestrial to freshwater and marine ecosystems, leading to eutrophication and a decrease in the dissolved oxygen content [9].

Conclusion

The present paper examines the long-term variation in the concentration and flux of nutrients (inorganic nitrogen and inorganic phosphorus) with atmospheric deposition in Sevastopol for 2015–2023.

It is shown that atmospheric deposition is an important source of inorganic nitrogen and phosphorus in the underlying surface. The maximum concentrations of the considered nutrients were determined in samples with minimal precipitation or following an extended dry period.

In general, the concentrations of nutrients in samples from the open sampler were higher than those from the wet-only one. However, this excess was found to be insignificant for inorganic forms of nitrogen. Conversely, the concentration of phosphorus in the open sampler was found to be three times higher than its concentration in the closed sampler.

A specific seasonal pattern is observed in the intra-annual variation in nitrate input with atmospheric precipitation. During the fall-winter period, the flux increases, while in the spring-summer period, it decreases. The input of ammonium is maximum in spring. The input of phosphorus with atmospheric precipitation in Sevastopol was less than the input of inorganic nitrogen. However, the flux of inorganic phosphorus showed a similar trend to that of ammonium, increasing from winter to spring.

The annual flux of nutrients varied during the study period depending on the precipitation amount and the average annual concentration. The average annual flux of nitrate for the wet-only sampler was 13.2 mmol·m^{-2} per year, whereas for the open sampler, it was 17.5 mmol·m^{-2} per year. For ammonium, the average annual flux values were 11.2 and 11.8 mmol·m^{-2} per year for the wet-only and open samplers, respectively. The average annual flux of inorganic phosphorus for the wet-only and open samplers was 0.13 and 0.43 mmol·m^{-2} per year, respectively.

The impact of inorganic nitrogen and phosphorus input with atmospheric precipitation on Sevastopol Bay was determined. The contribution of atmospheric precipitation to river runoff was determined to be 9.4–11.5% for nitrogen and 16.7–55.6% for phosphorus. However, during the low-water period, the removal of nutrients through river runoff is significantly less. Consequently, atmospheric precipitation is a more substantial source of nutrients, contributing 12–14% of inorganic nitrogen and 20–65% of phosphorus.

REFERENCES

1. Migliavacca, D.M., Teixeira, E.C., Wiegand, F., Machado, A.C.M. and Sanchez, J., 2005. Atmospheric Precipitation and Chemical Composition of an Urban Site, Guaíba Hydrographic Basin, Brazil. *Atmospheric Environment*, 39(10), pp. 1829-1844. https://doi.org/10.1016/j.atmosenv.2004.12.005

2. Fornaro, A. and Gutz, I.G.R., 2006. Wet Deposition and Related Atmospheric Chemistry in the São Paulo Metropolis, Brazil. Part 3: Trends in Precipitation Chemistry during 1983–2003. *Atmospheric Environment*, 40(30), pp. 5893-5901. https://doi.org/10.1016/j.atmosenv.2005.12.007

3. Decina, S.M., Hutyra, L.R. and Templer, P.H., 2020. Hotspots of Nitrogen Deposition in the World's Urban Areas: A Global Data Synthesis. *Frontiers in Ecology and the Environment*, 18(2), pp. 92-100. https://doi.org/10.1002/fee.2143

4. Casartelli, M.R., Mirlean, N., Peralba, M.C., Barrionuevo, S., Gómez-Rey, M.X. and Madeira, M., 2008. An Assessment of the Chemical Composition of Precipitation and Throughfall in Rural-Industrial Gradient in Wet Subtropics (Southern Brazil). *Environmental Monitoring and Assessment*, 144(1-3), pp. 105-116. https://doi.org/10.1007/s10661-007-9949-y

5. Fowler, D., Coyle, M., Skiba, U., Sutton, M.A., Cape, J.N., Reis, S., Sheppard, L.J., Jenkins, A., Grizzetti, B. [et al], 2013. The Global Nitrogen Cycle in the Twenty-First Century. *Philosophical Transactions of the Royal Society B*, 368(1621), 20130164. http://doi.org/10.1098/rstb.2013.0164

6. Lohse, K.A., Hope, D., Sponseller, R., Allen, J.O. and Grimm, N.B., 2008. Atmospheric Deposition of Carbon and Nutrients across an Arid Metropolitan Area. *Science of the Total Environment*, 402(1), pp. 95-105. https://doi.org/10.1016/j.scitotenv.2008.04.044

7. Yang, Y., Zhao, T., Jiao, H., Wu, L., Xiao, C., Guo, X. and Jin, C., 2022. Atmospheric Organic Nitrogen Deposition in Strategic Water Sources of China after COVID-19 Lockdown. *International Journal of Environmental Research and Public Health,* 19(5), 2734. https://doi.org/10.3390/ijerph19052734

8. Decina, S.M., Templer, P.H. and Hutyra, L.R., 2018. Atmospheric Inputs of Nitrogen, Carbon, and Phosphorus across an Urban Area: Unaccounted Fluxes and Canopy Influences. *Earth's Future*, 6(2), pp. 134-148. https://doi.org/10.1002/2017EF000653

9. Sumathi, M. and Vasudevan, N., 2019. Role of Phosphate in Eutrophication of Water Bodies and Its Remediation. *Journal of Chennai Academy of Sciences*, 1, pp. 65-86.

10. Van der Swaluw, E., Asman, W.A.H., Van Jaarsveld, H. and Hoogerbrugge, R., 2011. Wet Deposition of Ammonium, Nitrate and Sulfate in the Netherlands over the Period 1992–2008. *Atmospheric Environment,* 45(23), pp. 3819-3826. https://doi.org/10.1016/j.atmosenv.2011.04.017

11. Singh, A., Gandhi, N. and Ramesh, R., 2012. Contribution of Atmospheric Nitrogen Deposition to New Production in the Nitrogen Limited Photic Zone of the Northern Indian Ocean. *Journal of Geophysical Research: Oceans*, 117(C6), C06004. https://doi.org/10.1029/2011JC007737

12. Savenko, V.S. and Savenko, A.V., 2007. *Geochemistry of Phosphorus in the Global Hydrological Cycle*. Moscow: GEOS, 248 p. (in Russian).

13. Mahowald, N., Jickells, T.D., Baker, A.R., Artaxo, P., Benitez-Nelson, C.R., Bergametti, G., Bond, T.C., Chen, Y., Cohen, D.D. [et al.], 2008. Global Distribution of Atmospheric Phosphorus Sources, Concentrations and Deposition Rates, and Anthropogenic Impacts. *Global Biogeochemical Cycles*, 22(4), GB4026. https://doi.org/10.1029/2008GB003240

14. Violaki, K., Nenes, A., Tsagkaraki, M., Paglione, M., Jacquet, S., Sempéré, R. and Panagiotopoulos, C., 2021. Bioaerosols and Dust Are the Dominant Sources of Organic P in Atmospheric Particles. *npj Climate and Atmospheric Science*, 4, 63. https://doi.org/10.1038/s41612-021-00215-5

15. Dadashpoor, H., Azizi, P. and Moghadasi, M., 2019. Land Use Change, Urbanization, and Change in Landscape Pattern in a Metropolitan Area. *Science of the Total Environment*, 655, pp. 707-719. https://doi.org/10.1016/j.scitotenv.2018.11.267

16. Liu, Y., Luo, T., Liu, Z., Kong, X., Li, J. and Tan, R., 2015. A Comparative Analysis of Urban and Rural Construction Land Use Change and Driving Forces: Implications for Urban–Rural Coordination Development in Wuhan, Central China. *Habitat International*, 47, pp. 113-125. https://doi.org/10.1016/j.habitatint.2015.01.012

17. Yadav, A. and Pandey, J., 2017. Contribution of Point Sources and Non-Point Sources to Nutrient and Carbon Loads and Their Influence on the Trophic Status of the Ganga River at Varanasi,

India. *Environmental Monitoring and Assessment*, 189(9), 475. https://doi.org/10.1007/s10661-017-6188-8

18. Vitousek, P.M., Porder, S., Houlton, B.Z. and Chadwick, O.A., 2010. Terrestrial Phosphorus Limitation: Mechanisms, Implications, and Nitrogen-Phosphorus Interactions. *Ecological Applications*, 20(1), pp. 5-15. https://doi.org/10.1890/08-0127.1

19. Liousse, C., Andreae, M.O., Artaxo, P., Barbosa, P., Cachier, H., Gregoire, J.M., Hobbs, P., Lavoue, D., Mouillot, F. [et al.], 2004. Deriving Global Quantitative Estimates for Spatial and Temporal Distributions of Biomass Burning Emissions. In: C. Granier, P. Artaxo and C. E. Reeves, eds., 2004. *Emissions of Atmospheric Trace Compounds. Advances in Global Change Research*. Dordrecht, Netherlands: Springer. Vol. 18, pp. 71-113. https://doi.org/10.1007/978-1-4020-2167-1_3

20. Solórzano, L., 1969. Determination of Ammonia in Natural Waters by the Phenolhypochlorite Method. *Limnology and Oceanography*, 14(5), pp. 799-801. https://doi.org/10.4319/lo.1969.14.5.0799

21. Chebunina, N.S., Onischuk, N.A., Netsvetaeva, O.G. and Hodger, T.V., 2018. Dynamics of the Content of Mineral Forms of Nitrogen in Watercourses and Atmospheric Precipitation Listvyanka Settlement (South Baikal). *The Bulletin of Irkutsk State University. Series Earth Sciences*, 24, pp. 124-139. https://doi.org/10.26516/2073-3402.2018.24.124 (in Russian).

22. Bettez, N.D. and Groffman, P.M., 2013. Nitrogen Deposition in and near an Urban Ecosystem. *Environmental Science and Technology*, 47(11), pp. 6047-6051. https://doi.org/10.1021/es400664b

23. Kopáček, J., Kaňa, J., Porcal, P., Vrba, J. and Norton, S.A., 2019. Effects of Tree Dieback on Lake Water Acidity in the Unmanaged Catchment of Plešné Lake, Czech Republic. *Limnology and Oceanography*, 64(4), pp. 1614-1626. https://doi.org/10.1002/lno.11139

24. Furdui, V.I., Duric, M., Eskander, H.G. and Stacey, N., 2022. Temporal Trends of Phosphorus in Urban Atmospheric Aerosols. *Canadian Journal of Chemistry*, 100(7), pp. 538-544. https://doi.org/10.1139/cjc-2021-0220

25. Blake, K. and Templer, P.H., 2023. Interacting Effects of Urbanization and Climate on Atmospheric Deposition of Phosphorus around the Globe: A Meta-Analysis. *Atmospheric Environment,* 309, 119940. https://doi.org/10.1016/j.atmosenv.2023.119940

26. Varenik, A.V., 2019. Applying the Brandon Method to Estimate the Concentration of Inorganic Nitrogen in Precipitation. *Russian Meteorology and Hydrology*, 44(5), pp. 326-330. https://doi.org/10.3103/S1068373919050030

27. Varenik, A.V., 2020. Influence of Emissions from the Stationary Heat Sources upon the Atmospheric Precipitation Pollution with Inorganic Nitrogen in the Sevastopol Region. *Physical Oceanography*, 27(3), pp. 257-265. https://doi.org/10.22449/1573-160X-2020-3-257-265

28. Wright, L.P., Zhang, L., Cheng, I., Aherne, J. and Wentworth, G.R., 2018. Impacts and Effects Indicators of Atmospheric Deposition of Major Pollutants to Various Ecosystems - A Review. *Aerosol and Air Quality Research*, 18(8), pp. 1953-1992. https://doi.org/10.4209/aaqr.2018.03.0107

29. Savenko, V.S., 1996. Atmospheric Component of the Geochemical Balance of Phosphorus in the Modern Ocean. *Reports of the Academy of Sciences,* 350(3), pp. 390-392 (in Russian).

30. Singh, K.P., Singh, V.K., Malik, A., Sharma, N., Murthy, R.C. and Kumar, R., 2007. Hydrochemistry of Wet Atmospheric Precipitation over an Urban Area in Northern Indo-Gangetic Plains. *Environmental Monitoring and Assessment*, 131, pp. 237-254. https://doi.org/10.1007/s10661-006-9472-6

31. Hao, Z., Gao, Y., Yang, T. and Tian, J., 2017. Atmospheric Wet Deposition of Nitrogen in a Subtropical Watershed in China: Characteristics of and Impacts on Surface Water Quality.

Environmental Science and Pollution Research, 24(9), pp. 8489-8503. https://doi.org/10.1007/s11356-017-8532-5

32. Grimm, N.B., Faeth, S.H., Golubiewski, N.E., Redman, C.L., Wu, J., Bai, X. and Briggs, J.M., 2008. Global Change and the Ecology of Cities. *Science*, 319(5864), pp. 756-760. http://dx.doi.org/10.1126/science.1150195

33. Myslina, M.A., Varenik, A.V. and Tarasevich, D.V., 2024. Dynamics of Nutrients Concentration in the Chernaya River Waters (Crimean Peninsula) in 2015-2020. *Physical Oceanography*, 31(3), pp. 398-408.

Submitted 24.06.2024; approved after review 08.07.2024;
accepted for publication 20.11.2024.

About the author:

Alla V. Varenik, Senior Researcher, Marine Hydrophysical Institute of RAS (2 Kapitanskaya Str., Sevastopol, 299011, Russian Federation), CSc (Geogr.), **ORCID ID: 0000-0001-5033-4576, ResearcherID: H-1880-2014, Scopus Author ID: 56960448000**, alla.varenik@mhi-ras.ru

The author has read and approved the final manuscript.
The author declares that she has no conflict of interest.

ISSN 1573-160X, *PHYSICAL OCEANOGRAPHY*, Vol. 32, Iss. 1, pp. 99-115 (2025)
Original Russian Text © The Authors, 2025,
published in *Morskoy Gidrofizicheskiy Zhurnal*, 2025, Vol. 41, Iss. 1, pp. 66–82

Original article

Characteristics of Stratified Shear Flows Induced by Internal Waves on the Sakhalin Shelf (Sea of Okhotsk)

E. A. Rouvinskaya, O. E. Kurkina, A. A. Kurkin ✉

Nizhny Novgorod State Technical University n. a. R. E. Alekseev, Nizhny Novgorod, Russian Federation
✉ *aakurkin@gmail.com*

Abstract
Purpose. The work is purposed at studying the characteristics of shear flows induced by internal waves on the northeastern shelf of Sakhalin Island based on the results of numerical modeling of the transformation of barotropic tide along the selected two-dimensional (vertical plane) sections.
Methods and Results. The data from the WOA18 climate atlas with the 0.25° resolution for a summer season, and the bathymetry from GEBCO_2014 with the 1 min resolution are used to initiate a numerical model of the hydrodynamics of inviscid incompressible stratified fluid in the Boussinesq approximation. A tidal forcing from TOPEX/Poseidon Global Tidal Model (TPXO8) model which is based on satellite altimetry data is preset at the deep-sea boundary. For the near-bottom and near-surface velocities (at the fixed depths: 15 m above the bottom and 15 m below the surface), the diagrams of exceedance probability levels are constructed both allowing for the direction (sign) and according to the absolute value. Then the velocities at a probability level 0.05, 0.1 and 0.15 are identified, and conversely, the probability with which the velocity 0.25 or 0.3 m/s would be exceeded is determined. The maps are constructed based on the obtained values.
Conclusions. It is shown that the studied shear flows are nonlinear and characterized by significant asymmetry in distribution both in direction (from coast/to coast) and over depth (in the near-bottom and near-surface layers). In the areas where the sea depth is 700–800 m, there is a clearly defined zone where the absolute values of near-surface velocities are several times higher than those of the near-bottom ones. The main zones including the local maxima of velocity field are located in the north – from Cape Elizabeth to Piltun Bay, with one more from Cape Bellingshausen to Cape Terpeniya.

Keywords: Euler equations, internal gravity waves, velocity field, Sakhalin Island, Sea of Okhotsk, tides

Acknowledgements: The presented results are obtained within the framework of state assignment of Ministry of Science and Higher Education of the Russian Federation in the field of scientific activity (theme FSWE-2023-0004 "Nonlinear wave dynamics of the coastal zone under conditions of changing climate and anthropogenic impact").

For citation: Rouvinskaya, E.A., Kurkina, O.E. and Kurkin, A.A., 2025. Characteristics of Stratified Shear Flows Induced by Internal Waves on the Sakhalin Shelf (Sea of Okhotsk). *Physical Oceanography*, 32(1), pp. 99-115.

Introduction

Wave climate monitoring and forecasting, especially in the shelf zone, play a significant role when planning human economic activity, engineering surveys and determining potential impacts on the coastal ecosystem. Evaluation of wave field parameters and their mapping based on long-term observation data are necessary at the initial stages of designing various hydraulic engineering systems (from oil and gas platforms to wave energy converters [1]) and for further operation of marine infrastructure facilities since all these quantities are input parameters of models that make it possible to predict loads on structures, potential soil erosion and spread of impurities and pollutants. Thus, in the context of obtaining wave energy in recent decades, both global and regional (including consideration of seasonality) atlases of wave power have been actively created [2–4]. Significant wave heights and current directions are visualized for many economic needs using mathematical modeling and satellite observations. Material on this topic is presented in [5] as well as on the websites of the projects of the European Centre for Medium-Range Weather Forecasts https://charts.ecmwf.int/, the Bureau of Meteorology of Australian Government http://www.bom.gov.au/marine/waves.shtml, the National Renewable Energy Laboratory of the US Department of Energy https://portal.midatlanticocean.org/, etc. Thus, the mapping of wave field characteristics is a modern trend associated with the improvement of observation techniques and wave climate modeling.

The northeastern shelf of Sakhalin Island is affected by strong tides with a complex structure and seasonal variability (which is confirmed by detailed instrumental studies carried out over the past decades in connection with hydrocarbon exploration and the need to ensure environmental monitoring in oil and gas production areas [6, 7]).

Obviously, internal waves (and the currents induced by them) commonly recorded in satellite images as well are one of the key components of the wave climate in the region under study. Thus, new images of internal wave trains generated actively in the observation zone were obtained in [8] during satellite radar monitoring of oil spills.

Because of the specificity of spatial structure of the internal wave field, detailed description of their parameters with instrumental methods is an extremely complex task requiring huge financial investments. As noted in [9], despite the fact that modern sensors are more compact, reliable, sensitive and lightweight, consume less energy for recording and transmitting data, power consumption is still one of the main limitations for developing systems that provide long-term measurements with good spatial resolution. Therefore, the bulk of internal wave observations is carried out using remote sensing methods (see, e.g., one of the latest works on this topic [10]), which makes it possible to get an idea of the generation locations, periods and number of waves in trains, but does not provide an idea of the wave field vertical structure, which is especially important for assessing the impact of baroclinic flows on marine infrastructure facilities and ecosystem as a whole.

Two- and three-dimensional numerical modeling of internal wave dynamics provides partial compensation for the scarcity of field observations and the incompleteness of the obtained information about the wave field structure. Numerical models have become an indispensable tool for studying baroclinic processes since they provide a very realistic and accurate description of the scenarios of baroclinic wave transformation in the shelf zone. More details about modern models applied for this type of problem are given in the work[1] and in [11].

[1] Gouillon, F., 2009. *Internal Wave Modeling in Oceanic Numerical Models: Impact of the Model Resolution on the Wave Dynamic, Energetic and Associated Mixing: Dissertation Proposal*. Florida State University, 29 p.

At the first stage of our work, the transformation of multicomponent barotropic tide in the Sea of Okhotsk was studied within the framework of a completely nonlinear nonhydrostatic model. Estimates of the amplitudes of diurnal and semidiurnal baroclinic tide waves were obtained as geographical maps in terms of the displacement of isopycnic surfaces at different horizons. It was shown that the distribution of amplitudes depended significantly on depth, had a complex spatial structure with noticeable predominance of the amplitudes of baroclinic waves of diurnal period and the main extrema located on the shelf opposite Cape Elizabeth, Okhinskiy Isthmus and Cape Terpeniya [12].

This study is purposed at researching the spatial structure of baroclinic currents on the north-eastern shelf of Sakhalin Island, namely at mapping the distribution of horizontal near-surface (15 m from the surface) and near-bottom (15 m above the bottom) velocities directed from and to the coast, which will be exceeded with a probability of 0.05 or 0.15, and mapping the probability levels of exceeding near-bottom velocity values of 0.25 and 0.3 m/s directed from and to the coast as well.

Mathematical model and algorithms for constructing threshold value maps

Internal wave dynamics was studied within the framework of software package implementing the numerical integration procedure of a completely nonlinear (vertical plane) system of hydrodynamic equations of inviscid incompressible stratified fluid in the Boussinesq approximation with regard to the effect of barotropic tide and the Earth rotation [13]. At the open deep-water boundary of the selected sections, barotropic forcing was specified in the form of a multicomponent tide (M2, S2, K1, O1, P1, Q1), the amplitudes and phases of which were determined from TOPEX/Poseidon Global Tidal Model (TPXO8) based on satellite altimetry data [14]. It should be noted here that there are two ways to specify the tidal effect: by a boundary condition and by adding a volumetric force to the momentum balance equation [15]. In this work, we used the first method justified by the specifics of the applied model and repeated validation of the result, including comparison with *in situ* observational data [13]. Seawater density stratification information was taken from the WOA18 climate atlas with the 0.25° resolution for a summer season, and bathymetry was taken from GEBCO_2014 with the 1 min resolution. In order to take into account only the most characteristic features of vertical density profile and bottom bathymetry during modeling (data from atlases along the sections were additionally averaged over a width of 10–15 km depending on the relief), both functions were parameterized. Figure 1 shows a map of the sections along which the numerical modeling of internal wave dynamics was carried out.

Detailed descriptions of the model and wave dynamics along individual sections are given in our works [16, 17]. Here, we will discuss further processing of the obtained calculation results: identifying the velocity at a certain horizon, determining exceedance probability levels and constructing the maps of threshold values.

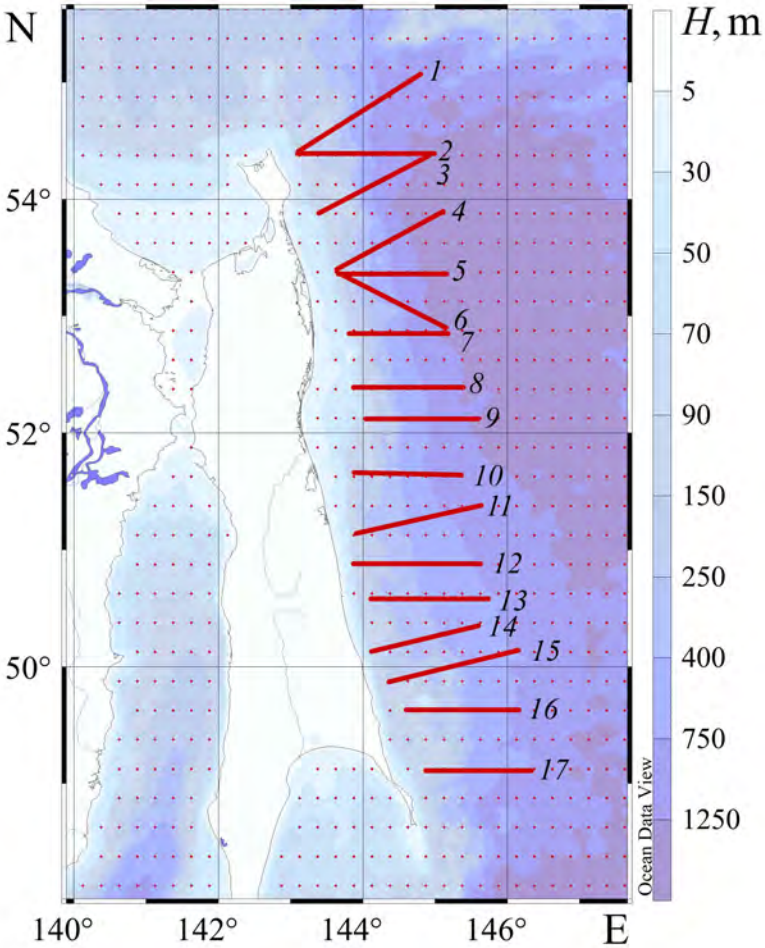

F i g. 1. Geographical location of sections, along which the internal wave dynamics were modeled, in the Sea of Okhotsk

At the first step of the algorithm, the values located on the lines 15 m below the surface and above the bottom were selected from the horizontal velocity field. If we talk about the bottom boundary layer (BBL), its thickness depends on many factors including tidal intensity, bottom slopes and latitudes [18]. A good review of existing empirical models applied for estimating the BBL thickness is given in [19]. It also demonstrates the results of a 15-day observation of the BBL thickness on an area of the continental shelf with a depth of 250 m and sufficiently strong tides (comparable in amplitude to those used in our model). It was revealed that, on average, the BBL was ~ 10 m. We also relied on the BBL estimates obtained by modeling the selected sections using the completely nonlinear nonhydrostatic model for viscous fluids SUNTANS [20]. Although the absence of viscosity in the model we used does not provide a realistic description of the flows arising in the boundary layer, generally, the differences in the wave fields obtained in the inviscid and viscous models will not be significant beyond its limits in subcritical regimes [21]. Guided by symmetry considerations and taking into account that horizon $z = -15$ m does not fall into the upper pycnocline for all sections, the authors analyzed the velocities at a selected depth of 15 m in the near-surface layer.

Figure 2 gives the example of the x–t diagram of near-surface horizontal velocities on section *16*.

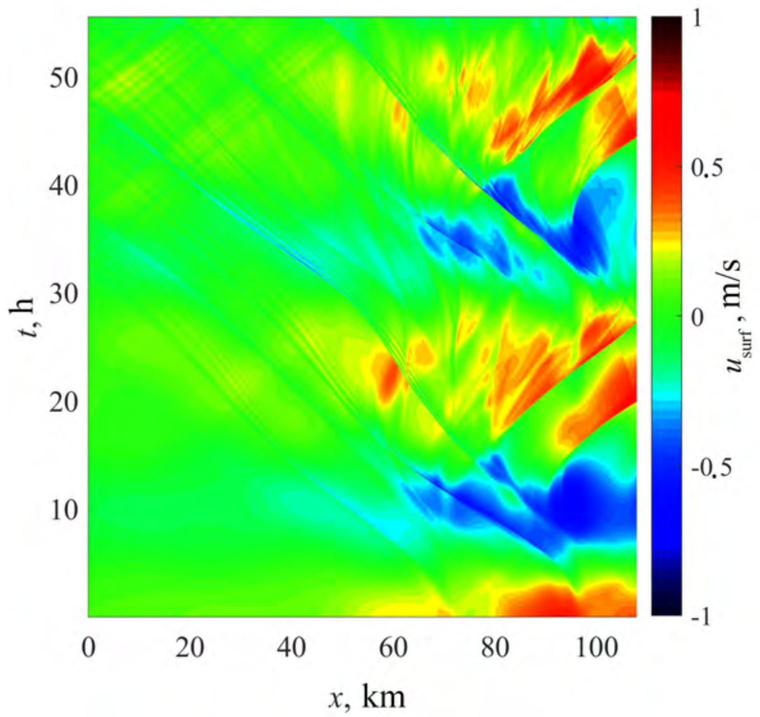

F i g. 2. Spatio-temporal (x–t) diagram for near-surface (fixed at the 15 m depth) velocities on section *16*

At the second step of the algorithm, diagrams of probability of level exceeding for the near-surface and near-bottom velocity were constructed allowing for the direction (sign) and according to the absolute value. Then, the velocities at a probability level 0.05, 0.1 and 0.15 were identified and, conversely, the probability with which the velocity 0.25 or 0.3 m/s would be exceeded was determined. The selection of such values is due to the estimates of the threshold velocities at which the displacement of soil particles can be observed. Thus, in [22], a method for determining the nature of bottom sediment movement is given based on the values of the dimensionless Rouse number (Ro), which is defined as the ratio of velocity (W_s) of hydraulic-size suspended particles fall to the dynamic velocity of vertically non-uniform water flow u^*:

$$\mathrm{Ro} = \frac{W_s}{\beta \kappa u^*}, \tag{1}$$

where β is ratio of eddy viscosity to eddy diffusion (approximately equal to unity); κ is Karman constant (equal to 0.4). Figure 3 represents a nomogram that makes it possible to determine the nature of sediment material movement: when Ro ≥ 7, the sediment movement is initiated by a wave flow and the particles begin to move in the form of rolling; an increase in the flow velocity at 7.5 ≥ Ro ≥ 2.5 leads to the movement of tractional sediments; at 2.5 ≥ Ro ≥ 1.2, saltation of sediment particles occurs; the movement of suspended sediments occurs at 1.2 ≥ Ro ≥ 0.8; intensive movement of bottom sediments, leading to significant deformations of the bottom, occurs at Ro ≤ 0.8 [22].

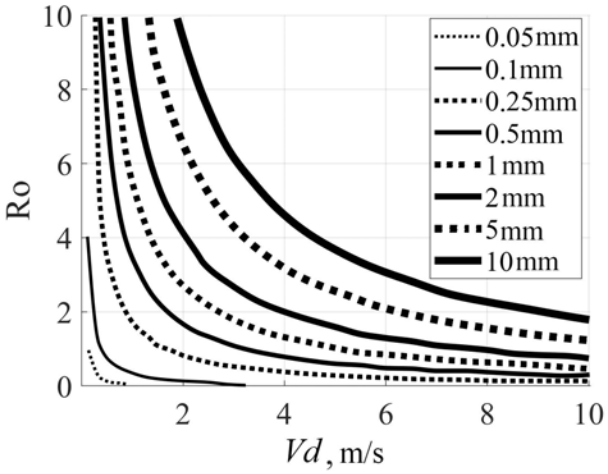

F i g. 3. Nomogram of sediment movement pattern (adapted from [22, p. 379]); *Vd* is near-bottom wave velocity

Let us use the map of the Sakhalin shelf bottom sediments from the National Atlas of Russia, Volume 2, available at https://nationalatlas.ru/tom2. It is evident that when moving from the coastline to the deep-water part, fine (0.1–0.25 mm in diameter), medium (0.25–0.5 mm) and coarse (0.5–1 mm) sands are replaced by coarse aleurites (0.01–0.05 mm), fine aleuritic silts, clay aleurites and clay silts at the maximum depth. Velocities ~ 0.25 m/s for aleurites are observed at Ro ≤ 0.8, which can lead to significant bottom deformations. Movement of fine and medium bottom sand is also possible, especially under periodic wave action. According to work [2], erosive velocities for fine sand are 0.2–0.4 m/s, for light sandy soil – 0.3–0.45 m/s; the same threshold velocity values can be found in regulatory documents. Although the baroclinic flow velocity was measured 15 m above the bottom level at the BBL conventional boundary, the same order of velocity values can be observed at the bottom. This is due to the fact that the currents induced by the observed solitons of internal waves reach a maximum velocity at the bottom

[2] Maksimovskiy, N.S., 1961. [*Cleaning of Sewage Waters*]. Moscow: Ministry of Public Utilities of RSFSR, 352 p. (in Russian).

and surface of the basin, and the model does not consider turbulent flows that can be generated at the bottom.

Figure 4 shows an example of a diagram of near-surface velocities on section *16*. The figure also represents a cut of a diagram of exceeding probability of the near-surface velocity level at value 0.25 m/s and a cut according to a probability 0.05. The upper part of the graph corresponds to positive (to coast) velocities, while the lower part corresponds to negative ones. The diagram asymmetry characterizes the wave field complex structure. The absolute values of velocities were also analyzed at each point of the route by the probability and velocity level.

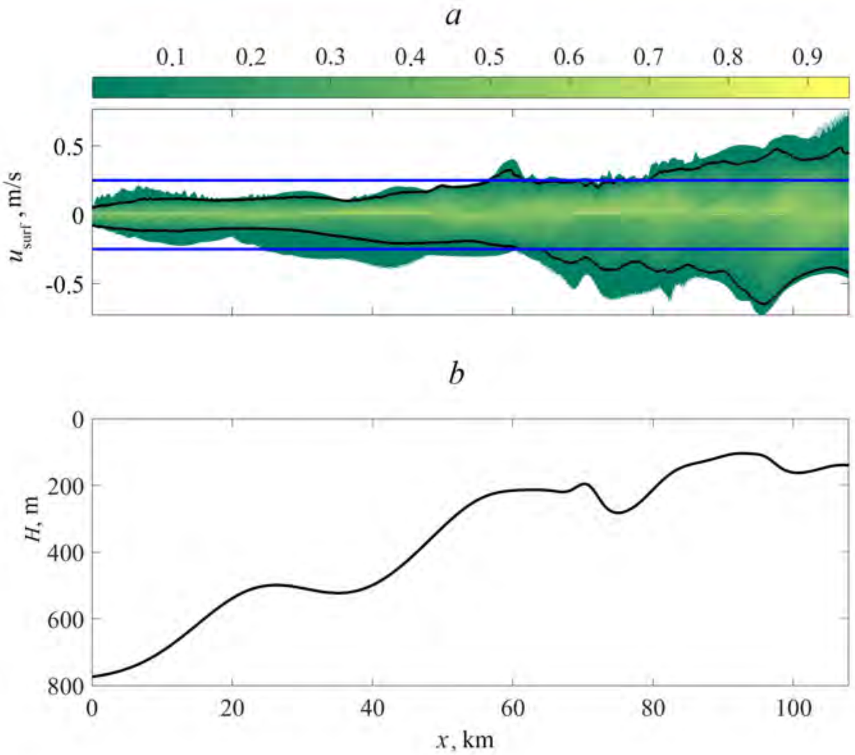

F i g. 4. Diagram of probability of exceeding near-surface (fixed at the 15 m depth) velocity level on section *16* allowing for the sign (direction): blue line is a cut at value 0.25 m/s; black curve is a cut according to a probability 0.05 (*a*); lower graph shows bottom bathymetry (*b*)

Maps of threshold values of baroclinic current velocities

We proceed to the analysis of the obtained results. Figure 5 contains the maps of probability levels of the bottom and surface velocities exceeding 0.25 m/s. Local probability maxima are reached in the shelf areas from Cape Elizabeth to the northern boundary of Piltun Bay, from the southern edge of Piltun Bay to Chaivo Bay, opposite Lunskiy Bay and near Cape Bellingshausen. For velocities allowing for the sign and their absolute values, the location of local maxima in the bottom and surface layers coincides. However, for absolute values and velocities directed from the coast, the probabilities in the bottom layer are generally not lower than in the surface layer. For velocities directed to the coast, on the contrary, the probabilities of exceeding the level of 0.25 m/s at the surface are generally not lower than in the bottom layer. In the northern part of the shelf (up to Chaivo Bay), the areas where the probability levels are within 0.8–1 for absolute values and 0.6–0.8 for velocities directed to and from the coast are located. The probabilities of exceeding the level 0.25 m/s reach 0.8 southwards of Chaivo Bay in very small areas for absolute velocities only, and they do not exceed 0.4 for velocities allowing for the sign.

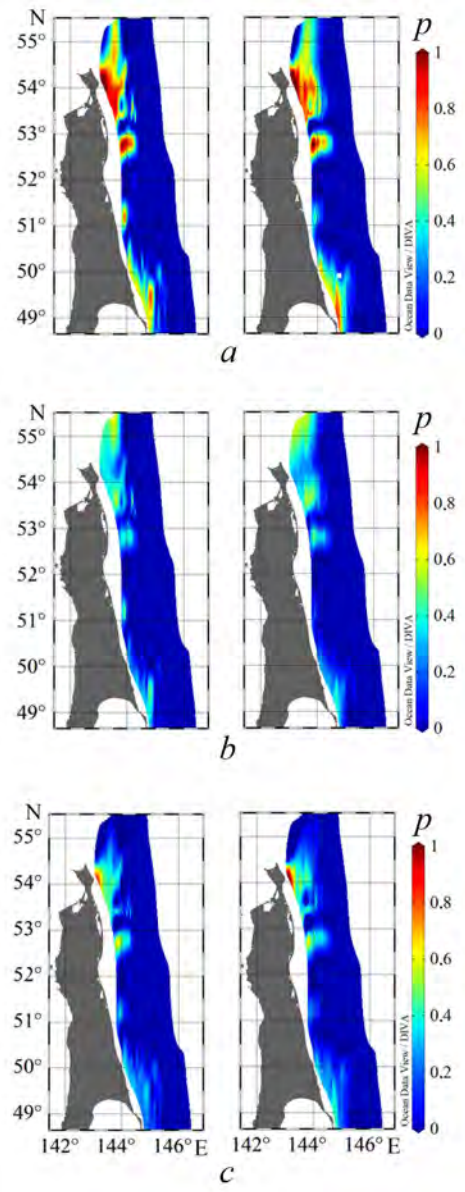

F i g. 5. Maps of probability levels of exceeding 0.25 m/s (p) for the near-bottom (*left*) and near-surface (*right*) velocities according to the absolute values (a), directed to the coast (b) and from the coast (c)

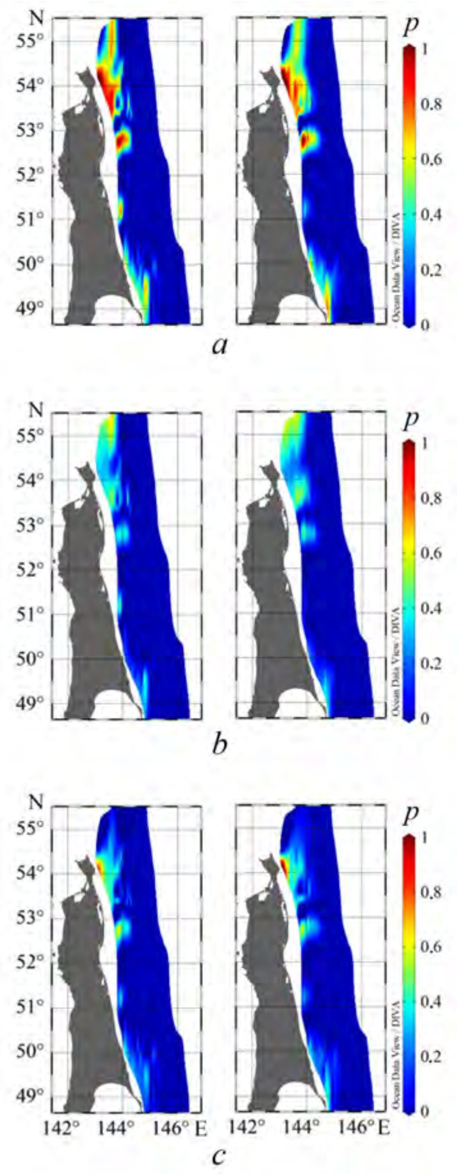

F i g. 6. The same as in Fig. 5, for velocity 0.3 m/s

Figure 6 represents the maps of probability levels of exceeding 0.3 m/s for the near-bottom and near-surface velocities. When comparing Figs. 5 and 6, it is clear that the maxima location coincides, although the probabilities are lower; this is especially noticeable for the areas located southwards of Chaivo Bay.

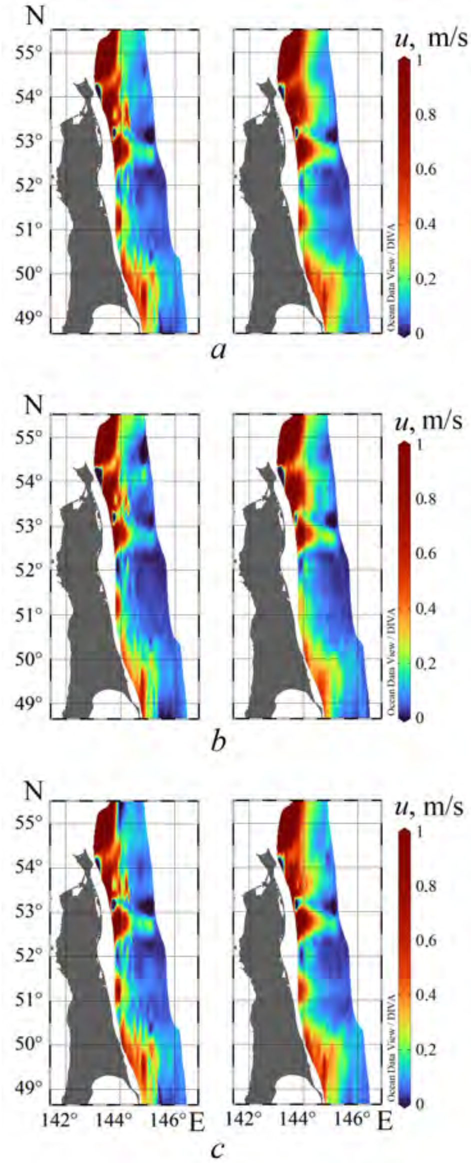

F i g. 7. Maps of distribution of the near-bottom (15 m above the bottom; left) and near-surface (15 m below the surface; right) velocities values according to their absolute values (*a*), directed to the coast (*b*) and from the coast (*c*) that will be exceeded with a probability 0.05

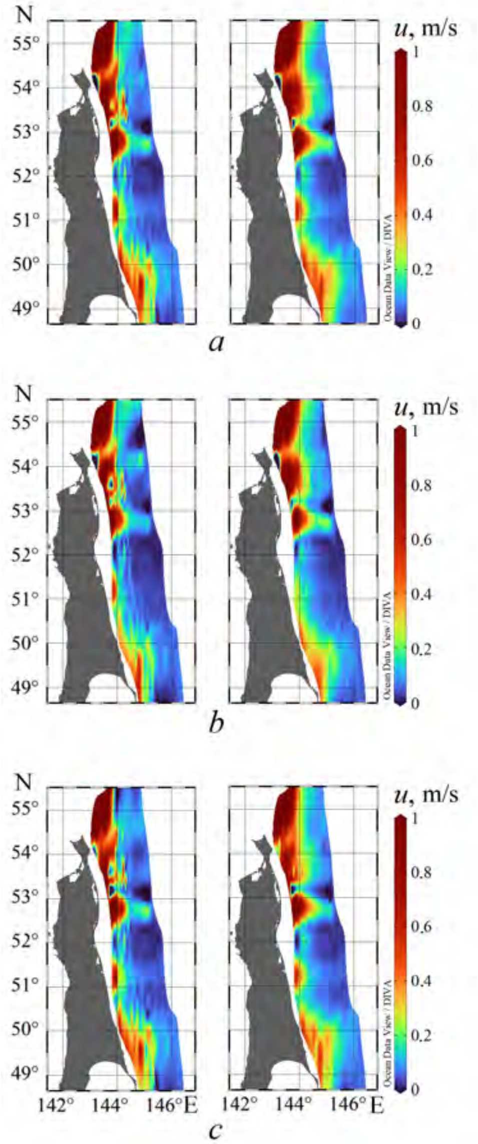

F i g. 8. The same as in Fig. 7, at exceeding with a probability 0.1

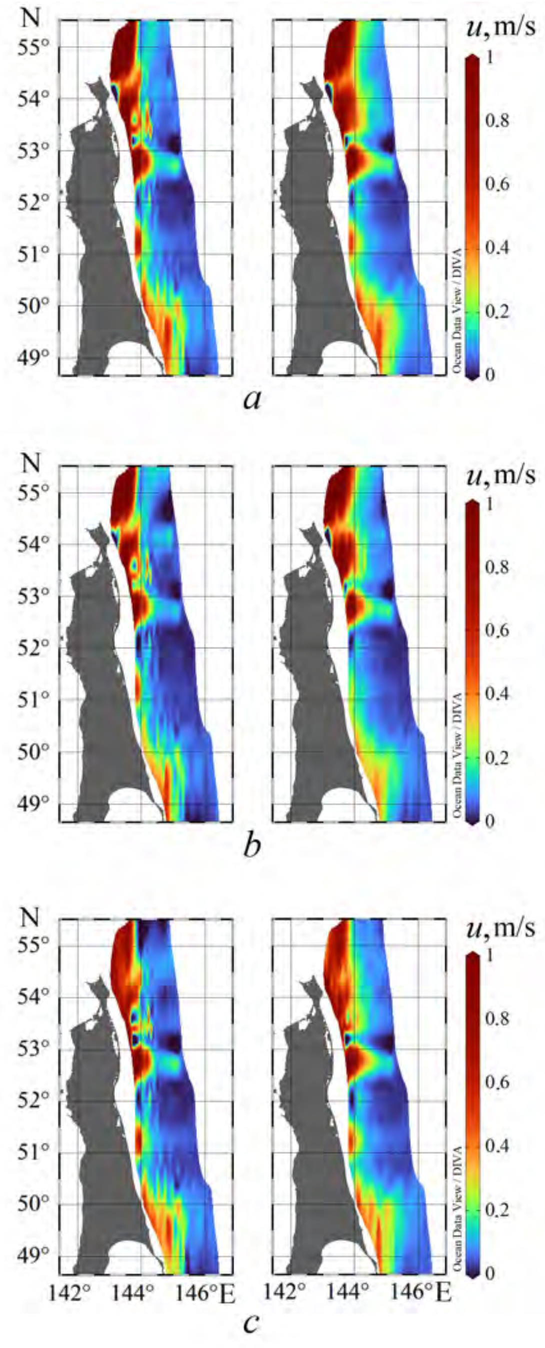

F i g. 9. The same as in Fig. 7, at exceeding with a probability 0.15

Figures 7–9 show the maps of distribution of the near-surface (15 m from the surface) and near-bottom (15 m above the bottom) velocities by absolute value, directed to and from the coast, that will be exceeded with a probability 0.05; 0.1; 0.15. The main maxima, close to 0.8 m/s, are located in the north – from Cape Elizabeth to Piltun Bay, the second zone of local maxima is in the south – from Cape Bellingshausen to Cape Terpeniya. In the remaining zones, the maximum velocities do not exceed 0.3 m/s. In the upper and lower layers, asymmetry regarding to direction (from or to the coast) is observed: in the northern zones, the velocities directed from the coast decrease significantly in magnitude (Figs. 7, *c*; 8, *c*; 9, *c*) within 1–0.7 m/s with a probability level increase, while in the direction to the coast (Figs. 7, *b*; 8, *b*; 9, *b*), changes are insignificant (velocities of ~ 1 m/s are reached in the bottom and surface layers). In the southern zone, when moving from a probability 0.05 to a level of 0.15, local maxima become less pronounced, especially in the surface layer and in the direction to the coast (velocities of ~ 0.5 m/s are reached only in the bottom layer near Terpeniya Peninsula and Lunskiy Bay).

Figures 10–12 represent the scatter diagrams of near-bottom and near-surface velocities by absolute value and allowing for direction depending on the total depth at the section point and the probability level at which these values can be exceeded. It is evident from Fig. 10 that all the diagrams show the maximum scatter of points in the sea areas of up to ~ 500 m depth, and the values of near-bottom and near-surface velocities over 0.5 m/s appear at a total depth of less than 300 m. With a probability level increase, the concentration of points in the upper part of the cloud (where the velocities are over 1 m/s) decreases naturally. At 700–800 m depths, a set of points where the absolute values of near-surface velocities are several times higher than the bottom velocities is clearly expressed. Consideration of velocity direction as well as its measurement depth (bottom or surface layer) increases significantly the scatter of points in the zones of up to 500 m (Fig. 10, *d*), which indicates the essentially nonlinear nature of currents once again.

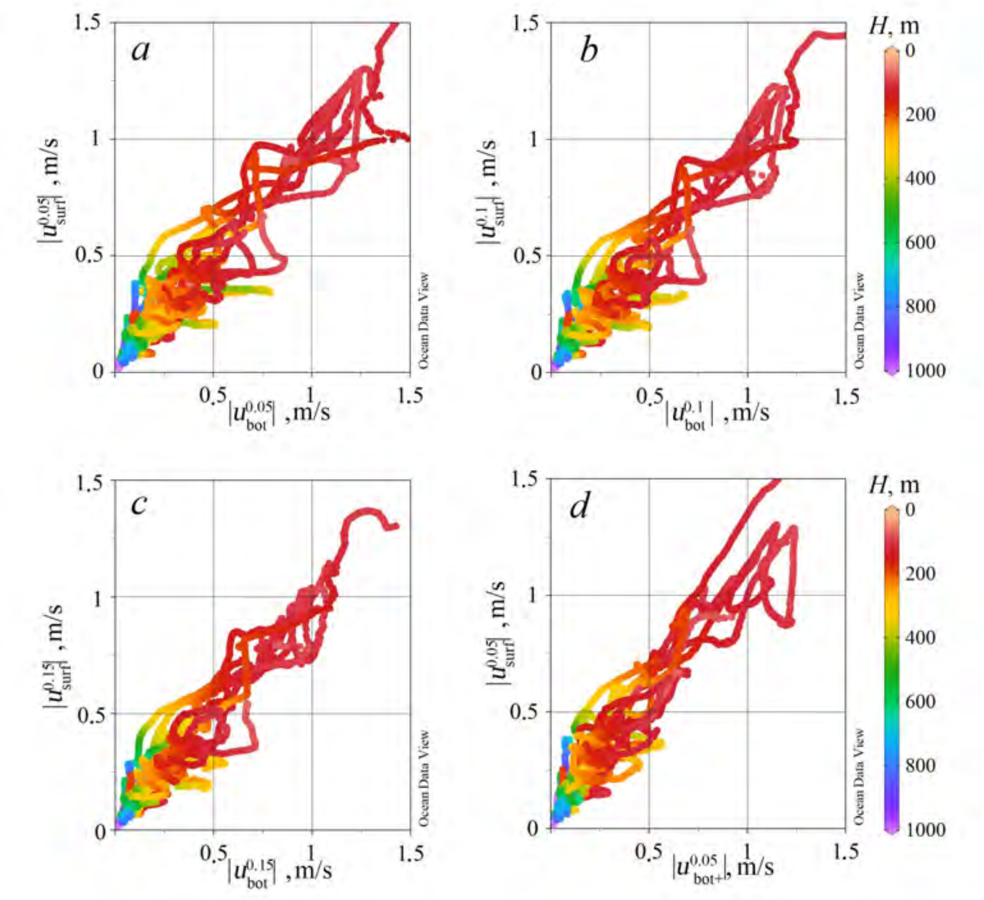

F i g. 10. Scatter plots of absolute values of the near-bottom and near-surface velocities at a probability level 0.05 (*a*), 0.1 (*b*) and 0.15 (*c*), as well as near-bottom velocity to the coast and absolute values of near-surface velocity at a probability level 0.05 (*d*). Color shows total depth at the point

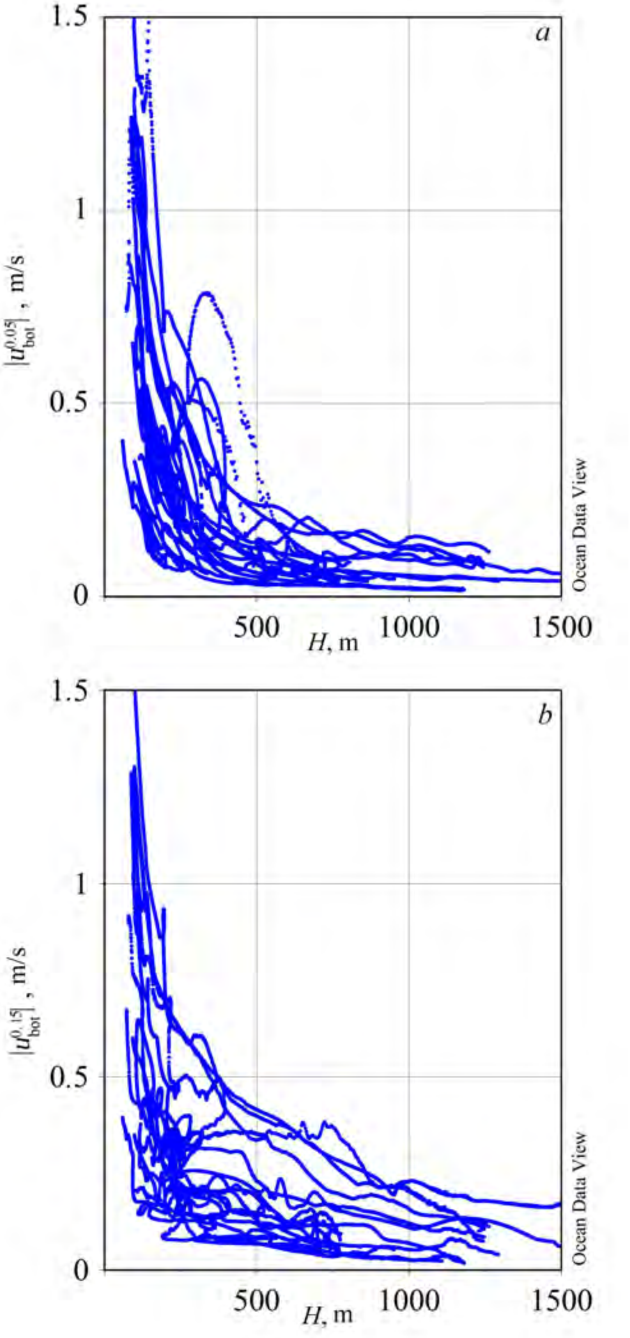

F i g. 11. Dependence of the near-bottom velocity absolute values at a probability level 0.05 (*a*) and 0.15 (*b*) upon the total depth at the point

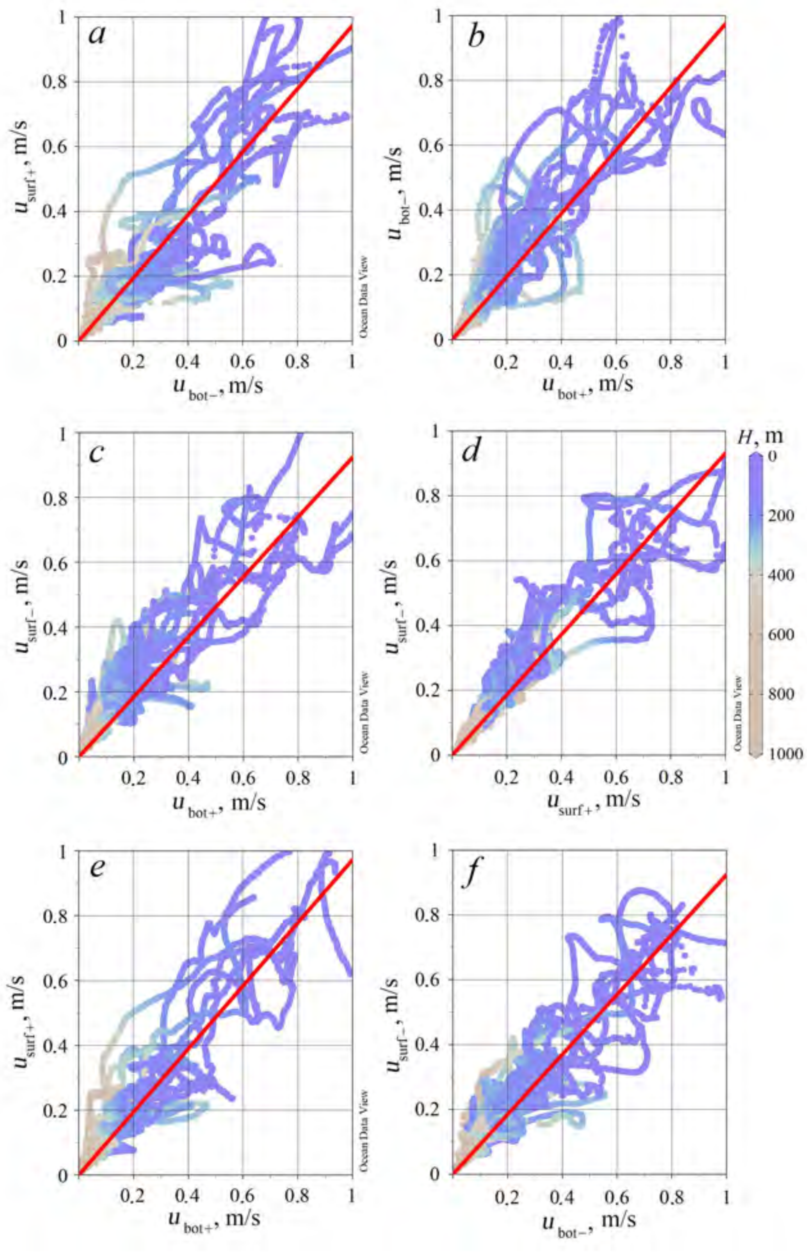

F i g. 12. Scatter plots of: the near-bottom velocity directed from the coast and the near-surface one – to the coast (*a*), the near-bottom velocity directed from and to the coast (*b*), the near-bottom velocity to the coast and the near-surface one – from the coast (*c*), the near-surface velocity to and from the coast (*d*), the near-bottom and near-surface velocities to the coast (*e*), the near-bottom and near-surface velocities from the coast (*f*) at a probability level 0.15. Color shows total depth at the point. Red line is linear regression

Figure 11 shows the distribution of near-bottom velocities by depth. It is clearly seen that 0.25 m/s velocities and higher are reached only at points with a sea depth of up to 500 m, while at depths from 100 to 500 m, bottom velocities within 0.25–0.5 m/s prevail at probability levels p 0.05 and 0.15.

When studying the correlation dependence of near-bottom/near-surface velocities, the directions (from the coast / to the coast) were taken into account (Fig. 12). When comparing Figs. 12 and 10, we can conclude that a due regard for the direction leads to the fact that the cloud of points in all diagrams becomes wider and the scatter increases. At the same time, the regression coefficient remains close to one in all graphs and is 0.9 (*a*, *c*), 0.95 (*b*), 0.94 (*d*, *e*), 0.89 (*f*) (Fig. 12).

Conclusion

In this work, the spatial structure of baroclinic currents on the northeastern shelf of Sakhalin Island is studied: maps of exceedance probability levels for values 0.25 and 0.3 m/s for the near-bottom (15 m above the bottom level) and near-surface (15 m from the surface) velocities (erosive velocities for fine sand and light sandy soil) by absolute value, directed to and from the coast are constructed and analyzed, as well as maps of the values distribution of the near-surface and near-bottom velocities by their absolute value, in the direction to and from the coast with probability of exceeding of 0.05; 0.1; 0.15. The precalculated horizontal velocity fields were obtained by modeling the dynamics of internal waves using 17 two-dimensional sections under a completely nonlinear model based on the Euler system of equations in the Boussinesq approximation. In all maps, the main local maxima of values are located in the shelf areas from Cape Elizabeth to the northern boundary of Piltun Bay, from the southern edge of Piltun Bay to Chaivo Bay, opposite Lunskiy Bay as well as near Cape Bellingshausen.

It is shown that the horizontal velocity field is essentially nonlinear: asymmetry is visible both in direction (from coast/to coast) and depth (in the bottom and surface layers). To demonstrate this conclusion, scatter plots of various combinations of the near-bottom and near-surface velocities are also constructed in absolute value and allowing for direction. The maximum scatter of points in all the plots is observed at sea depths of up to ~ 500 m, and values of near-bottom and near-surface velocities over 0.5 m/s are traced at depths of less than 300 m. Consideration of velocity direction and measurement depth (near-bottom/near-surface) leads to an increase in the scatter of points and the width of the point cloud cross-section (especially at values higher than 0.3 m/s), which is apparently associated with a complex nonlinear structure of the horizontal velocity field.

REFERENCES

1. Maisondieu, C., 2015. WEC Survivability Threshold and Extractable Wave Power. In: A. Clément, ed., 2015. *11th European Wave and Tidal Energy Conference (EWTEC 2015)*. Nantes, France, 8 p.

2. Arinaga, R.A. and Cheung, K.A., 2012. Atlas of Global Wave Energy from 10 Years of Reanalysis and Hindcast Data. *Renewable Energy*, 39(1), pp. 49-64. https://doi.org/10.1016/j.renene.2011.06.039

3. Gonçalves, J., Martinho, P. and Guedes Soares, C., 2014. Wave Energy Conditions in the Western French Coast. *Renewable Energy*, 62, pp. 155-163. https://doi.org/10.1016/j.renene.2013.06.028

4. García-Medina, G., Özkan-Haller, H.T. and Ruggiero, P., 2014. Wave Resource Assessment in Oregon and Southwest Washington, USA. *Renewable Energy*, 64, pp. 203-214. https://doi.org/10.1016/j.renene.2013.11.014

5. Grigorieva, V.G., Badulin, S.I. and Gulev, S.K., 2022. Global Validation of SWIM/CFOSAT Wind Waves against Voluntary Observing Ship Data. *Earth and Space Science*, 9(3), e2021EA002008. https://doi.org/10.1029/2021EA002008

6. Shevchenko, G.V. and Besedin, D.E., 2020. Cold-Season Characteristics of Currents off the Northeastern Shelf of Sakhalin Derived from Instrumental Observations. *Meteorologiya i Gidrologiya*, (6), pp. 87-97 (in Russian).

7. Yarichin, V.G., Vlasov, N.A., Oleinikov, I.S. and Shkileva, A.A., 2012. [Peculiarities of Spatial Variability of Harmonic Constants of Tidal Currents of Diurnal Waves on the Northeastern Shelf of Sakhalin Island (According to the Data of Environmental Monitoring of Oil-and-Gas Areas)]. *FERHRI Issues*, 154, pp. 145-186 (in Russian).

8. Kolesnikova, A.S., Dubina, V.A., Kruglik, I.A. and Rudenko, O.N., 2022. Satellite Radar Monitoring of Sakhalin Island Shelf. In: FESTFU, 2022. *Urgent Problems of the World Ocean Biological Resources Development: Proceedings of the VII International Scientific and Technical Conference.* Vladivostok: Far Eastern State Technical Fisheries University, pp. 108-112 (in Russian).

9. Vella, N., Foley, J., Sloat, J., Sandoval, A., D'Attile, L. and Masoumi, M., 2022. A Modular Wave Energy Converter for Observational and Navigational Buoys. *Fluids*, 7(2), 88. https://doi.org/10.3390/fluids7020088

10. Svergun, E.I., Zimin, A.V., Kulik, K.V. and Frolova, N.S., 2023. Surface Manifestations of Short-Period Internal Waves in the Sea of Okhotsk and the Kuril-Kamchatka Region of the Pacific Ocean. In: T. Chaplina, ed., 2023. *Complex Investigation of the World Ocean (CIWO-2023). CIWO 2023.* Springer Proceedings in Earth and Environmental Sciences. Cham: Springer, pp. 141-149. https://doi.org/10.1007/978-3-031-47851-2_17

11. Li, J., Zhang, Q. and Chen, T., 2022. ISWFoam: A Numerical Model for Internal Solitary Wave Simulation in Continuously Stratified Fluids. *Geoscientific Model Development*, 15(1), pp. 105-127. https://doi.org/10.5194/gmd-15-105-2022

12. Rouvinskaya, E.A., Kurkina, O.E. and Kurkin, A.A., 2023. Spatial Distribution of Internal Tidal Waves on the Northeastern Shelf of Sakhalin. *Doklady Earth Sciences*, 509(1), pp. 148-152. https://doi.org/10.1134/S1028334X22601778

13. Lamb, K.G., 1994. Numerical Experiments of Internal Wave Generation by Strong Tidal Flow across a Finite Amplitude Bank Edge. *Journal of Geophysical Research,* 99(C1), pp. 843-864. https://doi.org/10.1029/93JC02514

14. Egbert, G.D. and Erofeeva, S.Y., 2002. Efficient Inverse Modeling of Barotropic Ocean Tides. *Journal of Atmospheric and Oceanic Technology*, 19(2), pp. 183-204. https:/doi.org/10.1175/1520-0426(2002)019<0183:EIMOBO>2.0.CO;2

15. Vlasenko, V., Stashchuk, N. and Hutter, K., 2005. *Baroclinic Tides: Theoretical Modeling and Observational Evidence*. Cambridge: Cambridge University Press, 351 p. https://doi.org/10.1017/CBO9780511535932

16. Rouvinskaya, E.A., Kurkina, O.E. and Kurkin, A.A., 2021. [Particle Transport and Dynamic Effects during of a Baroclinic Tidal Wave Transformation in the Conditions of the Shelf of the Far Eastern Seas]. *Ecological Systems and Devices*, (11), pp. 109-118. https:/doi.org/10.25791/esip.11.2021.1270 (in Russian).

17. Kuznetsov, P.D., Rouvinskaya, E.A., Kurkina, O.E. and Kurkin, A.A., 2021. Transformation of Baroclinic Tidal Waves in the Conditions of the Shelf of the Far Eastern Seas. In: IOP, 2021. *IOP Conference Series: Earth and Environmental Science*. Vol. 946, 012024. https:/doi.org/10.1088/1755-1315/946/1/012024

18. Holloway, P.E. and Barnes, B., 1998. A Numerical Investigation into the Bottom Boundary Layer Flow and Vertical Structure of Internal Waves on a Continental Slope. *Continental Shelf Research*, 18(1), pp. 31-65. https://doi.org/10.1016/s0278-4343(97)00067-8

19. Zulberti, A.P., Jones, N.L., Rayson, M.D. and Ivey, G.N., 2022, Mean and Turbulent Characteristics of a Bottom Mixing-Layer Forced by a Strong Surface Tide and Large Amplitude Internal Waves. *Journal of Geophysical Research: Oceans*, 127(1), e2020JC017055. https://doi.org/10.1029/2020JC017055

20. Kuznetsov, P.D., Rouvinskaya, E.A., Kurkina, O.E. and Kurkin, A.A., 2023. Approximate Estimates of the Force Impact of Baroclinic Flows on Cylindrical Supports in the Conditions of the Sakhalin Shelf. *Ecological Systems and Devices*, (10), pp. 56-66. https://doi.org/10.25791/esip.10.2023.1406 (in Russian).

21. Soontiens, N., Stastna, M. and Waite, M., 2015. Topographically Generated Internal Waves and Boundary Layer Instabilities. *Physics of Fluids*, 27(8), 086602. https://doi.org/10.1063/1.4929344

22. Kuznetsova, M.N. and Plink, N.L., 2018. Methodological Calculations for the Preliminary Evaluation of Sediment Transport Characteristics. In: IO RAS, 2018. *Proceedings of the II Russian National Conference "Hydrometeorology and Ecology: Scientific and Educational Achievements and Perspectives"*. Saint Petersburg: Himizdat, pp. 377-380 (in Russian).

Submitted 29.05.2024; approved after review 11.06.2024;
accepted for publication 20.11.2024.

About the authors:

Ekaterina A. Rouvinskaya, Research Associate, Research Laboratory "Modeling of Natural and Industrial Disasters", Nizhny Novgorod State Technical University n. a. R. E. Alekseev (24, Minina str., 603155, Nizhny Novgorod, Russian Federation), CSc (Phys.-Math.) **ORCID ID: 0000-0002-3858-1731**, **Scopus Author ID: 54789183300**, **ResearcherID: A-2868-2014**, e.rouvinskaya@gmail.com

Oksana E. Kurkina, Leading Research Associate, Research Laboratory "Modeling of Natural and Industrial Disasters", Nizhny Novgorod State Technical University n. a. R. E. Alekseev (24, Minina str., 603155, Nizhny Novgorod, Russian Federation), CSc (Phys.-Math.), Associate Professor, **ORCID ID: 0000-0002-4030-2906**, **Scopus Author ID: 36676379700**, **ResearcherID: G-9577-2011**, Oksana.Kurkina@mail.ru

Andrey A. Kurkin, Vice-Rector for Research, Head of Applied Mathematics Department, Scientific Director of Research Laboratory "Modeling of Natural and Industrial Disasters", Nizhny Novgorod State Technical University n. a. R. E. Alekseev (24, Minina str., 603155, Nizhny Novgorod, Russian Federation), DSc (Phys.-Math.), Professor, Professor of RAS, **ORCID ID: 0000-0003-3828-6406**, **Scopus Author ID: 7003446660**, **ResearcherID: A-1972-2014**, aakurkin@gmail.com

Contribution of the co-authors:

Ekaterina A. Rouvinskaya – carrying out numerical calculations, preparation of the article text and graphic materials, participation in the discussion of the article materials

Oksana E. Kurkina – formulation of the goals and objectives of the study, qualitative and quantitative analysis of research results

Andrey A. Kurkin – scientific supervision, critical analysis and correction of the text

The authors have read and approved the final manuscript.
The authors declare that they have no conflict of interest.

ISSN 1573-160X, *PHYSICAL OCEANOGRAPHY*, Vol. 32, Iss. 1, pp. 116-132 (2025)
Original Russian Text © A. M. Chukharev, 2025,
published in *Morskoy Gidrofizicheskiy Zhurnal*, 2025, Vol. 41, Iss. 1, pp. 83–100

Original article

Non-Stationary Turbulence Model for the Upper Boundary Layer of the Sea

A. M. Chukharev

Marine Hydrophysical Institute of RAS, Sevastopol, Russian Federation
✉ *alexchukh@mail.ru*

Abstract
Purpose. The purpose of the study is to develop the physical concepts of dynamic interaction of two media on small and submesoscales, as well as to create an objective model for describing the turbulent regime of the sea near-surface layer.
Methods and Results. Significant scales of turbulence energy supply are established, and a non-stationary numerical model of turbulent exchange in the near-surface layer of the sea is proposed based on the large arrays of experimental data on marine turbulence intensity under different hydrometeorological conditions. Four basic generation mechanisms are considered as the sources of turbulence, namely drift current velocity shear, surface waves and their breakings, and submesoscale eddy structures. The influence of the latter is assessed through the structural function calculated using the synchronous measurements of current velocity in two points. The numerical solutions for velocity profiles, turbulence energy, and dissipation rate are compared to the experimental data, at that the necessary model constants are selected. Verification of the calculations has shown their good agreement with the measurements in a fairly wide range of wind speeds including the weak winds for which the other models yield the significantly lower results as compared to the experimental data.
Conclusions. A non-stationary model is proposed for calculating the turbulence characteristics in the upper mixed layer of the sea. The application of structural function in the turbulent energy balance equation improves the agreement between model calculations and experimental data. The developed model quite reliably describes the turbulent structure of the layer under study and permits to calculate the intensity of vertical turbulent exchange in different hydrometeorological conditions.

Keywords: sea turbulence, near-surface layer, turbulence generation mechanisms, structural function, non-stationary model of turbulence, dissipation rate, experimental data

Acknowledgements: Experimental studies and data preprocessing were carried out within the framework of theme of state assignment of FSBSI FRC MHI FNNN-2021-0004 "Oceanological processes". Data analysis, and model development and verification were performed with financial support of RSF grant 22-17-00150.

For citation: Chukharev, A.M., 2025. Non-Stationary Turbulence Model for the Upper Boundary Layer of the Sea. *Physical Oceanography*, 32(1), pp. 116-132.

Introduction

Air-sea interaction is one of the most important problems in the field of Earth sciences. The wide variety of physical processes occurring in both environments near the interface and their complex interrelations significantly complicate the development of reliable models describing the structure of the boundary layers. A large number of studies in this area have made it possible to achieve certain progress in studying the mechanisms of atmosphere-ocean exchange and to develop useful models for predicting certain physical characteristics in the atmospheric surface layer and in the near-surface layer of the sea. Nevertheless, the dynamic air-sea interaction remains an area of insufficient study in climate and weather theory, since the models developed to date often show significant discrepancies between the results of calculations and actual data, such as ocean surface temperature and mixed layer thickness [1].

A constituent part of this problem is a reliable description of the intensity of vertical turbulent exchange in the upper boundary layer of the sea. The ocean layer bordering the atmosphere experiences dynamic and other effects in a wide range of scales. This leads to the emergence of various processes that affect the turbulent exchange in this layer, such as drift currents, surface waves, Langmuir circulations, etc. The generation of turbulence by these mechanisms depends on the specific hydrometeorological situation and varies widely, thereby complicating the theoretical description. The mixing intensity in this context is strongly dependent on the tangential wind stress, the nature of waves, the presence of breaking waves, and the vertical stratification of the layer.

Vertical turbulent exchange plays a significant role in the formation of temperature fields, salinity, and other dissolved chemical substances in the water column. Furthermore, its effects on the rate of the sea's response to various natural and anthropogenic impacts have been demonstrated. Many hydrological structure features can be explained based on information about the mechanisms of vertical exchange, their intensity, and their spatial and temporal variability.

Sea surface processes, the relationship between surface gravity waves, wind, and currents in adjacent boundary layers play a key role in the global climate system [2]. Modern studies of turbulence in the upper ocean layer are aimed primarily at clarifying the role of individual mechanisms of turbulence generation in various hydrometeorological conditions, with a focus on storm conditions and light winds. This is due to the fact that existing models demonstrate a poor correspondence to *in situ* measurements in these wind speed ranges.

The most significant mechanisms of turbulence generation in the upper ocean layer include the instability of vertical velocity gradients in drift currents, the instability of motions induced by surface waves, and wave breaking [1]. In a number of models, one or two mechanisms are often given priority, which does not allow for a sufficiently accurate description of the turbulent regime [3–6]. These are either a current velocity shift, surface waves, or wave breaking in conjunction with a velocity shift. In the multiscale model [7], all three of the aforementioned generation mechanisms are considered; however, in a number of cases, the model does not provide good agreement with the experimental results. One potential reason for this is an incomplete understanding of the turbulence sources in the layer under consideration.

The paper [8] examines the structure of the ocean surface boundary layer in the presence of Langmuir turbulence and stabilizing surface heat fluxes. Diagnostic models are proposed for the equilibrium boundary layer and the mixed layer depth in the presence of surface heating. The study of differences in measurements from a fixed base and from drifters on the ocean surface using

[1] Monin, A.S. and Ozmidov, R.V., 1985. *Turbulence in the Ocean*. Dordrecht, Boston, Lancaster: D. Reidel Publishing Company, 248 p. (Environmental Fluid Mechanics Series, vol. 3).

structure functions is carried out in [9]. The calculation of the first, second, and third order structure functions uses quasi-Lagrange (drifter) and Euler data.

In the context of modeling the intensity of vertical turbulent exchange in the near-surface layer of the sea, a notable discrepancy was observed between the calculated and measured values of the turbulent energy dissipation rate. This discrepancy was particularly evident in conditions of low winds and small waves. In such instances, the experimental values could exceed those calculated by the models [3–7] by two orders of magnitude or more. It is estimated that this phenomenon arises due to local instabilities in the main horizontal current, since the Reynolds number in such currents is three to four orders of magnitude higher than the critical number [2]. It is proposed that taking this mechanism and instabilities associated with coherent structures into account will improve the reliability of model calculations.

The purpose of the present study is to develop a physical conceptualization of the dynamic interaction between two media on small and submesoscales, as well as to construct an objective model for describing the turbulent regime of the sea near-surface layer.

Experiments and *in situ* data

For several years, the staff of Marine Hydrophysical Institute of RAS (MHI) Turbulence Department have been carrying out experimental studies of near-surface turbulent mixing processes. These experiments are performed at the stationary oceanographic platform of MHI Black Sea Hydrophysical Subsatellite Polygon. The data collection system includes a wide range of measuring instruments: including meteorological parameter meters to measure wind speed and direction, a string wave recorder, current velocity meters (acoustic and spinner type), CTD meters, a Sigma-1 positional turbulimeter [10], and others (Fig. 1). Such a data set enables to record the necessary parameters of background and fluctuation quantities and obtain an objective representation of hydrophysical fields' variability over relatively extended periods of time. The collected *in situ* data is used to verify model estimates of the vertical distribution of hydrological quantities and turbulence intensity (turbulent energy dissipation rate ε).

Since the Sigma-1 turbulimeter can only measure current velocity fluctuations with a frequency higher than 0.1 Hz, slower oscillations, which ultimately affect the turbulent energy dissipation rate, are preferably recorded by meters with appropriate discreteness. In the present paper, the main emphasis was placed on the spectral and structural analysis of current velocity data obtained by acoustic meters at two points, 1 and 5 (Fig. 1), spaced approximately 10 m apart, and velocity vector fluctuation data measured by the Sigma-2 complex (Fig. 1). The remaining devices provided information on background hydrometeorological parameters and sea surface conditions. The duplication of individual measuring devices allowed for verification of the recorded values and elimination of gaps in the data series resulting from device failures. The configuration of the data collection system changed slightly during the course of different expedition periods.

[2] Even if we are limited to a horizontal scale of 100 m ($U \sim 0.1$ m/s; $L \sim 10^2$ m; $\nu \sim 10^{-6}$ m^2/s, $\mathrm{Re} \sim 10^7$; while $\mathrm{Re}_{cr} \sim 2 \cdot 10^3$).

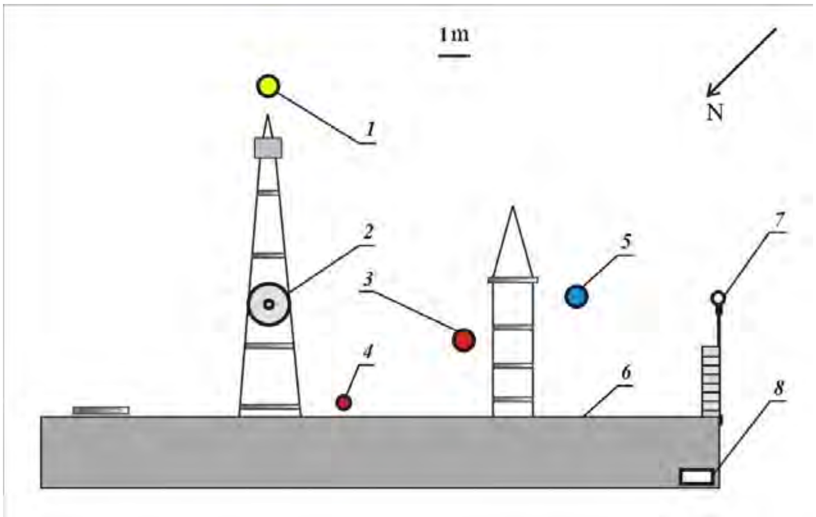

F i g. 1. Layout of the basic measuring systems at the oceanographic platform during the experiments in May – June, 2021: *1* – DVS-6000 acoustic Doppler profiler; *2* – Sigma-1 measuring system; *3* – Vostok-M current velocity meter; *4* – MHI-1308 current meters (4 pcs.); *5* – Workhorse Monitor acoustic Doppler profiler; *6* – oceanographic platform; *7* – string wave recorder; *8* – meteorological system

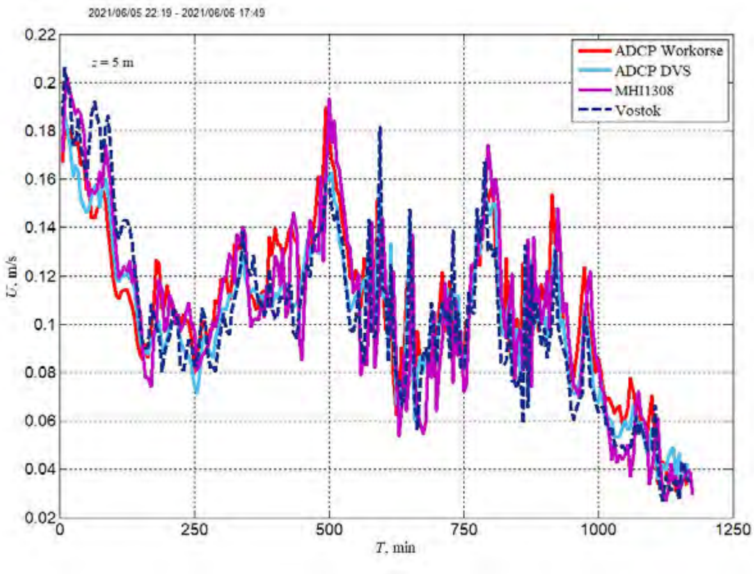

F i g. 2. Mean current velocity module based on measurements by various instruments at the 5 m depth in the area of the oceanographic platform on June 5–6, 2021. The data are reduced to a resolution of 5 min

The results of measurements obtained using different devices were subjected to preliminary processing and primary analysis. This process entailed the removal of faulty sections and implausible values. The sections of records selected for analysis were synchronized and reduced to the same level of discretization for joint processing. Figure 2 shows an example of synchronized and reduced to a single scale data on the current velocity module obtained by measuring simultaneously using different devices (acoustic and spinner) at different points. The averaged data analysis showed that the difference in the values of the current velocity module obtained from measurements conducted using acoustic complexes does not exceed 5%.

In addition to spectral and structural analysis of the measured values, wavelet analysis was used for more accurate identification of synchronous (asynchronous) variability in the current field and coherent structures. Specifically, wavelet analysis permits to identify the energy distribution of the measured values by scale and track its evolution [11]. The continuous wavelet transformation was used

$$W(a,b) = |a|^{-1/2} \int_{-\infty}^{\infty} \xi(t)\varphi\left(\frac{t-b}{a}\right)dt,$$

where W denotes the wavelet coefficients, a is the wavelet transformation scale, b indicates the time shift, ξ is the initial signal, φ is the mother wavelet, and t is the time. The Morlet wavelet was predominantly used as the mother wavelet:

$$\varphi(t) = \exp\left(-\frac{t^2}{2}\right)\cos(rt).$$

The global energy spectrum in wavelet analysis is an analogue of the power spectrum in harmonic analysis. It is generally accepted that this technique reliably reveals spectral peaks; however, it is inferior to the Fourier transform in terms of spectral resolution. The global spectrum was calculated using the following formula:

$$S(a) = \frac{1}{n}\sum_{i=0}^{n-1} |W_i(a)|^2 ,$$

where n denotes the number of readings in a row.

Basic relationships

The representation of turbulent flows as a set of eddies resulting from the successive decay of large ones into smaller ones, which in turn decay down to the smallest ones, dissipating into heat, has been confirmed in numerous experimental works. One of the most important theoretical assumptions in describing turbulence is A.N. Kolmogorov's hypothesis on the inertial interval existence in the turbulence spectrum [12]. He demonstrated that the structural function of velocity fluctuations is described by the universal dependence $D \sim l^{2/3}$, where l denotes the distance between two measurement points. This dependency is independent of the selection of the origin of coordinates, owing to the statistical homogeneity of velocity fluctuations, and is not influenced by the direction of the spacing of the points. However, it depends on the l value, which is the result of the statistical isotropy of turbulence. For the velocity vector components directed along l (longitudinal structural function),

$$D_{ll} = \overline{\left[u_l(r) - u_l(r+l)\right]^2} = C_v^2 l^{2/3}. \quad (1)$$

Here, C_v^2 is the structural parameter characterizing the transformation rate of eddy energy per unit mass. The temperature structural parameter (often referred to as a "structural feature") C_T^2 is calculated in a similar way based on the temperature difference at two points or the structural parameter of the refractive index in the atmosphere C_n^2 [13]. The calculation of structural functions and determination of structural parameters enables the assessment of the turbulence intensity level caused by the energy influx from local and coherent eddies in sea currents. According to Kolmogorov's theory, the structural parameter is associated with the dissipation rate of turbulent energy, and in the inertial range of the turbulence spectrum $C_v^2 = c\varepsilon^{2/3}$, where c is a constant [3].

Taking into account Taylor's "frozen turbulence" hypothesis, the structure function is also calculated from measurements at a specific point, thereby introducing the τ time shift:

$$D_u(\tau) = \overline{\left[u(t+\tau) - u(t)\right]^2} = C_\tau^2 \tau^\alpha, \ 0 < \alpha < 2. \quad (2)$$

The presence of structures in a turbulent flow is evidenced by a noticeable increase in the structural parameter when measured at fixed points. The scale of such eddy formations can be determined from the structural parameter spectrum.

In order to calculate the turbulence intensity and its change with depth in the near-surface layer of the sea, a non-stationary model has been developed [14]. This model is based on the equations of the balance of momentum and turbulent kinetic energy. However, as noted earlier [7, 14], there is a considerable discrepancy between the calculations and experimental data at low winds and slight waves in almost all of the models. In addition, the turbulence generation in the mean transport current is not considered.

In order to account for the impact of coherent structures and the transformation of kinetic energy of the current into turbulence due to local velocity shifts, this paper proposes to introduce an additional term $\frac{\partial D_{ll}}{\partial t}$ into the turbulent kinetic energy balance equation. This term describes turbulence generation by these eddy formations. In this form (variation in the structural function over time), the term is expressed in terms of the correspondence to the dimension (m^2/s^3). The physical meaning of this term is the description of the energy influx to turbulence in the turbulent energy balance equation due to inhomogeneity of the current.

The system of initial equations is expressed as follows:

[3] Monin, A.S. and Yaglom, A.M., 1975. *Statistical Fluid Mechanics: Mechanics of Turbulence*. Vol. 2. Cambridge, Massachusetts: MIT Press, 874 p.

$$\frac{\partial U}{\partial t} = fV - \frac{\partial(\overline{u'w'})}{\partial z}, \tag{3}$$

$$\frac{\partial V}{\partial t} = -fU - \frac{\partial(\overline{v'w'})}{\partial z}, \tag{4}$$

$$\frac{\partial E}{\partial t} = -\left(\overline{u'w'}\frac{\partial U}{\partial z} + \overline{v'w'}\frac{\partial V}{\partial z}\right) - \frac{\partial}{\partial z}\left(\overline{w'E} + \overline{w'E^w} + \frac{1}{\rho_0}\overline{w'p'}\right) + \frac{\partial D_{ll}}{\partial t} - \varepsilon, \tag{5}$$

where U and V are the average horizontal velocity components along the x and y axes, respectively; f is the Coriolis parameter; u', v', w' are the fluctuating velocity components; $E = \frac{(\overline{u'^2} + \overline{v'^2} + \overline{w'^2})}{2} = \frac{q^2}{2}$ is the turbulent kinetic energy; E^w is the energy of surface waves; p' are the pressure fluctuations; and ε is the dissipation rate. The system is closed through the relations linking the turbulent momentum flows with the turbulent viscosity coefficient:

$$\overline{u'w'} = -\nu_t\frac{\partial U}{\partial z}, \quad \overline{v'w'} = -\nu_t\frac{\partial V}{\partial z}, \quad \nu_t = S_m lq, \quad \varepsilon = \frac{q^3}{Bl}, \tag{6}$$

where ν_t is the turbulent viscosity coefficient; S_m is a constant; l is the turbulent length scale; and ε is the dissipation rate. The l scale depends on the depth as $l = \kappa(z + z_b)$; z is the depth; z_b is the reciprocal wave number of the shortest breaking waves [6]; κ is the von Kármán constant; and the B constant = 16.6.

The initial and boundary conditions, as well as the solution method, remain the same as in [14]. At the upper boundary,

$$E_0 = \alpha_1 u_*^{w2}, \qquad \nu_t\frac{\partial U}{\partial z} = \frac{\tau_0}{\rho^w}, \qquad \tau_0 = \rho^w u_*^{w2}, \qquad \nu_t\frac{\partial V}{\partial z} = 0, \tag{7}$$

at the lower boundary,

$$U = 0, \quad V = 0, \quad \frac{\partial E}{\partial z} = 0. \tag{8}$$

The D_{ll} structural function in the model is parameterized by a conventional harmonic function that incorporates empirical data. The written system of equations (3)–(8) was solved numerically by the sweep method.

Results

Relatively large coherent structures in the near-surface layer are observed in the energy turbulence spectra. An example of the Fourier spectrum of the root-mean-square velocity fluctuations $w_f = \sqrt{\overline{w'^2}}$ averaged over 5 min is shown in Fig. 3. The initial data were obtained at 100 Hz discreteness and then processed with a high-pass filter with a threshold of 1 Hz to remove fluctuations associated with surface waves. The spectra were constructed using the Welch method, where the time series is divided into overlapping segments, multiplied by the Hann time window, Fourier transformed, and then the spectral functions are averaged over all segments.

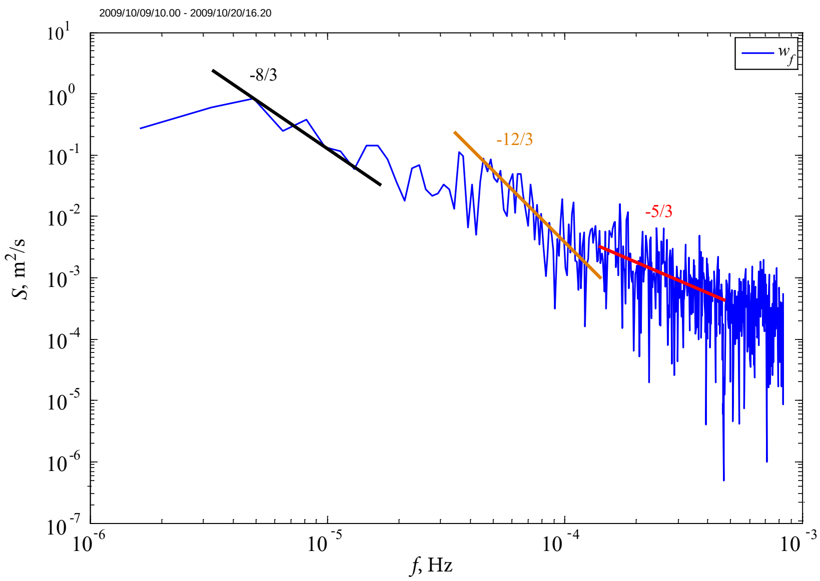

F i g. 3. Spectrum of filtered root-mean-square velocity fluctuations with 5-min averaging in the area of the oceanographic platform based on the measurement data obtained on October 9–20, 2009

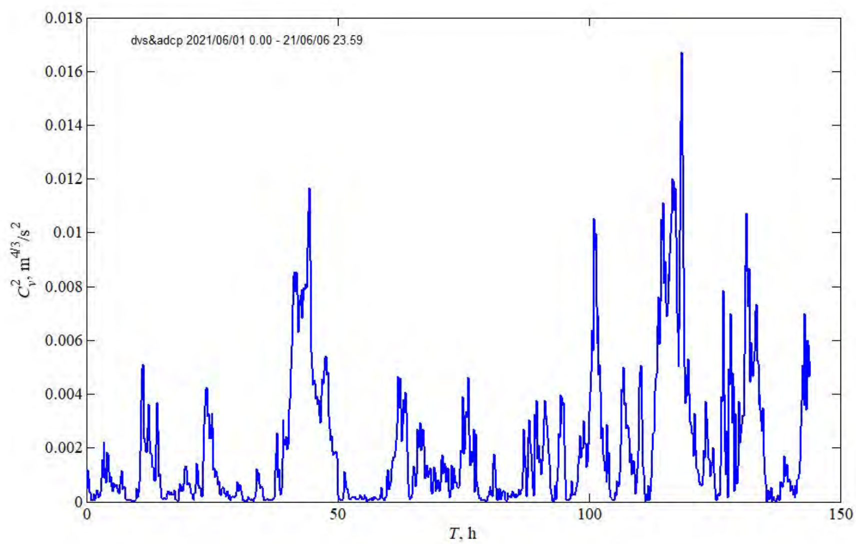

F i g. 4. Longitudinal structural parameter of current velocity fluctuations with 10-min averaging at the 5 m depth in the area of the oceanographic platform on June 1–6, 2021

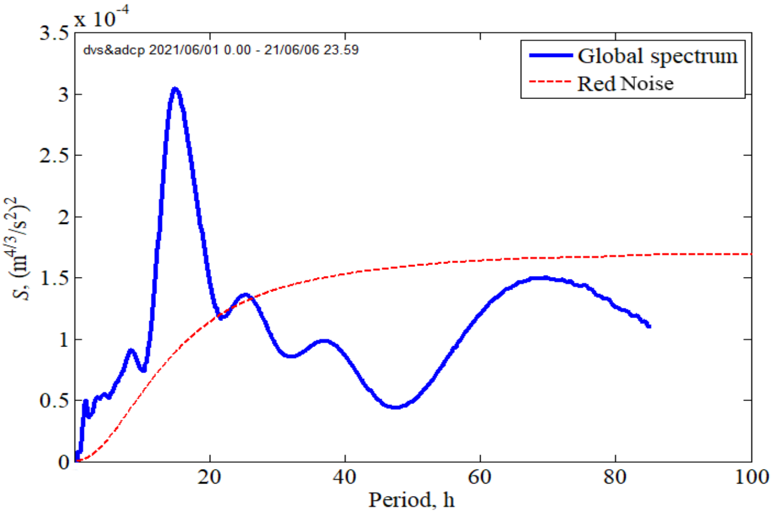

F i g. 5. Global spectrum of structural parameter C_v^2 for June 1–6, 2021

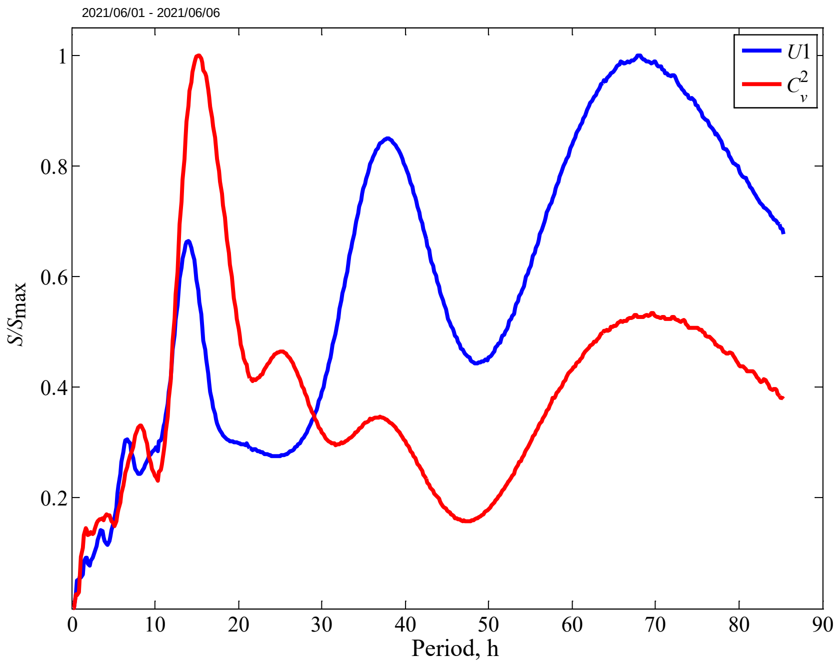

F i g. 6. Normalized global spectra of the current velocity module and structural parameter for June 1–6, 2021

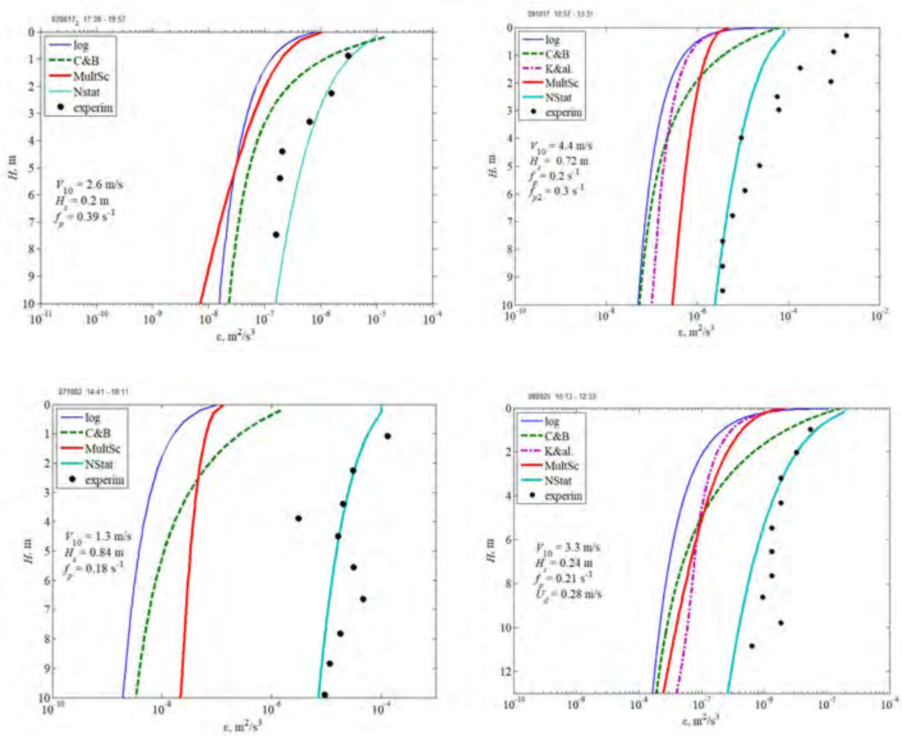

F i g. 7. Model and experimental values of the turbulent energy dissipation rate at low wind. Designations: log is wall turbulence model [4], C&B is model [5], K&al. is model [6]; MultSc is multiscale model [7]; NStat is improved non-stationary model, points are experimental data, V_{10} is wind speed at the 10 m height, H_S is height of significant waves, f_p is frequency of wave spectral peak, U_d – current velocity

As illustrated in the above figure, the spectrum exhibits a complex shape with various slopes across different ranges. Studies of atmospheric turbulence [13, 15] have demonstrated that coherent turbulence differs from Kolmogorov turbulence by a faster decrease in the spectrum (sections with −8/3 and −12/3 slope), i.e., the presence of such sections in our data indicates the existence of coherent structures.

The principal data array selected for the analysis of synchronous measurements of horizontal current velocity at spaced points and the calculation of structural functions was obtained during the active operational period (01 June 2021 – 06 June 2021) by the *DVS*-6000 and *WorkHorse Monitor* complexes (3 and 8 in Fig. 1). A fragment of the records is presented above in Fig. 2. The structural functions were calculated using relations (1) and (2), with the time shift varying from 5 min to 1 h in the latter case. The variability of the C_v^2 longitudinal structural parameter for the specified period is shown in Fig. 4, and the global spectrum calculated using wavelet analysis is shown in Fig. 5.

Figure 5 shows a clearly expressed maximum in the spectrum at a period of ~ 15 h. This indicates that such structures predominate over a time span of several days. However, when examining shorter intervals, particularly intra-day fluctuations in the intensity of velocity fluctuations, scales with the 1.5- and 3.5-hour periods are clearly visible. It is noteworthy that maxima exceeding the "red noise" level are considered significant in the global spectrum. The current velocity spectrum differs from the spectrum of the structural parameter. As illustrated in Fig. 6, which shows the C_v^2 global spectrum normalized to its maximum value and the current velocity spectrum calculated from the velocity modulus values, the contribution of currents to turbulence on larger time scales (peaks at ~ 40 and ~ 70 h) is significantly lower than on the 15-hour scale. This is evident from the spectral function level.

The MHI Turbulence Department staff has been conducting experimental observations on the oceanographic platform for a number of years, thus accumulating extensive arrays of data on the turbulent regime of the near-surface layer under various hydrometeorological conditions. The data, which include measurements of the vertical distribution of the turbulent energy dissipation rate, provide a valuable opportunity to verify various models across a range of wind speeds and wave types. As previously mentioned, a notable shortcoming in the modeling of vertical turbulent exchange in the near-surface layer is the discrepancy between calculated and measured values of the dissipation rate at weak winds. A comparison of calculations using the improved model and natural data demonstrated that this issue is largely solved by the proposed method of incorporating additional turbulization of the layer using the structural function.

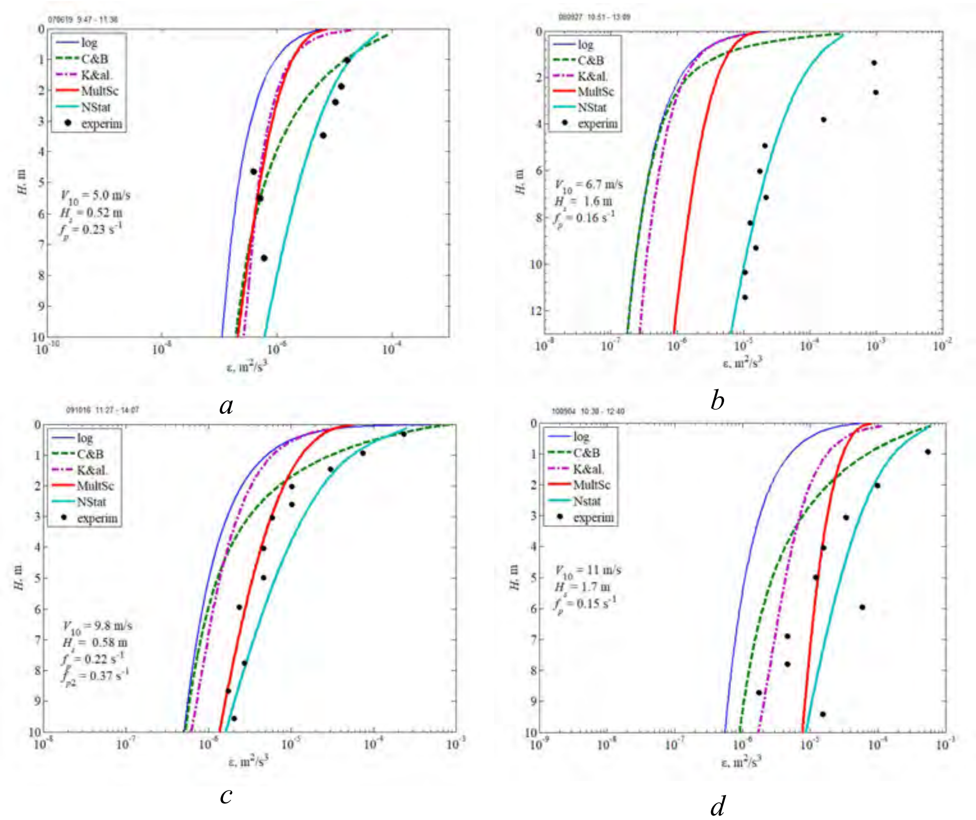

F i g. 8. Model and experimental values of the rate of turbulent energy dissipation at moderate (*a*, *b*) and strong (*c*, *d*) winds. The designations are the same as in Fig. 7

Figure 7 shows experimental data on the dissipation rate for weak winds along with the results of calculations using various models, including the improved non-stationary model discussed in this paper. A concise overview of the models used for comparison is provided in the Appendix. The figures indicate that the incorporation of an additional source of turbulence, represented by the structure function, significantly improves the agreement between the calculations and *in situ* measurements. Figure 8 showcases examples of calculations and experimental data for moderate and high winds. In the interest of illustration, preference was given to cases where other models did not align well with the experiments. The agreement between the data of the proposed model and the measurement results under such conditions is also quite satisfactory.

Discussion

According to modern concepts, in turbulent shear flows, the transfer of momentum, energy, and other quantities are predominantly determined by large-scale eddy motion rather than by chaotic small-scale motion. Large formations that emerge in turbulent flows are classified as coherent structures, also referred to as deterministic. According to the definition outlined in the work [16, p. 307], "*A coherent structure is a connected turbulent fluid mass with instantaneously phase-correlated vorticity over its spatial extent*". The necessity of parameterizing these structures is justified by the fact that they are able to transfer up to 80% of the total energy of a turbulent current [4]. In experimental data, it is quite difficult to differentiate between coherent and incoherent turbulence, since small-scale turbulence (by Kolmogorov) is also present in the coherent structures. The spectrum shown above (Fig. 3) contains sections that quite accurately correspond to the results of work [15]. Our measurements confirm the complex nature of the turbulent current and the presence of coherent structures within the studied layer. Consequently, the description of turbulent exchange requires additional consideration of this phenomenon. In our estimation, the calculated spectral function provides a reasonably objective characterization of the intensity of turbulence caused by local instabilities in sea currents within the coastal zone.

As illustrated in Fig. 5, structures with specific scales can dominate under certain conditions, thereby enabling the utilization of a model representation of the structural function with a relatively simple dependence at this stage. In this paper, the influence of coherent structures on the turbulence generation is parameterized by a harmonic function with an amplitude and period determined from the experimental values of the longitudinal structural function (Fig. 4). The current is assumed to be uniform along the vertical. The origin and evolution of such structures in the experimental zone require further study. However, it is highly probable that

---

[4] Garbaruk, A.V., Strelets, M.H. and Shur, M.L., 2012. [*Modeling of Turbulence in Complex Flows Calculations: Textbook*]. Saint Petersburg: Publisher of Polytechnic University, 88 p. (in Russian).

the formation of eddies in the coastal zone of Crimea is similar to the scheme proposed in [17]. Based on our estimates, the spatial scales of eddy formations that significantly affect the generation of turbulence range from several hundred meters to 4–6 km.

As previously stated, the prevalent models for describing vertical turbulent exchange in the upper boundary layer of the sea diverge greatly from observational data in weak and strong winds. Conversely, in moderate winds the models work quite satisfactorily. In our experiments with low winds the discrepancies between the calculation results obtained from different models and the measurement data could reach two orders of magnitude or more [7]. The implementation of the enhanced non-stationary model has improved the agreement between the model data and the experimental results under such weather conditions (Fig. 7).

Importantly, the experimental data presented were collected in different years and seasons, but in the overwhelming majority of experiments the discrepancies between these data and the model data were insignificant. For moderate and strong winds, the model also agrees well with the field measurements (see Fig. 8), and the model constant for the structural function is found to be quite universal, and the model functions well in about 80% of the cases considered. The model values are overestimated at low current velocities of 0.02–0.07 m/s, and underestimated in some cases under storm conditions. The reasons for the discrepancy require a separate analysis of the whole complex of hydrological and meteorological conditions. Thus, it can be tentatively concluded that the influence of coherent structures in the layer turbulence becomes predominant at weak winds, while at moderate and storm winds, their relative contribution to the generation of turbulence in the uppermost layer of the sea decreases.

Conclusion

Insufficient description of the complex exchange processes in the upper boundary layer of the sea gives rise to inaccuracies in forecasting such critical parameters as the mixed layer depth and the ocean surface temperature. In the climate models currently in use, a limited number of turbulence generation mechanisms are considered. These mechanisms determine the intensity of vertical mixing, which often leads to significant differences between the results of calculations and measurement data.

In this paper, an improved approach to vertical exchange description in the near-surface layer of the sea is proposed. This approach involves the incorporation of a term into the turbulent energy balance equation, which describes the generation of turbulence by coherent structures formed in the mean current. The physical substantiation of this approach is rooted in the idea of turbulence generation by local instabilities in the fluid flow at high Reynolds numbers and the shear effects on relatively large-scale eddy structures. The implementation of the structural function concept as a characteristic of the transformation of current energy into turbulence has yielded a highly encouraging result, significantly improving the agreement between the outcomes of calculations and experiments across a broad spectrum of hydrometeorological conditions. The quantitative assessment of the structural function and the structural parameter is founded on the synchronous measurement of current velocity using acoustic meters at horizontally spaced locations. The global spectrum of the structural parameter calculated using wavelet analysis revealed a dominant period of turbulence generation intensity fluctuations. This fluctuation period is apparently associated with the existence of coherent structures of the corresponding scale in coastal sea currents. The experimental data on the temporal variability of the structural function are parameterized by a harmonic function built into the model.

The proposed model was used to conduct calculations, which indicated a significant improvement in the correlation between the calculated results and the experimental data at low winds. The generation of turbulence by the current velocity shift and surface waves is negligible at these wind speeds. Additionally, the model demonstrated a strong agreement with *in situ* data at moderate and high winds.

Appendix
Turbulence models used for comparison with the non-stationary model proposed

1. In the model proposed in [4], the assumption is made that turbulence under the ocean surface is similar to turbulence near a solid wall. The rate of turbulent energy dissipation in this case is calculated according to the following formula:

$$\varepsilon = u_*^3 / \kappa z,$$

where $u_* = \sqrt{\tau / \rho}$ is the friction velocity in water; κ is the von Kármán constant; z is the depth. However, as previously mentioned in [4], the application of such an analogy requires the precise selection of the zero surface to filter out small irregular waves. Additionally, the correct averaging of the measured values is essential to obtain the structure of the mean current, similar to the turbulent boundary layer near a flat plate. This model is frequently called logarithmic, according to the velocity change law in a turbulent flow near a solid boundary.

2. One of the most well-known models of turbulence in the near-surface layer was developed in [5], where Prandtl's hypothesis on the mixing path is used to close the system of equations. This model demonstrates strong agreement with both natural and laboratory experiments [18, 19], and the results are found to be significantly influenced by the value of the z_0 roughness parameter and the choice of the l turbulence scale. The layer near the surface with an increased dissipation rate was interpreted as a consequence of the turbulent energy flow from waves through the surface.

In this model, the dissipation rate and kinetic energy of turbulence are defined as follows:

$$\varepsilon = q^3 / Bl, \qquad k = \frac{q^2}{2},$$

where q is the rate scale; l is the length scale; $B = 16.6$ is a constant; $l = \kappa\,(z + z_0)$, z is the depth, z_0 is the roughness parameter in water, κ is the von Kármán constant. The model yields both asymptotic analytical and numerical solutions. The dissipation rate is analytically expressed as follows:

$$\varepsilon = \varepsilon_{sh} + \varepsilon_{wv} = \frac{u_*^3}{B\kappa(z+z_0)}\left[\left(\frac{B}{S_M}\right)^{\frac{3}{4}} + \alpha\left(\frac{3B}{S_q}\right)^{\frac{1}{2}}\left(\frac{z_0}{z_0+z}\right)^{n}\right], \quad n = \left(\frac{3}{k^2 B S_q}\right)^{\frac{1}{2}} = 2.4\,,$$

$$S_M = 0.39, \quad S_q = 0.2.$$

To date, this model is the most widely used to describe turbulence near the sea surface and to compare with field and laboratory experiments.

3. In the Kudryavtsev et al. model [6], the velocity shift and wave breaking, including microbreaks, are identified as sources of turbulent energy in the near-surface layer of the sea. Breaking is considered as a volumetric source of energy and momentum, depending on the spectral composition of surface waves. The equation of turbulent energy balance is proposed to be neglected in this model, in contrast to the model from [5]. The z_0 roughness parameter in the surface layer is not included in this model. Numerical calculations using it showed quite satisfactory agreement with the experimental results from [20].

4. The multiscale turbulence model developed in [7] is based on the division of the turbulence spectrum into sections, where turbulence is generated by different mechanisms. For each section, a corresponding system of equations is compiled based on the k-ε model. The turbulence sources are the shift in the drift current velocity, nonlinear effects of surface waves and their breaking. Original parameterizations are proposed for the last two generation mechanisms, and the existence of turbulent diffusion of wave kinetic energy is also estimated. The model demonstrates good agreement across a broad spectrum of hydrometeorological conditions, both in terms of its own natural data and that of other researchers. Notably, the advantages of this model become particularly evident in storm conditions, setting it apart from other similar models.

REFERENCES

1. Belcher, S.E., Grant, A.L., Hanley, K.E., Fox-Kemper, B., Van Roekel, L., Sullivan, P.P., Large, W.G., Brown, A., Hines, A. [et al.], 2012. A Global Perspective on Langmuir Turbulence in the Ocean Surface Boundary Layer. *Geophysical Research Letters*, 39(18), L18605. https://doi.org/10.1029/2012GL052932

2. Sullivan, P.P. and McWilliams, J.C., 2010. Dynamics of Winds and Currents Coupled to Surface Waves. *Annual Review of Fluid Mechanics,* 42, pp. 19-42. https://doi.org/10.1146/annurev-fluid-121108-145541

3. Csanady, G.T., 1984. The Free Surface Turbulent Shear Layer. *Journal of Physical Oceanography*, 14(2), pp. 402-411. https://doi.org/10.1175/1520-0485(1984)014<0402:TFSTSL>2.0.CO;2
4. Benilov, A.Yu. and Ly, L.N., 2002. Modelling of Surface Waves Breaking Effects in the Ocean Upper Layer. *Mathematical and Computer Modelling*, 35(1-2), pp. 191-213. https://doi.org/10.1016/S0895-7177(01)00159-5
5. Craig, P.D. and Banner, M.L., 1994. Modelling of Wave-Enhanced Turbulence in the Ocean Surface Layer. *Journal of Physical Oceanography*, 24(12), pp. 2546-2559. https://doi.org/10.1175/1520-0485(1994)024<2546:MWETIT>2.0.CO;2
6. Kudryavtsev, V., Shrira, V., Dulov, V. and Malinovsky, V., 2008. On the Vertical Structure of Wind-Driven Sea Currents. *Journal of Physical Oceanography*, 38(10), pp. 2121-2144. https://doi.org/10.1175/2008JPO3883.1
7. Chukharev, A.M., 2013. Multitime Scale Model of Turbulence in the Sea Surface Layer. *Izvestiya, Atmospheric and Oceanic Physics*, 49(4), pp. 439-449. https://doi.org/10.1134/S0001433813040026
8. Pearson, B.C., Grant, A.L.M., Polton, J.A. and Belcher, S.E., 2015. Langmuir Turbulence and Surface Heating in the Ocean Surface Boundary Layer. *Journal of Physical Oceanography*, 45(12), pp. 2897-2911. https://doi.org/10.1175/JPO-D-15-0018.1
9. Pearson, J., Fox-Kemper, B., Pearson, B., Chang, H., Haus, B.K., Horstmann, J., Huntley, H.S., Kirwan, A.D., Lund, B. [et al.], 2020. Biases in Structure Functions from Observations of Submesoscale Flows. *Journal of Geophysical Research: Oceans*, 125(6), e2019JC015769. https://doi.org/10.1029/2019JC015769
10. Samodurov, A.S., Dykman, V.Z., Barabash, V.A., Efremov, O.I., Zubov, A.G., Pavlenko, O.I. and Chukharev, A.M., 2005. “Sigma-1” Measuring Complex for the Investigation of Small-Scale Characteristics of Hydrophysical Fields in the Upper Layer of the Sea. *Physical Oceanography*, 15(5), pp. 311-322. https://doi.org/10.1007/s11110-006-0005-1
11. Astaf’eva, N.M., 1996. Wavelet Analysis: Basic Theory and Some Applications. *Advances in Physical Sciences*, 39(11), pp. 1085-1108. https://doi.org/10.1070/PU1996v039n11ABEH000177
12. Kolmogorov, A.N., 1968. Local Structure of the Turbulence in an Incompressible Viscous Fluid at Very High Reynolds Numbers. *Soviet Physics Uspekhi,* 10(6), pp. 734-736. https://doi.org/10.1070/PU1968v010n06ABEH003710
13. Nosov, V.V., Kovadlo, P.G., Lukin, V.P. and Torgaev, A.V., 2012. Atmospheric Coherent Turbulence. *Atmospheric and Oceanic Optics*, 26(3), pp. 201-206. https://doi.org/10.1134/S1024856013030123
14. Chukharev, A.M. and Pavlov, M.I., 2024. Turbulent Exchange in Unsteady Air–Sea Interaction at Small and Submesoscales. *Izvestiya, Atmospheric and Oceanic Physics*, 60(1), pp. 87-94. https://doi.org/10.1134/S0001433824700105
15. Lukin, V.P., Nosov, E.V., Nosov, V.V. and Torgaev, A.V., 2016. Causes of Non-Kolmogorov Turbulence Manifestation in the Atmosphere. *Applied Optics*, 55(12), pp. B163-B168. https://doi.org/10.1364/AO.55.00B163
16. Hussain, A.K.M.F., 1986. Coherent Structures and Turbulence. *Journal of Fluid Mechanics*, 173, pp. 303-356. https://doi.org/10.1017/S0022112086001192
17. Zatsepin, A.G., Piotukh, V.B., Korzh, A.O., Kukleva, O.N. and Soloviev, D.M., 2012. Variability of Currents in the Coastal Zone of the Black Sea from Long-Term Measurements with a Bottom Mounted ADCP. *Oceanology*, 52(5), pp. 579-592. https://doi.org/10.1134/S0001437012050177

18. Agrawal, Y.C., Terray, E.A., Donelan, M.A., Hwang, P.A., Williams III, A.J., Drennan, W.M., Kahma, K.K. and Kitaigorodskii, S.A., 1992. Enhanced Dissipation of Kinetic Energy beneath Surface Waves. *Nature*, 359, pp. 219-220. https://doi.org/10.1038/359219a0
19. Cheung, T.K. and Street, R.L., 1988. The Turbulent Layer in Water at an Air-Water Interface. *Journal of Fluid Mechanics*, 194, pp. 133-151. https://doi.org/10.1017/S0022112088002927
20. Terray, E.A., Donelan, M.A., Agrawal, Y.C., Drennan, W.M., Kahma, K.K., Williams III, A.J., Hwang, P.A. and Kitaigorodskii, S.A., 1996. Estimates of Kinetic Energy Dissipation under Breaking Waves. *Journal of Physical Oceanography*, 26(5), pp. 792-807. https://doi.org/10.1175/1520-0485(1996)026<0792:EOKEDU>2.0.CO;2

Submitted 03.09.2024; approved after review 10.10.2024;
accepted for publication 20.11.2024.

About the author:

Alexandr M. Chukharev, Chief Research Associate, Marine Hydrophysical Institute of RAS (2 Kapitanskaya Str., Sevastopol, 299011, Russian Federation), DSc (Phys.-Math), **ORCID ID: 0000-0003-1078-6425**, **Scopus Author ID: 6603038462**, **ResearcherID: G-3180-2013**, alexchukh@mail.ru

The author has read and approved the final manuscript.
The author declares that he has no conflict of interest.

ISSN 1573-160X, *PHYSICAL OCEANOGRAPHY*, Vol. 32, Iss. 1, pp. 133-149 (2025)
Original Russian Text © D. V. Kalinskaya, 2025,
published in *Morskoy Gidrofizicheskiy Zhurnal*, 2025, Vol. 41, Iss. 1, pp. 101–118

Original article

Research of the Angstrom Parameter Variability over the Black Sea Region

D. V. Kalinskaya

Marine Hydrophysical Institute of RAS, *Sevastopol*, *Russian Federation*
✉ *kalinskaya_d_v@mail.ru*

Abstract
Purpose. The study is purposed at identifying the variability features of the Angstrom parameter values obtained at the Black Sea stations Sevastopol and *Section*_7 of the AERONET network from spring 2019 to spring 2024 based on the satellite and ground monitoring data, as well as the results of atmospheric dynamics modeling.
Methods and Results. Comparative analysis and assessment of the Angstrom parameter values involved application of the following information on atmospheric aerosol: the data of ground-based measurements derived by a portable SPM photometer, the photometer at the stations of the AERONET international aerosol monitoring network, the VIIRS radiometer platform from the Suomi NPP satellite, the data on concentrations of suspended particles of PM2.5 and PM10 resulted from the Espada M3 detector measurements, as well as the results of atmosphere dynamics modeling (data of the HYSPLIT and SILAM models). The comparative analysis made it possible to reveal the dates on which the optical characteristics corresponding to dust aerosol were recorded at one of two indicated stations in the Black Sea, whereas at the other one, no aerosol of this type (i.e. optical characteristics corresponded to a clean atmosphere) was detected. This fact confirms the different aerosol loading in the atmosphere over the western and central parts of the Black Sea, and also the spatial variability of aerosol basic optical characteristics during dust transport from the Sahara Desert. The measurements of the PM2.5 and PM10 particle concentrations performed on the days with the background optical characteristics of atmospheric aerosol permitted to obtain the values of background characteristics of suspended particles: PM2.5 = 7 μg/m^3 and PM10 = 8 μg/m^3).
Conclusions. Low values of the Angstrom parameter (less than 0.8) do not by themselves indicate the presence of an aerosol, such as dust or smoke, in the atmosphere. However, being combined with high (exceeding the background values by more than 1.5 times) values of aerosol optical thickness and concentrations of PM2.5 and PM10 particles (exceeding the background values by more than 3 times), the data set is an evidence of the presence of aerosol – dust or smoke – in the atmosphere. It is noted that the aerosols of such types can be detected by the measurements of PM2.5 and PM10 particle concentrations only when they are in the atmosphere surface layer. Therefore, the conclusions on presence of these types of aerosols in the atmosphere, being based only on the measurements of calculated concentrations, are not reliable.
Keywords: SPM, AERONET, VIIRS, SILAM, reverse trajectories, HYSPLIT, Angstrom parameter, dust aerosol, aerosol, smoke, spectral coefficient of sea brightness, aerosol optical thickness, AOD, Black Sea, atmospheric aerosol, satellite monitoring, ground monitoring, optical characteristics

Acknowledgements: The work was carried within the framework of theme of state assignment of Marine Hydriphysical Institute, RAS FNNN-2024-0012 “Analysis, nowcast and forecast of the state of hydrophysical and hydrochemical fields of marine water areas based on mathematical modeling using the data of remote and contact measurement methods”. The author is grateful to S.M. Sakerin and D.M. Kabanov for providing the *SPM* photometer and its software. The author thanks Tom Kucsera, Brent Holben, Giuseppe Zibordi and the group of Gene Feldman from *NASA* for providing the AOD data, calculating the *BTA* data, processing the measurement results obtained at the Sevastopol *AERONET* station, as well as for the opportunity to use high-quality photometric measurement data.

For citation: Kalinskaya, D.V., 2025. Research of the Angstrom Parameter Variability over the Black Sea Region. *Physical Oceanography*, 32(1), pp. 133-149.

Introduction

The need to study various types of aerosols is due to a number of factors affecting the upper layer of water in basins. Firstly, aerosols can be transported over significant distances from their sources, thereby influencing changes in the chemical composition of the atmosphere above regions [1, 2].

Secondly, aerosols of various origins affect the accuracy of the reconstruction of the spectral variability of the radiance coefficient of upward radiation [2–4]. Since the bio-optical characteristics of water bodies are analyzed by satellite data, in order to correctly assess these characteristics, it is necessary to consider what kind of aerosol is present in the atmosphere above the region under study [5–9]. Aerosols (such as dust and smoke) do not provide an opportunity to obtain objective estimates because the standard atmospheric correction algorithm used by NASA does not take into account the stratification of such aerosols [1, 10].

Thirdly, aerosol contains microelements, especially nitrogen, phosphorus, and silicon, which can serve as additional nutrient sources for phytoplankton when deposited in the upper layer of water bodies [11, 12]. Depending on which type of aerosol is identified in the atmosphere above the region under study as a result of transport, it is determined which microelements will end up in the upper layer of water after precipitation.

Currently, various aerosol fractions, i.e., the distribution of aerosol particles according to their size, are widely studied. The coarse fraction (0.6–10 μm) falls in the range of near-zero values of the Angstrom indices. The situation with the submicron fraction of the aerosol (0.1–0.6 μm) is more complicated, since the Angstrom parameter varies with a shift of the maximum of the size distribution function within this interval.

During the development of a dust storm, heat exchange processes and changes in the dynamics of microphysical processes are accompanied by strong winds and the intrusion of a cold air front. This leads to the transport of a large amount of the aerosol dust fraction with particles larger than 2 μm and to a decrease in the content of the finely dispersed (submicron) fraction, which is explained by the following causes:

1) intrusion of denser air masses with high dust content, which can lead to mechanical displacement of suspended particles of the submicron fraction into higher air layers;

2) adhesion of submicron fraction aerosol particles to coarse fraction dust particles;

3) expulsion of finely dispersed negatively charged dust particles by the negative electrostatic field of the earth’s surface.

Particles in the background submicron fraction that collide with larger dust storm particles and take electrons from them become negatively charged, and coarser particles become positively charged. The submicron particles then rise higher under the influence of the Earth's electrostatic field. The development of a dust storm promotes processes that include the acquisition of a negative charge as a result of collisions between fine particles and a positive charge between large particles, which promotes the stratification of the dust cloud. This is why dust haze can be observed in stripes [13]. As a result, the ejection of soil particles by electrostatic forces increases. Measurements of ion concentration in the dispersed phase of air at 500 and 6000 m level in a clean and dusty atmosphere [14–16] indicate an increase in the concentration of negatively charged ions and a simultaneous decrease in the number of positively charged ions during a dust storm, which also confirms the electrostatic hypothesis.

Heavy dust storms are often followed by prolonged torrential rainfall, even in summer. In this case, the most wash-out resistant component of the atmospheric aerosol is the submicron fraction. It remains in the atmosphere after intense rainfall, and the coarse fraction decreases to almost 0. After rainfall, the coarse fraction of the aerosol is completely restored in the atmosphere only after several days. An additional band appears in the spectrum at 1300 cm^{-1}; it is associated with an increase in the nitrate content of the aerosol. The decrease of the band at 1400 cm^{-1} compared to 1300 cm^{-1} is associated with the decrease of inorganic carbonates. The silicate content in the submicron fraction of the aerosol decreases.

Studies of the main optical properties over the Black Sea have been relevant and in demand since the beginning of the 20th century, although a detailed analysis of the spatio-temporal variability of the Angstrom parameters for this region is still a poorly understood problem in marine and atmospheric optics.

The purpose of the study is to perform a comparative analysis and estimation of Angstrom parameter values obtained at the Black Sea stations *Sevastopol* and *Section*_7 of the AERONET network from spring 2019 to spring 2024 using satellite and ground-based monitoring data, as well as the results of atmospheric dynamics modeling.

Research methods and instruments

In this work, the following types of atmospheric aerosol data have been used: data from measurements with a portable SPM photometer [17], photometers from stations of the international aerosol monitoring network AERONET, the VIIRS radiometer from the Suomi NPP satellite [18–20]; data from the HYSPLIT and SILAM models, as well as PM2.5 and PM10 particle concentrations obtained from measurements with the Espada M3 detector. Particulate matter (PM) is an atmospheric pollutant that is most often analyzed in terms of mass concentrations of particles.

The Angstrom parameter (α) is the exponent name in the formula for the dependence of aerosol optical thickness on the wavelength

$$\tau(\lambda)/\tau(\lambda_0) = (\lambda/\lambda_0)^{-\alpha}, \qquad (1)$$

where $\tau(\lambda)$ is the optical thickness at a given wavelength; $\lambda_0\lambda$; λ_0 is the standard (reference) wavelength [1].

The aerosol optical depth (AOD) of the atmosphere is most commonly calculated using the Bouguer law, which is based on the spectral attenuation of direct solar radiation. In this case, the light attenuation due to the Rayleigh molecular scattering and absorption by the gaseous components of the atmosphere is calculated to determine the AOD, which is then subtracted from the total optical depth of the atmosphere [21]. AOD is an indicator of the variability of the optical properties of the atmosphere due to the correlation between the concentrations of aerosol particles and the light attenuation coefficients, the data of which are obtained through the widespread use of satellite remote sensing methods [22, 23]. Various aerosol fractions, i.e., the distribution of aerosol particles according to their size, are widely studied nowadays. The coarse fraction (0.6-10 μm) falls in the range of near zero values of the Angstrom indices. The situation with the submicron fraction of the aerosol (0.1-0.6 μm) is more complicated, since the Angstrom parameter varies with a shift of the maximum of the size distribution function within this interval.

In this work, for the calculation of the AOD we use the measurements of photometers (SPM and CIMEL) at wavelengths λ within 340−2134 nm, except for the 936 nm channel, according to the measurements on which the water vapor content in the atmospheric column is determined [17, 22, 23].

The Visible Infrared Imaging Radiometer Suite (*VIIRS*) provides Deep Blue NASA Standard Level-2 (L2) aerosol products from the Joint Polar Satellite System (JPSS). VIIRS provides satellite measurements of AOD and aerosol properties over land and ocean as daily data with a 6-min step. To obtain AOD values, the VIIRS Deep Blue Aerosol (DB) algorithm has been proposed since February 17, 2018 [21]. Based on the results of the algorithms, an array of scientific data containing information on 55 layers is created. The DB algorithm is designed to determine the aerosol type over land, and the Satellite Ocean Aerosol Retrieval (SOAR) algorithm – over water (water areas). As a result of processing the signals received at certain operating ranges of VIIRS, the data on AOD L2DeepBlue are obtained by two algorithms, and this is a reference data at the wavelength of 550 nm [18−20].

Both algorithms allow to determine the atmospheric aerosol type during the daytime in the absence of clouds and snow. On land, the aerosol type is classified based on the AOD values, the Angstrom parameter (α), the Lambert Equivalent Reflectivity (LER), and the brightness temperature. The combined aerosol type over land and ocean is determined based on pixels that have passed the quality check [20].

The SILAM software package is widely used to study the impact of forest fires, volcanic eruptions, dust transport and other natural and industrial disasters on atmospheric pollution in general. The calculation scheme for these effects is based on the Lagrange – Euler model. The SILAM pollutant dispersion computer modeling system developed by the Finnish Meteorological Institute is a modern, powerful tool

---

[1] *Ångström A.*, 1929. On the Atmospheric Transmission of Sun Radiation and on Dust in the Air. *Geografiska Annaler*, 11(2), pp. 156-166. https://doi.org/10.1080/20014422.1929.11880498

for modeling the dispersion characteristics of aerosols, gas components, dust particles, radionuclides, and natural allergens in the atmosphere [24].

The SILAM model provides the maps showing concentrations of fine particles up to 2.5 μm in diameter (PM2.5) and coarse particles up to 10 μm in diameter (PM10) at 10 m above ground level. Local pollution cannot be identified with the SILAM model, but it visualizes global pollution well [24–27].

In order to find sources of different types of aerosols over the Black Sea, the HYSPLIT software package [2] for modeling reverse trajectories of flow motion is used in this work. For estimating the concentration of particulate matter, the results of measurements by the Espada M3 detector (http://www.ocrkj.com) of Chinese manufacture are used. They provide air quality monitoring according to the following parameters:

– PM2.5 is aerosol microparticles (PM2.5 and PM10 measurement range 0−2500 μg/m³);

– PM10 is aerosol particles larger than 10 μm;

– TVOC is volatile organic compounds, including toxic benzene and styrene (TVOC measurement range is 0 – 2.5 mg/m³);

– AQI is Air Quality Index, one of the integrated indicators of air pollution in the atmosphere. The air quality index is a piecewise linear function of the concentration of pollutants in the atmosphere: sulfur dioxide (SO_2), nitrogen dioxide (NO_2), PM10 and PM2.5, carbon monoxide (CO), and ozone (O_3). The US Environmental Protection Agency (EPA) has established national air quality standards for each of these pollutants. The AQI calculation is based on the ratio of the measured average concentration of a pollutant to its standard (allowable) concentration.

The detector has a color TFT display for showing information about the air condition on several screens. LED ring is an air quality indicator and can change color from green to red depending on the values of the measured parameters, where green corresponds to the norm and red – to the critical level of pollution.

Results

As a result of measurement data retrieval from the *SPM* photometer of *Sevastopol* station and the CIMEL photometer of the *Section*_7 station of the international AERONET network for the period from 27.08.2019 to 31.03.2024, 60 dates were obtained on which the calculated values of the Angstrom parameter at the stations differed by more than 2.5 times. Figure 1 indicates five dates where the α values differed by more than 10 times. Out of 60 dates of the period under study, 17 of them showed differences in values of more than 5 times. The maximum difference in the values of the Angstrom parameters (more than 27 times) was obtained on 09.09.2020 ($\alpha_{SPM} = 0.05$, and $\alpha_{AERONET} = 1.46$). Such a difference in values indicates

[2] Draxler, R.R. and Rolph, G.D., 2010. *HYSPLIT (HYbrid Single-Particle Lagrangian Integrated Trajectory) Model Access via NOAA ARL READY Website*. Silver Spring, MD: NOAA Air Resources Laboratory.

that different types of aerosol were observed in the atmosphere over the western and central parts of the Black Sea.

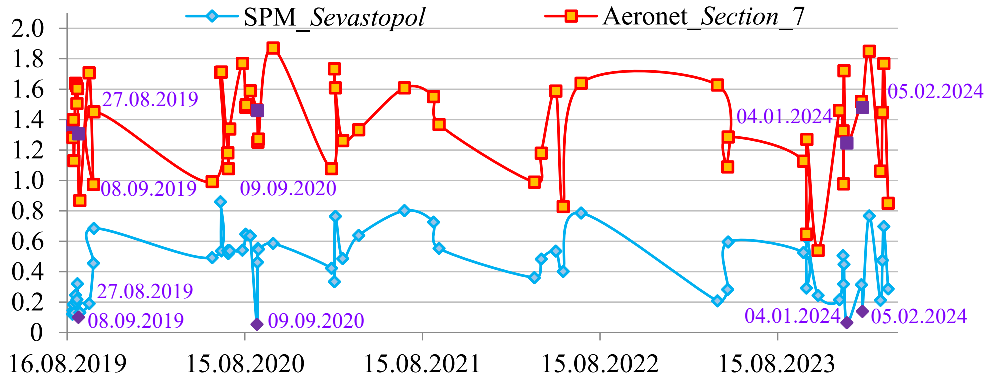

F i g. 1. The Angstrom parameter values at the stations of AERONET network: *Sevastopol* – based on the *SPM* photometer data, and *Section*_7 – based on the CIMEL photometer data

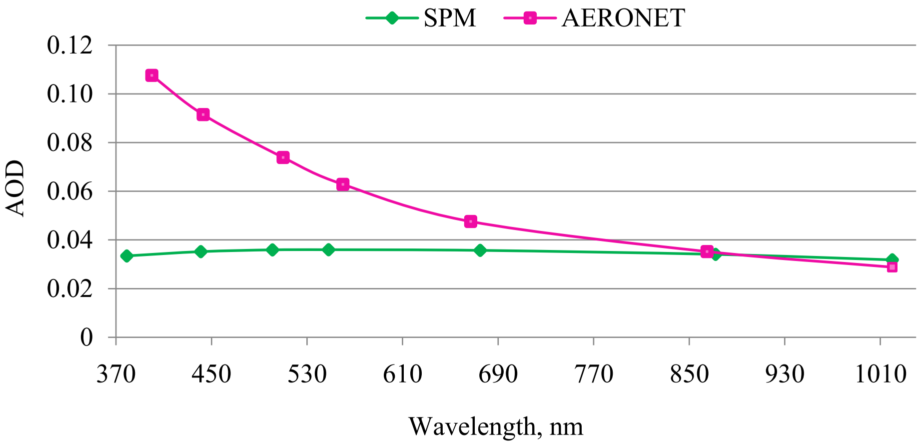

F i g. 2. Spectral variability of AOD values at the stations of AERONET network: *Section*_7 – based on the *CIMEL* photometer measurements, and *Sevastopol* – based on the *SPM* photometer data on 09.09.2020

The analysis of the main optical characteristics revealed that the AOD spectral behavior obtained from the data of two photometers for 09.09.2020 varies greatly in the wavelength range of 380-680 nm. For example, a comparative analysis of the AOD values at a wavelength of 500 nm (AOD(500)) showed a twofold difference in values. However, it is worth noting that both at *Sevastopol* station and *Section*_7 station the obtained AOD values are several times lower than the background values (for *Sevastopol* station AOD(500) = 0.036 at a background AOD(500) = 0.18, and for *Section*_7 AOD(510) = 0.074 at a background AOD(510) = 0.15 (Fig. 2)). When studying the atmosphere over different regions, the background characteristics of the atmospheric aerosol are determined to identify anomalous situations. In this paper, background aerosol refers to the average values of the optical properties, excluding outliers (jumps in values).

Analysis of satellite images on 09.09.2020 revealed that the atmosphere over the Black Sea was clear (minimal cloudiness) (Fig. 3, *a*). For all studied areas of the Black Sea region, the predominant aerosol type for that day was indicated using the *DB* algorithm: over the western part of the Black Sea – dust and mixed, and over the *Sevastopol* station – background (Fig. 3, *b*).

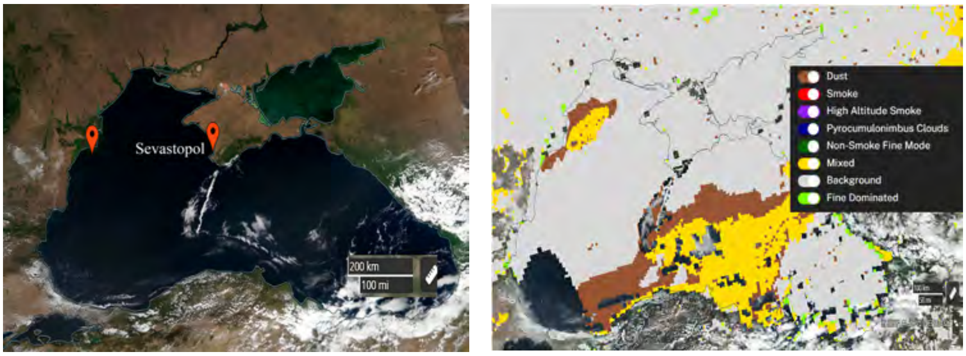

a *b*

F i g. 3. *VIIRS* spectroradiometer images: color-synthesized in natural colors (TrueColor) (*a*), and obtained using the Satellite Ocean Aerosol Retrieval algorithm (*b*) for 09.09.2020 (Source: AERDB_L2_VIIRS_NOAA20_NRT doi:10.5067/VIIRS/AERDB_L2_VIIRS_NOAA20_NRT.002; AERDB_L2_VIIRS_NOAA20 doi:10.5067/VIIRS/AERDB_L2_VIIRS_NOAA20.002)

For the day with the maximum variation of the α-values, the HYSPLIT modeling data of the reverse trajectories (Fig. 4) and the SILAM loading data of the dust aerosol (Fig. 5) were analyzed. The HYSPLIT model results revealed that at two heights (2000 and 3000 m) the transport from the northeast is recorded for both stations. The data on the transport direction at 1500 m height are different: for the western Black Sea station *Section*_7 transport from the northeast is observed, and for *Sevastopol* station (as well as for two other heights) – from the northwest (Fig. 4, *a*).

The dust aerosol loading data from the SILAM model were used to obtain the dust concentrations for both stations. As shown in Fig. 5, *a*, the dust concentration at *Sevastopol* station on 09.09.2020 was zero (no dust detected), while at the western Black Sea station its value reached 60 μg/m^3 at 14:00. According to Figure 5, *b*, the source of dust activity on this day moved from the Karakum Desert along the Caspian Sea towards the northwest, and the reverse trajectories, according to the HYSPLIT model results for *Section*_7 station, passed precisely through the area of the dust cloud (see Fig. 4, *b*).

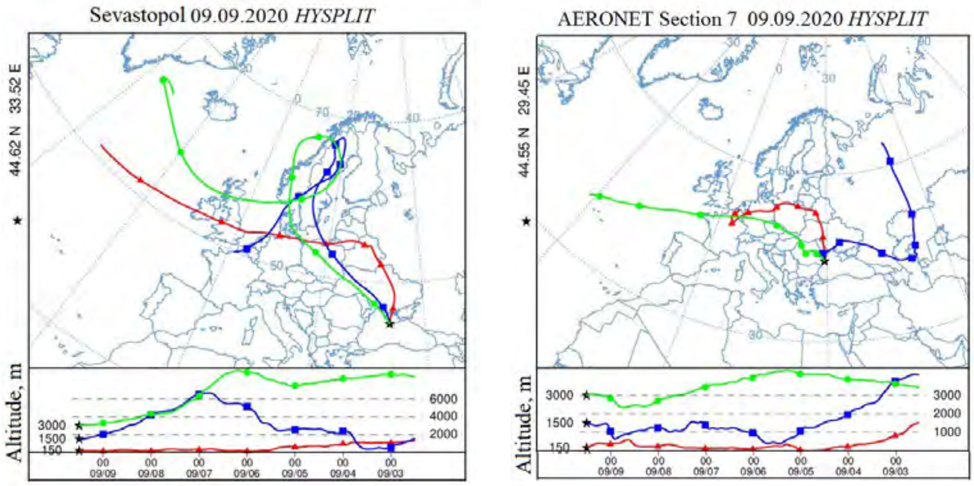

a *b*

F i g. 4. Reverse trajectories of air flow transfer based on the results of HYSPLIT modeling for the stations of AERONET network: *Sevastopol* (*a*) and *Section_7* (*b*) for 09.09.2020 (Available at: http://ready.arl.noaa.gov/HYSPLIT.php)

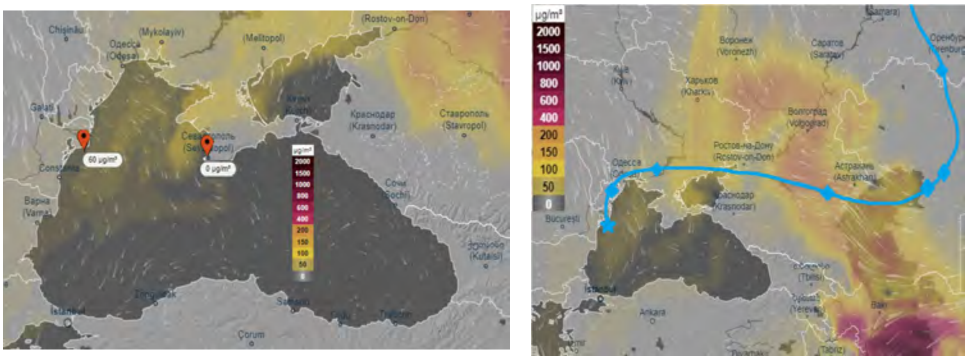

a *b*

F i g. 5. Results of modeling dust concentration in the atmosphere based on the SILAM data for the stations of AERONET network *Sevastopol* and *Section_7* for 09.09.2020 (Available at: https://thredds.silam.fmi.fi/thredds/catalog/catalog.html)

As a result of the analysis of variability of the Angstrom parameter (Fig. 1), the period from 27.08.2019 to 30.09.2019 was indicated, when the values of two stations differed by 5 times or more during the month. The maximum difference of 13 times was recorded on 08.09.2019 (α_{SPM} = 0.1, and $\alpha_{AERONET}$ = 1.31), and the minimum difference of 5 times was recorded on 06.09.2019 (α_{SPM} = 0.3, and $\alpha_{AERONET}$ = 1.6). The dates 27.08.2019 and 30.09.2019, when the Angstrom parameter values differed by 11 and 9 times, respectively, are also indicated in Fig. 6.

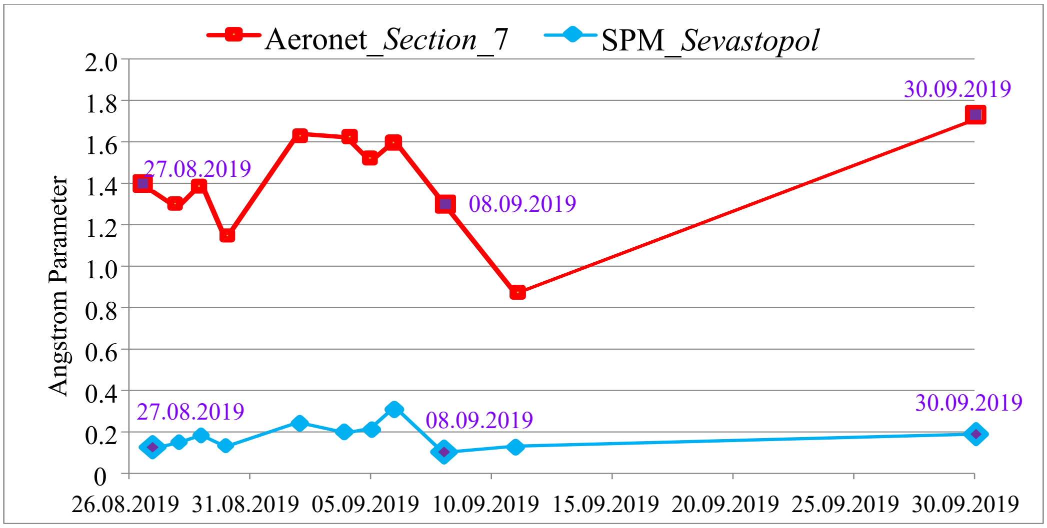

F i g. 6. The Angstrom parameter for the stations of AERONET network *Sevastopol* and *Section*_7 for the period 27.08.2019–30.09.2019

Another quality characteristic of atmospheric air and aerosol is the concentration of PM2.5 and PM10 particles. The concentration of particles is obtained only for the ground layer, which is why the characteristic cannot fully reflect the situation of aerosol loading. This characteristic is applied to estimate local emissions, for example, near industrial facilities or near agricultural fields where insecticides are utilized. AOD, unlike PM concentration, is measured in the entire column of the atmosphere [18, 22], thus, its analysis is more often used to determine the atmospheric condition over the region under study.

In order to exclude the influence of local emissions of aerosol pollution caused by large-scale aerosol transport from June 2023 to May 2024 on the accuracy of particle concentration determination, we analyzed a dataset comprising *PM*2.5 and PM10 particle concentrations obtained from the Espada M3 detector, AOD spectral values from the SPM photometer, VIIRS satellite data, and aerosol data from the SILAM model. Analysis of all these data is required to assess the impact of aerosol deposition on the surface layer of the Black Sea. The detection of aerosol containing trace elements (nitrogen, phosphorus, and silicon) is important, since during deposition it enters the upper layer of water bodies and can subsequently cause a short-term increase in phytoplankton bioproductivity [28−32]. When the additional supply of trace elements ceases, bioproductivity returns to the original level.

Previously, background values of the main optical characteristics were obtained for *Sevastopol* station [13, 33]. For days with such characteristics we performed variability analysis of PM2.5 and PM10 values, which made it possible to obtain background values of concentration of small and large particles: $PM2.5 = 7\ \mu g/m^3$, $PM10 = 8\ \mu g/m^3$.

Throughout the day of November 30, low AOD values relative to the background ones were observed (average daily value of AOD(500) = 0.06). However, the particle concentration values, according to the measurements of the Espada M3 detector, exceeded the background values for that day by more than three times (PM2.5 = 23 $\mu g/m^3$, PM10 = 25 $\mu g/m^3$). Analysis of the contribution of large and small particles to the total AOD distribution for this day revealed the dominance of fine aerosol (85%). Particle concentration data from the SILAM model demonstrated minimal discrepancies with the field data (Fig. 7). These values of AOD and particle concentrations show that on 30.11.2023 the aerosol did not reach the layers of the upper atmosphere, the aerosol effect was local in the surface layer of the atmosphere up to 50 m (measurements were carried out at 45 m height), and the ground aerosol made a minimal contribution to the total AOD value of the entire atmospheric layer.

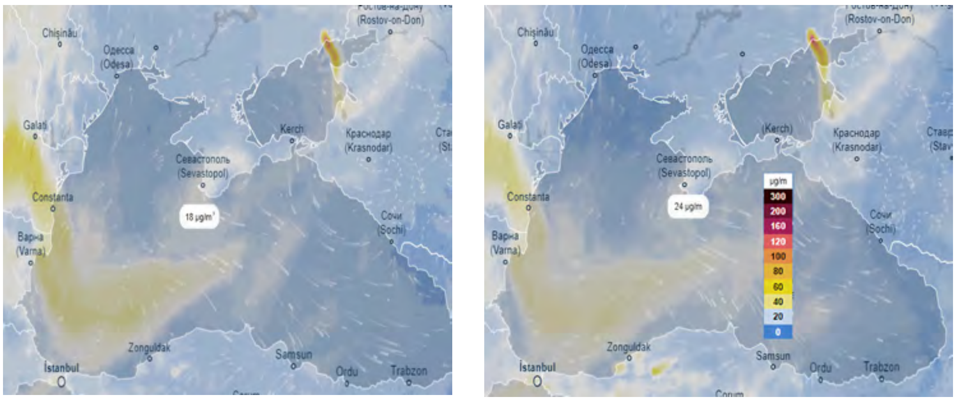

a *b*

F i g. 7. Results of simulating the concentrations of PM2.5 (a) and PM10 (b) particles based on the SILAM data at 22:00 on 29.11.2021

In the period from 07.10.2023 to 07.11.2023, abnormally low values of the Angstrom parameter and AOD were obtained (Fig. 8). Out of 13 days of measurements, only on one day (23.10.2023) the values of the aerosol optical depth (AOD(500) = 0.26) exceeded the background values, however, the values of the Angstrom parameter ($\alpha = 0.3$) for this day were also much lower than the background value ($\alpha = 1.25$). Sunny clear weather was observed on 23.10.2023 until 14:00. During this period of the day, the values of the main optical properties were different from the background values. This corresponds to the presence of aerosol in the atmosphere, such as dust aerosol or smoke. At the same time, according to the Espada M3 detector, the concentration values of PM2.5 particles did not exceed 12 $\mu g/m^3$ and PM10 – 13 $\mu g/m^3$.

After 14:00, a continuous dense haze appeared in the sky, making it impossible to continue measurements with the photometer. However, measurements with the detector do not depend on the presence of the sun, so the monitoring of the concentration values was continued. As a result of the measurements, a gradual increase in the concentration of particles was recorded: at 17:30 the PM2.5 values were 27 μg/m^3 and PM10 values were 34 μg/m^3; at 21:30 they reached a maximum – PM2.5 = 31 μg/m^3 and PM10 = 36 μg/m^3. This type of variability of atmospheric parameters indicates that aerosol particles were above the surface layer at the beginning of the day (which was confirmed by increased AOD values), and then, gradually settling on the underlying surface, began to coagulate moisture, forming a layer of haze.

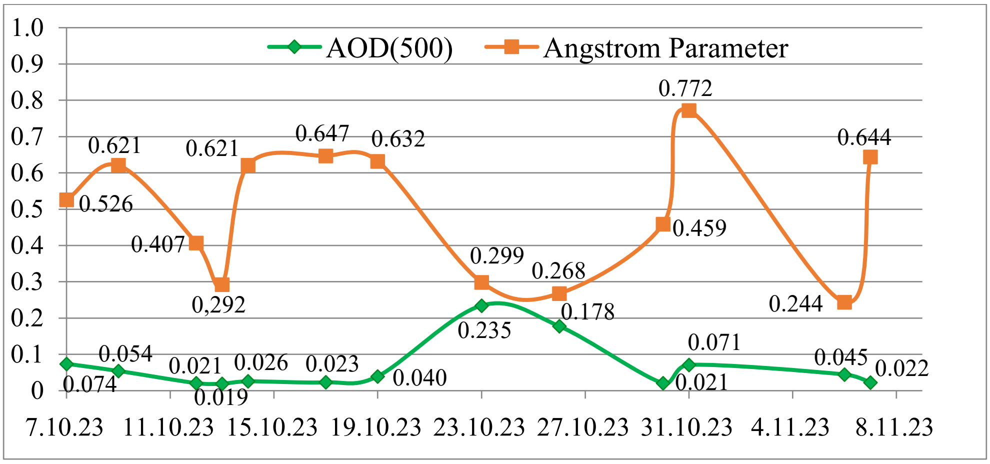

F i g. 8. The Angstrom parameter and AOD(500) based on the SPM photometer data at *Sevastopol* station

It is noteworthy that at the beginning and in the middle of the day large and small particles were present in the surface layer in average amounts (detector data within the annual average values of PM2.5 = 11 μg/m^3 and PM10 = 12 μg/m^3). Intense deposition of aerosol particles began after 14:00, due to this fact their maximum amount fell on the underlying surface at 21:30, which is confirmed by the maximum values of the concentration of PM2.5 and PM10 particles. Satellite data confirm the transport of dust aerosols from the Sahara on 23.10.2023 (Fig. 9, *a*, *b*). VIIRS AOD(500) values in the range from 0.27 to 0.275 (marked on the scale (Fig. 9, *c*)) are close to the photometric natural values obtained at *Sevastopol* station.

Previous studies have shown that dust transport events over the Black Sea last from 1 to 10 days [1, 13, 34]. To determine the onset of the transport event, data from the second half of October were analyzed. The AOD values on 19.10.2023 obtained at *Sevastopol* station from SPM measurements corresponded to the AOD values of a clear atmosphere (AOD(500) = 0.040), as did the VIIRS satellite data AOD(500) = 0.04, which are in complete agreement with the field data (marked on the AOD scale (Fig. 10, *a*)). The chlorophyll a concentration values for this day are typical for October (Fig. 10, *b*).

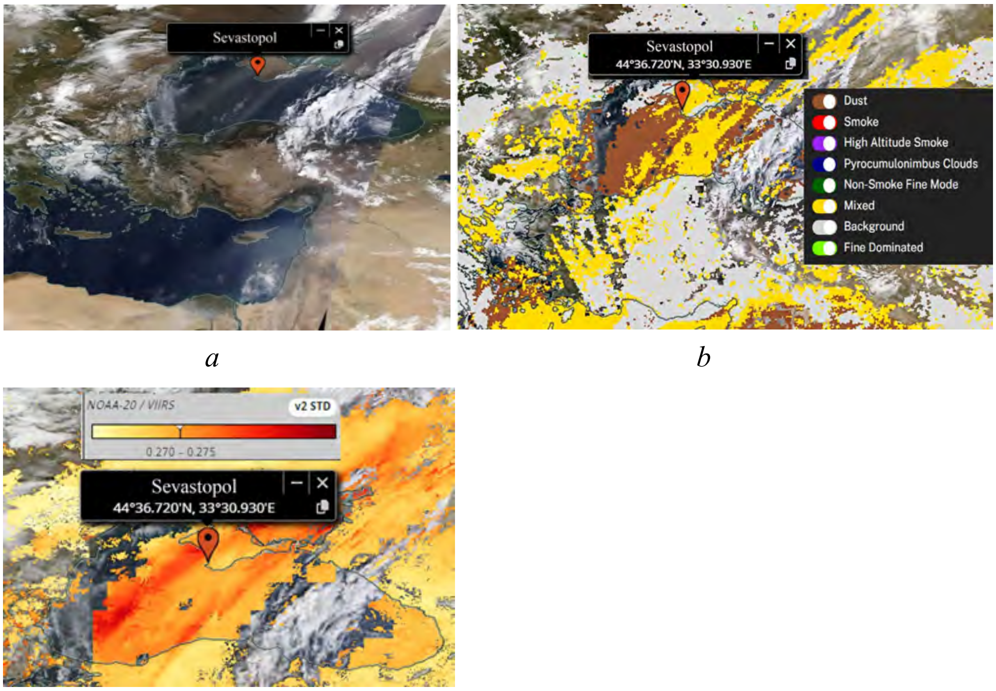

a *b*

c

F i g. 9. Satellite images of dust transfer obtained by the VIIRS spectroradiometer for 23.10.2023: color-synthesized in natural colors (TrueColor) (*a*); obtained using the Satellite Ocean Aerosol Retrieval algorithm (*b*) and obtained using satellite AOD(500) measurements (*c*)

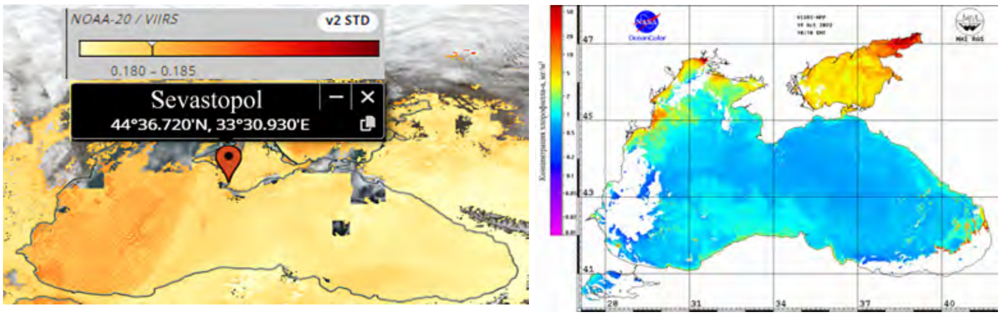

a *b*

F i g. 10. Spatial distribution of aerosol optical depth at a wavelength 500 nm (*a*) and chlorophyll a concentration based on the VIIRS satellite data obtained over the Black Sea region (*b*) for 19.10.2023

As early as 20.10.2023, the atmospheric parameters over the western part of the Black Sea water area and coast changed according to photometric, satellite and modeling data. It is the date of 20.10.2023 that marks the beginning of dust transport from the Sahara (Fig. 11). As can be seen in Fig. 11, the western part of the water surface, where the chlorophyll a concentration values were not determined, is not covered by clouds; thus, the absence of data can only be explained by the presence of a large number of aerosol particles over this area. This fact is confirmed by the high AOD values and the dominant dust type of aerosol according to the *VIIRS* radiometer data (Fig. 11).

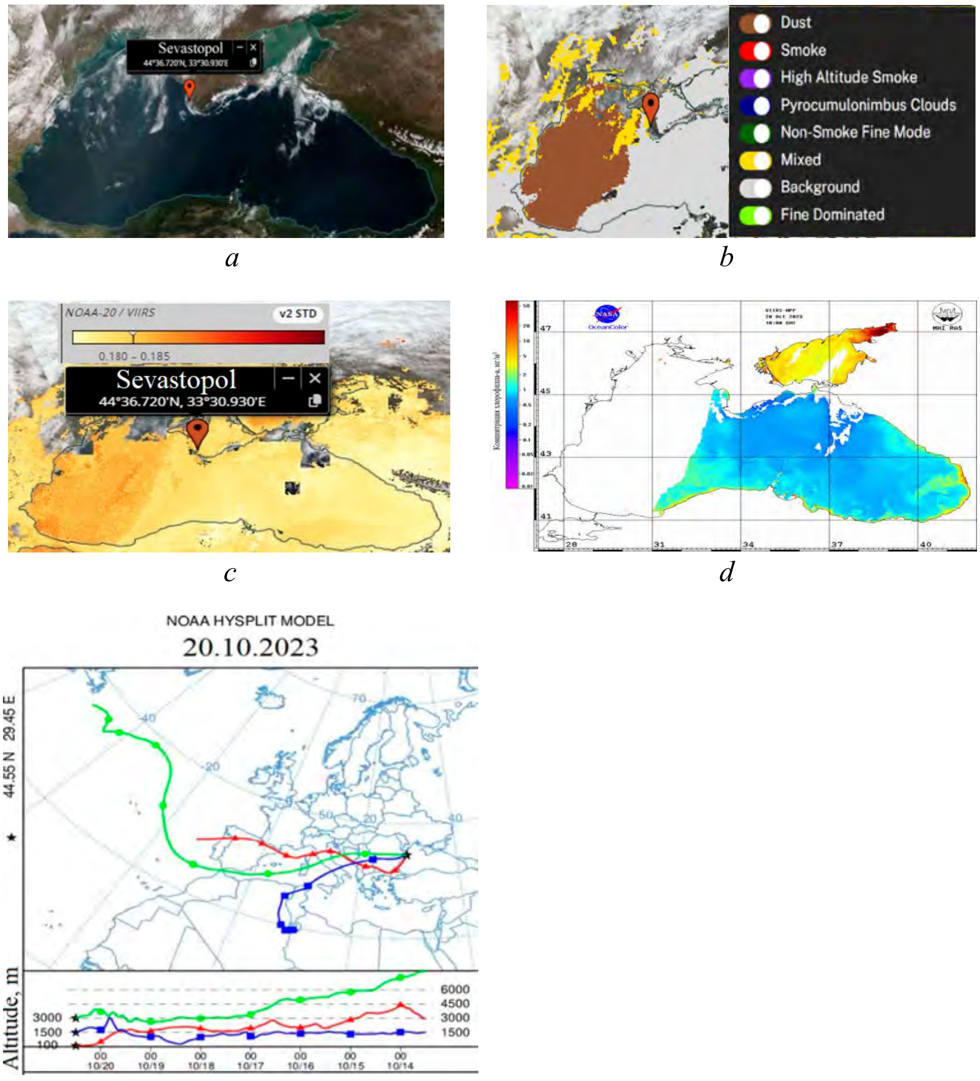

F i g. 11. Satellite images: color-synthesized in natural colors (*TrueColor*) (*a*), obtained using the Satellite Ocean Aerosol Retrieval algorithm (*b*), obtained using the AOD(500) satellite measurements (*c*) and chlorophyll a concentration (*d*) based on the VIIRS satellite data obtained over the Black Sea region on 20.10.2023; reverse trajectories of air flow transfer based on the results of HYSPLIT modeling for the western Black Sea station

Analysis of satellite, field and modeling data revealed that the end of dust transport over the Black Sea stations was recorded on 29.10.2023 (the dust plume shifted towards the southwestern coast during that day), and on 30.10.2023 dust aerosol was completely absent in the atmosphere over the entire Black Sea water area and coast. This means that low values of the Angstrom parameter alone do not indicate the presence of aerosol, such as dust or smoke in the atmosphere. However, in combination with high values of the aerosol optical thickness and the concentration of PM2.5 and PM10 particles, they give grounds to assert that there is an aerosol of these two types over the study area (at the same time, it cannot be asserted that it is present over the entire study area).

Conclusion

A comparative analysis of the Angstrom parameter values at the Black Sea stations *Sevastopol* and *Section_7* allowed us to identify the dates when optical characteristics corresponding to dust aerosol were recorded at one station, while this type of aerosol was not recorded at the other station. This confirms different aerosol load over the western and central parts of the Black Sea and spatial variability of the main optical properties of the aerosol when recording dust transport from the Sahara Desert.

The measurements of PM2.5 and PM10 particle concentrations on days with background optical characteristics of atmospheric aerosol allowed us to obtain the values of the background characteristics of suspended particles (PM2.5 = 7 μg/m^3, PM10 = 8 μg/m^3).

The principal conclusion of the study is that low values of the Angstrom parameter in combination with high (exceeding the background ones by more than 1.5 times) values of the aerosol optical depth as well as high (exceeding the background ones by more than 3 times) values of the concentration of $PM2.5$ and $PM10$ particles indicate the presence of dust aerosol or smoke from fires in the atmosphere over the study area. However, if only low values of the Angstrom parameter are obtained at the photometric station, this does not indicate the presence of an aerosol such as dust or smoke in the atmosphere. This work reveals that the presence of these types of aerosols over one area of the Black Sea region (over Sevastopol) does not mean their presence over the entire Black Sea region.

REFERENCES

1. Kalinskaya, D.V. and Varenik, A.V., 2019. *The* Research of the Dust Transport Impact on the Biogeochemical Characteristics of the Black Sea Surface Layer. In: SPIE, 2019. *Proceeding of SPIE. 25th International Symposium on Atmospheric and Ocean Optics: Atmospheric Physics*. Vol. 11208, 1120845. https://doi.org/10.1117/12.2540432
2. Korchemkina, E.N. and Kalinskaya, D.V., 2022. Algorithm of Additional Correction of Level 2 Remote Sensing Reflectance Data Using Modelling of the Optical Properties of the Black Sea Waters. *Remote Sensing*, 14(4), 831. https://doi.org/10.3390/rs14040831
3. Kopelevich, O.V., Saling, I.V., Vazyulya, S.V., Glukhovets, D.I., Sheberstov, S.V., Burenkov, V.I. and Yushmanova, A.V., 2018. *Bio-Optical Characteristics of the Seas, Surrounding the Western Part of Russia, from Data of the Satellite Ocean Color Scanners of 1998–2017*. Moscow: Institute of Oceanology RAS, 140 p. (in Russian).
4. Kopelevich, O.V., Sheberstov, S.V. and Vazyulya, S.V., 2020. [Underwater Light Field in the Surface Layer of the Barents Sea and the Spectral Brightness Coefficient of the Water Column under Various Oceanological Conditions]. In: SRI RAS, 2020. *Proceedings of the 18th All-Russian Open Conference "Modern Problems of Remote Probing the Earth from Space"*. Moscow: Space Research Institute of RAS Publishing, p. 216. https://doi.org/10.21046/18DZZconf-2020a (in Russian).

5. Korchemkina, E.N., Shibanov, E.B. and Lee, M.E., 2009. Atmospheric Correction Improvement for the Remote Sensing of Black Sea Waters. *Issledovanie Zemli iz Kosmosa*, (6), pp. 24-30 (in Russian).
6. Kopelevich, O.V., Burenkov, V.I. and Sheberstov, S.V., 2006. Development and Use of Regional Algorithms for Calculating the Bio-Optical Characteristics of the Seas of Russia from the Data of Satellite Color Scanners. *Current Problems in Remote Sensing of the Earth from Space*, 3(2), pp. 99-105 (in Russian).
7. Suetin, V.S., Korolev, S.N., Suslin, V.V. and Kucheryavyi, A.A., 2004. Manifestation of Specific Features of the Optical Properties of Atmospheric Aerosol over the Black Sea in the Interpretation of SeaWiFS Data. *Physical Oceanography*, 14(1), pp. 57-65. https://doi.org/10.1023/B:POCE.0000025370.99460.88
8. Suetin, V.S., Korolev, S.N., Suslin, V.V. and Kucheryavyi, A.A., 2008. Improved Interpretation of the Data of Observation of the Black Sea by a SeaWiFS Satellite Instrument in Autumn 1998. *Physical Oceanography*, 18(2), pp. 106-115. https://doi.org/10.1007/s11110-008-9011-9
9. Suetin, V.S., Korolev, S.N. and Kucheryavy, A.A., 2014. Application of Satellite Observations for Determining Spectral Dependencies of the Black Sea Waters Optical Characteristics. *Morskoy Gidrofizicheskiy Zhurnal*, (3), pp.77-86 (in Russian).
10. Khodzhakhon, M.I., Nazarov, B.I., Abdullaev, S.F. and Karieva, R.A., 2017. Mineralogical Composition of Dust Aerosol during Dust Storms. *Doklady Akademii Nauk Respubliki Tadzhikistan,* 60(1-2), pp. 64-67 (in Russian).
11. Varenik, A.V., 2017. Inorganic Nitrogen in the Atmospheric Precipitations in Sevastopol: Sources, Variations and Influence on the Surface Layer of Coastal Regions of the Black Sea. *Problems of Environmental Monitoring and Modeling of Ecosystems*, 28(6), pp. 75-84. https://doi.org/10.21513/0207-2564-2017-6-75-84 (in Russian).
12. Datsenko, Y.S. and Puklakov, V.V., 2020. Forecasting Phytoplankton Development in a Designed Low-Head Reservoir on the Don River. *Water Resources*, 47(1), pp. 103-112. https://doi.org/10.1134/S0097807820010042
13. Kalinskaya, D.V., 2012. Research of Optical Characteristics Features of Dust Aerosol over the Black Sea. In: MHI, 2012. *Ecological Safety of Coastal and Shelf Zones and Comprehensive Use of Shelf Resources*. Sevastopol: MHI. Iss. 26, vol. 2, pp. 151-162 (in Russian).
14. Kostianoy, A.G., 2017. Satellite Monitoring of the Ocean Climate Parameters. Part 1. *Fundamental and Applied Climatology*, (2), pp. 63-85. https://doi.org/10.21513/2410-8758-2017-2-63-85 (in Russian).
15. Kok, J.F. and Renno, N.O., 2006. Enhancement of the Emission of Mineral Dust Aerosols by Electric Forces. *Geophysical Research Letters*, 33(19), L19S10. https://doi.org/10.1029/2006GL026284
16. Nazarov, B.I., Maslov, V.A. and Abdulaev, S.F., 2010. Optical and Microphysical Parameters of Arid Dust Aerosol. *Izvestiya, Atmospheric and Oceanic Physics*, 46(4), pp. 468-474. https://doi.org/10.1134/S0001433810040055
17. Sakerin, S.M., Kabanov, D.M., Rostov, A.P., Turchinovich, S.A. and Knyazev, V.V., 2012. Sun Photometers for Measuring Spectral Air Transparency in Stationary and Mobile Conditions. *Atmospheric and Oceanic Optics*, 26(4), pp. 352-356. https://doi.org/10.1134/S102485601304012X
18. Cao, C., Xiong, J., Blonski, S., Liu, Q., Uprety, S., Shao, X., Bai, Y. and Weng, F., 2013. Suomi NPP VIIRS Sensor Data Record Verification, Validation, and Long-Term Performance Monitoring. *Journal of Geophysical Research: Atmospheres*, 118(20), pp. 11664-11678. https://doi.org/10.1002/2013JD020418
19. Wang, W., Mao, F., Pan, Z., Du, L. and Gong, W., 2017. Validation of VIIRS AOD through a Comparison with a Sun Photometer and MODIS AODs over Wuhan. *Remote Sensing*, 9(5), 403. https://doi.org/10.3390/rs9050403

20. Lee, J., Hsu, N.C., Kim, W.V., Sayer, A.M. and Tsay, S.-C., 2024. VIIRS Version 2 Deep Blue Aerosol Products. *Journal of Geophysical Research: Atmospheres*, 129(6), e2023JD040082. https://doi.org/10.1029/2023JD040082
21. Rosenberg, G.V., 1968. Optical Investigations of Atmospheric Aerosol. *Soviet Physics Uspekhi*, 11(3), pp. 353-380. https://doi.org/10.1070/PU1968v011n03ABEH003841
22. Dubovik, O. and King, M.D., 2000. A Flexible Inversion Algorithm for Retrieval of Aerosol Optical Properties from Sun and Sky Radiance Measurements. *Journal of Geophysical Research: Atmospheres*, 105(D16), pp. 20673-20696. https://doi.org/10.1029/2000JD900282
23. Dubovik, O., Holben, B., Eck, T.F., Smirnov, A., Kaufman, Y.J., King, M.D., Tanré, D. and Slutsker, I., 2002. Variability of Absorption and Optical Properties of Key Aerosol Types Observed in Worldwide Locations. *Journal of the Atmospheric Sciences*, 59(3), pp. 590-608. https://doi.org/10.1175/1520-0469(2002)059<0590:voaaop>2.0.co;2
24. Sofiev, M., Siljamo, P., Valkama, I., Ilvonen, M. and Kukkonen, J., 2006. A Dispersion Modelling System SILAM and Its Evaluation against ETEX Data. *Atmospheric Environment*, 40(4), pp. 674-685. https://doi.org/10.1016/j.atmosenv.2005.09.069
25. Frohn, L.M., Geels, C., Andersen, C., Andersson, C., Bennet, C., Christensen, J.H., Im, U., Karvosenoja, N., Kindler, P.A. [et al.], 2022. Evaluation of Multidecadal High-Resolution Atmospheric Chemistry-Transport Modelling for Exposure Assessments in the Continental Nordic Countries. *Atmospheric Environment*, 290, 119334. https://doi.org/10.1016/j.atmosenv.2022.119334
26. Tiwari, A., Soni, V.K., Jena, C., Kumar, A., Bist, S. and Kouznetsov, R., 2022. Pre-Operational Validation of Air Quality Forecasting Model SILAM for India. *Journal of Pollution Effects & Control*, 10(4), 343. https://doi.org/10.35248/2375-4397.22.10.343
27. Dementeva, A.L., Zhamsueva, G.S., Zayakhanov, A.S., Tcydypov, V.V., Starikov, A.V. and Balzhanov, T.S., 2019. Variability of Aerosol Concentrations of Fractions PM_{10} and $PM_{2.5}$ in the Atmosphere Surface Layer at the Reference Monitoring Station Boyarsky. In: SPIE, 2019. *Proceeding of SPIE. Vol. 12780: 29th International Symposium on Atmospheric and Ocean Optics: Atmospheric Physics*. 127805X. https://doi.org/10.1117/12.2690736
28. Migon, C. and Sandroni, V., 1999. Phosphorus in Rainwater: Partitioning Inputs and Impact on the Surface Coastal Ocean. *Limnology and Oceanography*, 44(4), pp. 1160-1165. https://doi.org/10.4319/lo.1999.44.4.1160
29. Griffin, D.W. and Kellogg, C.A., 2004. Dust Storms and Their Impact on Ocean and Human Health: Dust in Earth's Atmosphere. *EcoHealth*, 1(3), pp. 284-295. https://doi.org/10.1007/s10393-004-0120-8
30. Middleton, N. and Kang, U., 2017. Sand and Dust Storms: Impact Mitigation. *Sustainability*, 9(6), 1053. https://doi.org/10.3390/su9061053
31. Varenik, A.V. and Konovalov, S.K., 2021. Contribution of Atmospheric Precipitation to the Supply of Nutrients in the Area of the Crimean Coast. In: SSC RAS, 2021. *Regularities in the Formation and Impact of Marine and Atmospheric Hazards and Disasters on the Coastal Zone of the Russian Federation in the Context of Global Climatic and Industrial Challenges ("Hazardous Phenomena-III"). Proceedings of the International Scientific Conference.* Rostov-on-Don: Southern Scientific Center of the Russian Academy of Sciences, pp. 253-256.
32. Orekhova, N.A., 2021. Nutrients Dynamics in the Surface Waters of the Black Sea. *Physical Oceanography*, 28(6), pp. 660-676. https://doi.org/10.22449/1573-160X-2021-6-660-676
33. Kalinskaya, D.V., Kabanov, D.M., Latushkin, A.A. and Sakerin, S.M., 2017. Atmospheric Aerosol Optical Depth Measurements in the Black Sea Region (2015-2016). *Optika Atmosfery i Okeana*, 30(6), pp. 489-496. https://doi.org/10.15372/AOO20170607 (in Russian).
34. Kalinskaya, D.V. and Papkova, A.S., 2023. Variability of the Water-Leaving Radiance under the Conditions of Dust Transport by the Satellite Sentinel-3 Data on the Example of the Black Sea and Sevastopol. *Physical Oceanography*, 30(3), pp. 369-383.

Submitted 27.04.2024; approved after review 09.09.2024;
accepted for publication 20.11.2024.

About the author:

Daria V. Kalinskaya, Junior Research Associate, Marine Hydrophysical Institute of RAS (2 Kapitanskaya Str., Sevastopol, 299011, Russian Federation), **Scopus Author ID: 56380591500**, kalinskaya@mhi-ras.ru

The author has read and approved the final manuscript.
The author declares that she has no conflict of interest.